UNIVERSITY OF MANITOBA

DOCTORAL THESIS

Physics-based characterization of complex geomaterials using stress waves based on a hybrid poromechanical and inverse method

---

By

HONGWEI LIU

A thesis submitted to the Faculty of Graduate Studies of
The University of Manitoba
in fulfillment of the requirements for the degree of

Doctor of Philosophy

Department of Civil Engineering
University of Manitoba
Winnipeg, Manitoba, Canada

Declaration of Authorship

I, HONGWEI LIU, declare that this thesis titled, “Physics-based characterization of complex geomaterials using stress waves based on a hybrid poromechanical and inverse method” and the work presented in it are my own. I confirm that:

- This work was done wholly or mainly while in candidature for a research degree at this University.
- Where any part of this thesis has previously been submitted for a degree or any other qualification at this University or any other institution, this has been clearly stated.
- Where I have consulted the published work of others, this is always clearly attributed.
- Where I have quoted from the work of others, the source is always given. With the exception of such quotations, this thesis is entirely my own work.
- I have acknowledged all main sources of help.
- Where the thesis is based on work done by myself jointly with others, I have made clear exactly what was done by others and what I have contributed myself.

Abstract

HONGWEI LIU

Physics-based characterization of complex geomaterials using stress waves based on a hybrid poromechanical and inverse method

Non-destructive testing (NDT) plays an important role in the engineering, construction, and geophysical fields. The application of NDT in civil engineering is broad from quality control, structural health monitoring of infrastructure, geophysical and geotechnical field investigation and material characterization to detection of underground anomaly, among others. More specifically, in geotechnical and permafrost engineering, the physical and mechanical properties of foundation soils are of great importance in the design of earthquake-resistant and climate-adaptive structures. One of the frequently used NDT techniques for the characterization of geomaterials is based on the propagation of stress waves generated by an excitation source (e.g., piezoelectric transducers in laboratory-scale tests or vibroimpact sources in in-situ tests). However, the existing signal interpretation methods still predominantly rely on empirical relations or subjective judgements that are insufficient for the characterization of multiphase complex geomaterials. This research aims to develop novel physics-based signal interpretation methods to characterize physical and mechanical properties of multiphase geomaterials in both field and laboratory investigation scales. For this purpose, several hybrid inverse and poromechanical models are developed to qualitatively and quantitatively characterize dry, saturated, and frozen geomaterials subject to stress waves. First, a highly-efficient semi-analytical elastodynamic forward solver was proposed for the Multichannel Analysis of Surface Waves (MASW) using the spectral element technique to determine effectively and efficiently the soil stratigraphy as well as soil properties. Next, a coupled piezoelectric and solid mechanics model is proposed to study the real response of the bender element (BE) and its interaction with soil samples in the BE test. A comprehensive laboratory investigation is also performed to better understand the response of the BEs inside different soil types. Then, a two-phase poromechanics-based

signal interpretation model is developed for laboratory-scale ultrasonic non-destructive testing to determine the physical and mechanical properties of saturated soil samples based on the distribution of stress waves. Subsequently, a three-phase poromechanical transfer function model is developed using the spectral element technique for pore-scale characterizations of permafrost samples. Furthermore, a comprehensive ultrasonic testing program is conducted to determine the properties of permafrost samples (e.g., ice content, unfrozen water content, porosity, ice lenses, soil type, and mechanical properties) reconstituted in the laboratory. Thereafter, a hybrid inverse and three-phase poromechanical approach is proposed for in-situ characterization of permafrost sites using surface wave techniques. Finally, the GeoNDT software developed to provide physics-based solutions for the interpretation of non-destructive testing (NDT) measurements used in geotechnical and geophysical applications is presented. The advanced physics-based signal interpretation methods proposed in this thesis allow the quantitative characterization of geophysical and geomechanical properties of geomaterials and multilayered geosystems independently without making any simplified assumptions as common in the current practice.

Acknowledgements

I would like to express my deepest appreciation to my supervisor, Dr. Pooneh Maghoul, for providing countless guidance, feedback and support in many ways throughout this research. Her invaluable expertise in this research topic and insightful feedback have helped me finish this work at a higher level and it would not have been possible to complete this thesis without her contribution. Other than her technical support, I'm also extremely grateful to her for financial support, the countless award nominations, reference letters, valuable comments on proposals (e.g., Mitac, Banting postdoc and so on) and even job applications (CV, cover letter and so many other documents) that she has no obligation to do, but carefully and patiently prepared/reviewed for me time after time. I'm also grateful for her valuable personal advice in difficult decisions in my life and my future career development.

I would like to extend my sincere thanks to my co-supervisor, Dr. Ahmed Shalaby for providing paper reviews, constructive comments, and financial support throughout this research.

I would also like to extend my gratitude to Dr. Giovanni Cascante for the collaboration in Chapter 3. I am grateful for the training of Bender Element test, Resonant column test and ultrasonic test provided by Dr. Giovanni Cascante, Dr. Muhammad Irfan, Mr. Cristobal Abraham Lara at the University of Waterloo.

I would like to thank Dr. Douglas Thomson and Dr. Junhui Zhao for providing the ultrasonic setup used in Chapter 5 at the University of Manitoba. I am also grateful for Geoffrey Cao, Kerry Lynch, Shihao Cui, Nikhil Baral and Marziyeh Fathalikhani for their help with my ultrasonic experiments used in Chapter 5. I would like to acknowledge Dr. Mariusz Majdański, Mr. Artur Marciniak and Mr. Bartosz Owoc for sharing the MASW measurement used in Chapter 6.

I would also like to acknowledge Dr. Guillaume Mantelet for his professional guidance in implementing and packaging GeoNDT project in Chapter 7.

I would also like to acknowledge every former and current member of the Sustainable Infrastructure and Geomechanical Research Lab (SIGLab) for building such an excellent environment in this team.

I am grateful for the scholarships and awards that I received in my PhD program, including the Engineering Research Council of Canada (NSERC) - Engage Grants, the Mathematics of Information Technology and Complex Systems (Mitacs) Accelerate program, and the University of Manitoba Graduate Enhancement of Tri-Council Stipends (GETS) program.

Last but not least, I want to thank my parents, sisters and friends for their unconditional support and love.

List of Publications

Patents:

Maghoul P., Liu H., Mantelet G., Shalaby A., Filed May 2021. *Systems and Methods for In-situ Characterization of Permafrost Sites*, US Provisional Patent No: 63/190,310.

Maghoul P., Liu H., Shalaby A., *Systems and Methods for Ultrasonic Characterization of Permafrost and Frozen Soil Samples*, PCT/CA2021/050826.

Maghoul P., Liu H., Shalaby A., *Systems and Methods for Ultrasonic Characterization of Saturated Soil Samples*, United States Application No: 17/371,472.

Code License:

Liu H., Maghoul P., Mantelet G., and Shalaby A. *GeoNDT: a non-destructive testing software*, Disclosed by the University of Manitoba in June 2021.
Link to the basic version (the full version will be hosted on eValorix.com by September 2021): https://github.com/Siglab-code/GeoNDT.

Liu H., Maghoul P., and Shalaby A. *Intelligent MASW*, DOI: 10.5281/zenodo.3776875, Under open-source Apache License 2.0.
Link: https://github.com/Siglab-code/Intelligent-MASW.

Liu H., Maghoul P., and Shalaby A. *WaveFrost*, DOI: 10.5281/zenodo.5159712, Under open-source Apache License 2.0.
Link: https://github.com/Siglab-code/WaveFrost.

Liu H., Maghoul P., and Shalaby A., Thomson D. *UltraFrost*, DOI: 10.5281/zenodo.5242514, Under open-source Apache License 2.0.
Link: https://github.com/Siglab-code/UltraFrost.

Journal Papers:

The chapters of this thesis are reproduced, with modifications, from the following publications:

Chapter 2:
Liu H., Maghoul P., Shalaby A., Bahari A., and Moradi F., 2020. *Integrated approach for the MASW dispersion analysis using the spectral element technique and trust region reflective method*. Computers and Geotechnics, 125, 103689.
https://doi.org/10.1016/j.compgeo.2020.103689.

Chapter 3:
Liu H., Cascante G., Maghoul P. and Shalaby A., 2021. *Experimental investigation and numerical modeling of piezoelectric Bender Element motion and wave propagation analysis in soils*, Canadian Geotechnical Journal (Canadian Science Publishing), In Press.
https://doi.org/10.1139/cgj-2020-0757.

Chapter 4:
Liu H., Maghoul P., and Shalaby A., 2020. *Laboratory-scale characterization of saturated soil samples through ultrasonic techniques*. Scientific Reports (Nature), 10, 3216.
https://doi.org/10.1038/s41598-020-59581-4.

Chapter 5:
Liu H., Maghoul P., Shalaby A., Thomson D., 2021. *Pore-scale quantitative characterization of frozen and permafrost samples using ultrasonic waves*, Communications Engineering, Manuscript ID: COMMSENG-21-0018, in Review.

Chapter 6:
Liu H., Maghoul P., Shalaby A., 2021. *Seismic physics-based characterization of permafrost sites using surface waves*, The Cryosphere Discuss. [preprint], in Review.
https://doi.org/10.5194/tc-2021-219.

Chapter 7:
Liu H., Maghoul P., Mantelet G., Shalaby A., 2021. *GeoNDT: an open source physics-based multiphase geomechanical solver for geotechnical and geophysical applications*, Acta Geotechnica, Manuscript ID: AGEO-D-21-00565, in Review (2021).

Chapters in Edited Books (Refereed):

Liu H., Maghoul P., Shalaby A., 2021. *A Poro-elastodynamic solver for dispersion analysis of saturated multilayer systems*, In Barla M., Di Donna A., & Sterpi D. (Eds.), *Lecture Notes in Civil Engineering: Vol. 126. Challenges and Innovations in Geomechanics*, Springer International

Publishing, chapter 75.

Liu H., Maghoul P., 2021. *Apollo seismic data interpretation using an elastodynamic space-time spectral element technique and dispersion image inversion method*, In Roberts A.D., van Susante P., Koppelman J. (Eds.), *Earth and Space: Engineering for Extreme Environments*, American Society of Civil Engineering.

Amini-Baneh D., Liu H., Maghoul P., 2021. *Seismic site effect investigation for future moonquake-resistant structures by considering geometrical and geotechnical characteristics of lunar bases*, In Roberts A.D., van Susante P., Koppelman J. (Eds.), *Earth and Space: Engineering for Extreme Environments*, American Society of Civil Engineering.

Conference Papers/Abstracts:

Liu H., Cascante G., Maghoul P., Shalaby A., *Soil-Bender Element Interaction: Numerical and Experimental Results*, Canadian Geotechnical Conference (GeoNiagara 2021), Niagara, Canada.

Liu H., Maghoul P., *Identification of ultrasonic waves in multiphase frozen soils using the theory of poroelastodynamics*, Biot-Bažant Conference (2021), Evanston, United States.

Liu H., Maghoul P., *Laboratory characterization of permafrost samples using the ultrasonic pulse velocity technique*, CPA & NSERC PermafrostNet Virtual Annual General Meeting (2020).

Liu H., Maghoul P., Shalaby A., 2019. *Dynamic poroelasticity based method for falling weight deflectometer test analysis*, 72th Canadian Geotechnical Conference (GeoSt.John 2019), St. John, Canada.

Contributions of Authors

Chapter 2: Liu H., Maghoul P., Shalaby A., Bahari A., and Moradi F.

i. Liu: project conceptualization, analytical derivation and validation, algorithm implementation, results interpretation, original drafting and revising the paper.

ii. Maghoul: project conceptualization, analytical derivation, results interpretation, review and edit.

iii. Shalaby: results interpretation, review and edit.

iv. Bahari: analytical derivation, algorithm implementation

v. Moradi: paper review

Chapter 3: Liu H., Cascante G., Maghoul P. and Shalaby A.

i. Liu: project conceptualization, methodology development, laboratory work, numerical modelling, results interpretation, original drafting and revising the paper.

ii. Cascante: project conceptualization, criticized methodology, supervision of the laboratory work and numerical modelling, results interpretation, review and edit.

iii. Maghoul: project conceptualization, criticized methodology, supervision of the numerical modelling, review and edit.

iv. Shalaby: review and edit.

Chapter 4: Liu H., Maghoul P., and Shalaby A.

i. Liu: project conceptualization, analytical derivation and validation, algorithm implementation, results interpretation, original drafting and revising the paper.

ii. Maghoul: project conceptualization, analytical derivation, results interpretation, review and edit.

iii. Shalaby: results interpretation, review and edit.

Chapter 5: Liu H., Maghoul P., Shalaby A., and Thomson D.

i. Liu: project conceptualization, analytical derivation and validation, algorithm implementation, experimental tests, results interpretation, original drafting and revising the paper.

ii. Maghoul: project conceptualization, analytical derivation, experimental tests, results interpretation, review and edit.

iii. Shalaby: results interpretation, review and edit.

iv. Thomson: laboratory equipment arrangement

Chapter 6: Liu H., Maghoul P., Shalaby A.

i. Liu: project conceptualization, analytical derivation and validation, algorithm implementation, results interpretation, original drafting and revising the paper.

ii. Maghoul: project conceptualization, analytical derivation, results interpretation, review and edit.

iii. Shalaby: review and edit.

Chapter 7: Liu H., Maghoul P., Mantelet G., Shalaby A.

i. Liu: project conceptualization, algorithm implementation, results interpretation, original drafting and revising the paper.

ii. Maghoul: project conceptualization, results interpretation, review and edit.

iii. Mantelet: code development

iv. Shalaby: review and edit.

Contents

List of Tables

List of Figures

Chapter 1

Introduction

1.1 The big picture

Appropriate characterization of foundation soils and health monitoring of geo-structures are the twin pillars of engineering practice within a multi-hazard context. The ability to quantitatively and non-invasively characterize complex multiphase geomaterials and predict the performance of subsurface systems subject to complex loading are still a major challenge to the engineering, construction, and geophysical fields.

In remote areas, the development of portable, time-efficient and cost-effective techniques for the characterization of geomaterials can play an important role in the preliminary geotechnical investigation. In geotechnical practice, the physical and mechanical properties are obtained through field and laboratory geotechnical/geophysical testings. The conventional field methods require heavy equipment that may not be accessed in remote areas or extreme environments. For the laboratory tests, soil samples from sites under investigation are required to be transported to a geotechnical laboratory for various tests, which can cause the disturbance of soil samples and potentially lead to erroneous conclusions. Currently, the ability to quantitatively and non-invasively characterize geomaterials in remote areas is still a major challenge to the engineering and construction.

In the context of accelerating climate change, construction on foundation permafrost also requires remedial measures and an appropriate characterization of permafrost (e.g., ice content, unfrozen water content, porosity, ice lenses, soil type, and mechanical properties). The adverse effects of climate warming on the built environment in (sub)arctic regions are unprecedented and accelerating. According to Canada's Changing Climate Report (2019), in the Arctic regions, temperatures have been warming at approximately twice the rate of the rest of the world. This drastic trend in climate warming will no doubt affect

permafrost temperatures and conditions, continued rise in greenhouse gas emissions, and further adding to the high cost of development in northern regions. The construction on ice-rich permafrost foundations and studies on permafrost carbon feedback require appropriate measurements of permafrost properties. Furthermore, the early detection and warning systems to monitor infrastructure impacted by permafrost-related geohazards, and to detect the presence of layers vulnerable to permafrost carbon feedback and emission of greenhouse gases into the atmosphere require the fundamental understanding of permafrost properties.

In the light of the above, this research aims to pave the way to encompassing different fields including geomechanics, geophysics, geotechnical engineering, signal processing, and ultrasonic sensing to develop novel non-invasive investigation tools and physics-based interpretation methods for characterization of multiphase geomaterials using stress waves.

1.2 Background and literature review

A wide variety of field (in-situ) and laboratory techniques are available in geotechnical engineering and geophysical science for the measurement of physical and mechanical properties of geomaterials. Many techniques are oriented toward the measurement of properties at low strains (below 0.001%) and many others toward properties mobilized at larger strains. The literature review consists of four sections, aiming to review both field and laboratory techniques used for the characterization of geomaterials. Section 1.2.1 reviews the state of the art of near surface geophysics for the non-invasive in-situ site investigation. Section 1.2.2 reviews various borehole or subsurface geophysical methods used for the destructive in-situ site investigation. Section 1.2.3 reviews various dynamic penetration tests used in geotechnical site investigation for the estimation of dynamic soil properties at large strain levels. Finally, Section 1.2.4 reviews different laboratory techniques for the measurement of dynamic soil properties at various strain levels.

1.2.1 Near surface geophysics

The surface geophysical methods are non-invasive techniques that are carried out for the site investigation without any intrusion of the ground. In comparison to other techniques (e.g., subsurface geophysics and conventional dynamic penetration tests), the surface geophysical methods are considered as more rapid and cost-effective. The surface geophysical methods have particular application advantages in sites that are difficult to have

access or penetrate (such as pavements, underwater tunnel linings, retaining walls, and slopes) (Campanella, 1994). The surface geophysical methods are also appealing in other cases such as preliminary investigation over a large area, quality assurance and check of foundation structures as well as site monitoring. However, the interpretation of field measurements by surface geophysical techniques is normally difficult and associated with lots of uncertainties related to the ground properties and stratigraphy. Therefore, surface geophysical methods often require other complementary techniques to increase the reliability of interpreted results. It is often good practice to complement and calibrate the surface geophysical models with a few direct tests made by borehole investigations (e.g., seismic crosshole, down-hole and up-hole tests) or geotechnical tests (e.g., cone penetration tests or piezocone tests) (Lorenzo, Hicks, and Vera, 2014).

A wide variety of seismic methods are available for different applications. The seismic reflection test is used for the investigation of large-scale and very deep stratigraphy. This test is performed by producing an impulse load (rich in P wave content) at the source and measuring the P wave arrival time at the receiver location. However, the seismic reflection method often fails to detect near-surface targets due to the lack of high frequency (low wavelength) components (Steeples and Miller, 1998). Therefore, it is rarely used for the near-surface investigation. It also has a limitation with regard to determining the arrival time of the reflected waves due to the contamination of surface waves. Seismic refraction test is another seismic geophysical method used for in-situ soil investigations. The test measures the travel times of P and S waves using an array of geophones. However, the majority of available signal interpretation methods for seismic refraction is based on this assumption that the soil stiffness (wave velocity) increases with depth (Pelton, 2005).

The Spectral Analysis of Surface Waves (SASW) is another in-situ investigation method that uses surface wave for soil characterisation. The SASW test records data in two stations. In this test, a vertical impact is generated on the ground surface through an impulse source, which induces Rayleigh waves and can be used to map the near-surface shear velocity profile. Two geophones are normally used and the spacing between them are varied to cover the desired investigation depth. It is known that using only a pair of geophones, the different modes of wave propagation cannot be differentiated and the dispersion inversion can be difficult. The Multichannel Analysis of Surface Waves (MASW), on the other hand, samples data at multiple locations using several geophones. This allows the investigation of a broader area and depth from a single survey. The data interpretation techniques for the MASW test normally require a forward solver and an inverse algorithm. The

forward solver computes the dispersion curves for a given soil stratigraphy and the inverse algorithm updates the soil parameters until the calculated dispersion curves match well with the measured ones.

With regard to the in-situ characterization of permafrost sites, several in-situ techniques have been employed to characterize or monitor permafrost conditions. For example, the techniques such as remote sensing (Witharana, Bhuiyan, Liljedahl, Kanevskiy, Epstein, Jones, Daanen, Griffin, Kent, and Jones, 2020; Bhuiyan, Witharana, and Liljedahl, 2020; Zhang, Witharana, Liljedahl, and Kanevskiy, 2018), and the ground penetrating radar (GPR) (Munroe, Doolittle, Kanevskiy, Hinkel, Nelson, Jones, Shur, and Kimble, 2007; Christiansen, Matsuoka, and Watanabe, 2016; Williams, Haltigin, and Pollard, 2011) have been used to detect ice-wedge formations within the permafrost layers. Also, the electrical resistivity tomography (ERT) has been extensively used to qualitatively detect pore-ice or segregated ice in permafrost based on the correlation between the electrical conductivity and the physical properties of permafrost (e.g., unfrozen water content and ice content) (Glazer, Dobiński, Marciniak, Majdański, and Błaszczyk, 2020; Hauck, 2013; Scapozza, Lambiel, Baron, Marescot, and Reynard, 2011; You, Yu, Pan, Wang, and Guo, 2013). The apparent resistivity measurement by ERT is higher in areas having high ice contents (You, Yu, Pan, Wang, and Guo, 2013); however, at high resistivity gradients, the inversion results become less reliable, especially for the investigation of permafrost base (Hilbich, Marescot, Hauck, Loke, and Mäusbacher, 2009; Marescot, Loke, Chapellier, Delaloye, Lambiel, and Reynard, 2003). Furthermore, in ERT investigations, the differentiation between the ice and certain geomaterials can be highly uncertain due to their similar electrical resistivity properties (Kneisel, Hauck, Fortier, and Moorman, 2008). GPR has been also used for mapping the thickness of the active layer; however, its application is limited to a shallow penetration depth in conductive layers due to the signal attenuation and high electromagnetic noise in ice and water (Kneisel, Hauck, Fortier, and Moorman, 2008).

The MASW test (Dou and Ajo-Franklin, 2014; Glazer, Dobiński, Marciniak, Majdański, and Błaszczyk, 2020), passive seismic test with ambient seismic noise (James, Knox, Abbott, Panning, and Screaton, 2019; Overduin, Haberland, Ryberg, Kneier, Jacobi, Grigoriev, and Ohrnberger, 2015)), seismic reflection (Brothers, Herman, Hart, and Ruppel, 2016), and seismic refraction method (Wagner, Mollaret, Günther, Kemna, and Hauck, 2019) have been previously employed to map the permafrost layer based on the measurement of shear wave velocity. In the current seismic testing practice, it is commonly considered that the

permafrost layer (frozen soil) is associated with a higher shear wave velocity due to the presence of ice in comparison to unfrozen ground.

1.2.2 Borehole geophysics

Borehole or subsurface geophysical investigations (e.g., seismic cross-hole test, seismic down-hole test, seismic up-hole test and seismic cone test) can be used to map P-wave and S-wave velocities at different depths at low-strain levels. Borehole geophysics are most useful in site investigations where drilling is required (Campanella, 1994). In the seismic cross-hole test, two or three boreholes are used for setting up transmitters and receivers to measure the travel times of seismic waves between these boreholes. Several types of transmitter can be used for the generation of stress waves, such as mechanical wedge-type transmitter (Mok, Kim, and Kang, 2003), piezoelectric transmitters (Roblee, Stokoe, Fuhriman, and Nelson, 1994), solenoid-coil type transmitters (Roblee, Stokoe, Fuhriman, and Nelson, 1994) and blasting transmitters (Malmgren, Saiang, Töyrä, and Bodare, 2007). The geophone or accelerometer can be used as the receiver to measure the induced responses in the subsurface geophysical investigation. In the seismic down-hole test, a seismic source is set up at the ground surface and receivers are located in the borehole to measure the induced stress waves generated by the surface source (Takahashi, Takeuchi, and Sassa, 2006). The seismic up-hole method uses reverse source and receiver configurations to the down-hole method (with a down-hole source and surface receivers) (Takahashi, Takeuchi, and Sassa, 2006). The addition of a seismic sensor (a geophone or accelerometer) inside the barrel of a cone penetrometer is known as a Seismic Cone Penetrometer Test (SCPT) (Robertson, 1986). In the SCPT, the seismic source can be generated at the ground surface. Then the induced stress wave propagates into the ground and is captured by the sensors installed inside the cone penetrometer. By repeating the measurement at another depth, the SCPT can be used to determine the average seismic wave velocities over the depth from the measured signal traces (Butcher, Campanella, Kaynia, and Massarsch, 2005). In those seismic borehole geophysical tests, the seismic velocities are obtained by empirically selecting of first arrival time for P-wave and S-wave velocities.

In general, the cross-hole methods have the advantage of maintaining the signal-to-noise ratio with depth in comparison to the down-hole or up-hole methods, but do require additional boreholes and greater cost. The down-hole methods or up-hole methods, on the other hand, have the advantage of determining average parameters over discrete depth

intervals. Overall, all borehole seismic methods can measure the P-wave and S-wave velocity at various depths due to the direct access to geomaterials. However, the high cost of the drilling and uncertain drilling disturbance effects on geomaterials prevent the borehole geophysical methods from having a greater use in geotechnical site investigations (Campanella, 1994).

1.2.3 Dynamic penetration tests

Other than the surface and borehole geophysical methods, dynamic penetration tests are also used for the estimation of dynamic soil properties at large strain levels. Dynamic penetration techniques range from Standard Penetration Tests (SPT), to any other devices that are driven into the soil by the struck of hammers (e.g., the Large Diameter Penetrometer (LPT) and the Becker Penetrometer) (Schnaid, Odebrecht, Rocha, and Paula Bernardes, 2009). In these techniques, the penetrometer or sampler positioned on the end of the boring rod is lowered to the bottom of the borehole. The blow counts are recorded while the penetrometer or sampler is driven into the foundation soils. The recorded blow counts are then used to empirically estimate the dynamic soil properties and other parameters (e.g., shear strength, compressibility and liquefaction resistance of soils) (Schnaid, Odebrecht, Rocha, and Paula Bernardes, 2009). The cone penetration test (CPT) is another method used for the in-situ geotechnical investigation. In this test, a cone penetrometer is pushed into the ground at a controlled rate and the required thrusts are measured to determine the tip resistance as well as side friction (Budhu, 2015). Then the measured tip resistance and side friction are used to estimate soil properties (e.g., density, grain size distribution, hydraulic conductivity, friction angle and shear strength) based on empirical or statistic models (Lin, Li, Liu, and Chen, 2019; Tillmann, Englert, Nyari, Fejes, Vanderborght, and Vereecken, 2008; Eid and Stark, 1998; Wang, Wang, Liang, Zhu, and Di, 2018).

The dynamic penetration tests, in general, are straightforward to carry out and the measured blow counts can be used to estimate a wide range of parameters. However, the repeatability of test results is normally very poor in dynamic penetration tests. Other limitations of dynamic penetration tests include the inaccuracy and errors in the measurements of the blow counts due to the variability of procedures that are not fully standardized (Clayton, 1995). The uncertainties of the dynamic penetration test results also raise from the irrationality of available empirical methods in the interpretation of test results (Clayton, 1995).

1.2.4 Laboratory techniques

Since borehole sampling is always required in the stage of geotechnical design, laboratory techniques can also be used for the measurement of dynamic soil properties at various conditions.

In the laboratory-scale tests, the Resonant Column (RC) test, Bender Element (BE) test and Piezoelectric Ring-Actuator Technique (P-RAT) are frequently used for the measurement of low-strain dynamic properties (especially for the shear wave velocity), (Liu, Cascante, Maghoul, and Shalaby, 2021; Karray, Ben Romdhan, Hussien, and Éthier, 2015). The RC test is time-consuming, costly, bulky, and typically only used in laboratory investigations. The BE utilizes piezo-ceramic materials for the conversion of an electrical signal into mechanical energy. Two bender elements are placed at the two ends of the soil specimen in which one BE is used to introduce a mechanical impulse and the other one is used to receive the propagating pulse (normally in mV). The BE generates not only S-waves in the direction of their plane but also P-waves in the direction normal to their plane. The P-waves reflected from the cell walls can interfere with the generated S-waves (Lee and Santamarina, 2005). In comparison to the BE test, the P-RAT reduces the generation of P-waves due to the constraint in the potential compression from the direct contact between piezoelectric elements and the soil samples (Karray, Ben Romdhan, Hussien, and Éthier, 2015). However, the P-waves can still be generated in the P-RAT test (Karray, Ben Romdhan, Hussien, and Éthier, 2015), which interferes with the selection of S-wave arrival time in the current arrival time-based methods.

The ultrasonic test is another technique that can be used to evaluate the dynamic properties of geomaterials at low strain levels. The mechanical properties of geomaterial samples (mostly for P wave velocities) can be evaluated by interpreting the signal recorded by an ultrasonic receiver. In the current practice, the first arrival time is predominantly used for the evaluation of P wave velocity of geomaterials (especially for concrete).

Cyclic triaxial test is one of the most commonly used techniques for the evaluation of cyclic strength and strain-dependent dynamic soil properties at high strain levels. The cyclic triaxial apparatus comprises a load frame, dynamic actuator, triaxial cell, automatic pressure controllers, sensors (e.g., load measuring sensor, displacement measuring sensor and pore water pressure measuring sensor) and a data acquisition system. The typical frequencies used in the cyclic triaxial test can range from 0.1 Hz to 20 Hz (Kirar and Maheshwari, 2018). The cyclic loading can be applied to the soil sample by a mechanical

or hydraulic actuator. The stresses and strains measured in the cyclic triaxial test are then used to compute the shear modulus and damping ratio.

In the characterization of three-phase frozen geomaterials, the popular techniques used for unfrozen water content measurement include Time Domain Reflectometry (TDR), Frequency Domain Reflectometry (FDR), Time Domain Transmissometry (TDT) and Nuclear Magnetic Resonance (NMR) (Stein and Kane, 1983; Noborio, 2001; Yoshikawa and Overduin, 2005). In these techniques, the soil water content is estimated from the empirical relation between the relative dielectric permittivity and unfrozen water content of soil samples (Hallikainen, Ulaby, Dobson, El-Rayes, and Wu, 1985; Topp, Davis, and Annan, 1980). These methods require frequent laboratory calibration to obtain unique empirical relations based on soil types, test temperature, and the type of transducer (Yoshikawa and Overduin, 2005). Porosity can be measured using techniques such as Computed Tomography (CT scan) (Duliu, 1999; Périard, Gumiere, Long, Rousseau, and Caron, 2016), Imbibition methods (immersion of the soil sample in a fluid) (Gu, Zhu, Zhang, and Liu, 2019), Water Evaporation method (Schindler, Durner, Von Unold, Mueller, and Wieland, 2010; Castellini, Di Prima, and Iovino, 2018) and Mercury Intrusion (Yao and Liu, 2012). These techniques (all but CT method) are invasive such that the original soil state is disturbed. X-ray Computed Tomography imaging has been used in recent years to scan permafrost samples (Wagner, Lindsey, Dou, Gelvin, Saari, Williams, Ekblaw, Ulrich, Borglin, Morales, et al., 2018). Such a technique requires bulky and expensive instruments that are not suitable for field applications. Permafrost samples need to be transported to a laboratory, which can be costly and causes sample disturbance. Furthermore, the CT imaging can only shows the distribution of ice patches within the sample without any quantitative characterization; the CT imaging is also challenging to differentiate the water and ice from soil grains in fine-grained soils (Wu, Nakagawa, Kneafsey, Dafflon, and Hubbard, 2017).

1.3 Gaps in knowledge

This thesis mainly focuses on the stress wave-based Non-Destructive Testing (NDT) techniques that are developed for the characterization of multiphase geomaterials in terms of physical and mechanical properties at small strain levels. In the light of the above literature review, the main limitations and challenges in the characterization of multiphase geomaterials using existing non-invasive techniques (including MASW, BE and ultrasonic

tests) and interpretation methods are briefly summarized as follows:

Characterization of dry geomaterials

The data interpretation techniques for the MASW test normally requires a forward solver and an inverse algorithm. However, the available solvers of MASW technique have numerical instability to different extents, especially at high frequencies due to the exponential increasing terms. The inverse algorithms reported in the literature are mostly limited to gradient-free methods that have a extremely low convergence rate and high computational costs. In BE tests, the actual behavior of the BE inside a soil specimen still remains unknown. The current ASTM standard does not consider the interference of compressional and shear waves in the BE testing, which can lead to significant errors in the evaluation of shear wave velocities. The accurate interpretation of BE measurements and wave propagation analysis is impossible without knowing the motion of the BE inside the soil samples.

Characterization of saturated geomaterials

Rock physics models have been developed to provide a link between rock properties. These properties include porosity, fluid saturation, and lithology as well as mechanical properties such as velocities or impedances. These models are mostly used in oil and gas explorations, reservoir characterization, and quantitative seismic interpretation.

In these models, multiple velocity-porosity models are developed for the estimation of porosity based on the measured P-wave or/and S-wave velocity. Foti, Lai, and Lancellotta (2002) developed a velocity-porosity model based on the Biot's theory under the assumption that no relative movement occurs between the solid and the fluid phases in porous media. The model requires a) P-wave and S-wave velocity are measured experimentally; b) the density and bulk modulus of fluid are provided; c) the density, bulk modulus and shear modulus of the soil grain are provided (Foti, Lai, and Lancellotta, 2002). Geertsma and Smit (1961) proposed an empirical velocity-porosity model that relates bulk modulus to porosity in rocks with a porosity ranges from 0 to 0.3. Similarly, Wyllie, Gardner, and Gregory (1962) proposed a time-average relation that revealed a simple monotonic relation between P-wave velocity and porosity in fully saturated sedimentary rocks with relatively uniform mineralogy. However, the time-average relation can not be justified theoretically and is only applicable when a) the wavelength is smaller than the pore size and grain size; b) rocks

are isotropic and saturated with fluid and c) rocks are not unconsolidated or uncemented (Mavko, Mukerji, and Dvorkin, 2020). Raymer, Hunt, and Gardner (1980) proposed the 'Raymer–Hunt–Gardner' relations to expand the time-average relation proposed by Wyllie, Gardner, and Gregory (1962) for the rocks with porosity ranging from 0 to 1. However, the 'Raymer–Hunt–Gardner' model is still an empirical relation which has similar limitations as the time-average relation (as mentioned above). Han, Nur, and Morgan (1986), Tosaya and Nur (1982), and Castagna, Batzle, and Eastwood (1985) proposed several empirical relations that relate P-wave and S-wave velocities measured by ultrasonic methods to the porosity and clay content in shaly sandstones. However, these models are still empirical and only applicable for the set of rocks under high confining pressure (above 40 MPa) (Mavko, Mukerji, and Dvorkin, 2020).

In general, the existing rock physics models require the measurement of P-wave and S-wave velocities to estimate the porosity of geomaterials. However, the current techniques and interpretation methods still have problems in the measurement of S-wave velocity for soils. For the rock-physics models developed based on Biot's theory, the estimation of porosity requires to make assumptions of bulk modulus and shear modulus of the soil skeleton. In terms of the empirical rock physics models, they are only applicable under limited conditions.

In the ultrasonic test, the first arrival time is predominantly used for the evaluation of P wave velocity. There are no robust methods to interpret the remaining signals to obtain more information on the other properties of saturated soil samples, e.g., shear wave velocity, porosity or water content. The application of the ultrasonic test for soil characterization is still limited due to the difficulties with signal interpretation and complex nature of geomaterials. Currently, there are no available algorithms developed for the interpretation of ultrasonic signals in saturated soils.

Characterization of multiphase frozen geomaterials

In the characterization of three-phase frozen geomaterials using ultrasonic tests, the exact induced mechanical energy (force) still remains unknown due to the complexity of piezoelectric behavior and transducer structure. The existing literature mostly focused on the mechanism of wave propagation within frozen soils with assumed input force as boundary conditions. Therefore, these methods are incapable of interpreting the ultrasonic signals accurately. A literature search yielded no algorithms for the characterization of

frozen soils using ultrasonic techniques. In the current seismic testing practice, it is commonly considered that the permafrost layer (frozen soil) is associated with a higher shear wave velocity due to the presence of ice in comparison to unfrozen ground. However, the porosity and soil type can also significantly affect the shear wave velocity (Liu, Maghoul, and Shalaby, 2020b). In other words, a relatively higher shear wave velocity could be associated to an unfrozen soil layer with a relatively lower porosity or stiffer solid skeletal frame, and not necessarily related to the presence of a frozen soil layer. Therefore, the detection of the permafrost layer and permafrost base from only the shear wave velocity may lead to inaccurate and even misleading interpretations. Currently, there are no quantitative algorithms available for the characterization of multiphase frozen geomaterials.

1.4 Goals and objectives

The main objective of this research is to develop novel non-invasive investigation tools and physics-based interpretation methods for the characterization of multiphase geomaterials (e.g., dry, saturated and frozen soils) using stress waves at small strain levels. To address the limitations of the above-mentioned techniques and interpretation methods, this research specifically aims to:

- Develop a highly-efficient and stable semi-analytical elastodynamic forward solver for the MASW using the spectral element technique to characterize effectively and efficiently the soil stratigraphy as well as soil properties.
- Develop a coupled piezoelectric and solid mechanics model for the BE system to better understand the response of the BEs inside a soil sample. Also, investigate the soil-BE interaction and provide a new understating of the significant interactions of P-waves and S-waves within the soil sample in the BE test by the proposed coupled piezoelectric and solid mechanics model.
- Develop a physics-based hybrid inverse and two-phase poromechanical model for the characterization of saturated soil samples (e.g., shear wave velocity, compression wave velocity and porosity) based on the distribution of stress waves in the ultrasonic tests.
- Develop an ultrasonic sensing technique and a signal interpretation method based on a three-phase poromechanical transfer function approach for the characterization

of permafrost (e.g., ice content, unfrozen water content, porosity, ice lenses, soil type, and mechanical properties).

- Develop a novel algorithm for analysis of surface waves to quantitatively estimate the physical and mechanical properties of a permafrost site by decomposition of Rayleigh waves dispersion relations via a hybrid inverse and multiphase poromechanical approach.

- Develop a physics-based general-purpose computational tool, GeoNDT, for robust solutions in the interpretation of NDT measurements used in geotechnical and geophysical applications.

1.5 Validation of solvers

The Elastodynamic solver developed in Chapter 2 was validated numerically with the results presented by (Beaty, Schmitt, and Sacchi, 2002). The Piezoelectric solver developed in Chapter 3 was validated with laboratory tests using independent BE and RC tests performed in this research. The Poroelastodynamic solver developed in Chapter 4 was validated with the results presented by (Chai, Zhang, Lu, et al., 2015). The multiphase poromechanical transfer function solver used in Chapter 5 was validated with ultrasonic laboratory tests on reconstituted frozen samples. The multiphase poroelastodynamic solver used in Chapter 6 was validated with field seismic data provided by (Glazer, Dobiński, Marciniak, Majdański, and Błaszczyk, 2020).

1.6 Thesis structure

This thesis is composed of four parts in the order of complexity of the forward solver: 1) Elastodynamic and Piezoelectric Solver; 2) Poroelastodynamic Solver; 3) Multiphase Poroelastodynamic, as well as 4) Programming and Further Applications. The linkages of different chapters are summarized in Figure 1.1.

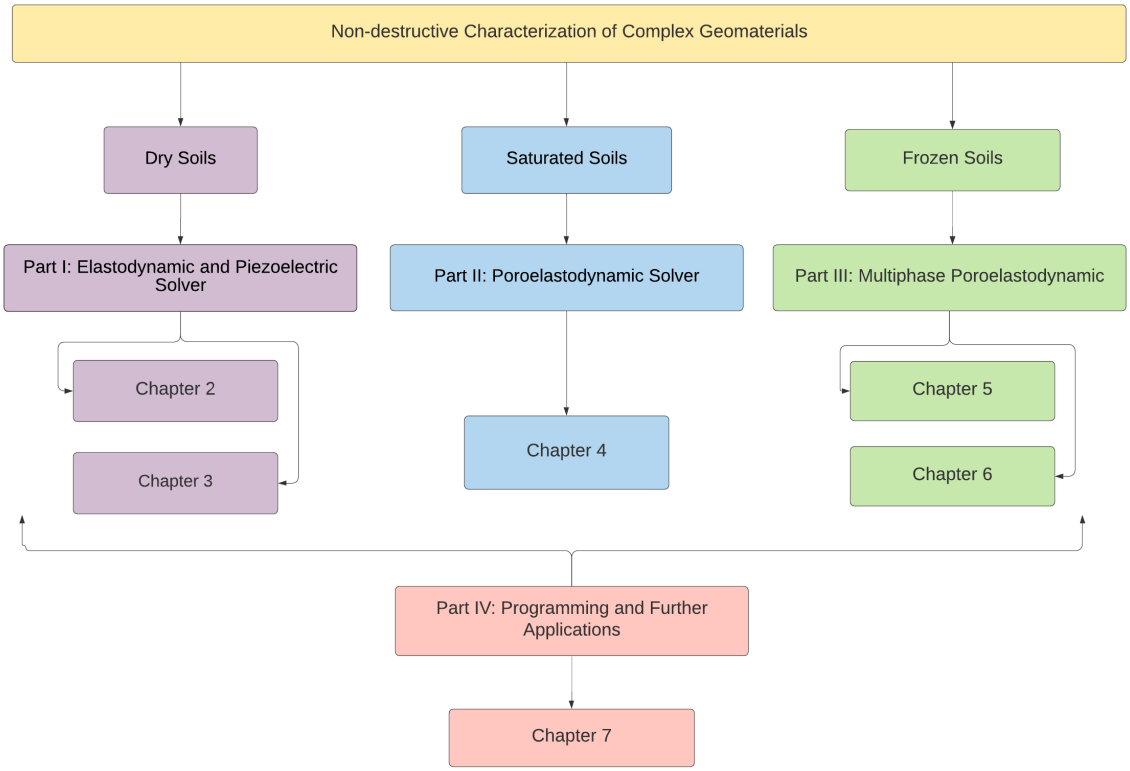

FIGURE 1.1: Linkages of different chapters for the NDT characterization of complex geomaterials

Each part contains one or two chapters and the style of each chapter is similar to a journal paper starting with an introduction which includes literature reviews, mathematical formulations, computational details, results and discussion, conclusion and supplementary materials (the order may vary in different chapters). Then, conclusions and potential future research plans are presented. The shared appendices and bibliography are given at the end of thesis.

The outlines of the four parts and seven chapters of this dissertation are as follows:

Part I: Elastodynamic and Piezoelectric Solver

- Chapter 2 *Integrated approach for the MASW dispersion analysis using the spectral element technique and trust region reflective method*

  In this chapter, a cylindrical-coordinate-based dispersion forward solver is developed using the spectral element method. A root finding method based on Brent's algorithm was proposed to accurately extract the dispersion curves. The trust region reflective method, an effective bound-supported least square algorithm, was applied for the inversion analysis of MASW data. Also, a parametric study was performed to determine the effect of discontinuity in the soil stratigraphy on the dispersion curves.

Finally, the integrated approach developed in this study was used to analyze the MASW data collected in a site in south Iceland.

- Chapter 3 *Experimental investigation and numerical modeling of piezoelectric BE motion and wave propagation analysis in soils*

  In this chapter, a piezoelectric-solid mechanics model is proposed to study the BE motion in different media. The model is validated using the BE motion in the air, transparent soil, and Ottawa sand monitored by a laser vibrometer device. The estimation of the soil parameters such as the shear wave velocity and damping ratio of the Ottawa sand using the piezoelectric-solid mechanics model developed in this paper is then compared with independent experimental data obtained via the conventional RC test. Finally, the propagation of P- and S-waves within a soil specimen due to the BE motion is thoroughly studied and the suitability of empirical methods in estimating the arrival time of the S-wave is discussed.

Part II: Poroelastodynamic Solver

- Chapter 4 *Laboratory-scale characterization of saturated soil samples through ultrasonic techniques*

  In this chapter, the laboratory-scale characterization of saturated soil samples through ultrasonic techniques is presented. The poro-elastodynamic forward solver was developed based on a semi-analytical solution which does not require intensive computational efforts encountered in standard numerical techniques such as the finite element method. A robust global optimization algorithm is then applied to characterize the porosity, density, and other mechanical properties for a soil sample given the ultrasonic signal measured at the receiver location.

Part III: Multiphase Poroelastodynamic

- Chapter 5 *Pore-scale quantitative characterization of permafrost samples using ultrasonic waves*

  In this chapter, the Quantitative Ultrasound (QUS) package is developed to interpret the measured ultrasonic electrical signal and efficiently determine the most probable permafrost properties using the proposed inverse spectral element multiphase poromechanical approach. Several case studies are performed on different soil types

including clay, silt, and till (a mix of clay, silt, sand, and limestone) to demonstrate the robustness of the proposed QUS setup in characterizing frozen soils in terms of both physical and mechanical properties.

- Chapter 6 *Quantitative and qualitative characterization of permafrost sites using surface waves*

  In this chapter, we present a hybrid inverse and multi-phase poromechanical approach for in-situ characterization of permafrost sites using surface wave techniques. The role of two different types of Rayleigh waves in characterizing the permafrost is presented based on an MASW seismic investigation in a field located at SW Spitsbergen, Norway. Multiphase poromechanical dispersion relations are developed for the interpretation of the experimental seismic measurements at the surface based on the spectral element method. Case studies are performed to demonstrate the potential of seismic surface wave testing accompanied with our proposed hybrid inverse and poromechanical dispersion model for the assessment and quantitative characterization of permafrost sites.

Part IV: Programming and Further Applications

- Chapter 7 *GeoNDT: a fast general-purpose computational tool for geotechnical non-destructive testing applications*

  In this chapter, we present the GeoNDT software, which is developed to provide fast and stable solutions for the interpretation of non-destructive testing (NDT) measurements used in geotechnical and geophysical applications. In this software, the above-mentioned multiphase models for the propagation of stress waves in dry (elastodynamic), saturated (two-phase poroelastodynamic), and three-phase frozen (multiphase poroelastodynamic) geomaterials using the meshless spectral element method are implemented.

- Chapter 8 *Conclusion and potential of future research plan*

  In this chapter, the contributions of this research along with the conclusions as well as the future research plan are outlined.

Part I: Elastodynamic and Piezoelectric Solver

Chapter 2

Integrated approach for the MASW dispersion analysis using the spectral element technique and trust region reflective method

Abstract

In this paper, a semi-analytical elastodynamic forward solver was proposed for the Multichannel Analysis of Surface Waves (MASW) using the spectral element technique for the first time. A root finding method based on Brent's algorithm was proposed to accurately extract the dispersion curves. The trust region reflective method, an effective bound-supported least square algorithm, was applied, for the first time, for the inversion analysis of MASW data. In comparison to the commonly used neighborhood algorithm, the proposed solver converges rapidly; the Euclidean distance between the measured and numerically calculated dispersion curves are significantly reduced within only 300 runs of the forward solver in comparison to over 10,000 runs using the neighborhood algorithm. Several numerical case studies were performed to demonstrate the selection of initial guesses as well as the bounds of each optimization parameter. Also, a parametric study was performed to determine the effect of discontinuity in the soil stratigraphy on the dispersion curves. Finally, the integrated approach developed in this study was used

Liu H., Maghoul P., Shalaby A., Bahari A., and Moradi F., 2020. *Integrated approach for the MASW dispersion analysis using the spectral element technique and trust region reflective method*. Computers and Geotechnics, 125, 103689. https://doi.org/10.1016/j.compgeo.2020.103689.

to analyze the MASW data collected in a site in south Iceland. It was concluded that the proposed approach determines effectively and efficiently the soil stratigraphy as well as soil properties.

2.1 Introduction

The seismic non-destructive testing (NDT) techniques have been widely used for the characterization of subsurface materials without disturbing their original state. The commonly used seismic NDT includes the Spectral Analysis of Surface Waves (SASW), Multichannel Analysis of Surface Waves (MASW), Continuous Surface Waves (CSW), and Falling Weight Deflectometer (FWD) methods. In these techniques, the determination of soil parameters requires a physical forward solver and a back-calculation algorithm to fit the field measurements. The SASW that records data in two stations was introduced in the 1980s by (Nazarian and Stokoe, 1984). In this test, a vertical impact is generated on the ground surface through an impulse source, which induces Rayleigh waves and can be used to map the near-surface shear velocity profile. Two geophones are normally used and the spacing between them is varied to cover the desired investigation depth. It is known that using only a pair of geophones, the different modes of wave propagation can not be differentiated and the dispersion inversion can be difficult (Lin, Lin, and Chien, 2017). The MASW, on the other hand, samples data at multiple locations using several geophones. This allows the investigation of a broader area and depth from a single survey. The displacement data measured at various locations at the ground surface can be first transformed into a dispersion image through methods such as the phase-shift method (Park, Miller, and Xia, 1998) and 2D FFT techniques. The dispersion image depicts the patterns of energy accumulation in the space and the desired dispersion curve can then be extracted manually or through mode picking algorithms.

The interpretation of MASW test data normally requires a forward solver and an inverse algorithm. The forward solver computes the dispersion curves for a given soil stratigraphy and the inverse algorithm updates the soil parameters until the calculated dispersion curves match well with the measured ones. Several forward solvers have been developed since 1950s. The two most popular approaches are the transfer function-based method and stiffness matrix (Global matrix)-based method. By using the transfer function matrix, the relation between the upper layer and lower layer can be obtained. Such techniques avoid the global stiffness matrix inversion by replacing it with a matrix multiplication. The well-known Thomson-Haskell matrix method was first proposed in 1953 by (Haskell, 1953). However, it was found that a numerical instability occurs in this method, especially at high frequencies due to the exponential increasing terms (Ke, Dong, Kristensen, and Thompson, 2011; Kamal and Giurgiutiu, 2014; Lowe, 1995; Wang and

Rokhlin, 2001). In addition, the displacement and stress components are placed in the same matrix. Since the stress components are normally much greater than the displacement components (roughly from 10^6 to 10^9 times greater), the inversion of such a matrix is highly unstable. Therefore, numerous attempts have been made through various scaling and matrix transformation including Schwab-Knopoff method (Schwab and Knopoff, 1972), Abo-Zena method (Abo-Zena, 1979), reflection and transmission (RT) matrix method (Kennett, 1974) among others.

In the global stiffness matrix-based method, the relations between the displacement and stress for each layer are obtained, which ensures the numerical stability even at high frequencies (Kamal and Giurgiutiu, 2014; Lowe, 1995). The fundamental global matrix method was first developed by (Knopoff, 1964) using the elstodynamic theory in Cartesian coordinates. A matrix-based method similar to finite element formulation was developed by (Rizzi and Doyle, 1992) to study the structure response in frequency and time domain. It was shown that such a formulation is more computationally efficient than the global matrix method. The global stiffness matrix-based method requires to solve four wave coefficients in each layer, whereas in spectral element method, only two quantities (u_r and u_z) are required to be computed (Rizzi and Doyle, 1992). Therefore, the system size is approximately doubled in the global stiffness matrix-based method (Rizzi and Doyle, 1992). The spectral element method was developed for the solution of elastodynamic problems, which are mostly used for the soil response analysis in the FWD test (Al-Khoury, Scarpas, Kasbergen, and Blaauwendraad, 2001; Lee, 2014). However, there is not enough attention paid in the dispersion relation analysis using the spectral element method. During the inversion process in the MASW test, the dispersion-based method are more commonly applied since the distribution of dispersion curve is independent of the applied loading source which is normally unknown in practice. The determination of dispersion curves requires solving the root-finding problem by setting the global stiffness matrix's determinant to zero. The computational cost increases with the size of the global stiffness matrix due to the determinant calculation. Therefore, the spectral element formulation improves the root-search speed in comparison to the global matrix method.

Several MASW inversion algorithms have been proposed in the literature. The neighbourhood algorithm, a gradient free method, was used by (Sambridge, 1999; Wathelet, Jongmans, and Ohrnberger, 2004) for the inversion of passive MASW test data in south of Brussels, Belgium. This method was also tested using several synthetic data and was proved to have predictions consistent with the borehole data. The simulated annealing

method was used by (Beaty, Schmitt, and Sacchi, 2002) and the inversion was applied to a site with glacial tills located at a depth of 10 m. A reasonable prediction was obtained despite of its large computational cost. A linearized algorithm that applies inequality constraints during the MASW inversion was developed by (Cercato, 2009) to address the non-uniqueness problem. The 2D genetic algorithm was applied by (Rehman, El-Hady, Atef, and Harbi, 2016) for the inversion of MASW dispersion curves obtained in vertically heterogeneous medium. It is reported that the genetic algorithm successfully locates the depth of the bedrock (varying from 4 to 30 m). Recently, MASWaves, an open source tool for the forward and inverse MASW test, proposed a trial and error method for the inversion analysis (Olafsdottir, Erlingsson, and Bessason, 2017). A good agreement was also achieved between the experimental and numerical dispersion curves.

In this paper, a cylindrical-coordinate-based dispersion forward solver is obtained using the spectral element method. The Brent root-finding method is used to accurately determine the phase velocity for a given frequency. It should be noted that this study still deals with horizontally distributed soil layers. Then, the trust-region reflective method, a bound supported least square algorithm, is applied in the inversion analysis. Finally, the performance of such an integrated approach is compared with the neighborhood algorithm proposed by (Sambridge, 1999).

2.2 Forward solver for the MASW dispersion analysis

2.2.1 Problem definition

A general schematic of the problem is illustrated in Figure 2.1. The domain is composed of horizontally distributed multilayers with different soil properties. Various impact loading sources (hammer, falling weight or vibrating machine) can be applied at the ground surface. The geophones are used to measure the corresponding soil responses at multiple locations.

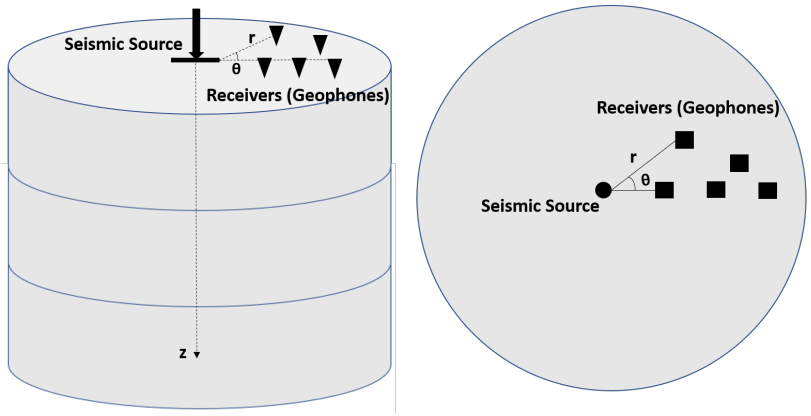

FIGURE 2.1: A general configuration of the problem

2.2.2 Conventions and assumptions

In this study, the state variables are the components of the displacement vector, u_i. The assumptions and conventions used in developing the governing equations are listed as follows:

- The domain consists of a multi-layered system.
- Each layer is composed of a continuum deformable solid body.
- The elastic medium of the skeleton is homogeneous, isotropic and linear.
- Transient conditions and infinitesimal deformations are considered.

2.2.3 Kinematic and constitutive model

The linearized form of the Green-Lagrange strain tensor, ε_{ij}, for infinitesimal deformations is described as:

$$\varepsilon_{ij} = \frac{1}{2}\left(u_{i,j} + u_{j,i}\right) \tag{2.1}$$

where $u_{i,j}$ represents $\frac{\partial u_i}{\partial x_j}$; u_i represents the displacement vector components in each direction and x_j represents the coordinates.

The constitutive law of soils that describes the stress-strain relations is defined as:

$$\sigma_{ij} = D_{ijkl}\,\varepsilon_{kl} \tag{2.2}$$

where σ_{ij} and ε_{kl} are the total stress and the strain tensor, respectively. Also, D_{ijkl} is the fourth-order linear elastic stiffness tensor described as:

$$D_{ijkl} = \lambda\delta_{ij}\delta_{kl} + \mu\left(\delta_{ik}\delta_{jl} + \delta_{il}\delta_{jk}\right) \tag{2.3}$$

in which λ and μ are the Lamé coefficients.

By replacing Equation (2.3) into Equation (2.2), the constitutive equation can be written as:

$$\sigma_{ij} = \lambda \delta_{ij} \varepsilon_{kk} + 2\mu \varepsilon_{ij} \tag{2.4}$$

2.2.4 Conservation of linear momentum

The conservation of the linear momentum for the elastodynamic medium is written as:

$$\sigma_{ij,i} + f_i = \rho \ddot{u}_i \tag{2.5}$$

where ρ is the bulk density of soil and f_i is the body force.

2.2.5 Governing equations

The Navier equation for the elastic wave propagation is obtained from Equation (2.1) to (2.5), as follows.

$$(\lambda + 2\mu)\, \nabla\nabla \cdot \mathrm{u} - \mu \nabla \times \nabla \times \mathrm{u} = \rho \ddot{\mathrm{u}} \tag{2.6}$$

where u is the displacement vector.

The Lamé coefficients (λ, μ) can be expressed in terms of Young's modulus (E) and Poisson's ratio (ν) through Equation 2.7.

$$\lambda = \frac{E\nu}{(1+\nu)(1-2\nu)} \tag{2.7a}$$

$$\mu = \frac{E}{2(1+\nu)} \tag{2.7b}$$

2.2.6 Helmholtz's decomposition

Using the Helmholtz decomposition theorem allows us to resolve the displacement field, **u**, into the longitudinal and transverse vector components as follows,

$$\mathrm{u} = \nabla \phi + \nabla \times \vec{\psi} \tag{2.8}$$

where ϕ is the scalar compressional (longitudinal) wave potential and $\vec{\psi}$ is the shear (transverse) wave vector potential. For the uniqueness of the solution, the following Gauge condition shall be satisfied as:

$$\nabla \cdot \vec{\psi} = 0 \tag{2.9}$$

By substituting Equation (2.8) into the field equation of motion, Equation (2.6), we obtain two sets of uncoupled partial differential equations relative to the compressional wave P related to the Helmholtz scalar potentials ϕ, and to the shear wave S related to the Helmholtz vector potential $\vec{\psi}$, respectively. In the axi-symmetric condition, only the second components exist in vector $\vec{\psi}$, which is denoted as $\hat{\psi}$. They can be written in the Laplace transform domain by considering zero initial conditions as follows:

$$c_p^2 \nabla^2 \hat{\phi} - s^2 \hat{\phi} = 0 \tag{2.10a}$$

$$c_s^2 \nabla^2 \hat{\psi} - s^2 \hat{\psi} = 0 \tag{2.10b}$$

where $c_p = \frac{\lambda+2\mu}{\rho}$ is the P wave velocity and $c_s = \frac{\mu}{\rho}$ is the S wave velocity.

The solution to the wave equations (2.10) is obtained using the Laplace transform and Fourier-Bessel series.

2.2.7 Time variable treatment

The time variable, t, in Equation (2.10) can be treated using the Laplace transform ($t \rightarrow s$) as

$$\mathcal{L}\{\theta(t)\} = \widehat{\theta}(s) = \int_{\gamma-i\infty}^{\gamma+i\infty} \theta(t) e^{-st} dt \tag{2.11}$$

2.2.8 Solutions for potential variables

Referring to Equation (2.10), the scalar potential $\hat{\phi}(r,z)$ and vector $\hat{\psi}(r,z)$ can be decomposed into two independent functions of $\hat{R}$ and $\hat{Z}$. For instance, $\hat{\phi}(r,z)$ in the cylindrical coordinates (r,θ,z) can be written as:

$$\hat{\phi}(r,z) = \hat{R}(r)\hat{Z}(z) \tag{2.12}$$

where r, θ and z denotes the radial, azimuthal, and vertical coordinates, respectively.

Substituting Equation (2.12) into Equation (2.10) and setting both sides of the equation equal to an arbitrary constant $-k^2$ (then move the k^2 term to left-hand side), we can obtain two independent ordinary equations (ODE) :

$$\frac{d^2\hat{R}(r)}{dr^2} + \frac{1}{r}\frac{d\hat{R}(r)}{dr} + k^2\hat{R}(r) = 0 \tag{2.13a}$$

$$\frac{d^2\hat{Z}(z)}{dz^2} - \left(\frac{s^2}{c_p^2} + k^2\right)\hat{Z}(z) = 0 \tag{2.13b}$$

Introducing variable $a = kr$ where k is known as the wavenumber and r is the distance between the impact source and the receiver in the radial direction, Equation 2.13a is transformed to Bessel's equation:

$$\frac{d^2\hat{R}(a)}{da^2} + \frac{1}{a}\frac{d\hat{R}(a)}{da} + \hat{R}(a) = 0 \tag{2.14}$$

The radial space variable treatment, shown in Equation 2.14 is refereed as the radial relaxation method. The solution of Equation (2.14) is a function of Bessel functions J_0 and Y_0 of first and second kind, respectively, as follows

$$\hat{R}_m(r) = A_{1m}J_0\ (k_m\, r) + A_{2m}Y_0\ (k_m\, r) \tag{2.15}$$

where m represents the mode number; A_{1m} and A_{2m} are the arbitrary coefficients for each mode; $k_m = \frac{\alpha_m}{R}$ (R represents the location where induced displacement becomes negligible, taken as 20m (Al-Khoury, Scarpas, Kasbergen, and Blaauwendraad, 2001)) is the wavenumber in radial direction for mode m; α_m is the positive roots of J_0 function (Abramowitz, 1985).

Since the oscillation at the origin ($r = 0$) is finite and the value of Y_0 goes to infinite at $r = 0$, the term with Y_0 is dropped (Al-Khoury, Scarpas, Kasbergen, and Blaauwendraad, 2001). Applying the boundary conditions that $\hat{R}_m(R) = J_0(kR) = 0$ when the distance is far enough ($r \to R$), the solution of $\hat{R}_m(r)$ is obtained in Equation 2.16. The applied boundary condition ensures that the response due to an impact load is damped at a long distance.

$$\hat{R}_m(r) = A_{1m}J_0\ (k_m\, r) \tag{2.16}$$

The solution for Equation (2.13b) is:

$$\hat{Z}(z) = A_{2m} e^{-k_p z} \tag{2.17}$$

where

$$k_p = \sqrt{\frac{s^2}{c_p^2} + k_m^2} \tag{2.18}$$

Therefore, the solution for the scalar potential $\hat{\phi}(r,z)$ is given by:

$$\hat{\phi}(r,z) = A_m \, e^{-k_p z} J_0(k_m \, r) \tag{2.19}$$

where A_m is the coefficient to be determined from boundary conditions.

Similarly, the solution for the vector potential $\hat{\psi}(r,z)$ is obtained as:

$$\hat{\psi}(r,z) = C_m \, e^{-k_s z} J_1(k_m \, r) \tag{2.20}$$

where J_1 is the first-kind Bessel function of order one.

$$k_s = \sqrt{\frac{s^2}{c_s^2} + k_m^2} \tag{2.21}$$

2.2.9 Two-node element for layers with finite thickness

By including both incident wave and reflected wave, the potentials for a layer with finite thickness can be written as:

$$\hat{\phi}(r,z) = \underbrace{\left(A_m \, e^{-k_p z} + B_m \, e^{-k_p (h-z)}\right)}_{\overline{\phi}} \, J_0(k_m \, r) \tag{2.22a}$$

$$\hat{\psi}(r,z) = \underbrace{\left(C_m \, e^{-k_s z} + D_m \, e^{-k_s (h-z)}\right)}_{\overline{\psi}} \, J_1(k_m \, r) \tag{2.22b}$$

where h (m) represents the thickness of each layer.

By substituting Equations (2.22) into Equation (2.8), the displacement components in the matrix form can be written as:

$$\begin{Bmatrix} \overline{u}_{r1} \\ \overline{u}_{z1} \\ \overline{u}_{r2} \\ \overline{u}_{z2} \end{Bmatrix} = \underbrace{\begin{bmatrix} -k_m & -k_m\, e^{-hk_p} & k_s & -k_s\, e^{-hk_s} \\ -k_p & k_p\, e^{-hk_p} & k_m & k_m\, e^{-hk_s} \\ -k_m\, e^{-hk_p} & -k_m & k_s\, e^{-hk_s} & -k_s \\ -k_p\, e^{-hk_p} & k_p & k_m\, e^{-hk_s} & k_m \end{bmatrix}}_{S_1'} \begin{Bmatrix} A_m \\ B_m \\ C_m \\ D_m \end{Bmatrix} \tag{2.23}$$

where $\overline{u}_r$ and $\overline{u}_z$ represents the radial and vertical displacement in frequency domain; the subscript 1 and 2 represents the top and bottom node.

The stress component can be also written in terms of potentials by combining Equations (2.4) and (2.23):

$$\begin{Bmatrix} \overline{\sigma}_{rz1} \\ \overline{\sigma}_{z1} \\ \overline{\sigma}_{rz2} \\ \overline{\sigma}_{z2} \end{Bmatrix} = \underbrace{\begin{bmatrix} 2k_pk_m\mu & -2k_mk_p\mu e^{-hk_p} & -(k_m^2+k_s^2)\mu & -(k_m^2+k_s^2)\mu e^{-hk_s} \\ k_n^2 & k_n^2\, e^{-hk_p} & -2k_mk_s\mu & 2k_mk_s\mu\, e^{-hk_s} \\ 2k_mk_p\mu\, e^{-hk_p} & -2k_mk_p\mu & -(k_m^2+k_s^2)\mu\, e^{-hk_s} & -(k_m^2+k_s^2)\mu \\ k_n^2 e^{-hk_p} & k_n^2 & -2k_mk_s\mu\, e^{-hk_s} & 2k_mk_s\mu \end{bmatrix}}_{S_2'} \begin{Bmatrix} A_m \\ B_m \\ C_m \\ D_m \end{Bmatrix} \tag{2.24}$$

where $k_n^2 = k_p^2(\lambda + 2\mu) - k_m^2\lambda$; A_m, B_m, C_m and D_m are the coefficients to be determined from boundary conditions.

According to the Cauchy stress principle, the traction force ($[\bar{T}_{rz1},\ \bar{T}_{z1},\ \bar{T}_{rz2}.\ \bar{T}_{z2}]^T$) is taken as the dot product between the stress tensor and unit vector along the outward normal direction. Due to the convention that the upward direction is negative, the upper boundary becomes ($[-\overline{\sigma}_{rz1},\ -\overline{\sigma}_{z1}]^T$). Similarly, to make the sign consistent, the N matrix is applied to matrix $S_2'\ \cdot {S_1'}^{-1}$. In the future, the matrix $N \cdot S_2'\ \cdot {S_1'}^{-1}$ will be denoted as G_i matrix, in which i denotes the layer number.

$$\begin{Bmatrix} \bar{T}_{rz1} \\ \bar{T}_{z1} \\ \bar{T}_{rz2} \\ \bar{T}_{z2} \end{Bmatrix}_i = \begin{Bmatrix} -\overline{\sigma}_{rz1} \\ -\overline{\sigma}_{z1} \\ \overline{\sigma}_{rz2} \\ \overline{\sigma}_{z2} \end{Bmatrix}_i = \underbrace{N \cdot S_2'\ \cdot {S_1'}^{-1}}_{G_i} \cdot \begin{Bmatrix} \overline{u}_{r1} \\ \overline{u}_{z1} \\ \overline{u}_{r2} \\ \overline{u}_{z2} \end{Bmatrix}_i \tag{2.25}$$

where

$$N = \begin{bmatrix} -1 & 0 & 0 & 0 \\ 0 & -1 & 0 & 0 \\ 0 & 0 & 1 & 0 \\ 0 & 0 & 0 & 1 \end{bmatrix} \tag{2.26}$$

2.2.10 One-node semi-infinite element

By assuming that no wave reflects back to a semi-infinite element, the displacement components for a layer with the infinite thickness in the matrix form can be written as:

$$\begin{Bmatrix} \overline{u}_r \\ \overline{u}_z \end{Bmatrix} = \underbrace{\begin{bmatrix} -k_m & k_s \\ -k_p & k_m \end{bmatrix}}_{S'_3} \begin{Bmatrix} A \\ C \end{Bmatrix} \tag{2.27}$$

Similarly, the stress component can be obtained in terms of potentials, as shown in Equation (2.28). The relation between the stress components and displacement components are shown in Equation (2.29). The matrix $-S'_4 \cdot {S'_3}^{-1}$ will be denoted as S matrix for simplicity in the future.

$$\begin{Bmatrix} \overline{\sigma}_r \\ \overline{\sigma}_z \end{Bmatrix} = \underbrace{\begin{bmatrix} 2k_m k_p \mu & -\mu(k_m^2 + k_s^2) \\ k_n^2 & -2k_m k_s \mu \end{bmatrix}}_{S'_4} \begin{Bmatrix} A \\ C \end{Bmatrix} \tag{2.28}$$

$$\begin{Bmatrix} -\overline{\sigma}_r \\ -\overline{\sigma}_z \end{Bmatrix} = \underbrace{-S'_4 \cdot {S'_3}^{-1}}_{\mathrm{S}} \cdot \begin{Bmatrix} \overline{u}_r \\ \overline{u}_z \end{Bmatrix} \tag{2.29}$$

After obtaining the matrix for each element, the global matrix can be obtained by applying the continuity conditions between layer interfaces. The stiffness assembling method is shown in Figure 2.2. The global stiffness is denoted as H matrix for simplicity. An example of global stiffness matrix for a three layer system is provided in Section 2.7.

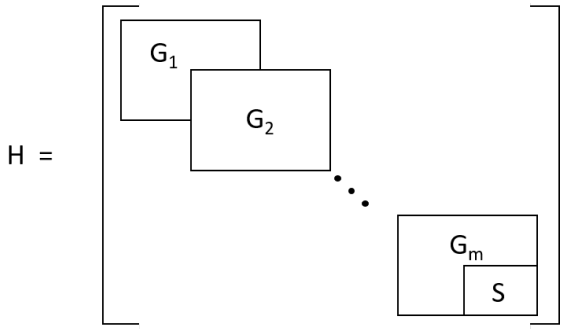

FIGURE 2.2: Global stiffness matrix construction

The system of equation then can be expressed as:

$$T = H\,U \tag{2.30}$$

where T is the external traction force vector; H is the stiffness matrix and U is the displacement vector.

The dispersion relation is obtained by setting a zero stress condition ($T = 0$) at the surface ($z = 0$). To obtain the non-trial solution, the determinant of the global stiffness matrix has to be zero, as expressed in Equation 2.31 (Zomorodian and Hunaidi, 2006).

$$\det H(\omega, k) = 0 \tag{2.31}$$

It should be noted that the global stiffness matrix, $H(\omega, k)$, is a function of angular frequency ω and wavenumber k. The relation between the angular frequency ω and s in Laplace domain is $\omega = -si$ where $-1 = \sqrt{i}$. The global matrix contains the terms related to k_s and k_p, which are dependent on the frequency. For a constant frequency, the value of wavenumber can be determined when the determinant of the global stiffness matrix is zero. This is similar to a root finding problem. The different wavenumbers determined at a given frequency corresponds to dispersion curves with different modes. For instance, the largest wavenumber for a frequency belongs to the fundamental mode and the second largest wavenumber belongs to the second mode. The dispersion curve is also commonly displayed as frequency versus phase velocity, $v = \frac{\omega}{k}$, in which k is the wavenumber.

In this paper, a simple algorithm is proposed to effectively find the wavenumber or phase velocity for a given frequency and soil parameters. The algorithm performs a sweep in a broad range of wavenumbers for a given frequency. A rough interval where roots exist needs to be found first and then Brent's method can be applied to accurately locates the roots. The following notations are used in the algorithm: ϵ for the wavenumber

sweep increment; n for the number of iterations; k_0 for the initial wavenumber, k for the wavenumber at the current step; k' for the wavenumber at the previous step; $f(k)$ gives the determinant value of the stiffness matrix at wavenumber k; δ for the tolerance used to check if the determinant of the stiffness matrix is close to zero; $Brent(k, k')$ is Brent's method that takes an internal (k, k') as input where $f(k)$ and $f(k')$ must have different sign; r is the root calculated from Brent's function.

The algorithm is shown as follows:

$$
\begin{cases}
Given\ \ \epsilon,\ k_0,\ \delta,\ n \\
for\ \ i = 1, 2, ...n \\
\quad k = k + \epsilon \\
\quad k' = k - \epsilon \\
\quad v1 = f(k) \\
\quad v2 = f(k') \\
\quad if\ \ v1 \cdot v2 \leq 0 \\
\qquad r = Brent(k, k') \\
\qquad if\ \ f(r) < \delta \\
\qquad\quad return\ \ r \\
end\ for
\end{cases}
\tag{2.32}
$$

In the dispersion analysis, the ultimate goal is to find pairs of frequency and wave number so that the determinant of the global stiffness matrix becomes zero. Therefore, the scaling can be applied to the stiffness matrix as long as the sign remains the same. It is found that by multiplying the stiffness matrix by 10^{-10}, the occurrences of large numbers are avoided in the determinant calculation, which enhances the stability of the proposed algorithm.

2.3 MASW inversion analysis

The determination of soil parameters requires a physical forward solver and a back-calculation algorithm to fit the field measurements. The inversion can be based on the dispersion curve of Rayleigh wave (known as the surface wave inversion).

2.3.1 Objective function

In this paper, the Euclidean norm is used to construct the objective function. The problem is formulated as the following form:

$$\begin{cases} minimize\ f(\boldsymbol{x}) = \frac{1}{2}\sum_{i=1}^{N}(y_i - \bar{y}_i(\boldsymbol{x}))^2 \\ subject\ to\ a_i \leq x_i \leq b_i,\ i\ = 1,\ \ldots, m \end{cases} \tag{2.33}$$

where $\boldsymbol{x} = (x_1, x_2, ...x_m)$ is the optimization variable; $f(x)$ is the objective function; the constant a_i and b_i are limits or bounds for each variable.

By assuming that the soil is elastic, the optimization parameter $\boldsymbol{x}$ normally includes soil's Young's modulus (E), Poisson's ratio (μ), density (ρ) and thickness (H) for each layer. The parameter y_i is the phase velocity at a frequency. The value of $\bar{y}_i$ is calculated using the proposed forward solver via the trial parameters $\boldsymbol{x}$.

It is known that the dispersion curve (or the objective function) is relatively less sensitive to the density and Poisson's ratio compared to Young's modulus. However, the predicted soil parameters and layer thicknesses can deviate from the real values even more if the assumed Poisson's ratio and density are not reasonable. Therefore, Poisson's ratio and density are required to be included in the optimization process unless their values are available based on prior information.

2.3.2 Trust-region reflective method

According to (Ahsan and Choudhry, 2017), the trust-region reflective method (TRR) offers higher accuracy with less cost as compared to Gauss-Newton and Levenberg Marquardt methods. Meanwhile, the TRR method supports the bounds for optimization variables. The trust region reflective method transform bounded least square algorithm into unconstrained optimization by incorporating the line search method. The general formulation is still similar to the traditional trust region method. In general, the trust region method approximates the objective function using Taylor-series expansion around the evaluation point. The gradient and Hessian matrix of residual function with respect to the optimization variable ($\boldsymbol{x}$) is obtained by evaluating:

$$\begin{cases} g(\boldsymbol{x}) = \nabla f(\boldsymbol{x}) = \sum_{j=1}^{m} r_j(\boldsymbol{x})\frac{\partial r_j}{\partial x_i} = J(\boldsymbol{x})^T r(\boldsymbol{x}) \\ H(\boldsymbol{x}) = \nabla^2 f(\boldsymbol{x}) == J(\boldsymbol{x})^T J(\boldsymbol{x}) + \sum_{j=1}^{m} r_j(\boldsymbol{x})\nabla^2 r_j(\boldsymbol{x}) \end{cases} \tag{2.34}$$

in which $r = y_i - \bar{y}_i$ and $J(\boldsymbol{x})$ is defined as:

$$J(\boldsymbol{x}) = \left[\frac{\partial r_j}{\partial x_i}\right]_{j=1,2,\ldots m \quad i=1,2,\ldots n} \tag{2.35}$$

An appealing feature of this problem is that by knowing the Jacobian $J(\boldsymbol{x})$, we can obtain Hessian ($\nabla^2 f(\boldsymbol{x})$) for free. Moreover, the first term, $J(\boldsymbol{x})^T J(\boldsymbol{x})$, usually is more important than the second term, $\sum_{j=1}^{m} r_j(\boldsymbol{x}) \nabla^2 r_j(\boldsymbol{x})$ since the residual is assumed to be small enough. Therefore, the second derivative, $\nabla^2 f(\boldsymbol{x})$, simply reduces to $J(\boldsymbol{x})^T J(\boldsymbol{x})$, which essentially is the advantage of the least square algorithm. It should be noted the $J(\boldsymbol{x})$ function is computed numerically in this paper.

To incorporate the bound constraint to the optimization variable, the first order necessary conditions for $\boldsymbol{x}$ to be a local minimum is shown in Equation (2.36).

$$g(\boldsymbol{x})_i = 0 \quad if\ l_i < x_i < u_i \tag{2.36a}$$

$$g(\boldsymbol{x})_i \leq 0 \qquad if\ x_i = u_i \tag{2.36b}$$

$$g(\boldsymbol{x})_i \geq 0 \qquad if\ x_i = l_i \tag{2.36c}$$

A vector $v(\boldsymbol{x})$ is defined to measure the distance to the bounds, as shown in Equation (2.37):

$$v(\boldsymbol{x})_i = \begin{cases} u_i - x_i & g(\boldsymbol{x})_i < 0 \ \ and\ u_i < \infty \\ x_i - l_i & g(\boldsymbol{x})_i > 0 \ \ and\ l_i > -\infty \\ 1 & otherwise \end{cases} \tag{2.37}$$

The first order necessary conditions are then modified in Equation (2.38). If the optimization variable ($\boldsymbol{x}$) falls on the bounds, $D(\boldsymbol{x})$ becomes zero. On the other hand, if the variable located between the lower and upper bounds, $g(\boldsymbol{x})$ becomes zero.

$$D(\boldsymbol{x})^2 g(\boldsymbol{x}) = 0 \tag{2.38}$$

in which $D(\boldsymbol{x})$ is defined as $Diag(v(\boldsymbol{x})^{1/2})$.

The trust region reflective formulation is similar to the traditional trust region method, except with different definitions for the gradient, Hessian and other parameters. After introducing Newton's step (line search method), the trust region subproblem is defined as

follows:

$$min \;\; m_i(\hat{p}) = \hat{g}^T \hat{p} + \frac{1}{2}\hat{p}^T \hat{H}_i \hat{p} \qquad \hat{p} \leq \Delta_i \tag{2.39}$$

where m represents the function value at current point; $\hat{g} = D\, g$ is the modified gradient; $\hat{p}$ is the modified trust region steps; $\hat{H} = D\, H\, D + C$ is the modified Hessian matrix where $C = diag(g) J_v$ and J_v is the Jacobian of $v(x)$; Δ_i is the trust region radius.

In each step, the trust region algorithm updates the size and an improvement ratio is defined to evaluate the performance of the approximation. In this case, a modified improvement ratio of the trust-region solution is computed as follows:

$$\rho_i = \frac{f(x_i) - f(x_i + p_i) + \frac{1}{2}\hat{P}^T C \hat{P}}{m_i(\hat{p}_i)} \tag{2.40}$$

It should be realized that if ρ_k is smaller than zero, which means the actual reduction is not achieved, then such step should be rejected. However, if ρ_k is close to one, it means that the model used to approximate the function has in a good agreement with the original function. Therefore, it is safe to expand the trust region. If the value is close to zero, we should shrink the trust region. With the modified parameters used in the trust region algorithm, the traditional update rule can then be applied. The detailed description is given in (Nocedal and Wright, 2006).

In the trust region reflective optimization, the gradient needs to be calculated before switching to the next trust region, which ensures that the cost function reduces in each step. However, such gradient dependent method could not utilize the parallel computing techniques since the calculation needs to be done step by step. To increase the calculation speed without sacrificing the advantages of using the trust region reflective method, the parallel computing is only implemented for the forward solver computation. The calculation of the phase velocity at different frequencies is independent and can be evaluated in parallel through multi-processing controls.

The integrated approach for the MASW forward and inversion algorithms, as presented above, is implemented in an open source code, Intelligent MASW, which can be find in (Liu, Maghoul, and Shalaby, 2020a) or `https://github.com/Siglab-code/Intelligent-MASW`.

2.4 Model validation

It should be noted that the dispersion curve and soil response analysis possess different features. The dispersion curve reflects the geometry and soil properties. Meanwhile, the

distribution of dispersion curves is an intrinsic property of the system and is independent of the applied loads. During the inverse process, such a feature can be beneficial since users are not required to measure the applied loads, which eventually reduces the computational effort.

2.4.1 Dispersion model validation

In this section, a case study was performed to validate the proposed integrated approach. A four-layer system was studied by (Beaty, Schmitt, and Sacchi, 2002) and the parameters used in the analysis are shown in Table 2.1.

TABLE 2.1: Soil Parameters used in the dispersion analysis (Beaty, Schmitt, and Sacchi, 2002) (Case Study 1)

Layer	v_s (m/s)	v_p (m/s)	ρ (kg/m^3)	Thickness (m)
1	80	185	1180	0.8
2	140	480	1780	3.7
3	140	1650	1780	2.5
4	1040	1650	2180	∞

The dispersion curves from the first to fourth modes were obtained by (Beaty, Schmitt, and Sacchi, 2002) using Menke's method in which the transfer function was used, as a forward solver, to obtain the dispersion relation of multilayered systems. The proposed approach in this paper, on the other hand, used the global matrix method. Figure 2.3 shows the results obtained from the proposed approach in this paper and Menke's method. Despite of different methodologies, a good agreement was achieved in dispersion curves, which proves the accuracy of the proposed algorithm.

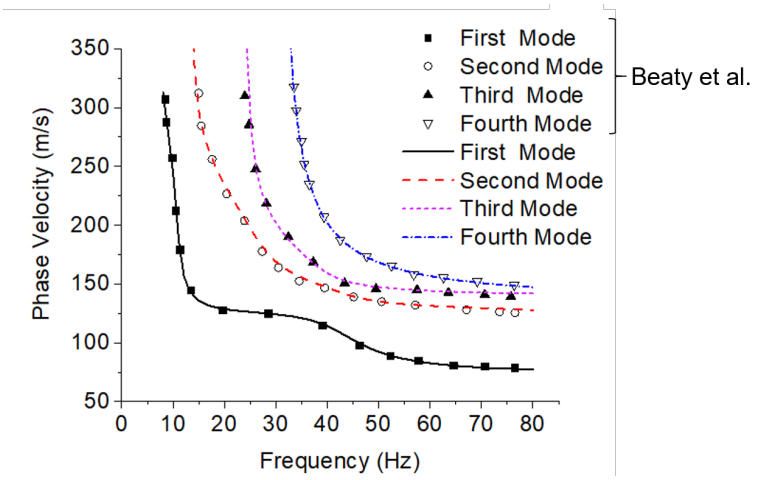

FIGURE 2.3: Comparison between the dispersion curves obtained through the integrated approach proposed in this study and data provided by (Beaty, Schmitt, and Sacchi, 2002)

For the system with low velocity half space, the model is validated with the case study performed by (Pan, Xia, and Zeng, 2013). In this case study, a six-layer system was studied and the corresponding soil parameters for each layer can be found in Table 2.2 (Pan, Xia, and Zeng, 2013). The dispersion curves are obtained at the locations where the determinant of the stiffness matrix is zero. As shown in Figure 2.4, the first-mode dispersion curve matched well with the results obtained by (Pan, Xia, and Zeng, 2013). Furthermore, the second and third modes are also given in this paper.

TABLE 2.2: Six-layer earth model with low velocity half-space layer ((Pan, Xia, and Zeng, 2013))

Layer number	v_s (m/s)	v_p (m/s)	ρ (kg/m^3)	Thickness (m)
1	194	650	1820	2.0
2	270	750	1860	2.3
3	367	1400	1910	2.5
4	485	1800	1960	2.8
5	603	2150	2020	3.2
6	350	1350	2090	infinite

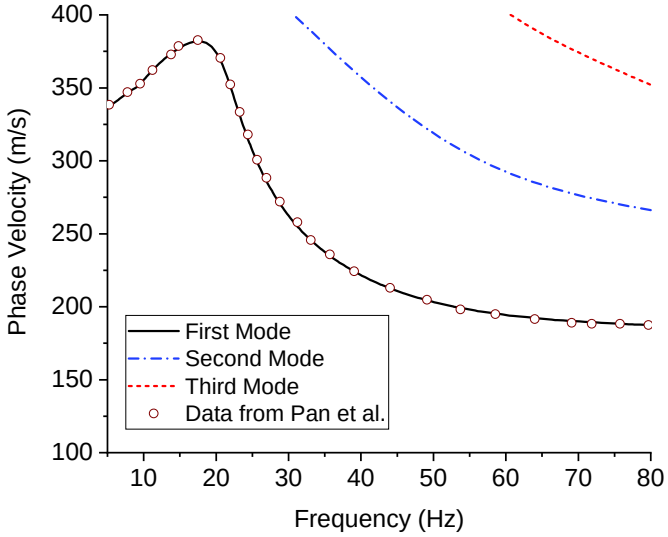

FIGURE 2.4: Comparison between the dispersion curves obtained through the integrated approach proposed in this study and data provided by (Pan, Xia, and Zeng, 2013)

2.5 Results and discussion

In this section, five different cases are studied, as follows. The soil domain in Cases 1 to 3 is composed of a four-layered system while in Cases 4 and 5 the soil domain is composed of a three-layered system.

- Case 1: in which the soil stiffness increases monotonically with depth. This is one of the most important assumptions made in the conventional seismic non-destructive testing analyses. The results demonstrated in the section 4.1 were obtained for this case.

- Case 2: in which it is assumed that a stiff layer is located between two relatively soft layers. This can represent a case when a frozen soil layer is located between a melting layer at the top and an unfrozen soil layer at the bottom.

- Case 3: in which it is assumed that a soft layer is located between two stiff layers. This can represent a case when a soft soil layer is located between a stiff layer at the bottom and a freezing soil layer at the top.

- Case 4 and Case 5: in which the stiffness of the soil layers increases with depth. This represents a simplified soil stratigraphy at the subsurface, which is followed by a bedrock layer.

2.5.1 The effect of soil stratigraphy on dispersion relations

To study the effect of soil stratigraphy on dispersion curves, the dispersion curves for Case 1 (shown in Table 2.1) and Case 2 are compared. As mentioned above, the soil stiffness in Case 1 increases monotonically with depth while in Case 2, it is assumed that a stiff layer is located between two relatively soft layers. The soil parameters can be found in Table 2.3.

TABLE 2.3: Soil parameters used in case study 2

Layer	v_s (m/s)	v_p (m/s)	ρ (kg/m^3)	Thickness (m)
1	80	185	1180	0.8
2	140	480	1780	3.7
3	1040	1650	2180	2.5
4	140	1650	1780	∞

A comparison of dispersion curves between Case 1 and Case 2 are shown in Figure 2.5. The dispersion curve distribution for each mode is different in Case 1 and Case 2. For the first mode (fundamental mode), the separation was visualized for frequencies less that 20 Hz. As frequency increases, the dispersion curve starts to overlap. The similar phenomenon was visualized for higher modes.

An interesting observation is that in Case 1 where the soil stiffness increases monotonically with depth, the phase velocity of each mode decreases continuously with frequency. When frequency is relatively low, the penetration depth of Rayleigh wave is deeper. Consequently, geomaterials located at greater depths with a higher stiffness affect the phase velocity profile more. Therefore, the phase velocity is higher at low frequencies than that at high frequencies when the soil stiffness increases monotonically with depth.

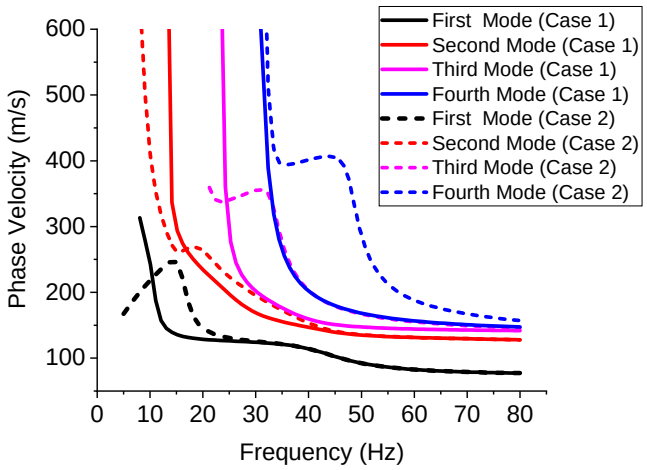

FIGURE 2.5: Dispersion curves for Case 1 and Case 2

The dispersion curve comparison between Case 1 and Case 3 is shown in Figure 2.6. The soil parameters used for Case 3 can be found in Table 2.4. At the same frequency, the phase velocity (Rayleigh wave velocity) is larger in Case 3, which is due to the stiffer materials in the second layer. The existence of a soft layer makes the dispersion curve non-continuous. A transition interval is observed between the phase velocities of 400 m/s and 500 m/s in Case 3.

TABLE 2.4: Soil Parameters used in Case study 3

Layer	v_s (m/s)	v_p (m/s)	ρ (kg/m^3)	Thickness (m)
1	80	185	1180	0.8
2	1040	1650	2180	2.5
3	140	480	1780	3.7
4	1040	1650	2180	∞

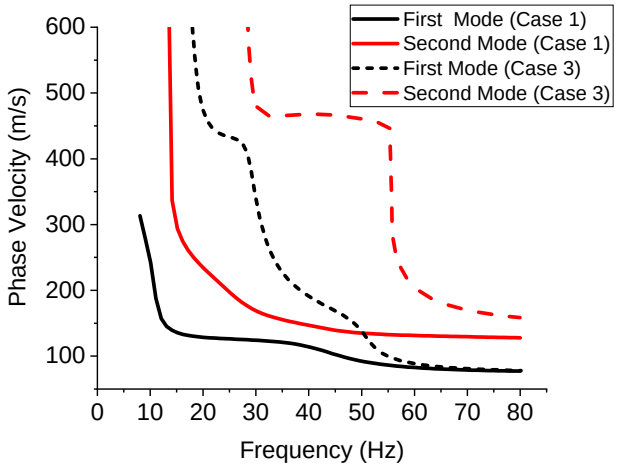

FIGURE 2.6: Dispersion curve for Case 1 and Case 3

As shown in Figure 2.7, four different slopes are visualized for the first mode in these three cases in terms of frequency-wavenumber, in which each slope represents one layer. For example, the layers are labeled for Case 3 in Figure 2.7. Therefore, it is concluded that the distribution of dispersion curves reflects the soil stratigraphy. When the stiffness of soil layers increases monotonically with depth (Case 1), the phase velocity decreases monotonically with frequency. The discontinuity (fluctuation) of soil layout, such as existence of a soft and stiff layer, also induces discontinuity in dispersion curves. The number of transition can roughly reflects the number of layers in the field. Such information could largely reduce the computational cost during the full wave inversion since the number of layers can be obtained from the dispersion curves.

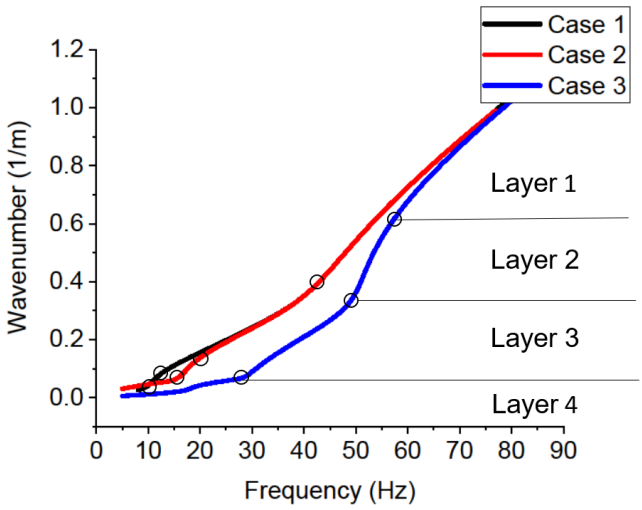

FIGURE 2.7: First mode dispersion curves for three Cases

2.5.2 Wavelength of dispersion curves considering various modes

In this section, the wavelength of fundamental and higher-mode dispersion curves in different cases are discussed. The following case studies are used to demonstrate the sensitivity of fundamental and higher-mode dispersion curves to soil layers located at a greater depth. A three-layered system is used for the case studies and parameters used in the analysis are listed in Table 2.5.

TABLE 2.5: Parameters used in the dispersion mode analysis

Case	Layer	v_s (m/s)	v_p (m/s)	ρ (kg/m^3)	Thickness (m)
Case 4	1	200	400	1600	20
	2	300	700	1800	30
	3	400	1200	2000	∞
Case 5	1	200	400	1600	20
	2	300	700	1800	30
	3	800	1200	2000	∞

In Case 4, the wavelength of each mode is shown in Figure 2.8. The phase velocity for frequencies less than 5 Hz is difficult to measure in practice. Therefore, only the data for frequencies higher than 5 Hz can be used in geotechnical non-destructive testing. As shown in Figure 2.8, the dispersion curves for higher modes give a relatively larger wavelength. For the fundamental mode, the largest wavelength is 41 m for the frequencies between 5 Hz and 40 Hz.

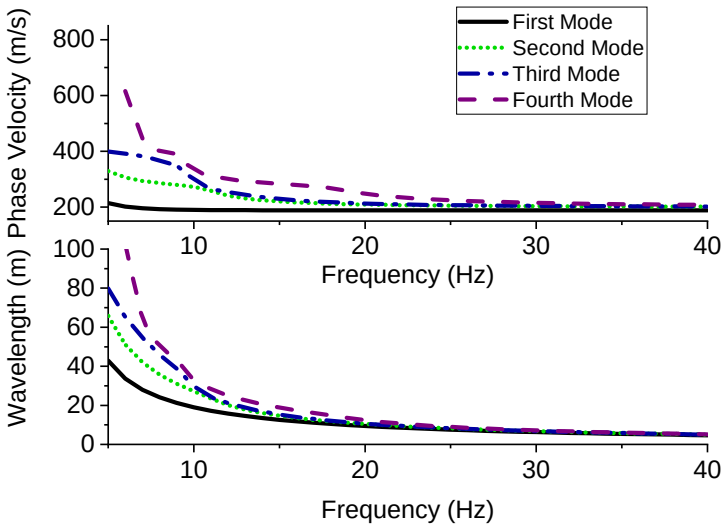

FIGURE 2.8: Phase velocity and wavelength variation with frequency in Case 4

In Case 5, the shear wave velocity of the third layer (50 m below the ground surface) increased to 800 m/s. The phase velocity variation with frequency in both cases are shown in Figure 2.9. Since the largest wavelength of the fundamental mode is 41 m, the soil parameter variation below 50 m is not captured by the fundamental mode, as shown in Figure 2.9. The wavelength of the second-mode dispersion curve are larger than 50 m for frequencies smaller than about 8 Hz. Therefore, the variation of phase velocity between Case 4 and Case 5 for frequencies between 5 Hz and 8 Hz can be visualized in Figure 2.9. The variations of phase velocity between Case 4 and Case 5 are amplified for the third mode and the fourth mode. Therefore, in this case, the higher-mode dispersion curves are important in determining the soil parameters for soil layers located at greater depths.

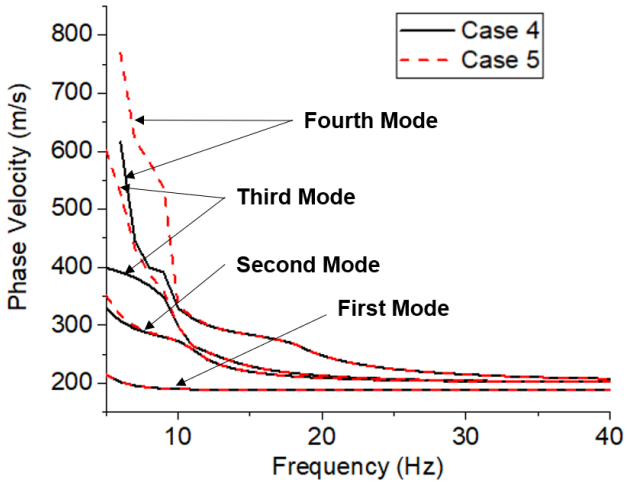

FIGURE 2.9: Phase velocity variation with frequency comparison for case 4 and case 5

2.5.3 MASW inversion case study

In this case study, the MASW data collected by (Olafsdottir, Erlingsson, and Bessason, 2017) in a site in Arnarbaeli (south Iceland) is used for the demonstration of the integrated approach proposed in this study. The data was collected using 24 geophones with a spacing of 1 m in between. The first geophone was located 10 m away from the source to avoid the near field effect. The detailed description of data collection is documented in (Olafsdottir, Erlingsson, and Bessason, 2017). The field measurement is shown in Figure 2.10a and the corresponding dispersion image is shown in Figure 2.10b.

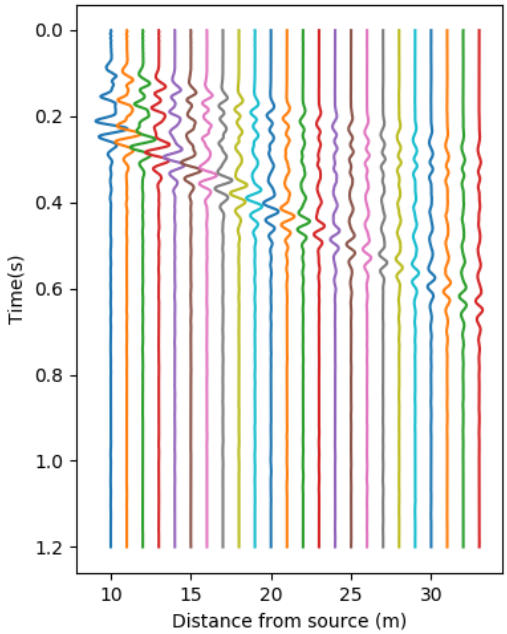

(A) MASW data in time domian

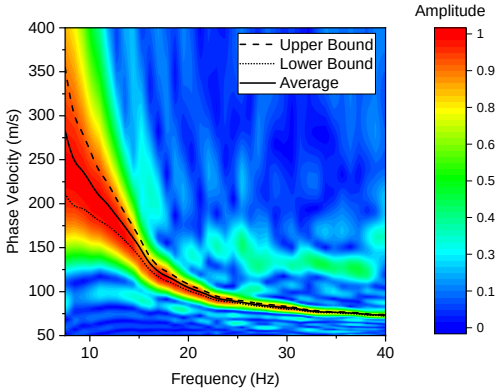

(B) MASW dispersion image

FIGURE 2.10: MASW filed measurement in Arnarbaeli in south Iceland with 24 channels

In this study, the inversion is performed based on the average dispersion curve shown in Figure 2.10b. Based on the frequency-wavenumber curves shown in Figure 2.11, two distinguished slopes are visualized, which might represent a two-layered system in the field based on the case study shown in Section 5.1. Out of conservative considerations, a four-layered system is initially assumed for this case study. In addition, the maximum wavelength is found to be around 30 m. Since only the fundamental mode is used for the inversion, the maximum investigation depth should be close to the maximum wavelength during the inversion. Therefore, the upper bound for thickness in each layer is set to be 30 m. Meanwhile, the phase velocity decreases with frequency, the shear wave velocity is initially assumed to increase monotonically with depth. The upper bound of shear wave velocity should be greater than the maximum value of the phase velocity, which is taken as 300 m/s. The lower bound for the shear velocity is taken as 15 m/s, which is smaller than the minimum phase velocity in the dispersion curve. The initial value and the lower/upper bound settings are shown in Table 2.6. It should be noted that Poisson's ratio is used as an optimization variable instead of P wave velocity due to the relatively easier implementation of bound constraint.

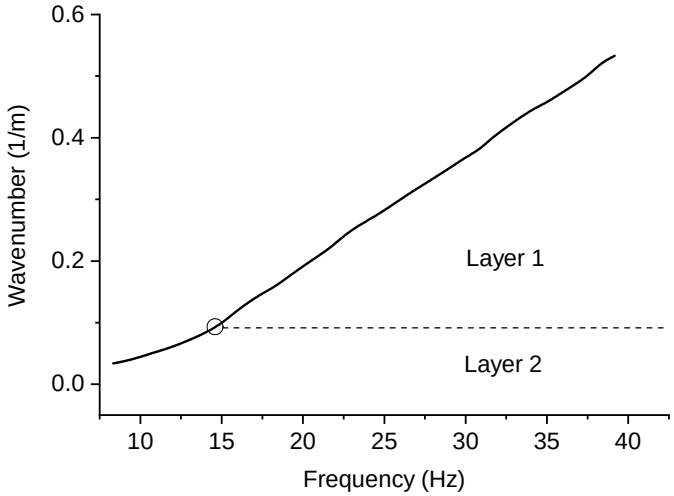

FIGURE 2.11: Frequency vs wavenumber/wavelength for Arnarbaeli in south Iceland (Olafsdottir, Erlingsson, and Bessason, 2017)

TABLE 2.6: Initial values and bounds setting for MASW Inversion

Layer number	v_s (m/s)	μ	ρ (kg/m^3)	Thickness (m)
1	30	0.35	2000	1
2	50	0.35	2000	5
3	75	0.35	2000	10
4	200	0.35	2000	infinite
Bounds	15 - 300	0.05-0.45	1200-5000	0.5-30

Through the trust region reflective method, the numerical dispersion curve quickly converges to the measured dispersion curve. Since the calculation of the phase velocity in each frequency is independent, the multiprocessing implementation can be used to significantly speed up the calculation. The calculation is done in a computer with Intel(R) Xeon(R) Gold 5115 CPU @ 2.40GHz and 40 cores. It is found that the inversion took around 62 seconds to finish. The loss function (Euclidean distance) reduced to 7 after 100 iterations, as shown in Figure 2.12.

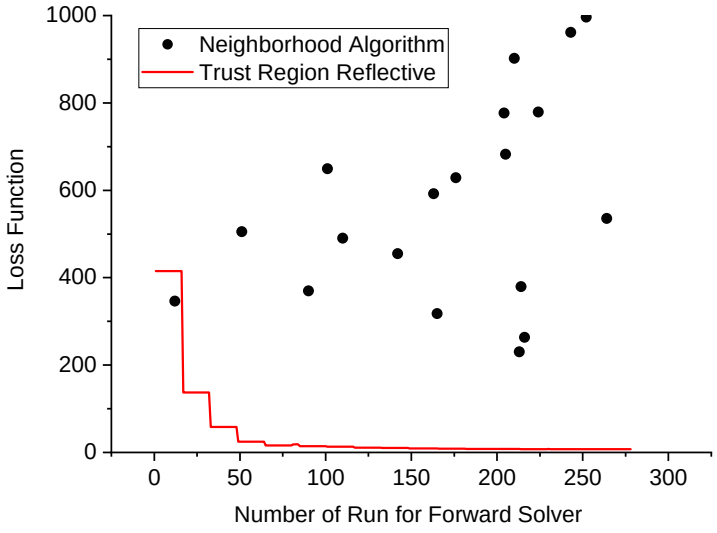

FIGURE 2.12: Loss function (neighborhood algorithm vs trust region reflective) with number of run for forward solver

A comparison between the commonly used neighborhood algorithm (10 samples are used for random sampling and neighborhood sampling) and the trust region reflective method is also given in Figure 2.12. The neighborhood algorithm can handle large-dimension inversion problems in which the gradients are costly to be evaluated. However, for the elastic-based MASW inversion, the trust region reflective method converges much faster and the minimum loss function can be obtained within 300 runs of the forward solver. Based on the inversion analysis of the MASW data, the final soil parameters for the site are shown in Table 2.7 and Figure 2.13. The comparison between the numerical predictions and measured dispersion curve is shown in Figure 2.14. A good agreement can be observed between the experimental data and the theoretical dispersion obtained through the integrated approach proposed in this study.

TABLE 2.7: Results for the MASW Inversion

Layer number	v_s (m/s)	v_p (m/s)	ρ (kg/m^3)	Thickness (m)
1	80.0	116.8	2144.4	1.1
2	137.0	451.7	2391.9	2.4
3	285.1	610.3	1376.5	7.9
4	305.5	468.7	2681.6	infinite

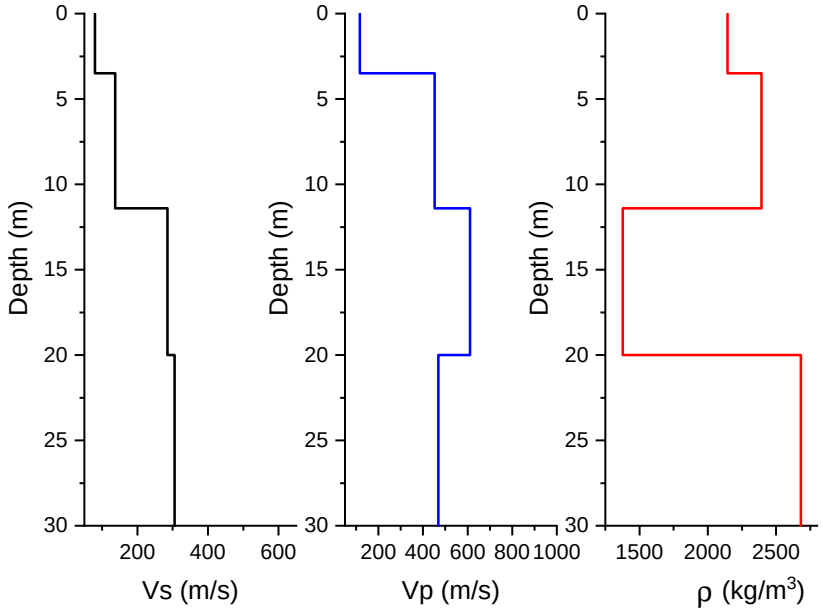

FIGURE 2.13: MASW inversion results for a site in Arnarbaeli in south Iceland

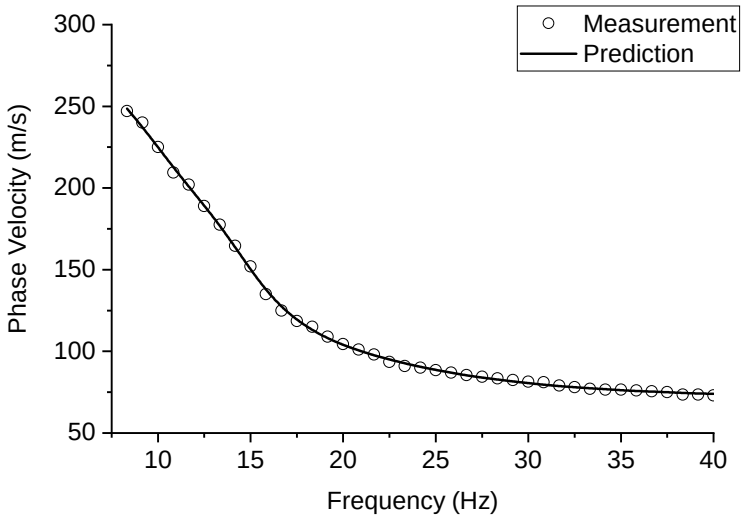

FIGURE 2.14: Comparison between experimental and theoretical dispersion curves

2.6 Conclusions

In this paper, a semi-analytical forward solver was obtained for the dispersion analysis using the spectral element method. An effective Brent's root-finding method was applied to obtain the exact dispersion curve. Based on the numerical case studies, it is concluded that when the stiffness of soil layers increases monotonically with depth, the phase velocity

decreases monotonically with frequency. The non-continuity of the soil stratigraphy, such as having soft or stiff intermediate layers, also induces non-continuity in the dispersion curves. The number of transition points reflects the number of layers in the field. Such an understanding of the dispersion curve can be used for the determination in initial guesses of the soil stratigraphy for the inversion analysis. The trust region reflective method was used in the inversion analysis to reduce the Euclidean distance between the experimental and numerically calculated dispersion curves. Based on a case study in Arnarbaeli in south Iceland, it is found that the integrated approach proposed in this study effectively determines the soil stratigraphy as well as the soil properties to match the measured dispersion curve within only 300 runs of the forward solver.

2.7 Supplementary materials

The stiffness matrix for a three-layered system is assembled as shown:

$$H = \begin{bmatrix} G^1_{11} & G^1_{12} & G^1_{13} & G^1_{14} & 0 & 0 \\ G^1_{21} & G^1_{22} & G^1_{23} & G^1_{24} & 0 & 0 \\ G^1_{31} & G^1_{32} & G^1_{33}+G^2_{11} & G^1_{34}+G^2_{12} & G^2_{13} & G^2_{14} \\ G^1_{41} & G^1_{42} & G^1_{43}+G^2_{21} & G^1_{44}+G^2_{22} & G^2_{23} & G^2_{24} \\ 0 & 0 & G^2_{31} & G^2_{32} & G^2_{33}+G^3_{11} & G^2_{34}+G^3_{12} \\ 0 & 0 & G^2_{41} & G^2_{42} & G^2_{43}+G^3_{21} & G^2_{44}+G^3_{22} \end{bmatrix}$$

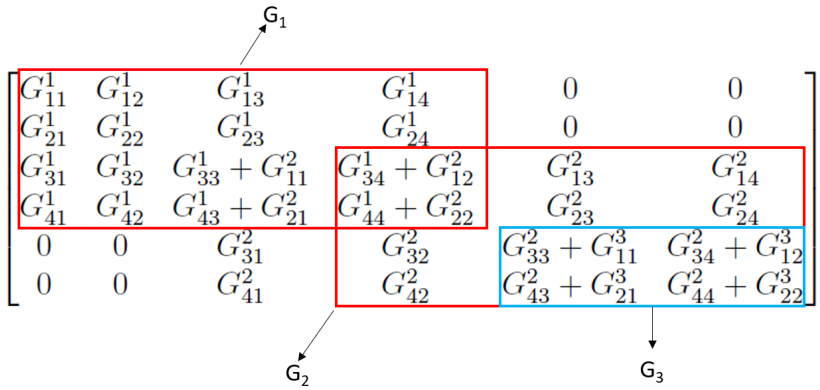

where G_1, G_2 and G_3 are the stiffness matrix for the first, second and third layer, respectively.

Chapter 3

Experimental investigation and numerical modeling of piezoelectric bender element motion and wave propagation analysis in soils

Abstract

The bender element (BE) test has been widely used for the dynamic characterization of soil specimens at low-shear strain levels. However, the actual behavior of the BE inside a soil specimen remains unknown. Thus, the current ASTM standard does not consider the interference of compressional and shear waves in BE testing, which can lead to significant errors in the evaluation of shear wave velocities. The main objective of this paper is to present a numerical model of the BE system to better understand the response of the BEs inside a soil sample. The model is calibrated, verified, and then used to demonstrate the importance of taking into consideration the interaction between compressional and shear waves for the correct interpretation of BE measurements. The model successfully captured the measured vibrations of the BE in air as well as inside transparent soils. More importantly, the numerical simulations provide a new understating of the significant interactions of P-waves and S-waves especially in clay soils. Thus, the proposed coupled piezoelectric and solid mechanics model can be used to study the soil-BE interaction so

Liu H., Cascante G., Maghoul P. and Shalaby A., 2021. *Experimental investigation and numerical modeling of piezoelectric Bender Element motion and wave propagation analysis in soils*, Canadian Geotechnical Journal (Canadian Science Publishing), In Press. https://doi.org/10.1139/cgj-2020-0757.

that sound recommendations can be given to improve the interpretation of BE tests in different soils.

3.1 Introduction

The dynamic soil properties play an important role in the design of earthquake-resistant structures and foundations. The bender element (BE) test and resonant column (RC) test are the most popular methods used for the evaluation of dynamic soil properties such as the shear wave velocity at low shear strains. The RC test is used to determine the resonant frequency of a soil column, which is related to the shear wave velocity and shear modulus. However, the RC test is time-consuming and costly in comparison to the BE test. The BE utilizes piezo-ceramic materials for the conversion of an electrical signal into mechanical energy. Two bender elements are placed at the two ends of the soil specimen in which one BE is used to introduce a mechanical impulse and the other one is used to receive the propagating pulse (normally in mV). The BE generates not only S-waves in the direction of their plane but also P-waves in the direction normal to their plane. The P-waves reflected from the cell walls can interfere with the generated S-waves (Lee and Santamarina, 2005).

The behavior of the BE has been studied both numerically and experimentally in the literature. For example, (Lee and Santamarina, 2005) showed that the P-wave reflected from the cell wall in the BE test arrives to the BE receiver earlier than the direct S-wave. In practice, the interpretation of the BE test results requires the consideration of the geometry of the specimen, such as the radius-to-height ratio (Lee and Santamarina, 2005). It is found that the resonant frequency of the BE embedded within the soil specimen depends on the stiffness of the BE, soil stiffness, and stress level in the soil (Camacho-Tauta, Cascante, Viana DA Fonseca, and, 2015). The BE has been also used in a triaxial apparatus for the measurement of anisotropy of fine-grained soils (Jovičić and Coop, 1998); it has shown that the BE is effective in measuring the inherent anisotropy resulting from the plastic strain history. (Youn, Choo, and Kim, 2008) compared the BE test with the resonant column test as well as the torsional shear test in sands; the results showed that the values of the shear wave velocity determined from the BE test correspond well with the resonant column test as well as the torsional test in dry conditions (Youn, Choo, and Kim, 2008). In saturated conditions, however, the current interpretation methods for BE measurements tends to overestimate the shear wave velocity in comparison to the two other tests (resonant column test and the torsional test), which is likely due to the interaction between the S- and P-waves (Youn, Choo, and Kim, 2008). The stiffness of unsaturated soils was tested with the BE and suction-controlled resonant column tests by (Hoyos, Suescún-Florez, and Puppala, 2015). A good agreement between the BE and resonant column tests was reported in terms

of the measurement in stiffness of silty sand under a suction-controlled condition. (Gu, Yang, Huang, and Gao, 2015) compared the results of the BE test with the RC test and the cyclic torsional shear test at various confining pressures, densities, and degrees of saturation. It was found that the travel time, under saturated conditions, obtained from the BE test is considerably smaller than that from the RC test due to the dispersion of the S-wave. However, this result could be attributed to the strong participation of P-waves observed in BE tests in saturated media. Recommendations in terms of the selection of the impulse frequency is given to reduce the subjectivity in interpreting the arrival time of S waves (Camacho-Tauta, Jimenez-Alvarez, and Reyes-Ortiz, 2012); a single sinusoidal pulse is recommended and the travel length-to-wavelength ratio should be high enough to reduce the near-field effect.

It is known that the transmitter response of the BE inside the soil specimen is very different from the input electrical signal. The BE response is not well represented by a cantilever beam as typically assumed in the literature (Karl, Haegeman, Pyl, and Degrande, 2003; Lee and Santamarina, 2005; Zhou, Chen, and Ding, 2007). Hence, to investigate the disparity between the input signal and the actual transmitter response, (Irfan, Cascante, Basu, and Khan, 2019) used a new BE test setup using a laser vibrometer. They used a transparent granular soil specimen such that the real transmitter response can be measured by the laser vibrometer. The BE was inserted in the water, sucrose solutions, mineral oils, and air to account for the effects of viscosity and density of the fluid medium and for the calibration of the BE transducer. The important findings from such experimental tests were: 1) the input square and step function pulses excite higher modes in comparison to the sine function pulses; 2) the fluid density dominates the transmitter response more than the viscosity of fluid; 3) there are P-wave components generated in typical BE tests.

Several methods have been developed in the past to interpret the signal obtained through the BE test. The first group is to calculate the shear wave velocity based on the first arrival time of S-wave, which includes the start-start method, peak-peak method, cross correlation method and cross power method. The cross correlation method is used to measure the degree of correlation of input and output signals (Viggiani and Atkinson, 1995) and the cross power method measures the correlation of input and output signal in frequency domain. However, the arrival-time based methods usually results in subjective and inaccurate interpretation of the shear wave velocity. Currently, it is still unclear which method provides the most reliable results (Gu, Yang, Huang, and Gao, 2015). An automatic shear wave velocity estimation method was developed by (Finas, Ali, Cascante,

and Vanheeghe, 2016) by applying the Akaike information criteria, which is effective for a signal-to-noise ratio (SNR) smaller than 4. This inherent complexity in the analysis of BE tests is clarified in this paper by the use of calibrated numerical simulations.

The behaviour of the BE has been numerically studied in the literature. (Arulnathan, Boulanger, and Riemer, 1998) used the finite element (FE) method to illustrate that the interpretation of the BE signals based on the cross correlation between the input and output signals is misleading due to the effects of wave interference at the boundaries, the phase lag between the mechanical energy and electrical input and multi-dimensional wave travel issues. A two-dimensional (2D) discrete element method was used by (O'Donovan, O'Sullivan, and Marketos, 2012) to study the response of an idealised granular material in the BE test. The particle velocity data was used to show the propagation of a central S-wave accompanied by P-waves moving along the sides of the soil specimen. A 2D finite element model was used by (Ingale, Patel, and Mandal, 2020) to study the effect of soil types and frequency on BE measurements. It was shown that the FE analysis is consistent with the S-wave velocity obtained through the peak-to-peak method. (Arroyo, Muir, Greening, Medina, and Rio, 2006) studied the effect of sample size on BE measurements by means of 3D finite element modeling. It was assumed that the displacement at the tip of the BE transmitter has the same displacement as the input voltage. However, this boundary condition assumed by (Arroyo, Muir, Greening, Medina, and Rio, 2006; Arulnathan, Boulanger, and Riemer, 1998; Hardy, Zdravkovic, and Potts, 2002; Jovicic, Coop, and Simic, 1996) does not consider the piezoelectric behavior of the BE transmitter and the disparity between the input signal and the actual transmitter response.

An analytical model of the piezoelectric BE motion was developed by (Zhou, Chen, and Ding, 2007) based on the first-order shear deformation theory by assuming a single rotation angle. An analytical modelling approach was also developed based on the beam theory under the quasi-static equilibrium condition, which can be used for the optimized design of piezoelectric bending actuators (Dunsch and Breguet, 2007). A close-form 3D piezoelectric model was developed by (Rabbani, Bahari, Hodaei, Maghoul, and Wu, 2019) to investigate the free vibration of triclinic piezoelectric hollow cylinder using the transfer matrix method and the state space method.

Despite the above-mentioned efforts, the actual behaviour of the BE inside the soil still remains unknown. Currently, there is no standard interpretation of the BE measurements due to the complex wave interaction introduced by the BE within the soil specimens. The accurate interpretation of BE measurements and wave propagation analysis is impossible

without knowing the motion of the BE inside the soil.

In this paper, a piezoelectric-solid mechanics model is proposed to study the BE motion in different media. The model is validated using the BE motion in the air, transparent soil, and Ottawa sand monitored by a laser vibrometer device. The estimation of the soil parameters such as the shear wave velocity and damping ratio of the Ottawa sand using the piezoelectric-solid mechanics model developed in this paper is then compared with independent experimental data obtained via the conventional RC test. Finally, the propagation of P- and S-waves within a soil specimen due to the BE motion is thoroughly studied and the suitability of empirical methods in estimating the arrival time of the S-wave is discussed.

3.2 Methodology and experimental setup

In this work, a FE model of a BE-soil sample is calibrated and verified using the laser vibrometer measurements on a) BE in air, b) BE in transparent soil, and c) BE in Ottawa sand specimen. Then, the results are independently verified using resonant column measurements. The detailed procedure is summarized in Figure 3.1.

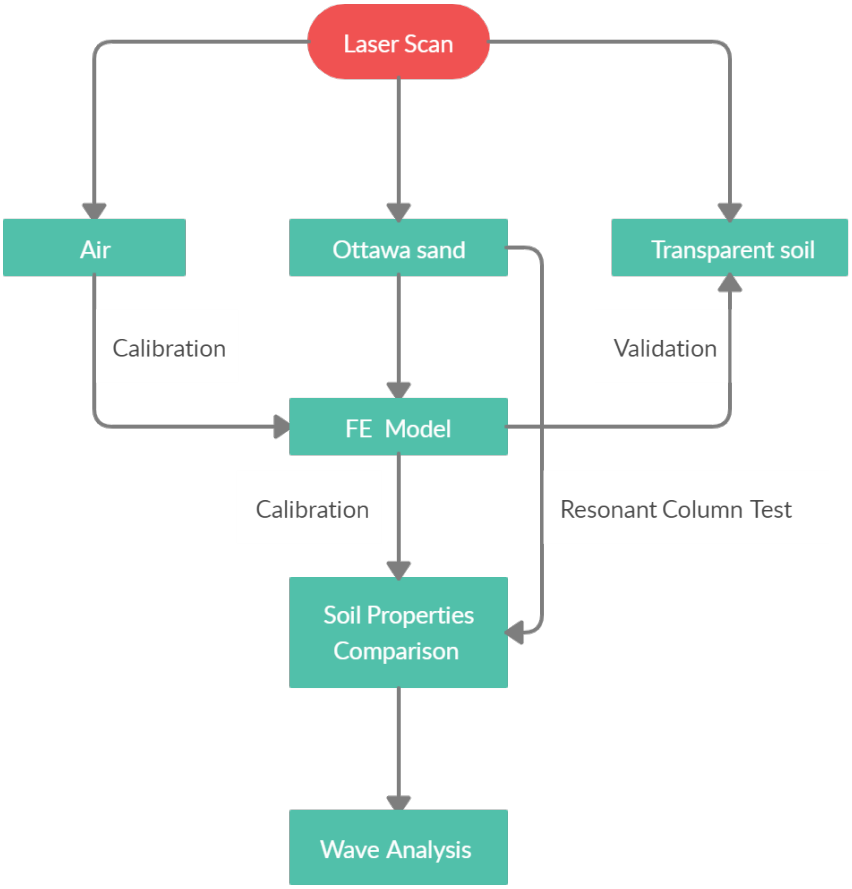

FIGURE 3.1: Flowchart of the detailed procedures for the calibration and verification of the BE motion as well as wave analysis within a soil specimen.

3.2.1 Experimental setup

A general schematic of the experimental setup is illustrated in Figure 3.2. The soil specimen is vibrated at the bottom via a piezoelectric BE. The generated P wave and S wave contribute to the overall displacement at the top surface of the soil specimen. The BE motion is then studied through the laser vibrometer readings as well as a piezoelectric-solid mechanics FE modeling using two main soil sample configurations: a) transparent soil to evaluate the BE response and b) an Ottawa sand specimen to evaluate the surface response induced by the BE.

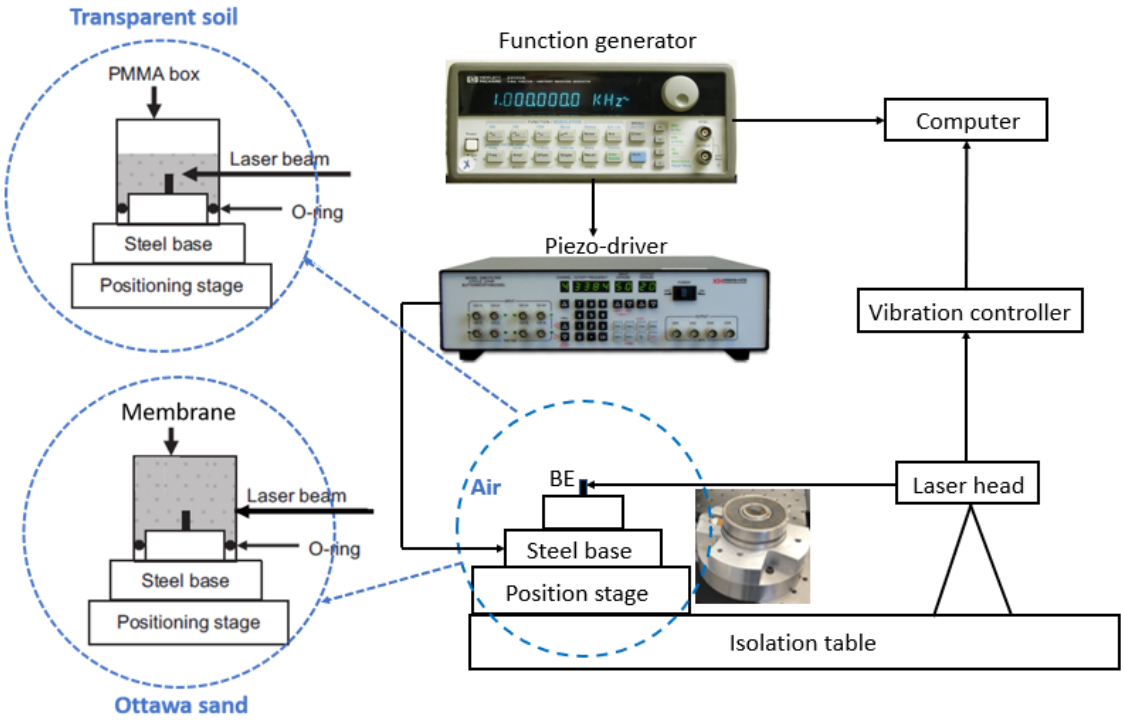

FIGURE 3.2: Configuration of the BE test and the laser vibrometer apparatus

The BE response under a sinusoidal electrical impulse is monitored in the air through a laser vibrometer apparatus. Based on the response of the BE, a coupled piezoelectrical-solid mechanics finite element model is calibrated so that the numerical prediction fits with the laser vibrometer measurements. The calibrated model in the air is then verified against the laser vibrometer readings in a transparent soil. In the end, the calibrated model is used to predict independent vibrations induced by the BE motion within an Ottawa sand specimen under a confining pressure of 100 kPa. The soil parameters determined through trial and error from the FE model are then compared with the values obtained from a conventional RC test.

3.2.2 Experimental tests

In the experimental BE tests shown in Figure 3.2, a function generator (model HP-33120A) generates the desired input voltage signal applied to the BE transmitter through the steel base. The signal is monitored by the oscilloscope (HP-54645A). The BE transforms the electrical energy into the mechanical energy, which then applies an ultrasonic impulse to the soil specimen. The BE transmitter used in this test protrudes 6 mm into the soil specimen and has a 14 mm by 1.0 mm cross section. The laser vibrometer (polytec, 2013) measures the displacement at a single point.

The measurements from the Ottawa sand specimen are used for the further verification of the proposed numerical model. The soil sample is 7.0 cm in diameter and 14 cm in height. The density of the dry sand is 1,848 kg/m^3. The soil specimen is slightly compacted and covered with a latex membrane to hold the sand in place. A 100 kPa vacuum pressure is applied at the bottom of the sand specimen. The vibration introduced by the BE transmitter was captured through the laser vibrometer on the wall of the soil specimen membrane, as shown in Figure 3.3. The measurements along the specimen are taken for every 1 cm. A reflective adhesive tape is applied to the membrane wall to improve the signal intensity. The rubber membrane has a negligible effect on the displacement measurement as it is very thin (0.2 mm thick).

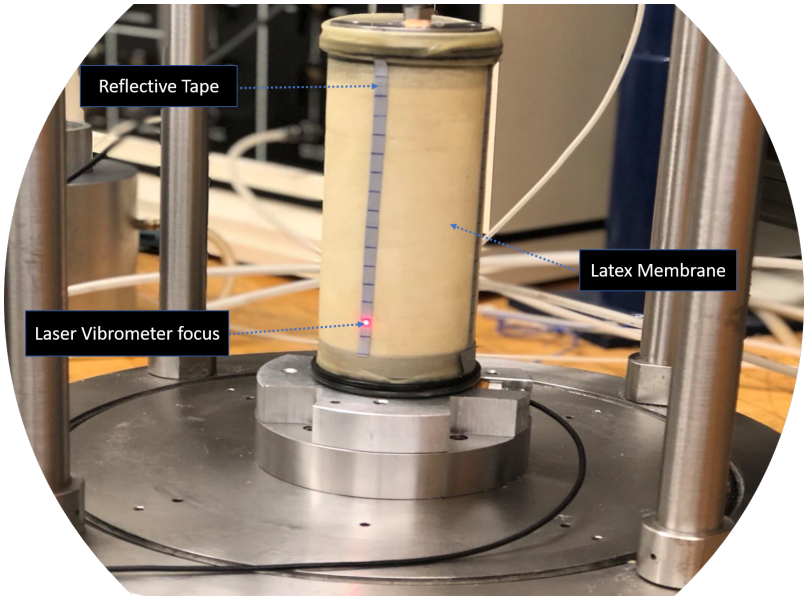

FIGURE 3.3: Vibration measurements through the laser vibrometer for the Ottawa sand specimen

Furthermore, the resonant column test is performed based on the ASTM standard D4015-15e1, 2015 for verification of the BE measurements at 100 kPa. The built-in source in the spectrum analyzer (HP-35670A) is used to apply a sinusoidal sweep input voltage. Due to the limited power in the spectrum analyzer, the power amplifier (Bogen GS-250) is used to amplify the input voltage. Such input current introduces the vibration of the magnets, which in turn induce a torsional excitation in the soil sample. The response of the specimen is recorded in terms of acceleration via the accelerometers (PCB353A78 and PCB 353B65) mounted on the driving plate. The current in the coils and the acceleration are amplified and filtered (200 Hz low pass) using a filter amplifier (KrohnHite 3384) before being processed by the spectrum analyzer for the transfer function calculations. The

spectrum analyzer calculates the transfer function in real time. The resonance frequency and damping ratio of the soil specimen are computed from the transfer function.

3.3 Theoretical background

The motion of the BE in different media considering the converse piezoelectric effect can be numerically simulated using a piezoelectric-solid mechanics theoretical framework. Also, the soil is considered as a solid, isotropic, and homogeneous medium. This framework can be then implemented in a FE numerical tool for further analyses. In this section, we will briefly review the assumptions and field equations. The FE modeling is then discussed.

3.3.1 Kinematic assumptions

The linearized form of the Green-Lagrange strain tensor, ε_{ij}, for infinitesimal deformations of solid media (BE and soil) and electrical field E_i^f are described, respectively, as follows Matin, Akai, Kawazu, Hanebuchi, Sawada, and Ishida, 2010.

$$\begin{aligned} \varepsilon_{ij} &= \frac{1}{2}\left(u_{i,j} + u_{j,i}\right) \\ E_i^f &= -\phi_{,i} \end{aligned} \tag{3.1}$$

where $u_{i,j}$ represents $\frac{\partial u_i}{\partial x_j}$; u_i represents the displacement vector components of the solid medium in each direction and x_j represents the coordinates; E_i^f denotes the electrical field vector; ϕ is the electric potential.

3.3.2 Constitutive models

The constitutive models that describe the stress-strain and electrical displacement-field relationships are defined as:

$$\begin{aligned} \sigma_{ij} &= C_{ijkl}\,\varepsilon_{kl} - e_{kij}E_k \\ D_i &= e_{ikl}\varepsilon_{kl} + \epsilon_{ik}E_k \end{aligned} \tag{3.2}$$

where σ_{ij} is the stress tensor; e_{kij} and ϵ_{ik} denote the piezoelectric tensor and dielectric permittivity tensor, respectively. D_i represents the electrical displacement. C_{ijkl} is the fourth-order linear elastic stiffness tensor described in Equation 3.3 for isotropic materials Liu, Maghoul, Shalaby, Bahari, and Moradi, 2020; Mase and Mase, 2009:

$$C_{ijkl} = \lambda\delta_{ij}\delta_{kl} + \mu\left(\delta_{ik}\delta_{jl} + \delta_{il}\delta_{jk}\right) \tag{3.3}$$

where $C_{11} = C_{33} = \frac{E'(1-\nu)}{(1+\nu)(1-2\nu)}$; $C_{12} = C_{13} = \frac{E'\nu}{(1+\nu)(1-2\nu)}$; $C_{44} = C_{55} = C_{66} = \frac{E'}{2(1+\nu)}$; E' and μ are Young's modulus and Poisson's ratio, respectively. It is worth mentioning that the stress-strain relationship for soils can be written as $\sigma_{ij} = C_{ijkl}\varepsilon_{kl}$. Also, the piezoelectric tensor e_{ijk} (coulomb$/m^2$) is written as Myers, Anjanappa, and Freidhoff, 2010:

$$e = \begin{Bmatrix} 0 & 0 & 0 & 0 & e_{15} & 0 \\ 0 & 0 & 0 & e_{15} & 0 & 0 \\ e_{31} & e_{31} & e_{33} & 0 & 0 & 0 \end{Bmatrix} \tag{3.4}$$

Piezoelectric materials have the ability to produce an electrical voltage with an applied load; vice versa, motions are generated if an electric field is applied. Such phenomena is described through the piezoelectric tensor.

3.3.3 Conservation laws

Conservation of the linear momentum for a solid medium (BE and soil) is written as:

$$\sigma_{ij,j} = \rho\ddot{u}_i \tag{3.5}$$

where ρ is the bulk density.

Gauss's law is used to describe the conversation of charge in the piezoelectric BE:

$$D_{i,i} = 0. \tag{3.6}$$

3.3.4 Field equations

The governing equations for the BE can be written in terms of the displacement vector u_i as well as the electric field vector E_i^f as:

$$\begin{aligned} \mu u_{i,jj} + (\lambda+\mu)u_{j,ji} - e_{kij,j}E_k^f &= \rho\ddot{u}_i \\ e_{ikl,i}\varepsilon_{kl} + \epsilon_{ik,i}E_k^f &= 0. \end{aligned} \tag{3.7}$$

It should be noted the field equation 3.7 is obtained through the conservation of momentum and the conservation of charge, respectively. The coupled field equations are then solved simultaneously due to the coupling tensor e_{ikl}, which represents the inherent properties of the piezoelectric materials.

Similarly, the field equation governing the propagation of stress waves into the soil specimen due to the piezoelectric BE motion can be written as

$$\mu u_{i,jj} + (\lambda + \mu) u_{j,ji} = \rho \ddot{u}_i. \tag{3.8}$$

3.3.5 Finite element modeling and boundary conditions

The 2D FE method is used to solve the field equations described above via COMSOL Multiphysics (Multiphysics, 1998). The triangular element type is used for the analysis. The direct solver is used instead of an iterative solver due to its robust nature (Liu, Maghoul, Bahari, and Kavgic, 2019). There are 5,145 elements with an average quality of 0.8592 (length to width ratio). Based on a extensive mesh sensitivity analysis, it is found that the numerical results are no longer sensitive to the mesh size if a finer mesh is used. With such settings in COMSOL Multiphysics, the relative error can be controlled to an acceptable tolerance. The mesh distribution in the soil specimen and BE is shown in Figure 3.4.

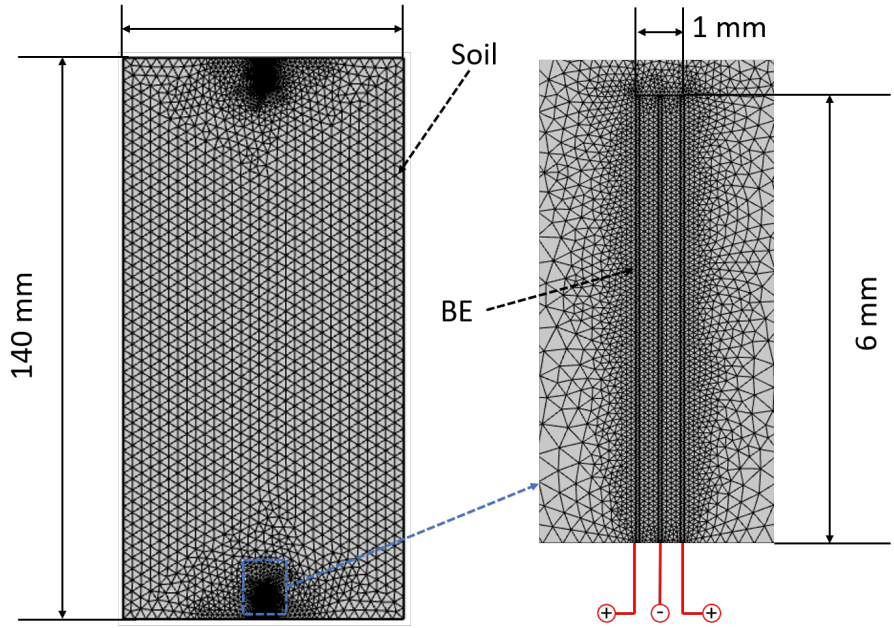

FIGURE 3.4: Mesh distribution for the BE test

The BE having a height of 6 mm, a length of 14 mm, and a width of 1.0 mm is shaped as a cantilever beam and contains two layers of piezoelectric ceramic plates with a metal plate in the middle. If the poling direction of these two layers of piezoelectric elements is in the same direction, it would be called parallel and if the poling direction is in opposite directions, it would be called series type. The parallel type needs a low voltage to work, but the series type needs, for the same application, twice the voltage magnitude to work

(Zhou, Chen, Ding, and Chen, 2008; Mulmi, Sato, and Kuwano, 2008). The parallel BE is used as an transmitter and the series type is used as a receiver (Zhou, Chen, Ding, and Chen, 2008; Mulmi, Sato, and Kuwano, 2008). The Ottawa sand specimen has a width of 70 mm and a height of 140 mm.

A sinusoidal impulse voltage with a frequency of 9 kHz, which is close to the resonant frequency of the BE used in our tests, is applied to the BE (plus sign in Figure 3.4). A fixed boundary condition is applied to the top and bottom of the soil specimen. A fixed boundary condition is also applied to one end of the BE transmitter (lower end) and receiver (upper end). The remaining boundaries are considered as a free surface (zero stress) to allow the reflection of stress waves. The interface between the BE and surrounding soil is modeled by meeting the continuity conditions. The initial displacement and velocity of the BE and surrounding soils are set to be zero. The components of the coupling tensor in Equation 3.4 has the following values: $e_{31} = -5.35\ \mathrm{C/m^2}$; $e_{15} = 15.78\ \mathrm{C/m^2}$ and $e_{33} = 12.29\ \mathrm{C/m^2}$ (Myers, Anjanappa, and Freidhoff, 2010). The density of the piezoelectric ceramic plates used in the BE structure is 7,870 $\mathrm{kg/m^3}$. The mechanical properties of the piezoelectric ceramic plates and the metal plate used in the BE structure, transparent soil and Ottawa sand are obtained through the calibration procedure by trial and error as presented in Section 3.4.1 and Section 3.4.2.

3.4 Results and discussion

3.4.1 BE motion calibration and verification

The laser pointer is concentrated at a point with a height of 5 mm shown in Figure 3.2. The comparison of the BE motion in the air between the experimental measurements and numerical predictions in time and frequency domains is shown in Figures 3.5a and 3.5b, respectively. As can be seen in Figure 3.5, the numerical results using the calibrated piezoelectric-solid mechanics model are in good agreement with the experimental measurements.

The mechanical properties of the BE are calibrated through trial and error to best fit the numerical predictions with the laser measurements. The best matching between the numerical results and the laser measurements was achieved when Young's modulus and Poisson's ratio of the piezoelectric ceramic plates are 65 GPa and 0.3, respectively; Young's modulus of the metal plate used in the BE structure is 243 GPa; and, the damping ratio for the piezoelectric ceramic plates and the metal plate used in the BE structure is 2.5%.

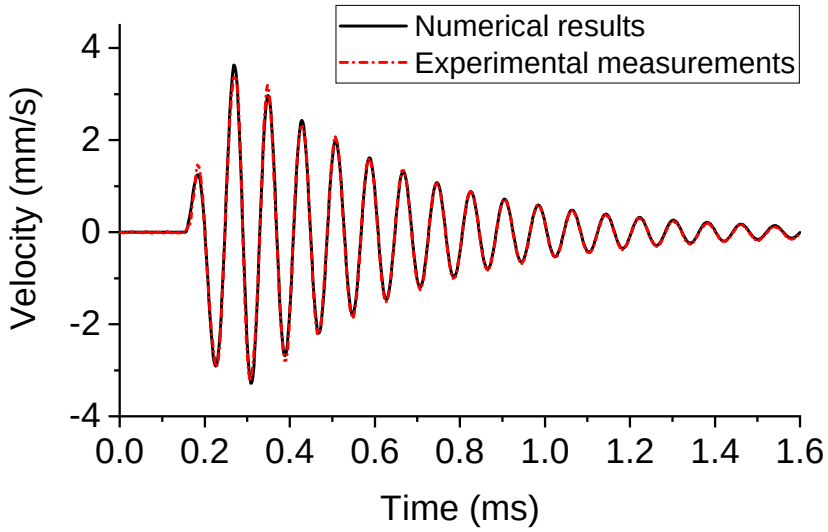

(A) time domain

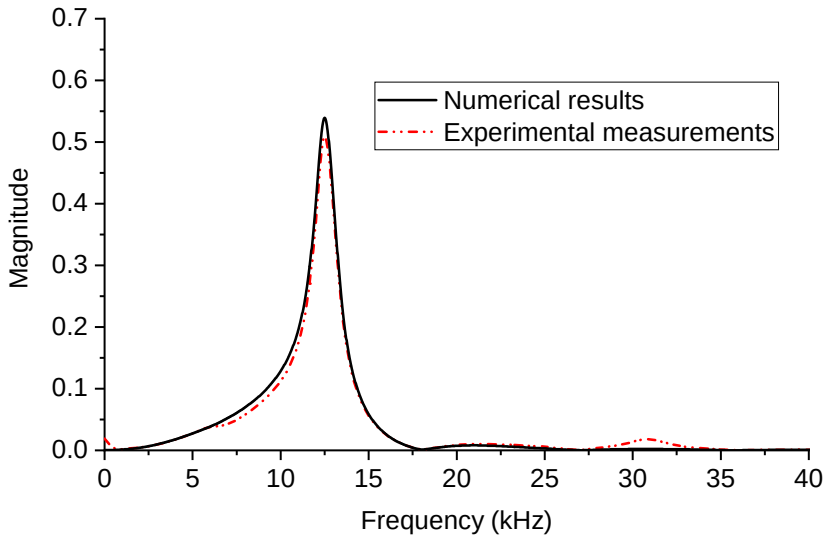

(B) frequency domain

FIGURE 3.5: Comparison between the experimental measurements and numerical results for the BE motion in the air in (a) time domain, (b) frequency domain.

The calibrated FE model is further verified through the experimental BE tests on the transparent soil (made of silica and oil) where the BE motion was monitored via the laser vibrometer. Under the same impulse voltage, the comparison between the numerical FE results and the experimental measurements of the BE motion are shown in Figure 3.6 in time and frequency domains.

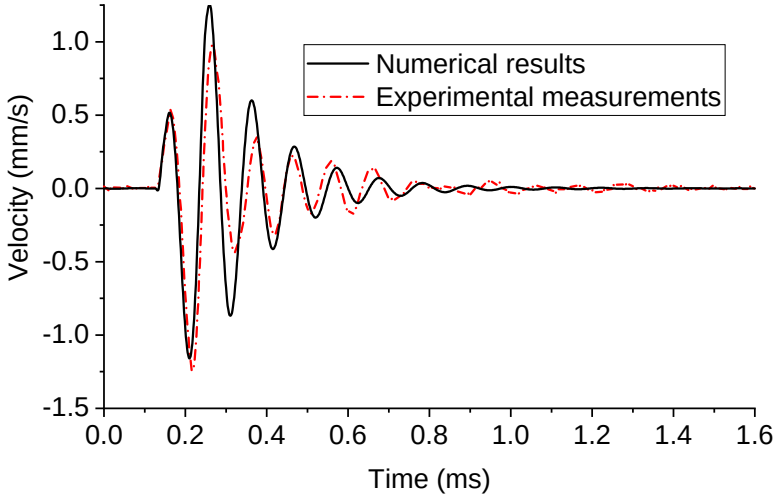

(A) Time domain

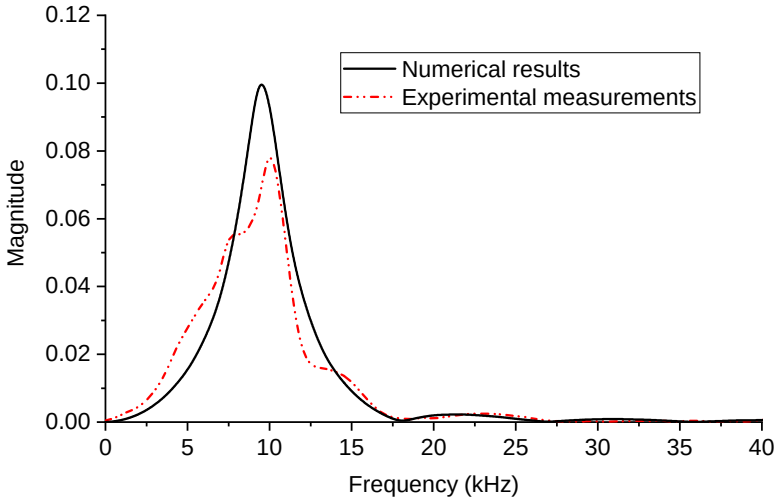

(B) Frequency domain

FIGURE 3.6: Comparison between the experimental measurements and numerical results for the BE motion in the transparent soil in (a) time domain, (b) frequency domain.

The mechanical properties of the transparent soil used in the FE analysis are calibrated by trial and error. It is found that the speeds of the P wave and S wave in the transparent soil studied in this test are approximately 1,200 m/s and 15 m/s, respectively. The equivalent damping ratio of the transparent soil including the visco-elastic effect is assumed as 0.3. This damping value is high because it is representing not only the damping of the soil, but also the effect of the added mass of the transparent soil to the response of the BE (Irfan, Cascante, Basu, and Khan, 2019). The very low shear wave velocity derived numerically is due to the fact that the confining pressure is practically zero in this experiment. The high value of the P-wave velocity is generated because of the saturated conditions. The

calibrated piezoelectric-solid mechanics model for the BE motion is still able to capture the motion of the BE in the transparent soil.

3.4.2 BE motion in Ottawa sand

The BE motion can be directly monitored in the air and transparent soil through the laser vibrometer since the laser light can penetrate into these media. It is not, however, the case for the BE test performed on real soils. Therefore, the displacement at the sides of the soil specimen is monitored instead of the BE itself. The setup for this test can be seen in Figure 3.3. The original laser measurements at the elevations of 2.5 cm (trace 0) to 13.5 cm (trace 12), with an interval of 1 cm, are shown in Figure 3.7. This signal is contaminated with the higher resonant modes of the BE motion (Lee and Santamarina, 2005). Since the applied voltage signal is 9 kHz, the components above 15 kHz are removed through the wavelet synchrosqueezed transform (Daubechies, Lu, and Wu, 2011). The components below 15 kHz are obtained through the inverse wavelet synchrosqueezed transform.

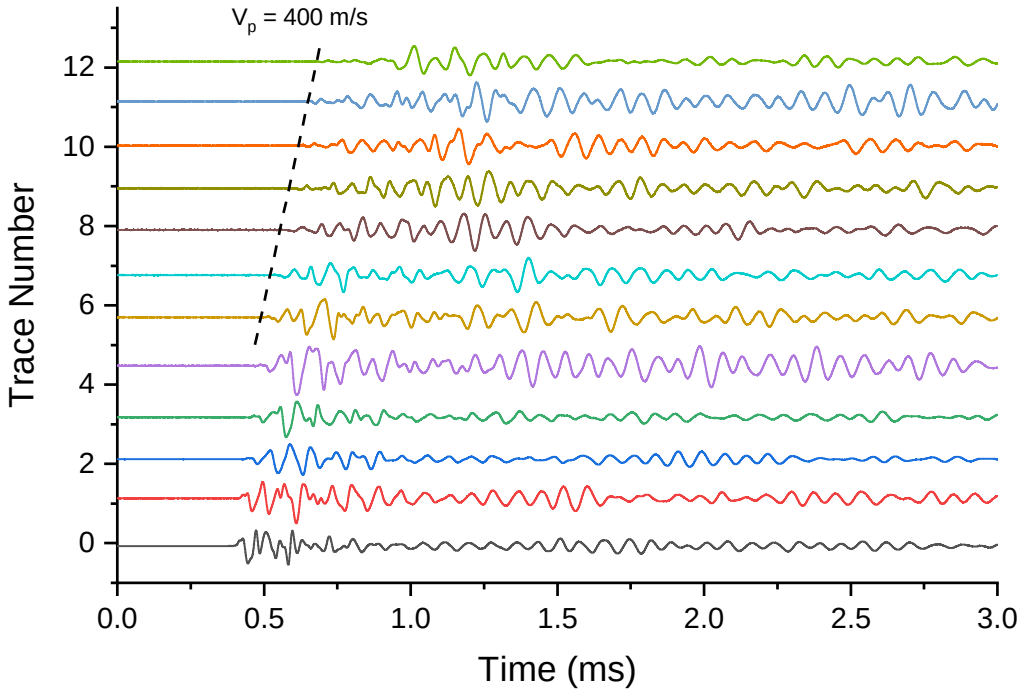

FIGURE 3.7: Original displacement measurement along Ottawa sand specimen using the laser vibrometer

Based on the calibrated piezoelectric-solid mechanics model for the BE, the soil parameters are then modified through trial and error to match the filtered laser vibrometer

measurements. For example, the comparison between numerical and experimental displacements is shown in Figure 3.8. The best fitting was achieved by using the shear wave velocity of 240 m/s, compression wave velocity of 380 m/s (equivalent to a Young's modulus of 249 MPa and a Poisson's ratio of 0.17), and a damping ratio of 1% for the Ottawa sand. The determined P and S wave velocities can also be verified from the original laser measurements. A constant slope (400 m/s slope) is also clearly visualized in the original displacement measurements, as labeled in Figure 3.7. The determined P wave velocity (380 m/s) was relatively close to the P wave velocity (400 m/s) visualized in the original laser measurements. Furthermore, the dispersion curves were also computed using the numerical and measured displacement data. Figure 3.9 shows the comparison between the measured and numerical dispersion curves for both symmetric and antisymmetric modes. The symmetric modes, also called longitudinal modes, are generated due to the wave propagation in the longitudinal direction. On the other hand, the antisymmetric modes are generated because of the wave propagation in the transverse direction (Graff, 1991).

The numerical predictions showed a reasonable agreement with the laser measurements in terms of the distribution of dispersion curves. Therefore, the P wave and S wave velocities for the Ottawa sand are 380 m/s and 240 m/s, which is verified through comparison in displacement measurements and dispersion curves. The RC test was also performed to validate the shear wave velocity and damping ratio of the Ottawa sand under various confining pressures. Under a confining pressure of 100 kPa, the shear wave velocity and damping ratio are found to be 263 m/s and 1.06%, which are consistent with the values used in the numerical model through trial and error.

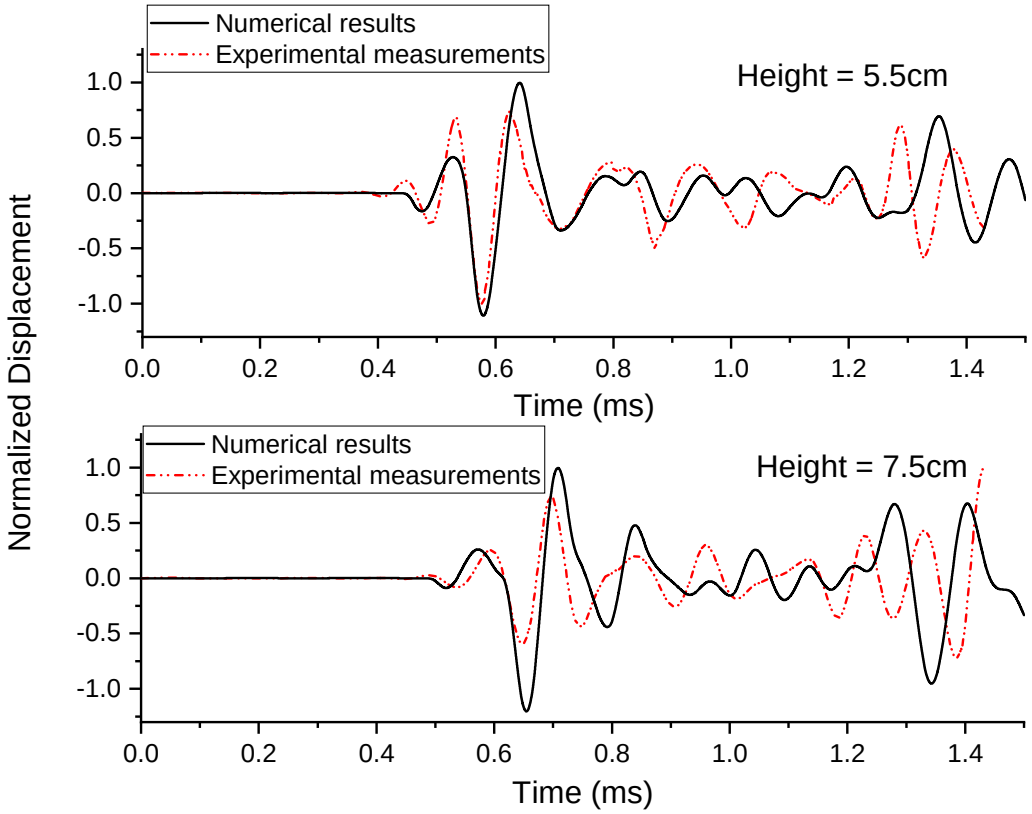

FIGURE 3.8: Comparison between the numerical results and experimental displacement measured at a distance of 5.5 and 7.5 cm from the bottom

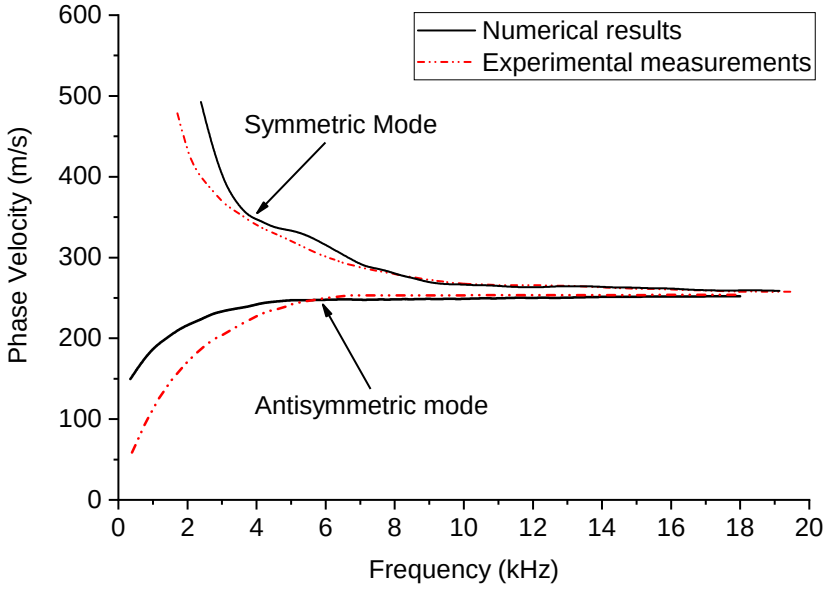

FIGURE 3.9: Comparison between the numerical and experimental dispersion curves

3.4.3 Wave analysis within soil specimen

The wave propagation is further analyzed through the displacement distribution within the Ottawa sand specimen. The transmitter started the generation of mechanical energy around $t = 0.31$ ms. This reference value is shown by *Trigger Point* in Figure 3.10.

The S wave velocity determined by the BE is relatively higher than the value obtained by the standard RC test (Fam, Cascante, and Dusseault, 2002). The S wave velocity in the BE test is commonly calculated as travel distance divided by the S wave arrival time. However, the arrival time of the S wave is normally empirically selected around the first peak in the output signal. Based on the determined S wave velocity from previous discussion, the exact S wave arrival time can be located around 0.53 ms relative to the beginning of impulse (as labeled by Trigger Point in Figure 3.10). The measured response in BE testing is given in terms of voltage (Volts) while the numerical response is given by displacement (nm). These two signals are not expected to be identical as the received signal does not have units of displacement, velocity, or acceleration. The comparison between the measured and numerically calculated signal at the BE receiver location is shown in Figure 3.10. A reasonable agreement between the numerical results and experimental data is achieved. The S wave arrival time is normally selected shortly before the peak in the BE receiver signal. However, it is shown that the S wave arrival time is actually affected by the interaction with the P-wave. Therefore, the proposed numerical model can be used to improve the interpretation of the effects of P-waves on BE tests results.

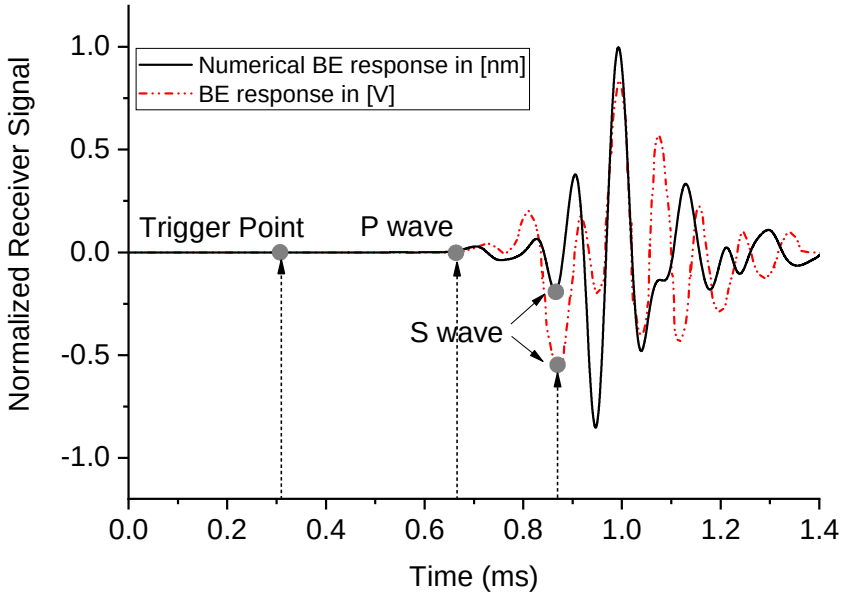

FIGURE 3.10: Comparison between the experimental data and numerical results at the location of the BE receiver (this figure shows a relative comparison; the BE signals are not linearly related to the vibration measurements in terms of displacement, velocity, or acceleration).

The horizontal displacement contours corresponding to the travel times equal to one up to five excitation periods of BE are shown in Figure 3.11. The positive and negative displacements are shown in blue and red colors, respectively. A full wavelength is defined by a positive (red) and negative displacement (blue) wavefronts. For the dominant frequency of 8.7 kHz for the BE vibration in Ottawa sand, the S and P waves' wavelengths can be calculated as $\lambda_s = 2.8$ cm and $\lambda_p = 4.4$ cm, respectively. Two wavelengths are identified due to the different propagation speeds of P and S waves. In the BE test, the generation of the S wave mode (in terms of its amplitude) is much stronger than that of the P wave mode. Only a half wavelength (blue front) was identified for the P wave mode due to its weaker generation in the BE test. Furthermore, P wave attenuates with travelling distance and the identification of its full wavelength becomes impractical. Therefore, only a half wavelength of the P wave mode is labeled in Figure 3.11. After the first period (1T), the reflection of P and S waves can be visualized clearly. The separation between the P wave and S wavefronts increased from the 2^{nd} and 3^{rd} periods. The P wavefront arrives at the BE receiver tip sometime between the 3^{rd} and 4^{th} periods. Similarly, the S wavefront arrives at the BE receiver tip sometime between the 4^{th} and 5^{th} periods.

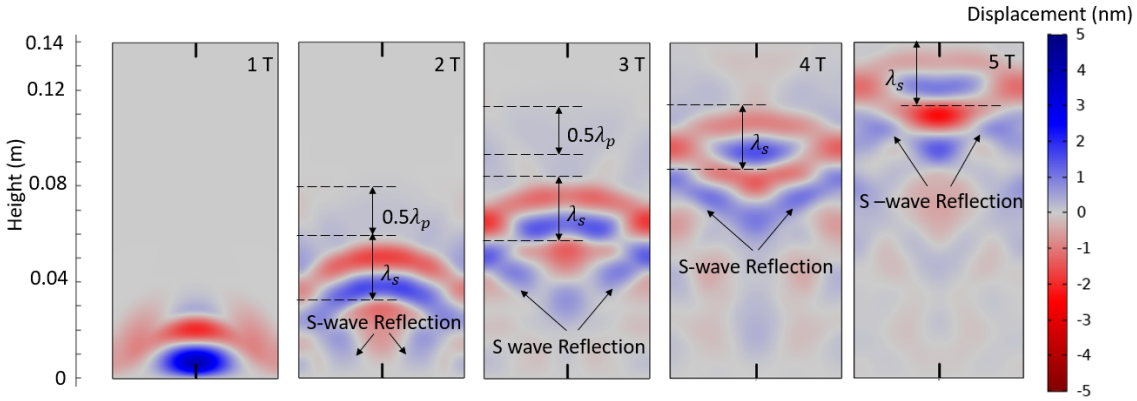

FIGURE 3.11: Horizontal displacement contour in Ottawa sand (video 1 in the Supplementary materials)

Based on previous studies (e.g., (Khan, Moon, and Ku, 2020; Leong, Yeo, and Rahardjo, 2005)), it is recommended that the wave path length to wavelength ratio is at least 3.33. In our BE measurement, as shown in Figure 3.10, the wavelength is 2.8 cm and the length of the sample is 14 cm. Thus, the length to wavelength ratio is 5, which is bigger than the recommended 3.33. However, the interference of the P wave still exists, and these effects of P-wave reflections were not included in previous recommendations.

3.4.4 Numerical study of the effect of different Poisson's ratios (loose sand, soft clay)

The wave propagation is also investigated in two different soil specimens using the piezoelectric-solid mechanics FE model. In Case 1, the P and S wave velocities are 120 m/s and 69.3 m/s (equivalent to a Young's modulus of 22 MPa and a Poisson's ratio of 0.25) to simulate a loose sand specimen. In Case 2, a soft clay soil sample with a P wave velocity of 120 m/s and an S wave velocity of 35.2 m/s (equivalent to a Young's modulus of 6.7 MPa and a Poisson's ratio of 0.45) is studied. The horizontal displacements at the BE receiver location are shown in Figure 3.12 for Case 1 and Case 2. The exact P wave travel time is 1.07 ms relative to the beginning of the impulse as labeled by Trigger Point. In Case 1, the exact S wave travel time is 1.85 ms relative to the beginning of the impulse. Similarly, in Case 2, the S wave travel time is 3.63 ms.

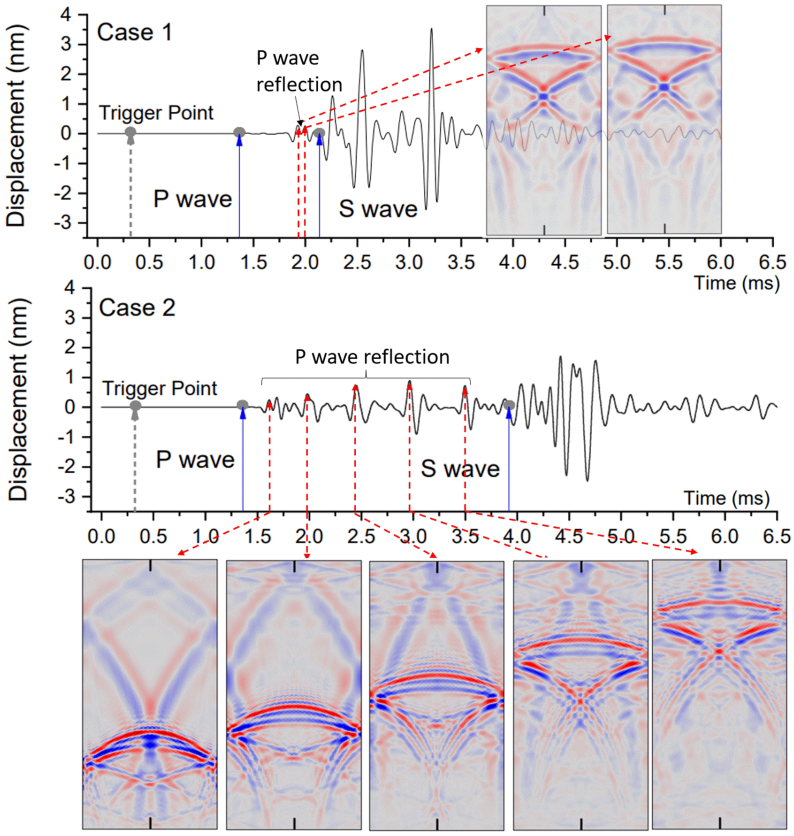

FIGURE 3.12: Horizontal displacement at the receiver location for Case 1 (Poisson's ratio = 0.25, loose sand, video 2 in the Supplementary materials) and Case 2 (Poisson's ratio =0.45, soft clay, video 3 in the Supplementary materials)

The signal obtained in Case 2 is more contaminated by the P wave because of its slower S wave velocity. The components located between the first P wave arrival time (1.37 ms) and first S wave arrival time (3.94 ms) are due to the P wave reflection from the sides of the soil specimen. This can be captured by the horizontal displacement contour at various wave peaks before the S-wave arrival, as illustrated in Figure 3.12. The horizontal displacement contour at various time (normalized in terms of the period) is shown in Figure 3.14. In this case, the selection of the S wave arrival time is rather challenging and unpredictable based on the empirical methods (e.g., start-start method and peak-peak method). However, the real arrival time of the S wave is not closely near to the largest amplitude, as shown in Figure 3.12.

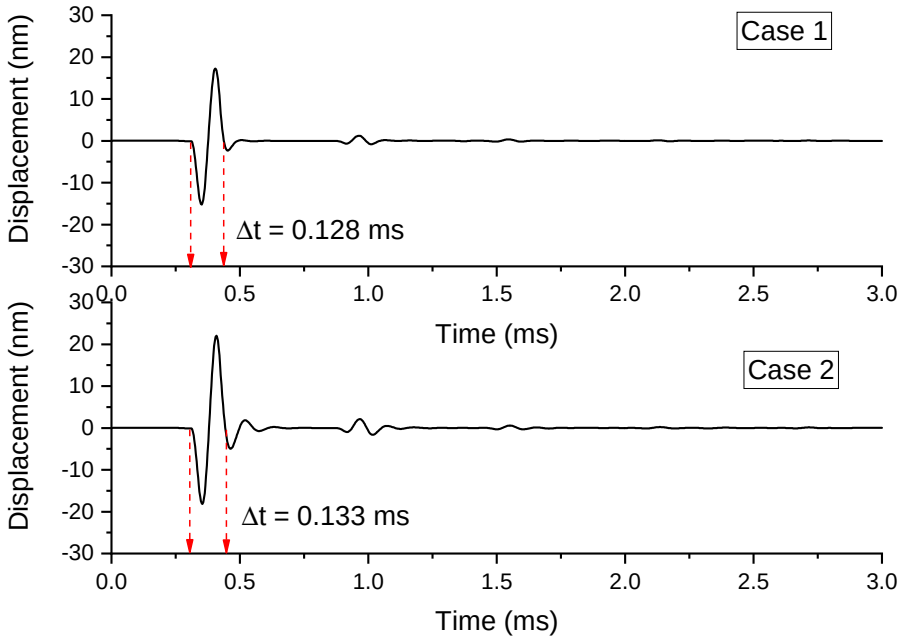

FIGURE 3.13: Horizontal displacement of BE transmitter numerically predicted at a height of 5 mm for Case 1 (Poisson's ratio = 0.25, loose sand) and Case 2 (Poisson's ratio =0.45, soft clay)

The horizontal displacement of the BE transmitter is shown in Figure 3.13 for both Case 1 and Case 2. From Figure 3.13, it is found that the BE transmitter vibrates with the dominant frequency of 7.8 kHz for the BE vibration in Case 1. Corresponding, the S and P waves' wavelengths can be calculated as $\lambda_s = 0.89$ cm and $\lambda_p = 1.5$ cm, respectively. In Case 2, the dominant frequency of the BE motion is 7.5 kHz and the S and P waves' wavelengths can be calculated as $\lambda_s = 0.47$ cm and $\lambda_p = 1.6$ cm, respectively. The displacement contours at different times (normalized in terms of period) are shown in Figure 3.14 and Figure 3.15 for Case 1 and Case 2, respectively. It is confirmed from Figure 3.14 and Figure 3.15 that the reflected P waves from the sides of the specimen can arrive at the BE receiver location faster than the shear wavefront. Therefore, the wave interactions of P and S waves with soil boundaries can largely increase the complexity of the selection of the S wave arrival time. The traditional empirical methods ((e.g., start-start method and peak-peak method)) cannot accommodate the complex nature of wave interaction and may result in misleading predictions of the S wave velocity.

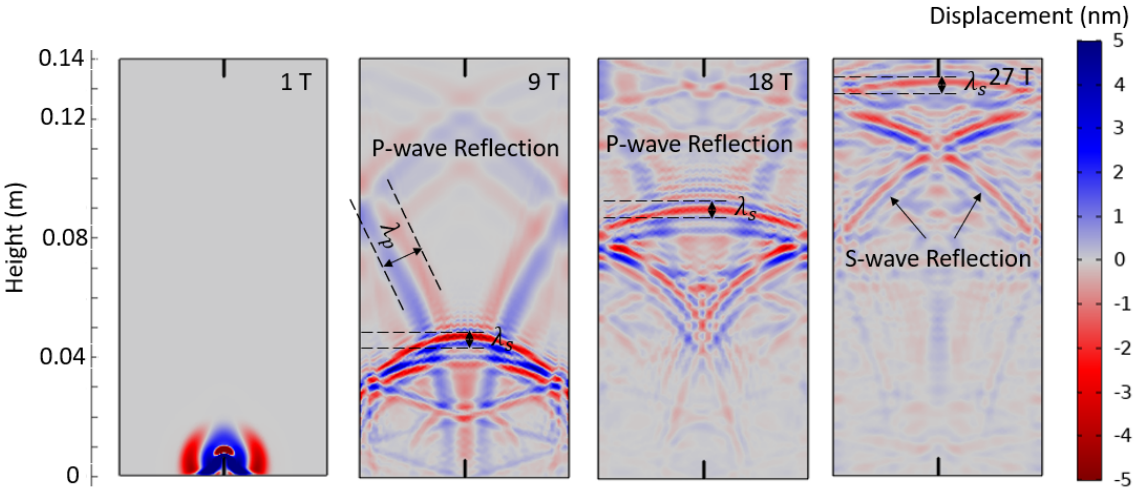

FIGURE 3.14: Horizontal displacement contour in low-stiffness clay for Case 2 (Poisson's ratio =0.45, soft clay, video 3 in the Supplementary materials)

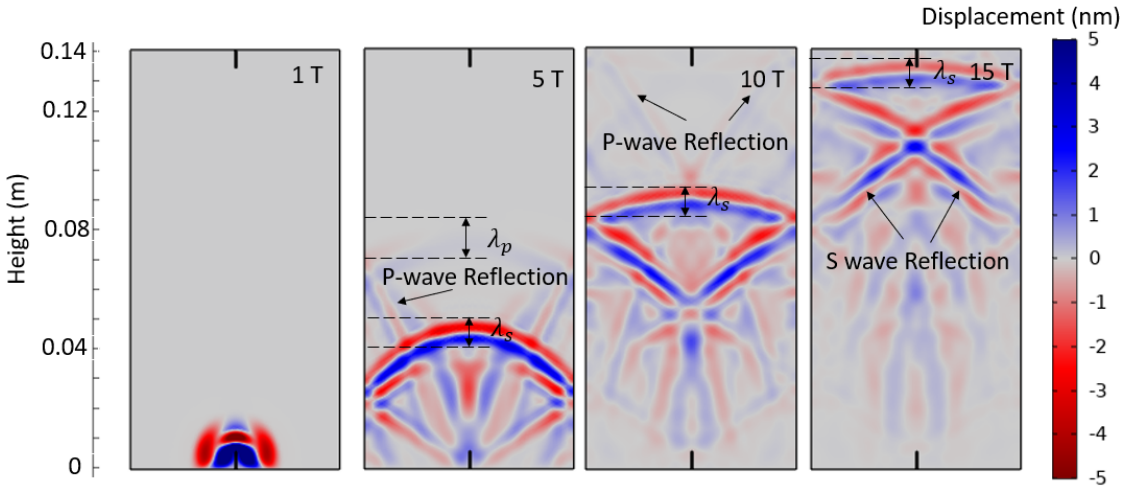

FIGURE 3.15: Horizontal displacement contour in low-stiffness sand for Case 1 (Poisson's ratio = 0.25, loose sand, video 2 in the Supplementary materials)

3.5 Conclusion

In this paper, the response of different media to a BE motion is thoroughly studied via a piezoelectric-solid mechanics FE model as well as experimental tests. The numerical results are compared with the motion of the BE in the air, transparent soil, as well as the Ottawa sand captured by a laser vibrometer. It is concluded that:

- The proposed piezoelectric-mechanical model captures the motion of the BE with sufficient accuracy in the air, transparent soil, as well as the Ottawa sand. The best agreement was achieved for the BE motion in the air.

- The numerical response obtained by the proposed model is consistent with the laser vibrometer measurement at the sides of the Ottawa sand specimen. Furthermore, the numerical predictions show a reasonable agreement with the laser measurements in terms of the distribution of dispersion curves for both symmetric and antisymmetric modes.

- A reasonable agreement between the numerical BE response and experimental BE measurement is achieved at the receiver location. The shear wave velocity and damping ratio obtained through the proposed model are consistent with the ones obtained by the resonant column test.

- The proposed numerical method shows that there is a significant P-wave/S-wave interaction that demonstrates why the empirical methods for the selection of S-waves in BE testing could be incorrect depending on the different parameters that affect the participation of P-waves.

- The proposed piezoelectric-solid mechanics model can be used to study the complex wave interactions, which significantly improves the interpretation of the effects of P-waves on BE test results. The proposed model clearly show that the interpretation of BE measurements in clays could be more challenging because of the strong participation of P-waves on the response of the BE.

Connecting section

Part I, consisting of Chapter 2 and 3, presented elastodynamic and Piezoelectric solvers for the characterization of dry geomaterials. Chapter 2 presented a semi-analytical elastodynamic forward solver was proposed for the analysis of MASW measurements using the spectral element technique. Several numerical case studies were performed to demonstrate the selection of initial guesses as well as the bounds of each optimization parameter. Also, a parametric study was performed to determine the effect of discontinuity in the soil stratigraphy on the dispersion curves. Finally, the integrated approach developed in this study was used to analyze the MASW data collected in a site in south Iceland. It was concluded that the proposed approach determines effectively and efficiently the soil stratigraphy as well as soil properties. Chapter 3 presented a coupled piezoelectric and solid mechanics model to better understand the response of the BEs inside a soil sample. The model was calibrated, verified, and then used to demonstrate the importance of taking into consideration the interaction between compressional and shear waves for the correct interpretation of BE measurements. The model successfully captured the measured vibrations of the BE in air as well as inside transparent soils. More importantly, the numerical simulations provide a new understating of the significant interactions of P-waves and S-waves especially in clay soils.

The next part, Part II, presents a poroelastodynamic solver for the laboratory-scale characterization of saturated soil samples in terms of the physical and mechanical properties based on the distribution of stress waves.

Part II: Poroelastodynamic Solver

Chapter 4

Laboratory-scale characterization of saturated soil samples through ultrasonic techniques

Abstract

The propagation of poroelastic waves in a soil specimen is dependent on the physical and mechanical properties of the soil. In geotechnical practice, such properties are obtained through in-situ geotechnical testings or element soil testings in the laboratory. These methods require advanced equipment and both testing and sample preparation may be expensive and time-consuming. This paper aims to present an algorithm for a laboratory-scale ultrasonic non-destructive testing to determine the physical and mechanical properties of saturated soil samples based on the distribution of stress waves. The ultrasonic setup, in comparison to most conventional soil lab testing equipment, is low-cost and non-invasive such that it reduces the soil disturbance. For this purpose, a poro-elastodynamic forward solver and differential evolution global optimization algorithm were applied to characterize the porosity, density, and other mechanical properties for a soil column. The forward solver was developed based on a semi-analytical solution which does not require intensive computational efforts encountered in standard numerical techniques such as the finite element method. It was concluded that the proposed high-frequency ultrasonic technique characterizes effectively the saturated soil samples based on the output stress wave measured by the receiver. This development makes geotechnical

Liu H., Maghoul P., and Shalaby A., 2020. *Laboratory-scale characterization of saturated soil samples through ultrasonic techniques.* Scientific Reports 10, 3216. https://doi.org/10.1038/s41598-020-59581-4.

investigations time-efficient and cost-effective, and as such more suited to applications in remote areas.

4.1 Introduction

Characterizing foundation soils is the first step in design and construction of civil infrastructure. The measurement of physical and mechanical properties of soils (e.g shear wave velocity, compression wave velocity, density and porosity) requires intensive in-situ or laboratory tests, which can be time consuming and costly. Soil samples, especially from projects in remote areas, are required to be transported to a geotechnical laboratory for various tests. This can cause the disturbance of soil samples, and laboratory tests on disturbed samples may lead to erroneous conclusions.

The laboratory methods for measuring the shear wave velocity of soil samples include the resonant column test, bender element test among others. However, there is no established standard developed for the interpretation of the dynamic test results (Da Fonseca, Ferreira, and Fahey, 2008). The bender element method was developed in the 1980s and its simplicity is widely recognized: one transducer is placed at one end of a soil specimen for the generation of stress waves; one receiver is placed at the other end to record the induced stress waves. Various interpretation methods have been proposed in the past. The shear wave velocity can be calculated from the time difference between the input and output waves by assuming the absence of reflected or refracted waves (Arulnathan, Boulanger, and Riemer, 1998). However, it is well known that the identification of the arrival time of the output wave is subjective (Da Fonseca, Ferreira, and Fahey, 2008). Other signal processing techniques such as the cross-correlation of the input and output stress waves (Viggiani and Atkinson, 1995) and the second arrival of the output wave (Lee and Santamarina, 2005) are based on the peak values of the stress wave for the estimation of the shear wave velocity. Some other methods (e.g. π-point identification (Brocanelli and Rinaldi, 1998) and frequency spectral analysis (Greening, Nash, Benahmed, Ferreira, and Fonseca, 2003)) are used for estimating the relation between the phase angle and shear wave velocity in the frequency domain.

The elastodynamic theory has been also used by several researchers (O'Donovan, O'Sullivan, and Marketos, 2012; Arroyo, Medina, and Muir Wood, 2002; O'Donovan, O'sullivan, Marketos, and Wood, 2015) through the finite difference, finite element, and discrete element methods to interpret the output stress waves. The elastodynamic algorithm assumes that the domain is composed of solid materials. Under a dynamic load, the generated P waves and S waves penetrate into different layers of a soil and the reflected waves received at the receiver can be used to determine the soil strata. However,

the estimation of the shear wave velocity is still based on the simple signal processing techniques. In addition, in elastodynamic algorithms, the effect of porous structure of soil layers and pore water in dynamic responses of geomaterials is neglected. In fact, the wave propagation in porous soil layers can be better represented by using dynamic poroelastic models instead of elastodynamic models, especially in fully saturated soils in which the pore water can significantly attenuate the stress waves, and in high frequency regimes. The dynamic poroelastic models consider the coupling effect between the pore water and solid skeleton, which induces three types of waves (fast P wave, slow P wave, and S wave in the solid skeleton). Under an impact load, those three waves travel at different speeds, which are captured by the receiver placed at the end of the soil specimen in an ultrasonic setup.

The problem of dynamic poroelasticity (Biot, 1956a; Biot, 1956b) has been solved using various analytical and numerical methods. A direct boundary element approach for solving three-dimensional problems of dynamic poroelasticity in the time domain was developed by (Wiebe and Antes, 1991). Such a technique was based on an integral equation formulation in terms of solid displacements and fluid stress. The 2D and 3D fundamental solutions of dynamic poroelasticity was further developed by (Chen, 1994b; Chen, 1994a; Maghoul, Gatmiri, and Duhamel, 2011a; Maghoul, Gatmiri, and Duhamel, 2011b). The solutions were obtained in both time and Laplace transform domain, and can be recovered to elastodynamics and steady-state poroelasticity. In layered saturated media, similar approaches have been reported by (Jianwen and Hongbing, 2004; Rajapakse and Senjuntichai, 1995). Other than the boundary element method, the finite element method has also been applied by (Panneton and Atalla, 1997). The finite difference method is also used to simulate the wave propagation in heterogeneous poroelastic media by (Wenzlau and Müller, 2009).

In a conventional geotechnical apparatus used to determine the dynamic properties of a soil specimen, the focus is mainly on the estimation of shear wave velocity and the interpretation method is mostly based on the time interval difference between the input and output stress waves. To the best of our knowledge, there is currently no laboratory-scale ultrasonic setup which is able to determine a range of physical and mechanical properties of a soil sample. Furthermore, the development of cheaper, faster and portable means of soil characterization may significantly lower the cost of overall soil testing, and make better assessments possible in sensitive locations.

This paper aims to present an ultrasonic-based poroelastodynamic algorithm, which can be used in an ultrasonic setup to determine a range of physical and mechanical

properties of a soil sample such as shear wave velocity, compression wave velocity, density and porosity. Such a setup can also be used for geotechnical investigation on extracted soil samples. In this algorithm, the poro-elastodynamic forward solver for the characterization of soil samples in high frequency regimes is developed using the spectral element method. Such a meshless semi-analytical technique reduces significantly the computational efforts by avoiding unnecessary calculations for the entire domain. Instead, only the response at the receiver location is calculated, which will then be used during the optimization process. A robust global optimization algorithm is then applied to predict the soil properties given the stress signal measured by the receiver.

4.2 Problem statement

A general schematic of the problem is illustrated in Figure 4.1. The domain is composed of a saturated porous medium. The transmitter located at one end of the sample generates the stress waves which travel through the specimen and is received by a receiver at the other end of the sample. The soil properties (Young's modulus, Poisson's ratio, density and porosity) will be captured by the proposed solver using the distribution of transmitted stress waves.

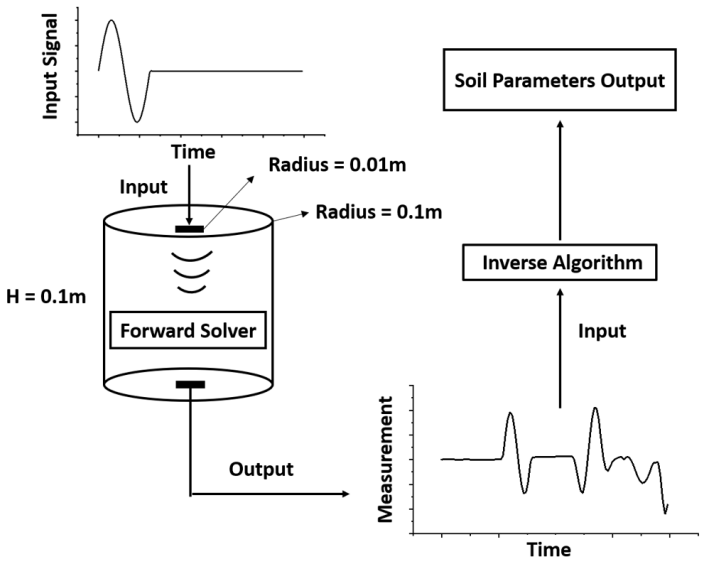

FIGURE 4.1: General schematic of the problem

4.3 Dynamic poroelastic forward solver

By assuming the infinitesimal deformation of solid skeleton, the dynamic poroelastic governing equations are written as follows:

$$\mu u_{i,jj} + (\lambda_c + \mu) u_{j,ji} + \alpha M w_{j,ji} = -\rho b_i + \rho \ddot{u}_i + \rho_f \ddot{w}_i, \tag{4.1a}$$

$$\alpha M u_{j,ji} + M w_{j,ji} = -f + \rho_f \ddot{u}_i + m \ddot{w}_i + b \dot{w}_i, \tag{4.1b}$$

where u is the displacement vector of the solid skeleton; w is the fluid displacement relative to the solid skeleton; λ and μ are the Lamé constants; α is the Biot coefficient; p is the pore-water pressure; M is $1/(\frac{\phi}{K_f} + \frac{\alpha - \phi}{K_s})$ in which K_f is the bulk modulus of the fluid; K_s is the bulk modulus of the solid skeleton and ϕ is the porosity. $\lambda_c = \lambda + \alpha^2 M$; $m = \rho_f \beta / \phi$ in which β is the tortuosity which is used to describe the diffusion properties in porous media, and ρ_f is the density of pore-water, taken as 1000 kg/m^3. The drag-force damping coefficient b is calculated as (Zhang, Xu, and Xia, 2011):

$$b = \eta / \kappa \, F, \tag{4.2}$$

where η is the fluid dynamic viscosity and κ is the permeability coefficient; F is the viscous correction factor (Johnson, Koplik, and Dashen, 1987):

$$F(\omega) = \sqrt{1 + \frac{i}{2} M_s \frac{\omega}{\omega_c}}, \quad \omega_c = \frac{\eta \phi}{2\pi \beta \rho_f \kappa}, \tag{4.3}$$

in which M_s is taken as 1; $i = \sqrt{-1}$ and ω is the angular frequency.

The governing equations can be written in frequency domain through the Fourier transform by performing convolution with $e^{-i\omega t}$ in which $i = \sqrt{-1}$; ω is the frequency and t denotes time variable. The governing equations in Laplace domain can be obtained by replacing ω with $-i\,s$ where s is the Laplace variable.

To obtain the analytical solution, the Helmholtz decomposition is used to decouple the P and S waves. The displacement vector is usually expressed in terms of a scalar potential (ϕ) and a vector potential ($\vec{\psi} = [\psi_r, \psi_\theta, \psi_z]$), as shown in Equation (4.4). In axisymmetric conditions, only the components in r and z directions are considered. Since P wave exists

in solid skeleton and fluid, two P wave potentials are used, ϕ_s and ϕ_f, respectively.

$$\vec{u}(r,z) = \nabla\phi_s(r,z) + \nabla \times \vec{\psi}_s(r,z) \quad and \quad \nabla \cdot \vec{\psi}_s(r,z) = 0, \tag{4.4a}$$

$$\vec{w}(r,z) = \nabla\phi_f(r,z) + \nabla \times \vec{\psi}_f(r,z) \quad and \quad \nabla \cdot \vec{\psi}_f(r,z) = 0. \tag{4.4b}$$

The governing equations in frequency domain in terms of potentials are finally obtained as shown in Equation (4.5):

$$(\lambda_c + 2\mu)\nabla^2\hat{\phi}_s(r,z) + \alpha M\nabla^2\hat{\phi}_f(r,z) = -\rho\omega^2\hat{\phi}_s(r,z) - \rho_f\omega^2\hat{\phi}_f(r,z), \tag{4.5a}$$

$$-\mu\nabla^2\hat{\vec{\psi}}_s(r,z) = \rho\omega^2\hat{\vec{\psi}}_s(r,z) + \rho_f\omega^2\hat{\vec{\psi}}_f(r,z), \tag{4.5b}$$

$$\alpha M\nabla^2\hat{\phi}_f(r,z) + M\nabla^2\hat{\phi}_f(r,z) = -\omega^2(\rho_f\hat{\phi}_f(r,z) + \rho_m\hat{\phi}_f(r,z)), \tag{4.5c}$$

$$0 = \rho_f\omega^2\hat{\vec{\psi}}_s(r,z) + \rho_m\omega^2\hat{\vec{\psi}}_f(r,z), \tag{4.5d}$$

where $\rho_m = m - ib/\omega$; $\hat{}$ represents the terms in frequency domain.

4.3.1 Solution of dilation wave (P waves) using Eigen decomposition

The equations in terms of P wave potentials (Equation (4.5a) and (4.5b)) in a matrix form is shown as:

$$\underbrace{\begin{bmatrix} \lambda_c + 2\mu & \alpha M \\ \alpha M & M \end{bmatrix}}_{K_P} \begin{Bmatrix} \nabla^2\hat{\phi}_s(r,z) \\ \nabla^2\hat{\phi}_f(r,z) \end{Bmatrix} = -\omega^2 \underbrace{\begin{bmatrix} \rho & \rho_f \\ \rho_f & \rho_m \end{bmatrix}}_{\mathrm{M}} \begin{Bmatrix} \hat{\phi}_s(r,z) \\ \hat{\phi}_f(r,z) \end{Bmatrix}. \tag{4.6}$$

It can be seen from Equation (4.6) that $\hat{\phi}_s$ and $\hat{\phi}_f$ are coupled in the governing equations. The diagonalization of such a matrix is required to decouple the system. The Equation (4.6)

is then rearranged into:

$$\begin{Bmatrix} \nabla^2\hat{\phi}_s(r,z) \\ \nabla^2\hat{\phi}_f(r,z) \end{Bmatrix} = \underbrace{\begin{bmatrix} k_{11} & k_{12} \\ k_{21} & k_{22} \end{bmatrix}}_{\mathrm{K}} \begin{Bmatrix} \hat{\phi}_s(r,z) \\ \hat{\phi}_f(r,z) \end{Bmatrix}, \tag{4.7}$$

where

$$k_{11} = \frac{\omega^2\left(\rho - \alpha\rho_f\right)}{M\alpha^2 - 2\mu - \lambda_c}, \quad k_{12} = \frac{\omega^2\left(\rho_f - \alpha\rho_m\right)}{M\alpha^2 - 2\mu - \lambda_c},$$

$$k_{21} = \frac{\omega^2\left(\left(2\mu + \lambda_c\right)\rho_f - M\alpha\rho\right)}{M\left(M\alpha^2 - 2\mu - \lambda_c\right)}, \quad k_{22} = \frac{\omega^2\left(\left(2\mu + \lambda_c\right)\rho_m - M\alpha\rho_f\right)}{M\left(M\alpha^2 - 2\mu - \lambda_c\right)}.$$

The K matrix can be rewritten using the Eigen decomposition method:

$$K = P\,D\,P^{-1}, \tag{4.9}$$

where P is the eigenvector matrix and D is the eigenvalue matrix of the K matrix:

$$P = \frac{1}{k_{21}} \begin{Bmatrix} -\frac{\sqrt{(k_{11}-k_{22})^2+4k_{12}k_{21}}-k_{11}+k_{22}}{2} & \frac{\sqrt{(k_{11}-k_{22})^2+4k_{12}k_{21}}+k_{11}-k_{22}}{2} \\ k_{21} & k_{21} \end{Bmatrix},$$

$$D = \begin{Bmatrix} \frac{1}{2}\left(-\sqrt{\left(k_{11}-k_{22}\right)^2+4k_{12}k_{21}}+k_{11}+k_{22}\right) & 0 \\ 0 & \frac{1}{2}\left(\sqrt{\left(k_{11}-k_{22}\right)^2+4k_{12}k_{21}}+k_{11}+k_{22}\right) \end{Bmatrix}.$$

It should be noted that Equation (4.9) is still valid after neglecting the term $\frac{1}{k_{21}}$ in the eigenvector matrix P due to the existence of the term P^{-1}. Introducing Equation (4.9) into Equation (4.7) and by multiplying P^{-1} and P in the left and right sides, respectively, we can obtain:

$$P^{-1}\,\nabla^2\hat{\vec{\phi}}(r,z)\,P = D\,P^{-1}\,\hat{\vec{\phi}}(r,z)\,P. \tag{4.10}$$

By setting $\hat{\vec{\phi}}(r,z) = P\,\vec{y}(r,z)$ in which $\vec{y}(r,z) = [\hat{\phi}_{p1}(r,z), \hat{\phi}_{p2}(r,z)]$, the system is finally decoupled as:

$$\nabla^2\vec{y}(r,z) = D\vec{y}(r,z). \tag{4.11}$$

Under axisymmetric conditions, Equation (4.11) for $\vec{y}(r,z) = [\hat{\phi}_{p1}(r,z), \hat{\phi}_{p2}(r,z)]$ in cylindrical coordinates is written as:

$$\left(\frac{\partial^2\hat{\phi}_{p1}(r,z)}{\partial r^2} + \frac{1}{r}\frac{\partial\hat{\phi}_{p1}(r,z)}{\partial r} + \frac{\partial^2\hat{\phi}_{p1}(r,z)}{\partial z^2}\right) - D_{11}\hat{\phi}_{p1}(r,z) = 0, \tag{4.12a}$$

$$\left(\frac{\partial^2\hat{\phi}_{p2}(r,z)}{\partial r^2} + \frac{1}{r}\frac{\partial\hat{\phi}_{p2}(r,z)}{\partial r} + \frac{\partial^2\hat{\phi}_{p2}(r,z)}{\partial z^2}\right) - D_{22}\hat{\phi}_{p2}(r,z) = 0. \tag{4.12b}$$

Since the variables $\hat{\phi}_{p1}(r,z)$ and $\hat{\phi}_{p2}(r,z)$ are a function of r and z in the cylindrical coordinates, the separation of variable $\hat{\phi}_{p1} = \hat{R}(r)\,\hat{Z}(z)$ can be used. By setting the both sides equal to $-k^2$ where k is the wavenumber in the radial direction, we can obtain the following equations:

$$\frac{d^2\hat{R}(r)}{dr^2} + \frac{1}{r}\frac{d\hat{R}(r)}{dr} + k^2\hat{R}(r) = 0, \tag{4.13a}$$

$$\frac{d^2\hat{Z}(z)}{dz^2} - (k^2 + D_{11})\,\hat{Z}(z) = 0. \tag{4.13b}$$

The solutions to Equation (4.13) are:

$$\hat{R}(r) = C_1\,J_0(kr), \tag{4.14a}$$

$$\hat{R}(z) = C_2\,e^{-\sqrt{k^2+D_{11}}\,z}, \tag{4.14b}$$

in which J_0 is the Bessel function of the first kind; C_1 and C_2 are the coefficients to be determined from the boundary conditions. Similarly, the solution for $\hat{\phi}_{p1}$ can be obtained. The solution for $\vec{y} = [\hat{\phi}_{p1}, \hat{\phi}_{p2}]$ is summarized as:

$$\hat{\phi}_{p1}(r,z) = Ae^{-\sqrt{k^2+D_{11}}\,z}J_0(kr), \tag{4.15a}$$

$$\hat{\phi}_{p2}(r,z) = Be^{-\sqrt{k^2+D_{22}}\,z}J_0(kr), \tag{4.15b}$$

where A and B are the coefficients to be determined from the boundary conditions. For simplicity, the term $\sqrt{k^2+D_{11}}$ and $\sqrt{k^2+D_{22}}$ is denoted as k_{p1} and k_{p2}, respectively.

Since $\hat{\vec{\phi}} = P\vec{y}$, the solution for $\hat{\phi}_s$ and $\hat{\phi}_f$ can be finally obtained as:

$$\hat{\phi}_s(r,z) = p_{11}Ae^{-\sqrt{k^2+D_{11}}\,z}J_0(kr) + p_{12}Be^{-\sqrt{k^2+D_{22}}\,z}J_0(kr), \tag{4.16a}$$

$$\hat{\phi}_f(r,z) = p_{21}Ae^{-\sqrt{k^2+D_{11}}\,z}J_0(kr) + p_{22}Be^{-\sqrt{k^2+D_{22}}\,z}J_0(kr). \tag{4.16b}$$

4.3.2 Solution of rotational wave (S wave)

The rotational wave is governed by Equations (4.5c) and (4.5d). By replacing $\hat{\vec{\psi}}_f$ by $\hat{\vec{\psi}}_s$, we obtain:

$$\nabla^2\hat{\vec{\psi}}_s(r,z) - \frac{\left(\frac{\rho_f^2}{\rho_m}-\rho\right)\omega^2}{\mu}\hat{\vec{\psi}}_s(r,z) = 0. \tag{4.17}$$

Under axisymmetric conditions, the solution for Equation (4.17) in the cylindrical coordinates is obtained as:

$$\hat{\psi}_s(r,z) = Ce^{-\sqrt{k^2+\frac{\left(\frac{\rho_f^2}{\rho_m}-\rho\right)\omega^2}{\mu}}\,z}J_1(k\,r), \tag{4.18}$$

where C is the coefficient to be determined from the boundary conditions and J_1 is the Bessel function of the first kind of order one. For simplicity, the term $\sqrt{k^2+\frac{\left(\frac{\rho_f^2}{\rho_m}-\rho\right)\omega^2}{\mu}}$ is denoted as k_s.

4.3.3 Displacement, stress and pore-water pressure in terms of potentials

In the cylindrical coordinates (r,θ,z), considering the axisymmetric conditions ($\frac{\partial}{\partial\theta}=0$), the vector potential $\hat{\vec{\psi}}$ has only the component in the θ direction that does not vanish. For simplicity, the vector potential $\hat{\vec{\psi}}$ in the θ direction is denoted as $\hat{\phi}_s$ and $\hat{\phi}_f$ for solid skeleton and porewater, respectively. This property reduces the displacement to the following forms:

$$\hat{u}_r(r,z) = \frac{\partial\hat{\phi}_s(r,z)}{\partial r} - \frac{\partial\hat{\psi}_s(r,z)}{\partial z}, \quad \hat{u}_z(r,z) = \frac{\partial\hat{\phi}_s(r,z)}{\partial z} + \frac{1}{r}\frac{\partial(r\hat{\psi}_s(r,z))}{\partial r}, \tag{4.19a}$$

$$\hat{w}_r(r,z) = \frac{\partial \hat{\phi}_f(r,z)}{\partial r} - \frac{\partial \hat{\psi}_f(r,z)}{\partial z}, \quad \hat{w}_z(r,z) = \frac{\partial \hat{\phi}_f(r,z)}{\partial z} + \frac{1}{r}\frac{\partial (r\hat{\psi}_f(r,z))}{\partial r}. \tag{4.19b}$$

The effective stress and pore-water pressure are written as:

$$\hat{\sigma}'_{zr}(r,z) = \mu\left(\frac{\partial \hat{u}_r(r,z)}{\partial z} + \frac{\partial \hat{u}_z(r,z)}{\partial r}\right), \tag{4.20a}$$

$$\hat{\sigma}'_{zz}(r,z) = \lambda\left(\frac{\partial \hat{u}_r(r,z)}{\partial r} + \frac{\hat{u}_r(r,z)}{r} + \frac{\partial \hat{u}_z(r,z)}{\partial z}\right) + 2\mu\frac{\partial \hat{u}_z(r,z)}{\partial z}, \tag{4.20b}$$

$$\hat{p}(r,z) = -\alpha M\left(\frac{\partial^2 \hat{\phi}_s(r,z)}{\partial r^2} + \frac{1}{r}\frac{\partial \hat{\phi}_s(r,z)}{\partial r} + \frac{\partial^2 \hat{\phi}_s(r,z)}{\partial z^2}\right) \tag{4.20c}$$

$$- M\left(\frac{\partial^2 \hat{\phi}_f(r,z)}{\partial r^2} + \frac{1}{r}\frac{\partial \hat{\phi}_f(r,z)}{\partial r} + \frac{\partial^2 \hat{\phi}_f(r,z)}{\partial z^2}\right). \tag{4.20d}$$

4.3.4 Spectral element formulation for dynamic poroelasticity

In u-w formulation (displacement of solid and relative displacement of porewater), the displacement components w_r and w_z are linearly dependent. In this paper, only w_z is used in the stiffness matrix. For two-node elements where a layer has a finite thickness, the matrix for the displacement components are written as follows:

$$\begin{bmatrix} \hat{u}_{r1}(r,z) \\ \hat{u}_{z1}(r,z) \\ \hat{w}_{z1}(r,z) \\ \hat{u}_{r2}(r,z) \\ \hat{u}_{z2}(r,z) \\ \hat{w}_{z2}(r,z) \end{bmatrix} = \underbrace{\begin{bmatrix} -kp_{11} & -kp_{12} & k_s & -e^{-hk_{p1}}kp_{11} & -e^{-hk_{p2}}kp_{12} & -e^{-hk_s}k_s \\ -k_{p1}p_{11} & -k_{p2}p_{12} & k & e^{-hk_{p1}}k_{p1}p_{11} & e^{-hk_{p2}}k_{p2}p_{12} & e^{-hk_s}k \\ -k_{p1}p_{21} & -k_{p2}p_{22} & -\frac{\rho_f}{\rho_m}k & e^{-hk_{p1}}k_{p1}p_{21} & e^{-hk_{p2}}k_{p2}p_{22} & -\frac{\rho_f}{\rho_m}e^{-hk_s}k \\ -e^{-hk_{p1}}kp_{11} & -e^{-hk_{p2}}kp_{12} & e^{-hk_s}k_s & -kp_{11} & -kp_{12} & -k_s \\ -e^{-hk_{p1}}k_{p1}p_{11} & -e^{-hk_{p2}}k_{p2}p_{12} & e^{-hk_s}k & k_{p1}p_{11} & k_{p2}p_{12} & k \\ -e^{-hk_{p1}}k_{p1}p_{21} & -e^{-hk_{p2}}k_{p2}p_{22} & -\frac{\rho_f}{\rho_m}e^{-hk_s}k & k_{p1}p_{21} & k_{p2}p_{22} & -\frac{\rho_f}{\rho_m}k \end{bmatrix}}_{S'_1} \begin{bmatrix} A_1 \\ B_1 \\ C_1 \\ A_2 \\ B_2 \\ C_2 \end{bmatrix} \tag{4.21}$$

Similarly, the matrix for effective stress components and porewater pressure in frequency domain is shown in Equation 4.22 in which the components for matrix S'_2 can be

found in Appendix A.

$$\begin{bmatrix} \hat{\sigma}'_{zr1}(r,z) \\ \hat{\sigma}'_{zz1}(r,z) \\ \hat{p}_1(r,z) \\ \hat{\sigma}'_{zr2}(r,z) \\ \hat{\sigma}'_{zz2}(r,z) \\ \hat{p}_2(r,z) \end{bmatrix} = \underbrace{\begin{bmatrix} m_{11} & m_{12} & m_{13} & m_{14} & m_{15} & m_{16} \\ m_{21} & m_{22} & m_{23} & m_{24} & m_{25} & m_{26} \\ m_{31} & m_{32} & m_{33} & m_{34} & m_{35} & m_{36} \\ m_{41} & m_{42} & m_{43} & m_{44} & m_{45} & m_{46} \\ m_{51} & m_{52} & m_{53} & m_{54} & m_{55} & m_{56} \\ m_{61} & m_{62} & m_{63} & m_{64} & m_{65} & m_{66} \end{bmatrix}}_{S'_2} \begin{bmatrix} A_1 \\ B_1 \\ C_1 \\ A_2 \\ B_2 \\ C_2 \end{bmatrix}. \tag{4.22}$$

According to the Cauchy stress principle, the traction force ($[\bar{T}_{rz1},\ \bar{T}_{z1},\ \bar{T}_1\ \bar{T}_{rz2}.\ \bar{T}_{z2},\ \bar{T}_2]^T$) is taken as the dot product between the stress tensor and the unit vector along the outward normal direction. Due to the convention that the upward direction is negative, the upper boundary becomes ($[-\hat{\sigma}_{rz1},\ -\hat{\sigma}_{zz1}, -\hat{p}_1]^T$). Similarly, to make the sign consistent, the N matrix is applied to matrix $S'_2 \cdot S'^{-1}_1$. In the future, the matrix $N \cdot S'_2 \cdot S'^{-1}_1$ will be denoted as the G_i matrix, in which i denotes the layer number.

$$\begin{Bmatrix} \bar{T}_{rz1} \\ \bar{T}_{z1} \\ \bar{T}_1 \\ \bar{T}_{rz2} \\ \bar{T}_{z2} \\ \bar{T}_2 \end{Bmatrix}_i = \begin{Bmatrix} -\hat{\sigma}_{rz1}(r,z) \\ -\hat{\sigma}_{zz1}(r,z) \\ -\hat{p}_1(r,z) \\ \hat{\sigma}_{rz2}(r,z) \\ \hat{\sigma}_{zz2}(r,z) \\ \hat{p}_2(r,z) \end{Bmatrix}_i = \underbrace{N \cdot S'_2 \cdot S'^{-1}_1}_{G_i} \cdot \begin{Bmatrix} \hat{u}_{r1}(r,z) \\ \hat{u}_{z1}(r,z) \\ \hat{w}_{z1}(r,z) \\ \hat{u}_{r2}(r,z) \\ \hat{u}_{z2}(r,z) \\ \hat{w}_{z2}(r,z) \end{Bmatrix}_i, \tag{4.23}$$

where

$$N = \begin{bmatrix} -1 & 0 & 0 & 0 & 0 & 0 \\ 0 & -1 & 0 & 0 & 0 & 0 \\ 0 & 0 & -1 & 0 & 0 & 0 \\ 0 & 0 & 0 & 1 & 0 & 0 \\ 0 & 0 & 0 & 0 & 1 & 0 \\ 0 & 0 & 0 & 0 & 0 & 1 \end{bmatrix}. \tag{4.24}$$

After obtaining the stiffness matrix for each element, the global stiffness matrix can be obtained by applying the continuity conditions between the layer interfaces. The stiffness assembling method is shown in Figure 4.2. The global stiffness is denoted as H matrix for

simplicity. An example of the global stiffness matrix for a two layer system is provided in Appendix B.

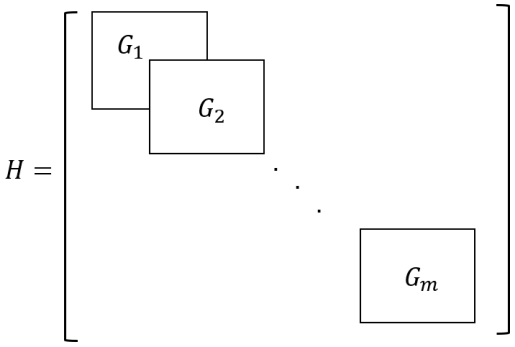

FIGURE 4.2: Global stiffness matrix construction

4.3.5 Soil response under dynamic load (boundary conditions)

In the ultrasonic tests, a vertical impulse load $f(t,r)$ is applied to one end of the soil specimen. The surface is assumed to be permeable, which implies the porewater pressure at the surface is zero. Under such conditions, the displacements in the frequency domain can be written as:

$$\begin{Bmatrix} 0 \\ \hat{f}(s,r) \\ 0 \\ . \\ . \\ . \\ 0 \end{Bmatrix} = \begin{Bmatrix} \\ \\ H \\ \\ \\ \\ \end{Bmatrix} \begin{Bmatrix} \hat{u}_{r1} \\ \hat{u}_{z1} \\ \hat{w}_{z1} \\ . \\ . \\ . \\ \hat{w}_{zn} \end{Bmatrix}. \tag{4.25}$$

The impulse load f is firstly defined in time domain and can decomposed into two independent functions in terms of time variable $f_n(t)$ and radial variable $f_r(r)$:

$$f(t,r) = f_n(t)\, f_r(r). \tag{4.26}$$

The mathematical expression for the function $f_n(t)$ depends mainly on the type of impulse loads created by the signal generator. In this paper, a sinusoidal impulse function is used as the external load to simulate the applied load. The load with amplitude of one is mathematically described in Equation (4.27).

$$f_n(t) = sin(2\pi f t)\, [1 - H(t - 1/f)], \tag{4.27}$$

where $t(s)$ is time and $f(Hz)$ is the frequency; $H()$ is the Heaviside step function.

Meanwhile, the function $f_r(r)$ is normally written using the Fourier-Bessel series:

$$f_r(r) = \sum_{m=1}^{\infty} F_m J_0(k_m r), \tag{4.28}$$

where

$$F_m(m) = \frac{2r_0 \sin(r_0 k_m)}{r_\infty^2 k_m J_1^2(r_\infty k_m)} \frac{n + 1 - m}{n+1},$$

where r_0 is the radius of the contact area; k_m is the mode number; n is the total mode number; r_∞ is the diameter of the soil specimen.

4.4 Model validation

4.4.1 Limiting case: Elastodynamics

By setting α, ρ_f, m, b and M to approach zero, the parameters in Equation (4.7) are reevaluated as:

$$k_{11} \xrightarrow{\alpha=0,\rho_f=0,M=0} \frac{\omega^2\rho}{-2\mu-\lambda}; \quad k_{12} \xrightarrow{\alpha=0,\rho_f=0,M=0} 0 \tag{4.29a}$$

$$k_{21} \xrightarrow{\alpha=0,\rho_f=0,M=0} 0; \quad k_{22} \xrightarrow{\alpha=0,\rho_f=0,M=0} 0 \tag{4.29b}$$

The wavenumber terms k_{p1}, k_{p2} and k_s in the limiting case become:

$$k_{p1} = \sqrt{k^2 - \frac{\omega^2\rho}{-2\mu-\lambda}} = \sqrt{k^2 - \frac{\omega^2}{c_p^2}} \tag{4.30a}$$

$$k_{p2} = k \tag{4.30b}$$

$$k_s = \sqrt{k^2 - \frac{\rho\omega^2}{\mu}} = \sqrt{k^2 - \frac{\omega^2}{c_s^2}} \tag{4.30c}$$

in which $c_p = \sqrt{\frac{\lambda+\mu}{\rho}}$ and $c_s = \sqrt{\frac{\mu}{\rho}}$.

Then the eigenvector matrix (P) in Equation (4.9) becomes:

$$P \xrightarrow{\alpha=0,\rho_f=0,M=0} \begin{Bmatrix} \sqrt{k^2 - \frac{\omega^2}{c_p^2}} & 0 \\ 0 & 0 \end{Bmatrix} \tag{4.31}$$

Finally we can see that by taking the limits of fluid-related parameters, the obtained potentials are the same as in the elastodynamic conditions shown by Al-Khoury, Scarpas, Kasbergen, and Blaauwendraad, 2001.

$$\hat{\phi}_s(r,z) = k_{p1} A e^{-k_{p1}\, z} J_0(kr) = B e^{-k_{p1}\, z} J_0(kr) \tag{4.32a}$$

$$\phi_f(r,z) = 0 \tag{4.32b}$$

$$\hat{\psi}_s(r,z) = C e^{-k_s\, z} J_0(kr) \tag{4.32c}$$

4.4.2 Validation using a four-layer system

The dispersion relation for a four-layered saturated soil system was investigated by (Chai, Zhang, Lu, et al., 2015) through the modified 'thin-layer matrix' method. For the purpose of model validation, the same four-layered system is studied using the proposed algorithm in this paper. The soil properties for each layer are shown in Table 4.1.

TABLE 4.1: Soil properties of each layer Chai, Zhang, Lu, et al., 2015

Layer	C_p (m/s)	C_s (m/s)	ρ (kg/m^3)	n	κ (m^2)	Thickness (m)
1	1532	149.2	2000	0.388	10.2×10^{-6}	1
2	1597	182.7	2000	0.388	10.2×10^{-6}	4
3	1637	217.3	2000	0.388	10.2×10^{-6}	10
4	1745	235.9	2000	0.388	10.2×10^{-6}	∞

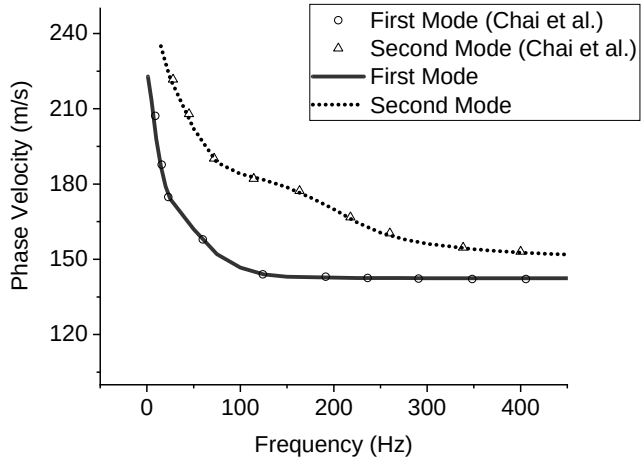

FIGURE 4.3: Model validation with data provided by Chai, Zhang, Lu, et al., 2015

The dispersion curves calculated by using the proposed algorithm and the dispersion curves obtained by Chai, Zhang, Lu, et al., 2015 are shown in Figure 4.3. The first and second modes of Rayleigh waves are used for the comparison. It can be seen that the proposed model is in good agreement with the method used by Chai, Zhang, Lu, et al., 2015, despite of different methods used for solving the dynamic poroelastic problem.

The displacement obtained in Equation (4.25) is in the frequency domain. To obtain the soil response in time domain, the numerical Durbin inverse transform method is applied (Abate and Valkó, 2004):

$$\mathcal{L}^{-1}\{\hat{\theta}(s)\} = \theta(t) = \int_0^{\infty} \hat{\theta}(s) e^{st} ds. \tag{4.33}$$

4.5 Results and discussion

The characterization of porosity has been a challenge because soil porosity can not be captured through traditional low-frequency tests. Such limitations can be explained by comparing the size of pore space and wavelength. A sensitivity analysis of the soil porosity is performed to verify such limitations. In this study, a soil column with a height and radius of 0.1m is studied. The impulse load is applied to an area with a radius of $1cm$ at the center of the top end of the soil column. The displacement at the center ($r = 0$) in the other end is recorded and compared.

The typical values of Young's modulus, porosity, density, permeability and Poisson's ratio are well documented in the literature (Obrzud, 2012; Kézdi and Rétháti, 1974; Prat,

Bisch, Millard, Mestat, Pijaudier-Calot, et al., 1995; Kulhawy and Mayne, 1990). For example, high-plasticity clay (CH based on the Unified Soil Classification System (USCS)) has a Young's modulus ranging from 0.35 to 32 MPa and porosity from 0.39 to 0.59; Silts and clays of low plasticity (ML, CL) have a typical value of Young's modulus ranging from 1.5 to 60 MPa and porosity from 0.29 to 0.56; poorly graded sands (SP) normally have a Young's modulus from 10 to 80 MPa and porosity from 0.23 to 0.43; The Young's modulus of well-graded gravel (GW) is between 30-320 MPa and its porosity is from 0.21 to 0.32. The average dry density ranges from 1700 to 2300 kg/m^3. The average permeability varies from 5×10^{-10} (clay of high plasticity) to 0.4 m/s (sand and gravel). The typical values of Poisson's ratio vary from 0.1 to 0.49 for clay and from 0.3 to 0.35 for silt.

In this paper, two groups of soils are studied: the first group includes clay, silt, sand and loose gravel which generally have a relatively low Young's modulus (lower than 100 MPa). The second group includes dense gravel which has a Young's modulus equal or greater than 200 MPa.

4.5.1 The effect of frequency and soil parameters on dynamic response

The effect of impulse load frequency and soil parameters on the dynamic soil response is studied in this section for the above-mentioned groups of soils. For the first group, the soil properties are taken as: Young's modulus is 20 MPa; Poisson's ratio is 0.35; dry density is 1800 kg/m^3. The wavelength can be calculated using the algorithm shown in Section 4.7.3. Several sensitivity analyses under three impulse loads with various predominant frequencies are performed. The impulse load distributions in time and frequency domains are shown in Figure 4.4. The loads 1, 2 and 3 have a predominant frequency of 0.05, 0.5 and 5 kHz, respectively. The amplitude of the input force is assumed to be 1 kN. The corresponding soil response at the receiver location is shown in Figure 4.5.

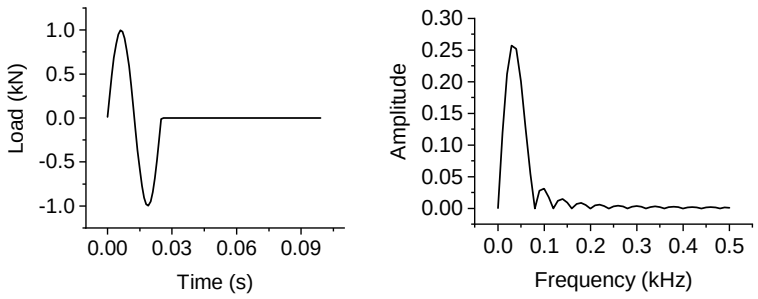

(A) Load 1

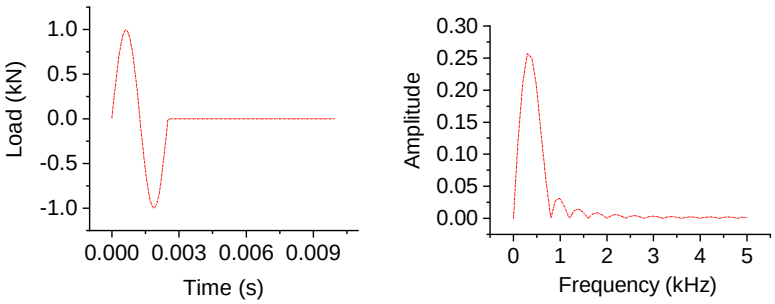

(B) Load 2

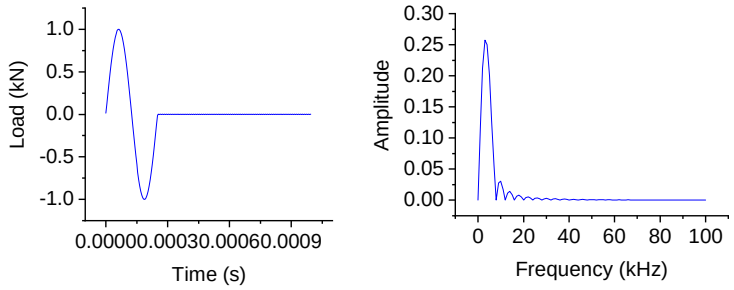

(C) Load 3

FIGURE 4.4: Impulse load in time and frequency domains

As shown in Figure 4.5, the different porosities (0.2, 0.4 and 0.6) give similar output displacement for load 1 and 2, which verifies that the size of pore space is not captured by the low-frequency impulse loads. In the inversion process, the porosity will be located at the shallow dimension, which makes the optimization algorithm difficult to be updated. Therefore, the characterization of saturated soil under low-frequency impulse load (below 5 kHz in this case) is nearly impossible. However, in the case of load 3 with a predominant frequency around 5 kHz, the effect of porosity is clearly triggered. The pore-scale of sand, for example, is around 760 μm as reported by (Lee, Truong, and Lee, 2010). Through the root search algorithm described in Section 4.7.3, the wavelength under the load 3 is calculated around 1000-2000 μm, which is close to the poro-space scale of the studied soil. Therefore, the impulse load 3 is a good choice for the lab-scale characterization of soil specimens for group 1.

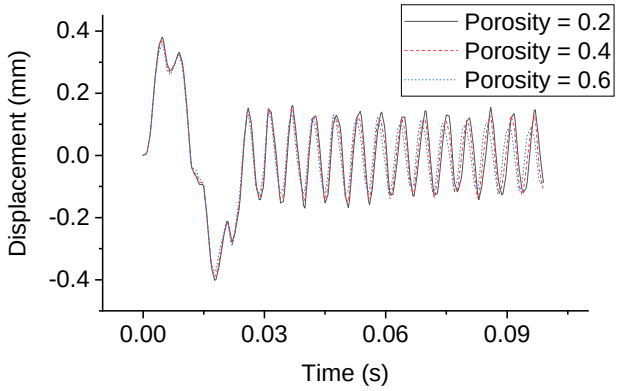

(A) Load 1

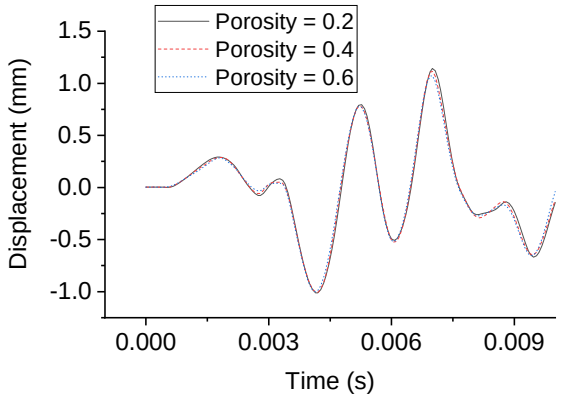

(B) Load 2

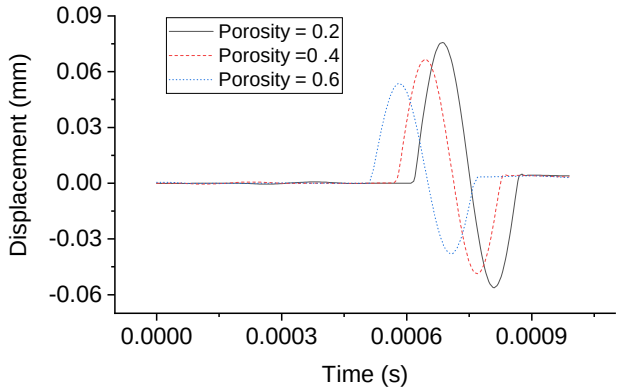

(C) Load 3

FIGURE 4.5: Sensitivity analysis of porosity under (a) load 1 (b) load 2 and (c) load 3

Similarly, the sensitivity analyses are performed by considering different densities, Young's modulus and Poisson's ratios. The output displacement is shown in Figure 4.6. The effects of Young's modulus, Poisson's ratio and density of soil are also shown in Figure 4.6. A higher Young's modulus leads to a faster wave travelling speed and a smaller

amplitude of the output wave. A higher density, on the contrary, leads to a lower travelling wave speed. Poisson's ratio that measures the tendency of material to expand in directions perpendicular to the direction of compression has an inverse relation with the wave speed. Therefore, it can be seen that the distribution of the output stress wave is a function of porosity, density, Young's modulus and Poisson's ratio.

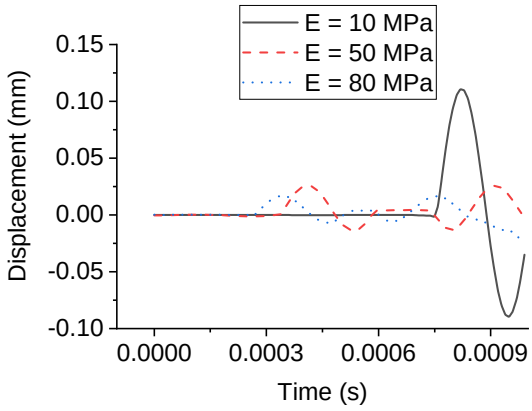

(A) Young's Modulus

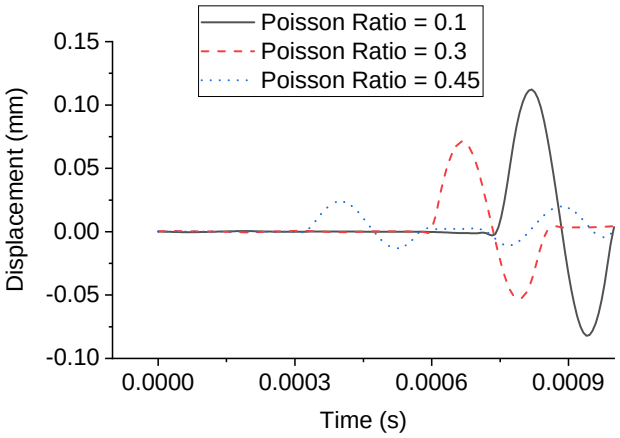

(B) Poisson Ratio

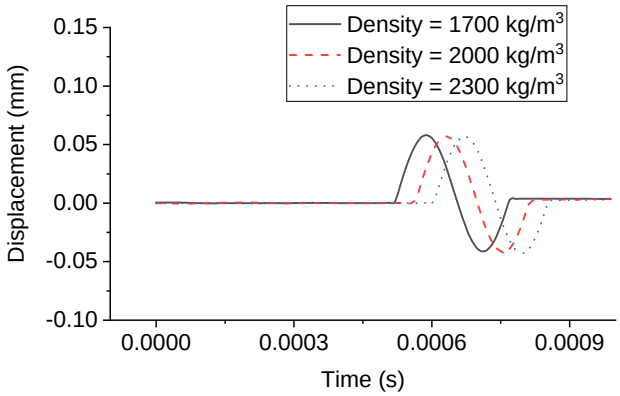

(C) Density

FIGURE 4.6: Sensitivity analysis of soil (group 1) parameters under impulse load

In the case of soil group 2, dense gravel whose Young's modulus is up to 320 MPa, it is found that the load 3 (up to 5kHz) generates similar displacement outputs at different porosities (0.1, 0.3 and 0.5), as shown in Figure 4.7. It means that load 3 can not trigger the effect of porosity. In order to characterize the porosity for very dense soils, one of the techniques is to further reduce the wavelength of the stress wave by increasing the frequency of the impulse load. It is found that an impulse load 4 with a higher predominant frequency (up to 0.5 MHz), as shown in Figure 4.8, can effectively differentiate dense soils with various porosities.

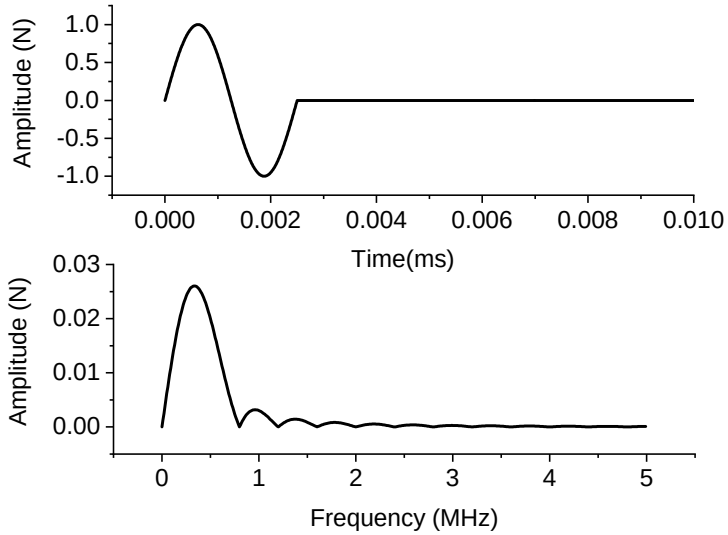

FIGURE 4.8: High-frequency (ultrasonic) impulse load 4 in time and frequency domain

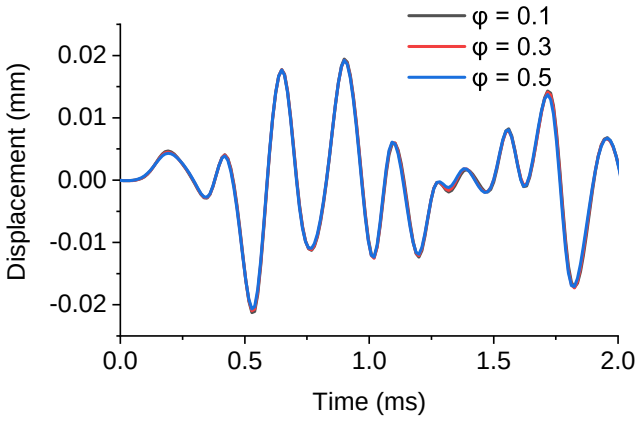

(A) load 3

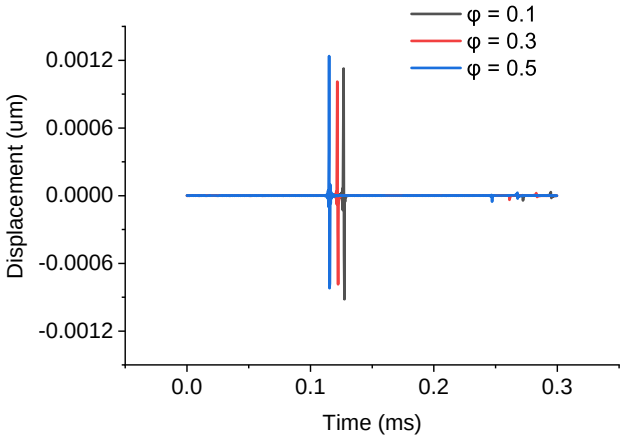

(B) load 4

FIGURE 4.7: Sensitivity of soil parameters under impulse load for dense gravel

4.5.2 Case study

In this section, a case study is presented to show the process of saturated soil characterization. For this purpose, synthetic data is firstly generated to simulate real measurements. For simplicity, the results are only presented for soil group 1. The nature of this inversion problem and inversion algorithm selection are discussed in detail in the following sections. At the end, the inversion results (soil parameters) are given based on the synthetic data and selected inversion algorithm.

Synthetic data

A synthetic data set (the displacement measured by a piezoelectric receiver) is firstly obtained using the following settings: Young's modulus is 20 MPa; Poisson's ratio is 0.35; density of solid skeleton is 1800 kg/m^3 and porosity is taken as 0.3; The time interval

is set to be 2 ms. Under the impulse load 3, as shown in Figure 4.4, the snap shot of displacement contours (symmetric) at various time spans are shown in Figure 4.9. The locations of impulse load and receiver are shown in Figure 4.9. It is shown that the stress wave propagates through the sample and reaches the receiver at about 0.6 ms. The wave reflection at the bottom boundary is clearly visualized at time 0.8 ms and 0.9 ms.

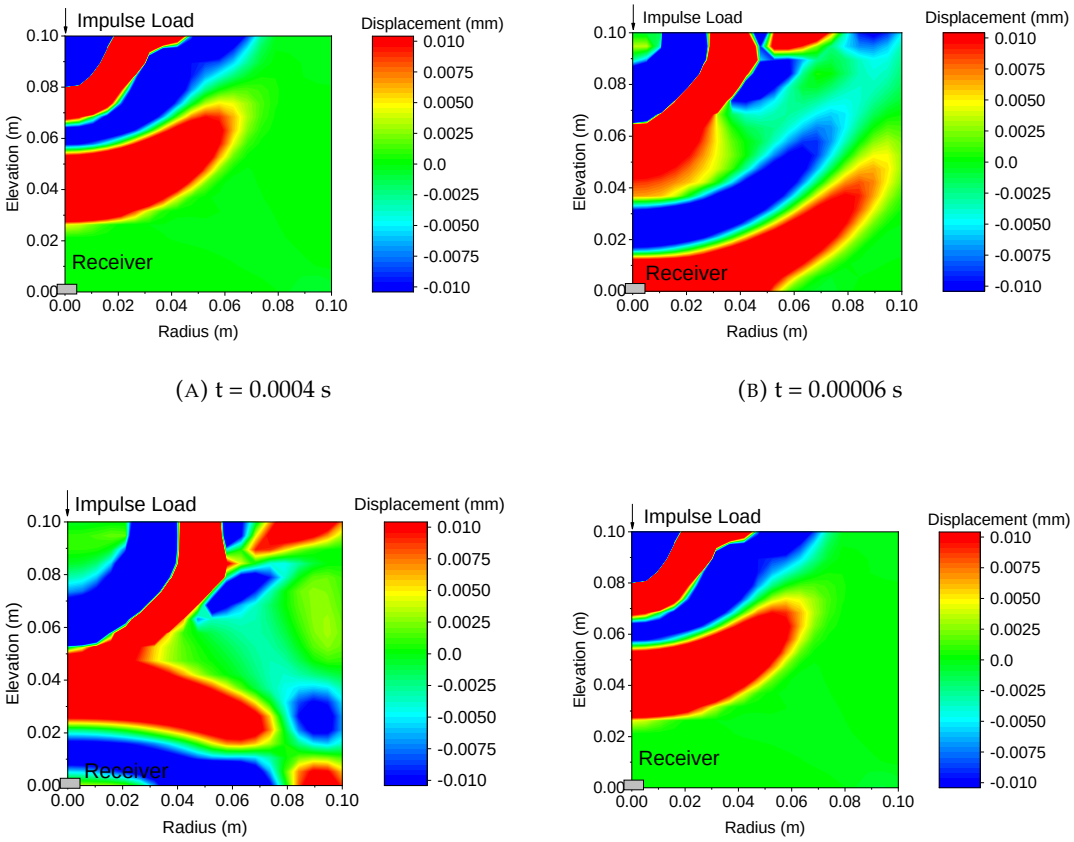

(A) t = 0.0004 s

(B) t = 0.00006 s

(C) t = 0.0008 s

(D) t = 0.0009 s

FIGURE 4.9: Displacement contour snap shots at various time

The response measured at the receiver location is summarised in Figure 4.10. In the laboratory ultrasonic test, the soil response is only recorded at the receiver location. Thus, in the following inversion process, only the results at the receiver location will be used as the input instead of the displacement at the entire domain.

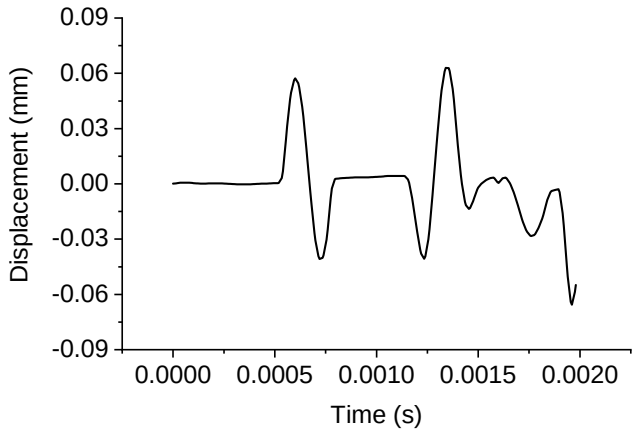

FIGURE 4.10: Soil dynamic response measured at the receiver location under impulse load 3

Inversion algorithm

The inversion algorithm takes the measured displacement at the receiver location (shown in Figure 4.10) as the input. The goal of the inversion process is to predict the soil properties including Young's modulus, Poisson's ratio, density and porosity based on the receiver signals. Given the initial guesses for the soil parameters, the inversion algorithm updates the prediction based on the difference between the displacement measured by the receiver and the predicted displacement response.

The update process can be achieved through the gradient-based and gradient-free optimization method. The gradient-based optimization is efficient in large convex problems such as linear least square problems and are commonly used in large optimization problems (e.g. deep learning and adjoint method). Therefore, the gradient based method is preferred in most cases, especially for convex optimization problems. However, such a method is highly likely to be affected by the local minimum since the gradient at any local minimum is zero. Thus, it is not favorable for non-convex problems.

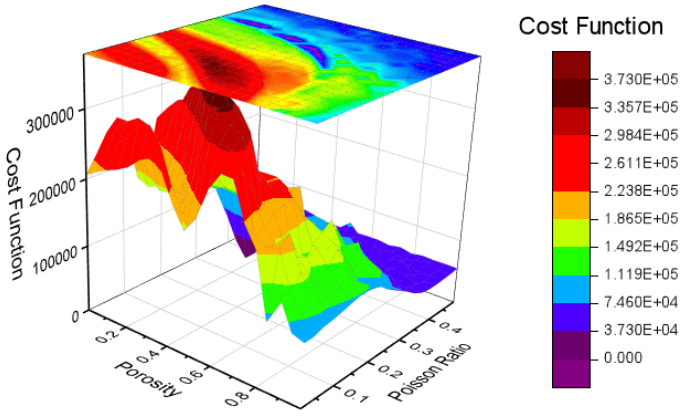

FIGURE 4.11: Non-convex optimization space for porosity and Poisson's ratio

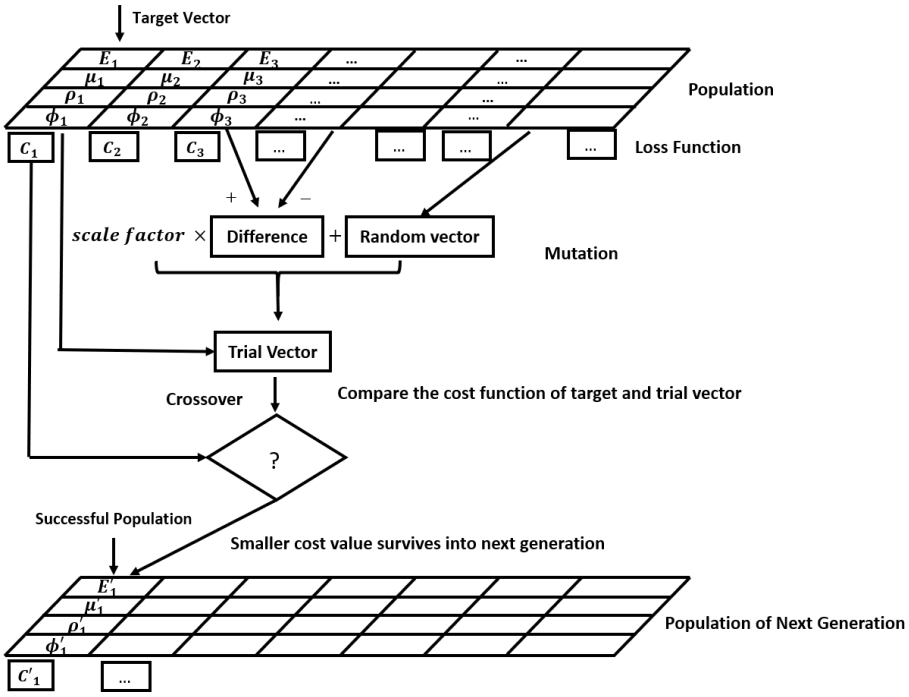

FIGURE 4.12: Flowchart of differential evolution for the optimization of soil parameters

An analysis was performed to show the nature of the soil characterization optimization problem. It is important to determine whether such application belongs to convex or non-convex problem. Then the corresponding optimization algorithm can be selected based on the nature of the problem. The aim (cost) function is defined as the Euclidean norm between the synthetic and predicted data. The optimization space can be visualized by performing parameter sweep. For example, the optimization space for the porosity and Poisson's ratio is shown in Figure 4.11.

It is shown in Figure 4.11 that a multiple local minimum exists in the optimization space. Therefore, the characterization of soil parameters is a non-convex optimization problem. If the gradient-based optimization algorithm is applied, the predictions will be highly dependent on the initial guess, which may leads to erroneous predictions in most cases. To make the estimation robust and accurate, a global optimization algorithm is favorable. In this work, the differential evolution algorithm that is designed for nonlinear and non-differential problems is used. Such an algorithm requires fewer control variables in comparison to other algorithms (e.g. genetic algorithm) and can be easily implemented in parallel computation (Storn and Price, 1997).

A brief description of the differential evolution algorithm is given in Figure 4.12. First, a population of candidate solutions are generated randomly; Then by moving around in the search space through a combination of the existing temporary solutions, a series of better solutions is expected to be obtained. In the differential evolution, the mutation constant is taken in the range of 0.5 to 1 and the recombination constant is recommended to be 0.9 (Montgomery and Chen, 2010).

Inversion results

Combining the synthetic data (as the input) shown in Figure 4.10 and the differential evolution algorithm described above, the updates of the soil parameters and the corresponding values of the cost function are shown in Figure 4.13. The iteration number shows the number of times that the forward problem is solved independently. After 200 iterations, the differential evolution algorithm stabilizes. The predicted soil parameters are as follows: Young's modulus is 20 MPa; Poisson's ratio is 0.35; density is 1800 kg/m^3; porosity is 0.3 and loss function is 0. It can be seen that the prediction of soil parameters based on the transmitted wave measured by the receiver (as shown in Figure 4.10) is exactly the same as the original input.

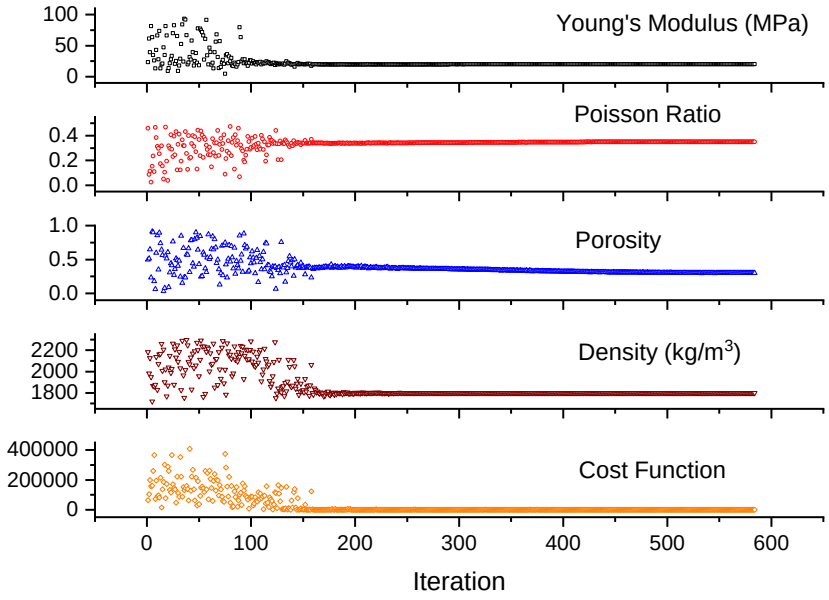

FIGURE 4.13: Updates of each parameter through a differential evolution algorithm

The differential evolution algorithm successfully finds the global minimum, despite of the existence of multiple local minimum. The spatial distribution of soil parameters updates are shown in Figure 4.14 and 4.15. Through the projection of each parameter, it can be seen that Young's modulus is relatively easier to update. For the other three parameters (Poisson's ratio, density and porosity), there are multiple locations where cost function is close to zero. Thus, it took more number of iterations to update to the true values. However, it can be seen such a multidimensional optimization problem is well handled by the differential evolution algorithm.

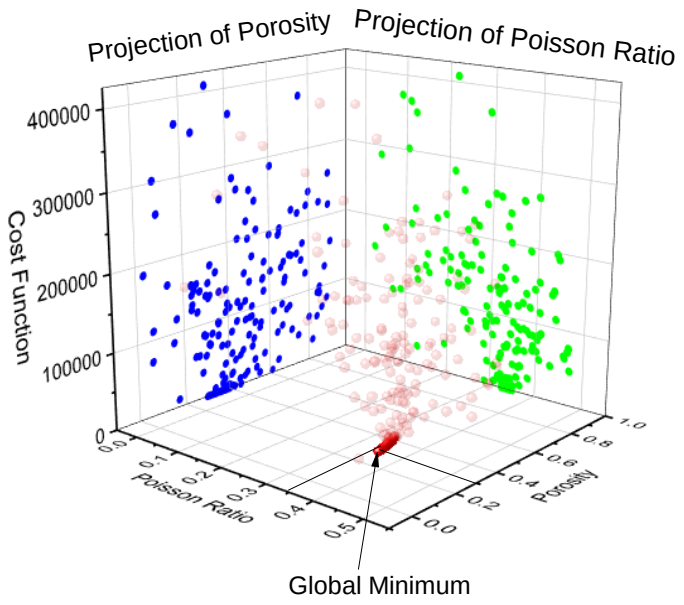

FIGURE 4.14: Updates of Poisson's ratio and porosity through a differential evolution algorithm

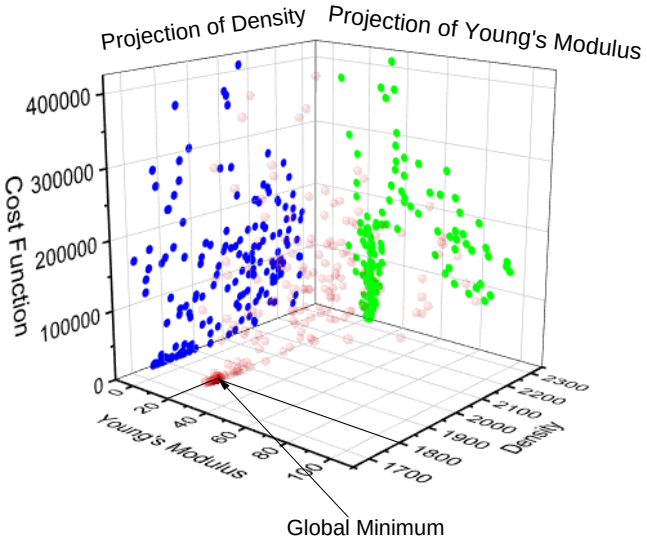

FIGURE 4.15: Updates of Young's modulus and density through a differential evolution algorithm

4.5.3 Uncertainty analysis

The predicted soil properties (Young's modulus, Poisson's ratio, density and porosity) are likely to be affected by the noise level of the measurement data, which could be introduced by the sensor measurement errors and ambient noise. In this uncertainty analysis, random white noise is added to measured displacement data with targeted signal-to-noise (SRN) ratio. For example, the noisy data with 10 and 20 dB of SRN is shown in Figure 4.16a. A normal distributed probability density function of SRN is used as the input to account the uncertainty introduced by noise, as shown in Figure 4.16b. It is assumed that there is a 28% possibility to have a SRN of 20 dB in measured data.

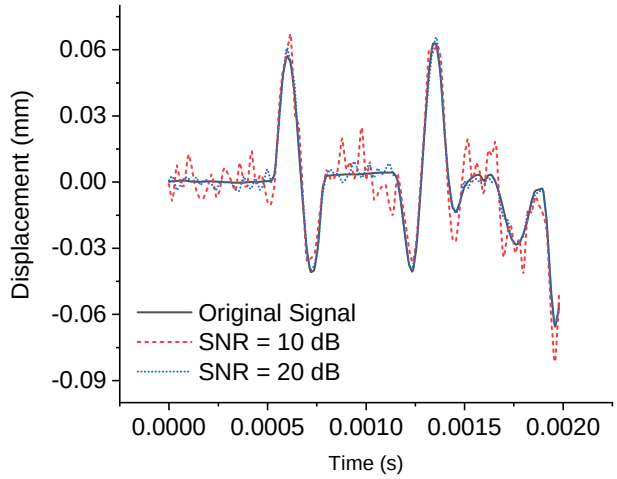

(A) noisy data

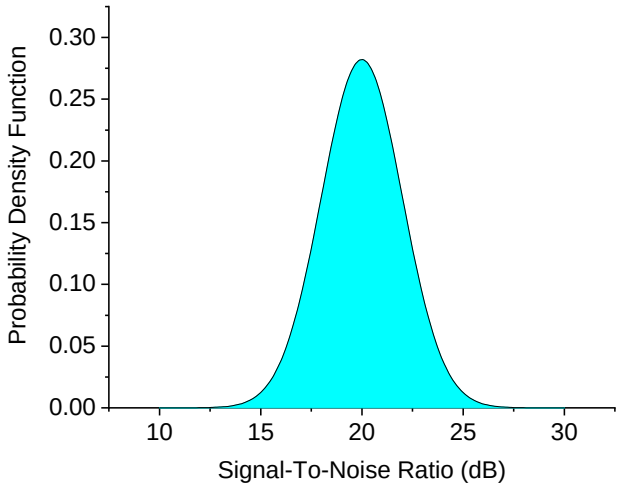

(B) SRN

FIGURE 4.16: Probability density function for the signal to noise ratio

In addition, the uncertainty can be introduced by the unknown coupling performance

in the interface of piezoelectric sensors and soil specimens. The input electricity signal does not necessarily generate the desired input pressure. To account for such uncertainties, the magnitude of input load is assumed to be in normal distribution, as shown in Figure 4.17a. The uncertainty also comes from the inherent soil property assumptions made in soil specimen during the inversion analysis, such as hydraulic conductivity. Thus, a normal probability distribution is also applied to account such uncertainty, as shown in Figure 4.17b.

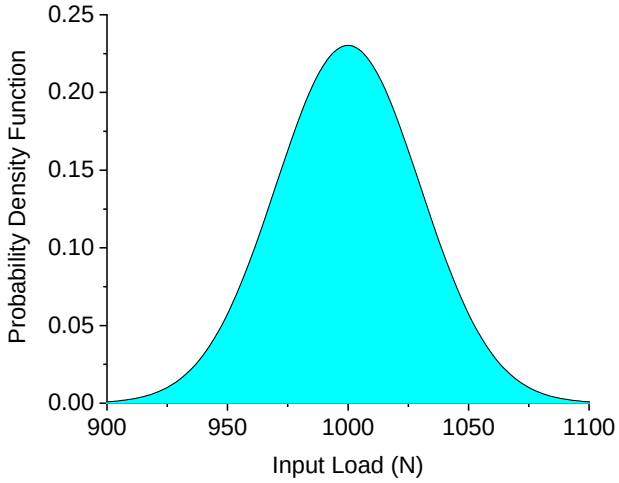

(A) Input Load

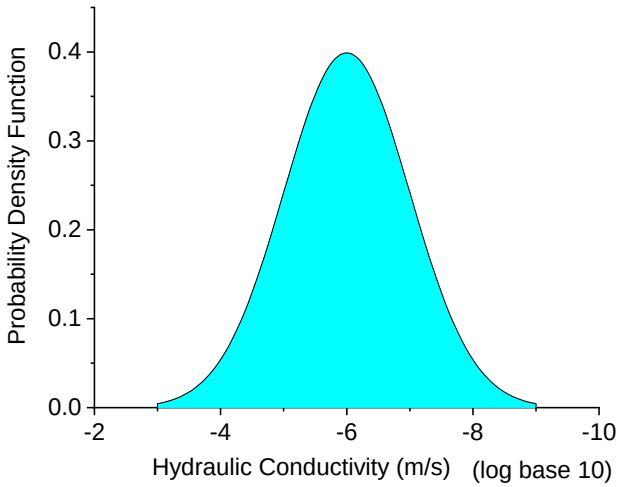

(B) Hydraulic Conductivity

FIGURE 4.17: Probability density function for input load and hydraulic conductivity

The generalized Polynomial Chaos Expansions (PCE) method developed by (Xiu and Hesthaven, 2005) is used for the uncertainty analysis in this paper. The PCE technique, as a rigorous uncertainty quantification method, provides reliable numerical estimates of

uncertain physical quantities. It was also reported that the PCE is much faster than Monte Carlo methods when the number of uncertainty parameters are lower than 20 (Crestaux, Le Maıtre, and Martinez, 2009). The 90% confident interval of the displacement at the receiver location is calculated through the PCE technique, shown in Figure 4.18.

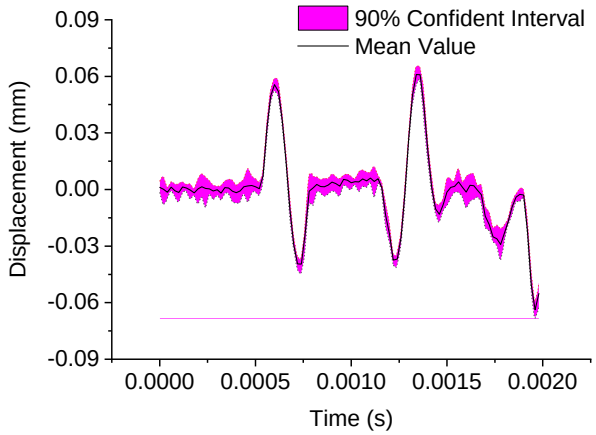

FIGURE 4.18: The 90% confidence interval of displacement distribution

Then, based on the inversion analysis, the predicted soil properties in the 90% confidence interval are shown in Table 4.2. Then, the variation ratio is calculated by comparing the mean values (obtained through uncertainty analysis) with the original predictions. It is found the prediction of porosity could be affected by the uncertainty introduced by the white Gaussian noise, coupling effect between transmitter and soil specimen as well as other factors. However, various signal processing methods can be used to improve the noisy measurements.

TABLE 4.2: The soil parameter variation range based on uncertainty analysis

Soil Properties	Lower Bound	Higher Bound	Variation Ratio
Young's Modulus (MPa)	20.42	20.92	3.3%
Poisson Ratio	0.352	0.354	0.3%
Density (kg/m^3)	1813.59	1878.58	2.6%
Porosity	0.26	0.27	11.7%

4.6 Conclusions

In this paper, an ultrasonic-based characterization of soil specimens is developed for the instant measurement of soil properties including Young's modulus and Poisson's ratio (compression/shear wave velocity), density and porosity. The developed meshless semi-analytical algorithm reduces the computational effort significantly in comparison to standard numerical techniques such as the finite element method. In fact, the advantage of such a solution is that the dynamic response is evaluated at the receiver location only rather than the entire domain. The soil response in other locations is not measured in the real application and does not factor in soil characterization. It is concluded that high-frequency impulse loads (with predominant frequency of up to 5 kHz) is required to trigger the effect of porosity for soils with relatively low Young's modulus (e.g clay, silt and sand). For stiffer materials, such as very dense gravels, an impulse load with predominant frequency of 0.5 MHz is required to characterize their porous nature. The characterization of soil properties has been proved as a highly non-convex optimization problem in this paper. The differential evolution algorithm, as a global optimization method, is found efficient and effective in finding the optimum soil properties, such that the difference between the predicted and measured stress waves is minimized. In conclusion, the developed method in interpreting dynamic response of saturated soil can be used for the immediate characterization of Young's modulus, Poisson's ratio, density and porosity for a given soil specimen.

4.7 Supplementary materials

4.7.1 Components of matrix S_2'

The components of the matrix S_2' for effective stress components and porewater pressure in frequency domain is shown as follows:

$$
\begin{aligned}
m_{11} &= 2kk_{p1}p_{11}\mu & m_{12} &= 2kk_{p2}p_{12}\mu & m_{13} &= -\left(k^2+k_s^2\right)\mu \\
m_{14} &= -2e^{-hk_{p1}}kk_{p1}p_{11}\mu & m_{15} &= -2e^{-hk_{p2}}kk_{p2}p_{12}\mu & m_{16} &= -e^{-hk_s}\left(k^2+k_s^2\right)\mu \\
m_{21} &= p_{11}\left(k_{p1}^2(\lambda+2\mu)-k^2\lambda\right) & m_{22} &= p_{12}\left(k_{p2}^2(\lambda+2\mu)-k^2\lambda\right) & m_{23} &= -2kk_s\mu \\
m_{24} &= e^{-hk_{p1}}p_{11}\left(k_{p1}^2(\lambda+2\mu)-k^2\lambda\right) & m_{25} &= e^{-hk_{p2}}p_{12}\left(k_{p2}^2(\lambda+2\mu)-k^2\lambda\right) & m_{26} &= 2e^{-hk_s}kk_s\mu \\
m_{31} &= (k-k_{p1})(k+k_{p1})M(p_{21}+p_{11}\alpha) & m_{32} &= (k-k_{p2})(k+k_{p2})M(p_{22}+p_{12}\alpha) & m_{33} &= 0 \\
m_{34} &= e^{-hk_{p1}}(k-k_{p1})(k+k_{p1})M(p_{21}+p_{11}\alpha) & m_{35} &= e^{-hk_{p2}}(k-k_{p2})(k+k_{p2})M(p_{22}+p_{12}\alpha) & m_{36} &= 0 \\
m_{41} &= 2e^{-hk_{p1}}kk_{p1}p_{11}\mu & m_{42} &= 2e^{-hk_{p2}}kk_{p2}p_{12}\mu & m_{43} &= -e^{-hk_s}\left(k^2+k_s^2\right)\mu \\
m_{44} &= -2kk_{p1}p_{11}\mu & m_{45} &= -2kk_{p2}p_{12}\mu & m_{46} &= -\left(k^2+k_s^2\right)\mu \\
m_{51} &= e^{-hk_{p1}}p_{11}\left(k_{p1}^2(\lambda+2\mu)-k^2\lambda\right) & m_{52} &= e^{-hk_{p2}}p_{12}\left(k_{p2}^2(\lambda+2\mu)-k^2\lambda\right) & m_{53} &= -2e^{-hk_s}kk_s\mu \\
m_{54} &= p_{11}\left(k_{p1}^2(\lambda+2\mu)-k^2\lambda\right) & m_{55} &= p_{12}\left(k_{p2}^2(\lambda+2\mu)-k^2\lambda\right) & m_{56} &= 2kk_s\mu \\
m_{61} &= e^{-hk_{p1}}(k-k_{p1})(k+k_{p1})M(p_{21}+p_{11}\alpha) & m_{62} &= e^{-hk_{p2}}(k-k_{p2})(k+k_{p2})M(p_{22}+p_{12}\alpha) & m_{63} &= 0 \\
m_{64} &= (k-k_{p1})(k+k_{p1})M(p_{21}+p_{11}\alpha) & m_{65} &= (k-k_{p2})(k+k_{p2})M(p_{22}+p_{12}\alpha) & m_{66} &= 0
\end{aligned}
$$

4.7.2 Stiffness matrix of a two-layer system

$$
H = \left[\begin{array}{ccccccccc}
\multicolumn{6}{c}{\multirow{3}{*}{G_1}} & 0 & 0 & 0 \\
 & & & & & & 0 & 0 & 0 \\
 & & & & & & 0 & 0 & 0 \\
G_{41}^1 & G_{42}^1 & G_{43}^1 & G_{44}^1+G_{11}^2 & G_{45}^1+G_{12}^2 & G_{46}^1+G_{13}^2 & G_{14}^2 & G_{15}^2 & G_{16}^2 \\
G_{51}^1 & G_{52}^1 & G_{53}^1 & G_{54}^1+G_{21}^2 & G_{55}^1+G_{22}^2 & G_{56}^1+G_{23}^2 & G_{24}^2 & G_{25}^2 & G_{26}^2 \\
G_{61}^1 & G_{62}^1 & G_{63}^1 & G_{64}^1+G_{31}^2 & G_{65}^1+G_{32}^2 & G_{66}^1+G_{33}^2 & G_{34}^2 & G_{35}^2 & G_{36}^2 \\
0 & 0 & 0 & \multicolumn{3}{c}{\multirow{3}{*}{G_2}} & G_{44}^2 & G_{45}^2 & G_{46}^2 \\
0 & 0 & 0 & & & & G_{54}^2 & G_{55}^2 & G_{56}^2 \\
0 & 0 & 0 & & & & G_{64}^2 & G_{65}^2 & G_{66}^2
\end{array}\right]
$$

where G_1 and G_2 are matrix for the first and second layer, respectively.

4.7.3 Phase velocity

The algorithm performs a sweep in a broad range of wavenumbers for a given frequency. A rough interval where roots exist needs to be found first and then the classic Brent's method can be applied to accurately locates the roots. The following notations are used in the algorithm: ϵ for the wavenumber sweep increment; n for the number of iterations; k_0 for the initial wavenumber, k for the wavenumber at the current step; k' for the wavenumber at the previous step; $f(k)$ gives the determinant value of the stiffness matrix at wavenumber k; δ for the tolerance used to check if the determinant of the stiffness matrix is close to zero; $Brent(k', k)$ is the Brent's method that takes an internal (k', k) as input where $f(k)$ and $f(k')$ must have different sign; r is the root calculated from Brent function.

The algorithm is shown as follows:

$$
\begin{cases}
Given\ \ \epsilon,\ k_0,\ \delta,\ n \\
for\ \ i = 1, 2, ...n \\
\quad k' = k \\
\quad k = k + \epsilon \\
\quad v' = f(k') \\
\quad v = f(k) \\
\quad if\ \ v' \cdot v \leq 0 \\
\qquad r = Brent(k', k) \\
\qquad if\ \ |f(r)| < \delta \\
\qquad\quad return\ \ r \\
end\ for
\end{cases}
\tag{4.34}
$$

Connecting section

Part II presented an algorithm for a laboratory-scale ultrasonic non-destructive testing to determine the physical and mechanical properties of saturated soil samples based on the distribution of stress waves. A poro-elastodynamic forward solver and differential evolution global optimization algorithm were applied to characterize the porosity, density, and other mechanical properties for a soil sample. It was concluded that the proposed high-frequency ultrasonic technique characterizes effectively the saturated soil samples based on the output stress wave measured by the receiver.

The next part, Part III (Chapter 5 and 6), presents multiphase poroelastodynamic solvers for both laboratory and in-situ characterization of permafrost soils. Chapter 5 presents a physics-based characterization method for the laboratory-scale ultrasonic non-destructive testing to determine the physical and mechanical properties of saturated soil samples based on the distribution of stress waves. Chapter 6, presents a hybrid inverse and multi-phase poromechanical approach for in-situ characterization of permafrost sites using surface wave techniques.

Part III: Multiphase Poroelastodynamic

Chapter 5

Pore-scale quantitative characterization of frozen and permafrost samples using ultrasonic waves

Abstract

The ability to quantitatively and non-invasively characterize complex multiphase geomaterials is still a major challenge to the engineering, construction, and geophysical fields. In the context of accelerating climate change, construction on foundation permafrost requires remedial measures and an appropriate characterization of permafrost (e.g., ice content, unfrozen water content, porosity, ice lenses, soil type, and mechanical properties). Current techniques are insufficient for efficient characterization of permafrost samples. Here, we propose an ultrasonic sensing technique and a signal interpretation method based on a spectral element multiphase poromechanical approach to overcome critical gaps in permafrost characterization. Ultrasonic sensing produces high-quality response signals that are sensitive to the permafrost properties. We show that our proposed transfer function, i.e. a ratio of induced displacement and applied force in the frequency domain, is independent of the distribution of the stress force applied by the transducer to the permafrost sample. This finding allows us to interpret the measured electrical signal using a theoretical transfer

Liu H., Maghoul P., Shalaby A., Thomson D., 2021. *Pore-scale quantitative characterization of frozen and permafrost samples using ultrasonic waves*, Communications Engineering, Manuscript ID: COMMSENG-21-0018, in Review.

function relation and efficiently determine the most probable permafrost properties from response signals using our proposed inverse spectral element multiphase poromechanical approach. Our study demonstrates the potential of the ultrasonic sensing technique for the rapid characterization of permafrost samples in terms of both physical and mechanical properties. The Quantitative Ultrasound (QUS) package developed in this study can be used in a laboratory setup or brought to the site for in-situ investigation of permafrost samples.

5.1 Introduction

Design and construction of infrastructure on permafrost (frozen soil) normally follow one of two broad principles which are based on whether the frozen foundation is thaw-stable or thaw-unstable (ice-rich permafrost). The distinction between thaw-stable or thaw-unstable permafrost soils is a function of the amount of ice within the soil mass (Subcommittee, 1988). Ice-rich permafrost contains ice in excess of the water content at saturation. Thawing permafrost will experience significant thaw-settlement and suffer a significant loss of strength in comparison to frozen state. Consequently, any remedial measures for excessive soil settlements or new design of infrastructure in ice-rich permafrost zones affected by climate warming requires a reliable estimate of ice (pore ice and ice lenses) within the permafrost. Another important factor that affects the rate of settlement of permafrost foundation is the mechanical properties of foundation soils defined by its stiffness and creep properties (Wang, Qi, Yu, and Liu, 2016).

The characterization of permafrost or frozen soil includes the measurement of both physical properties (e.g., unfrozen water, ice, and porosity) and mechanical properties (e.g., bulk modulus and shear modulus, or compression and shear wave velocity). It is well known that the freezing point in soils lies below 0°C (freezing-point depression) and some amount of pore water may remain unfrozen (Liu, Maghoul, and Shalaby, 2019). The popular techniques used for unfrozen water content measurement include Time Domain Reflectometry (TDR), Frequency Domain Reflectometry (FDR), Time Domain Transmissometry (TDT) and Nuclear Magnetic Resonance (NMR) (Stein and Kane, 1983; Noborio, 2001; Yoshikawa and Overduin, 2005). In these techniques, the soil water content is estimated from the empirical relation between the relative dielectric permittivity and unfrozen water content of soil samples (Hallikainen, Ulaby, Dobson, El-Rayes, and Wu, 1985; Topp, Davis, and Annan, 1980). These methods require frequent laboratory calibration

to obtain unique empirical relations based on soil types, test temperature, and the type of transducer (Yoshikawa and Overduin, 2005). Porosity can be measured using techniques such as Computed Tomography (CT scan) (Duliu, 1999; Périard, Gumiere, Long, Rousseau, and Caron, 2016), Imbibition methods (immersion of the soil sample in a fluid) (Gu, Zhu, Zhang, and Liu, 2019), Water Evaporation method (Schindler, Durner, Von Unold, Mueller, and Wieland, 2010; Castellini, Di Prima, and Iovino, 2018) and Mercury Intrusion (Yao and Liu, 2012). These techniques (all but CT method) are limited to the applications in unfrozen soils and are invasive such that the original soil state is disturbed. X-ray Computed Tomography imaging has been used in recent years to scan permafrost samples (Wagner, Lindsey, Dou, Gelvin, Saari, Williams, Ekblaw, Ulrich, Borglin, Morales, et al., 2018). Such a technique requires bulky and expensive instruments that are not suitable for field applications. Permafrost samples need to be transported to a laboratory, which can be costly and causes sample disturbance. Furthermore, the CT imaging can only shows the distribution of ice patches within the sample without any quantitative characterization; the CT imaging is also challenging to differentiate the water and ice from soil grains in fine-grained soils (Wu, Nakagawa, Kneafsey, Dafflon, and Hubbard, 2017).

The Bender Element (BE) test, Piezoelectric Ring-Actuator Technique (P-RAT) and Resonant Column (RC) test are frequently used for the evaluation of dynamic soil properties, such as the shear wave velocity (Liu, Cascante, Maghoul, and Shalaby, 2021; Karray, Ben Romdhan, Hussien, and Éthier, 2015). The RC test is used to determine the resonant frequency of a soil column, which is related to the shear wave velocity and shear modulus (Liu, Cascante, Maghoul, and Shalaby, 2021). However, the RC test is time-consuming, costly, bulky, and typically only used in laboratory investigations. The BE generates shear waves (S-waves) in the direction of their plane and also primary waves (P-waves) in the direction normal to their plane. The P-waves reflected from the cell walls can interfere with the generated S-waves (Lee and Santamarina, 2005). The arrival time-based methods usually result in subjective and inaccurate interpretation of the shear wave velocity. The lack of efficient contact between the BE and surrounding soils as well as protruding the BE into opposite ends of a soil sample are among the main drawbacks of the application of bender element test for frozen soils. In comparison to the BE test, the P-RAT reduces the generation of P-waves due to the constraint in the potential compression from the direct contact between piezoelectric elements and the soil samples (Karray, Ben Romdhan, Hussien, and Éthier, 2015). However, the P-waves can still be generated in the P-RAT test (Karray, Ben Romdhan, Hussien, and Éthier, 2015), which interferes with the selection

of S-wave arrival time in the current arrival time-based methods. Currently, those available techniques and interpretation methods are insufficient for the characterization of soil samples(Gu, Yang, Huang, and Gao, 2015).

Ultrasonic techniques are another method frequently used to evaluate the properties of construction materials such as concrete, however its use for soil characterization has been limited due to difficulties in signal interpretation and the complex nature of geomaterials (Liu, Maghoul, and Shalaby, 2020b). In theory, the mechanical properties of a soil sample can be computed from the P-wave arrival times. However, there are several uncertainties in the interpretation of the obtained signals. In the current practice, the first arrival time can be used for the evaluation of P wave velocity. However, the P wave velocity alone is insufficient for full characterization of soil samples, especially for determining the physical properties. There are no robust methods to interpret the remaining signals to obtain more information on other properties of soil samples, e.g., shear wave velocity, porosity, ice content and unfrozen water content, and no available algorithms for the interpretation of ultrasonic signals in frozen soils.

Several studies on the effect of ice content on the compression and shear wave velocities of frozen soils have been reported in the literature. The compression and shear wave velocities of frozen clay, loess, and sand were measured through the ultrasonic test by Wang, Zhu, Ma, and Niu (2006). The experimental results showed that the wave velocities increased with ice content at a different rate (following order: clay<loess<sand). The relationship between the P-wave velocity and ice content was also studied by Dou, Nakagawa, Dreger, and Ajo-Franklin (2016) and Dou, Nakagawa, Dreger, and Ajo-Franklin (2017). The volumetric unfrozen water content was firstly related to temperature through empirical water retention curves; then, the P-wave velocity was measured at the corresponding temperature for a correlation with ice content. Laboratory experiments were performed by Matsushima, Suzuki, Kato, Nibe, and Rokugawa (2008) in partially frozen brine. A positive relationship between the attenuation of ultrasonic waves and unfrozen brine was observed in a frequency range of 350-600 kHz.

Several theoretical studies have been performed for the estimation of frozen soil properties based on the correlation between the mechanical properties and ice content. The Kuster-Toksoz-Leurer model was proposed for the calculation of P-wave and S-wave velocities in two-phase media saturated with water or air (Kuster and Toksöz, 1974). This model was modified by King, Zimmerman, and Corwin (1988) to estimate P-wave and S-wave velocities in frozen soils by assuming that ice plays the same role as solid skeleton;

for example, the original bulk modulus (K_s) of solid skeleton is replaced by the volumetric average modulus of ice (K_i) and solid skeleton bulk modulus (i.e., $K_s \rightarrow (1-n)K_s + nS_rK_i$ where n is the porosity and S_r is the degree of saturation of unfrozen water). As a result of the interaction between the solid skeleton, pore-water and pore-ice, three types of P-waves and two types of S-waves are generated in three-phase frozen soils (Carcione, Gurevich, and Cavallini, 2000; Lee and Waite, 2008). The degree of saturation of unfrozen water in frozen soils depends on the P1 wave (the fastest P-wave among the three types of P-waves) and S1 wave (the fastest S-wave among the two types of S-waves) velocities among others. However, the mechanical and physical properties of soils still can not be inversely determined given the P1 wave and S1 wave velocities. The wave propagation within a three-phase medium using the Biot theory of poroelasticity was developed by Leclaire, Cohen-Ténoudji, and Aguirre-Puente (1994), Carcione, Gurevich, and Cavallini (2000), Carcione and Seriani (2001), Carcione, Santos, Ravazzoli, and Helle (2003), Maghoul, Gatmiri, and Duhamel (2011a), Maghoul, Gatmiri, and Duhamel (2011b), and Liu, Maghoul, and Shalaby (2021b). The solution was obtained through various numerical methods, such as a grid method based on the Fourier differential operator and a Runge–Kutta time-integration algorithm (Carcione and Seriani, 2001), finite element method (Santos and Sheen, 2007), Zener element method for poro-viscoacoustic model (Liu, Greenhalgh, and Zhou, 2009), and boundary element method (Maghoul, Gatmiri, and Duhamel, 2011b; Maghoul and Gatmiri, 2017).

In ultrasonic tests, an ultrasonic transmitter transforms electrical energy into mechanical energy (piezoelectric effect) to generate stress waves within a soil sample. However, the exact induced mechanical energy (force) still remains unknown due to the complexity of piezoelectric behavior and transducer structure. The existing literature mostly focused on the mechanism of wave propagation within frozen soils with assumed input force as boundary conditions. Therefore, these methods are incapable of interpreting the ultrasonic signals accurately. A literature search yielded no algorithms for the characterization of frozen soils using ultrasonic techniques.

Here we present a spectral element multiphase poromechanical transfer function method for the signal interpretation of ultrasonic measurements for the first time. Our signal interpretation approach provides an objective result, unlike the existing subjective empirical signal interpretation methods. Our proposed ultrasonic sensing technique can directly measure several physical and mechanical properties of frozen soils in a single ultrasonic test by interpreting the full signal unlike existing techniques that normally

relate only one or two parameters for a soil sample to the measured signal in each test. Similar to other problems involving inverse analyses, we can ensure the accuracy of the results or reduce the uncertainty in the inverse analysis by providing complementary information through conventional tests to determine temperature, soil type, density, and so on. Our results demonstrate the proposed ultrasonic sensing technique and the signal interpretation method based on the spectral element multiphase poromechanical approach can be used in a laboratory setup or in the field for rapid and reliable characterization of permafrost samples.

5.2 Methods

5.2.1 Methodology overview

Figure 5.1 shows an overview of the proposed Quantitative Ultrasound (QUS) sensing system for the ultrasonic characterization of frozen or permafrost soil samples using our spectral element multiphase poromechanical approach. Firstly, the ultrasonic test is performed with the calibration bar. Based on the ultrasonic measurements (Figure 5.1a) for the calibration bar, we can determine the product of transfer function H_1 and H_3, as shown in Figure 5.1b. Then, from the ultrasonic measurements for frozen soils (Figure 5.1c), we can obtain the experimental P1 wave velocity and transfer function H_2, as shown in Figure 5.1d. A random sample of soil properties (Figure 5.1e)is initially generated to ensure that soil parameters are not affected by a local minimum. Then our proposed forward spectral element multiphase poromechanical transfer function is used to compute the theoretical P1 wave velocity and transfer function H_2 (Figure 5.1f). Then we rank the samples based on the L_2 norm between the experimental and theoretical values. Based on the ranking of each sample, the Voronoi polygons (Neighborhood sampling method) are used to generate better samples with a smaller objective function until the solution converges (Figure 5.1h). We can select the best two candidate clusters (Figure 5.1i) based on the ranking of the loss function (L_2 norm) and obtain the most likely physical and mechanical properties considering other complementary information of the test sample (Figure 5.1j).

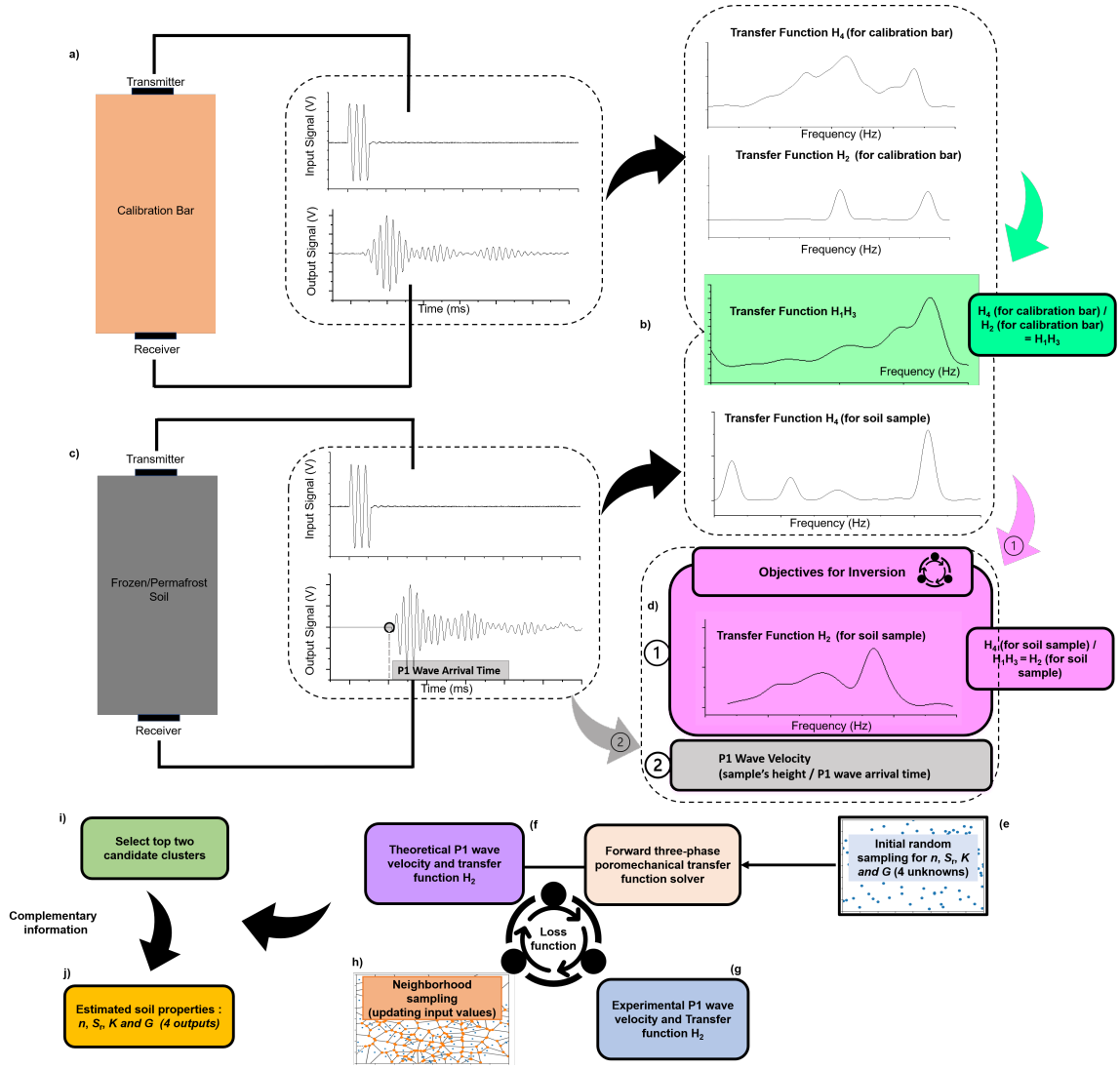

FIGURE 5.1: Overview of the proposed Quantitative Ultrasound (QUS) sensing system and the inverse spectral element multiphase poromechanical approach for the ultrasonic characterization of frozen or permafrost soil samples. **a** Ultrasonic signals obtained from the calibration bar. **b** The product of transfer function H_1 and H_3 determined in the calibration process. **c** Ultrasonic signals obtained from experimental tests for frozen soils. **d** Experimental transfer function H_2 and P1 wave velocity (objective for the inversion). **e** Initial guess of the physical and mechanical properties of the frozen or permafrost sample. **f** Calculation of the theoretical P1 wave velocity and transfer function H_2 using the forward spectral element multiphase poromechanical transfer function. **g** Solution ranking based on L_2 norm (experimental vs theoretical). **h** Neighborhood sampling for the reduction of L_2 norm. **i** Select the best two candidate clusters based on the rank of the L_2 norm. **j** Obtain the physical properties and mechanical properties of the frozen or permafrost sample considering other complementary information.

5.2.2 Spectral element multiphase poromechanical transfer function

We consider the frozen soil sample to be composed of three phases: solid skeleton, pore-water, and pore-ice. Through the infinitesimal kinematic assumption (Equation 5.8),

the stress-strain constitutive model (Equation 5.9), and the conservation of momentum (Equation 5.10), the field equations can be written in the matrix form as presented in Equation 5.11. The matrix $\bar{\rho}$, $\bar{b}$, $\bar{R}$ and $\bar{\mu}$ are given in Appendix A. The field equations can also be written in the frequency domain by performing convolution with $e^{i\omega t}$. The field equations in the Laplace domain are obtained by replacing ω with $i \cdot s$ ($i^2 = -1$ and s the Laplace variable).

To obtain the analytical solution, the Helmholtz decomposition is used to decouple the P waves (P1, P2, and P3) and S waves (S1 and S2). The displacement vector ($\bar{u}$) is composed of the P wave scalar potentials ϕ and S wave vector potentials $\bar{\psi} = (\psi_r, \psi_\theta, \psi_z)$. Since P waves exist in the solid skeleton, pore-ice and pore-water phases, three P wave potentials are used, including ϕ_s, ϕ_i and ϕ_f (Equation 5.13). The detailed steps for obtaining analytical solutions for P waves and S waves using the Eigen decomposition are summarized in Section 5.5.3.

In the ultrasonic tests, an assumed impulse load $\hat{f}(\omega, r)$ is applied to one end of the soil sample. The surface is assumed to be permeable, which implies the pore water pressure at the surface is zero. Under such conditions, the relation for load vector $\vec{f}$, stiffness matrix G and displacement vector $\vec{u}$ in the frequency domain is shown the Equation 5.1:

$$\underbrace{\begin{bmatrix} 0 \\ \hat{f}(\omega, r) \\ 0 \\ . \\ . \\ . \\ 0 \end{bmatrix}}_{\vec{f}} = \begin{bmatrix} \\ \\ \\ \\ \\ \\ \\ \end{bmatrix} G \begin{bmatrix} \\ \\ \\ \\ \\ \\ \\ \end{bmatrix} \underbrace{\begin{bmatrix} u_{r1}^1 \\ u_{z1}^1 \\ u_{z1}^2 \\ . \\ . \\ . \\ u_{zn}^3 \end{bmatrix}}_{\vec{u}} \tag{5.1}$$

where G is the stiffness matrix described in Equation 5.28 by means of the spectral element method. The displacement of the solid skeleton and the relative displacements of pore water and pore ice are denoted by u_i^1, u_i^2 and u_i^3. The radial and vertical components of the displacement vector is denoted by the subscripts r and z, respectively. The subscript n represents the node number, taken as 1 and 2 for the ultrasonic transmitter and receiver locations, respectively.

The main steps for the derivation of the stiffness matrix G by means of the spectral element method are given in Section 5.5.3, such as the derivation of solutions for the

longitudinal waves (P waves) and shear waves (S waves) by eigen-decomposition.

The impulse load can be decomposed into two independent functions in terms of Fourier or Laplace variable $f_n(\omega)$ and radial variable $f_r(r)$:

$$f(\omega, r) = f_n(\omega)\, f_r(r) \tag{5.2}$$

The mathematical expression for the function $f_n(\omega)$ depends mainly on the type of impulse loads created by a function generator and the mechanical force transformed by the ultrasonic transmitter. Meanwhile, the function $f_r(r)$, written using the Fourier-Bessel series (Equation 5.30), depends on the diameter of the ultrasonic transmitter. Then the transfer function H_2 (independent of the applied load distribution f_n) is defined as follows:

$$H_2 := \frac{u_{z2}(\omega)}{f_n(\omega)} = \sum_{m=1}^{\infty} \hat{u}_{z2} F_m J_0(k_m r) \tag{5.3}$$

where u_{z2} is the displacement at the ultrasonic receiver location; $\hat{u}_{z2}$ is the displacement component before applying the external load; f_n is the input force at the ultrasonic transmitter location; m is the total mode number; F_m is the Fourier-Bessel series components (Equation 5.30); J_0 is the first kind of Bessel function; k_m is the mode number; r is the radial location of the ultrasonic receiver.

5.2.3 Inversion

We used the distance between the experimentally measured and numerically predicted P1 wave velocity as well as the Euclidean norm between the experimental and numerical transfer functions H_2 as the components of the loss function. The problem is formulated as follows:

$$\begin{cases} minimize\ f(\boldsymbol{x}) = \frac{1}{2}\sum_{i=1}^{N} w(y_i - \bar{y}_i(\boldsymbol{x}))^2 + (1-w)\ |(V_{p1} - \bar{V}_{p1})| \\ subject\ to\ a_i \leq x_i \leq b_i,\ i\ = 1, \ldots, m \end{cases} \tag{5.4}$$

where f is the loss function; $\boldsymbol{x} = (x_1, x_2, ...x_m)$ is the optimization variable (e.g., porosity, the degree of saturation of unfrozen water, bulk modulus and shear modulus of solid skeleton); the constant a_i and b_i are the limits or bounds for each variable; m is the total number of variables; y and $\bar{y}$ are the numerical and experimental normalized transfer functions H_2. V_{p1} and $\bar{V}_{p1}$ are the the numerical and experimental P1 wave velocities,

respectively; w the weight for the L_2 norm to balance the contribution of transfer function and P1 wave velocity, taken as 800.

Here, we used the Neighborhood algorithm that benefits from the Voronoi cells to search the high-dimensional parameter space and reduce overall cost function (Sambridge, 1999). The algorithm contains only two tuning parameters. The Neighborhood sampling algorithm includes the following steps: a random sample is initially generated to ensure the soil parameters are not affected by the local minimum. Based on the ranking of each sample, the Voronoi polygons are used to generate better samples with a smaller objective function. The optimization parameters are scaled between 0 and 1 to properly evaluate the Voronoi polygon limit. After generating a new sample, the distance calculation needs to be updated. Through enough iterations of these processes, the aim function can be reduced. The detailed description of the neighborhood algorithm is described by Sambridge (1999).

5.3 Results

5.3.1 Instrumentation and system calibration

The ultrasonic setup consists of a function generator, receiver amplifier, oscilloscope, ultrasonic transmitter and receiver. The ultrasonic setup is summarized in Figure 5.2a. Figure 5.2b illustrates the components of an ultrasonic transducer, mainly the matching layer, a piezoelectric element and backing material. The matching layer reduces the reflection of transmitted waves so that the acoustic waves can efficiently enter the object. With an applied electrical impulse, the piezoelectric element generates a mechanical force that depends on the design of the backing material, matching layer and other components. The backing material (a highly attenuative and very dense material) is used to reduce the vibration of the transducer crystal by absorbing the energy that radiates from the back face of the piezoelectric element (Medina, Buiochi, and Adamowski, 2006). Due to the complexity of the mechanical response of ultrasonic transducer and the coupling between the transducer and soil sample, the induced force generated by the ultrasonic transmitter cannot be determined reliably (Figure 5.2c). The function waveform generator applies direct digital-synthesis techniques to create a stable, accurate output signal for the ultrasonic test. An applied electrical charge is transmitted to the ultrasonic transmitter to generate the mechanical energy used in the ultrasonic test (Figure 5.2c). The ultrasonic wave travels through the soil sample (Figure 5.2d) and is captured by an ultrasonic receiver which transforms the displacement into electrical output (Figure 5.2e). Due to the attenuation

of waves propagating within soil and water, a receiver amplifier is needed to reduce the noise content in the ultrasonic measurement. The input and output signals are displayed and exported through an oscilloscope.

In the proposed ultrasonic sensing system, the output voltage measured at the ultrasonic receiver can be related to the input voltage exciting the ultrasonic transducer in the frequency domain, as shown in Equation 5.5:

$$\underbrace{\frac{\text{Force}(\omega)}{\text{Voltage}_{in}(\omega)}}_{H_1} \times \underbrace{\frac{\text{Displacement}(\omega)}{\text{Force}(\omega)}}_{H_2} \times \underbrace{\frac{\text{Voltage}_{out}(\omega)}{\text{Displacement}(\omega)}}_{H_3} = \underbrace{\frac{\text{Voltage}_{out}(\omega)}{\text{Voltage}_{in}(\omega)}}_{H_4} \tag{5.5}$$

where ω is the angular frequency of the input or output signal; H_1 is the ratio of the induced force and the input voltage in the frequency domain; H_2 is the ratio of the calculated displacement at the receiver location and the force at the transmitter location in the frequency domain; H_3 is the ratio of the output voltage and the displacement at the receiver location in the frequency domain; and H_4 is the output voltage over the input voltage in the frequency domain.

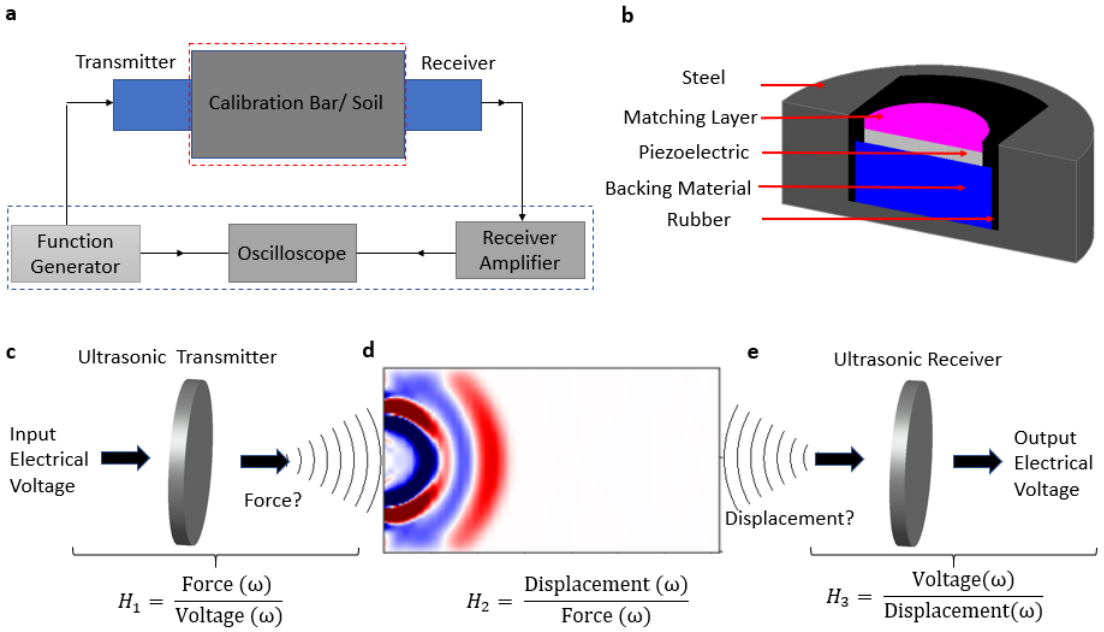

FIGURE 5.2: Ultrasonic sensing system working principle. **a** Schematics of the proposed ultrasonic setup. **b** Inner structure of ultrasonic transducer that include several different components.**c** Ultrasonic transmitter working principles and the defined transfer function H_1 in the frequency domain. **d** Wave propagation in three-phase frozen soil samples with an assumed force as well as the transfer function H_2 defined with calculated displacement and arbitrary input force in the frequency domain. **e** Ultrasonic receiver working principles and the defined transfer function H_3 in the frequency domain

The transfer function H_2, which is calculated by means of a spectral element multiphase poromechanical solver, is defined in Equation 5.3 in Methods. The transfer function H_2 is dependent on the properties of the soil sample, sample geometry, and the transducer diameter. Based on Equation 5.3, the transfer function H_2 is independent of the distribution of the applied force to the soil sample in both time and frequency domains. Hence, in the ultrasonic sensing system (as explained in Figure 5.2 and Equation 5.5), we can determine the transfer function H_2 given the testing material properties, sample geometry and transducer diameter. The transfer function H_4 can be measured based on the input and output electrical signals in the frequency domain. Therefore, despite the unknown induced force of the ultrasonic transmitter under an electrical impulse, we can still determine the product of H_1 and H_3 given the transfer function H_2.

In the calibration process, we firstly used the calibration bar (polymethyl methacrylate with the P-wave and S-wave velocities of 2,717 m/s and 1,516 m/s, respectively, and the density of 2,400 kg/m^3 (Proceq, 2006) to obtain the transfer function H_2. With the measured transfer function H_4, we can finally determine the product of the transfer functions H_1 and H_3. Figure 5.3a and 5.3b shows the ultrasonic input and output signals at the transmitter and receiver location during the calibration process, respectively. Figure 5.3c summarizes the transfer function H_4 (calculated using the ultrasonic output signal divided by the input signal in the frequency domain), transfer function H_2 (calculated using the spectral element multiphase poromechanical solver given the above-mentioned material properties) and consequently the product of H_1 and H_3 by dividing H_4 by H_2. Figure 5.3d shows the real laboratory setup for the proposed ultrasonic sensing technique in the calibration process. The product of H_1 and H_3 physically and quantitatively describes the transformation from electrical energy to mechanical energy (transmitter) and vice versa (receiver). The product of H_1 and H_3 depends on the inherent properties of the ultrasonic transducer components. Therefore, under the same electrical input, the product of H_1 and H_3 is believed to have the same distribution regardless the type of the test samples.

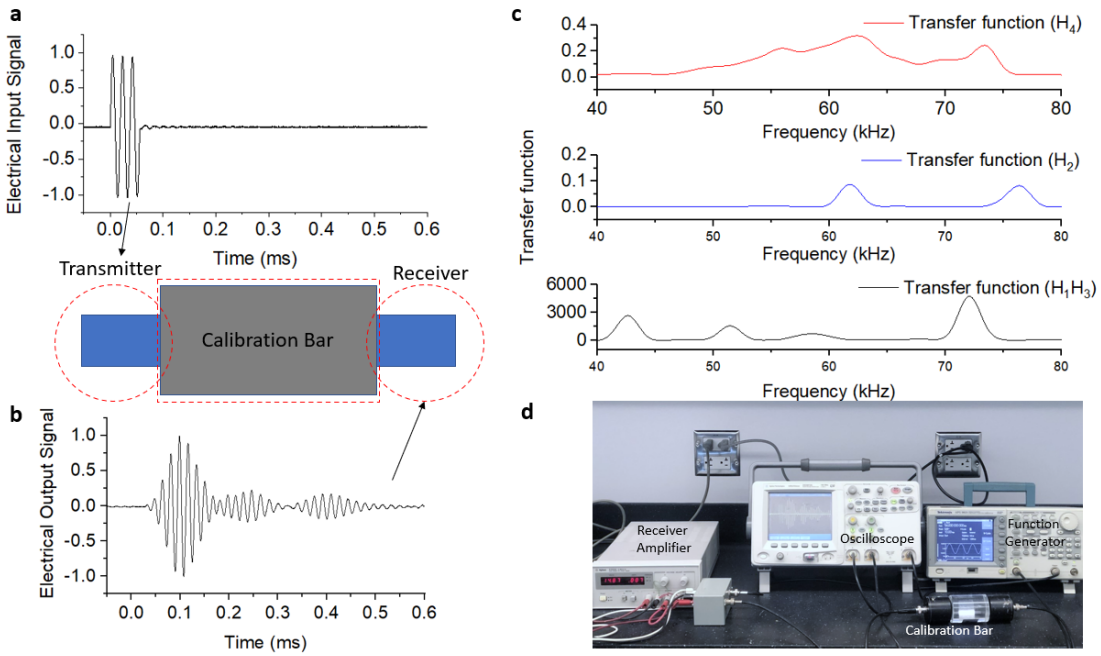

FIGURE 5.3: Ultrasonic sensing system calibration. **a** Ultrasonic transmitter input electrical signal. **b** Ultrasonic output electrical signal at the receiver location. **c** Results of the transfer functions H_4 and H_2 and the product of $H1$ and H_3. **d** Laboratory setup for the ultrasonic sensing system calibration.

5.3.2 Frozen soil (permafrost) characterization.

Different soil types including clay, silt, and till (a mix of clay, silt, sand, and limestone) are used to demonstrate the robustness of the proposed QUS setup in characterizing frozen soils. The soils were reconstituted and saturated to minimize the inhomogeneity of the soil samples. Some specimens extracted from the different saturated soil samples were dried in an oven at 110°C for three days based on the ASTM standards (Testing and Materials, 2005) to determine the initial porosity of those samples. These samples were then under different isothermal freezing conditions (-20°C, -10°C and -2°C) prior to the ultrasonic test. All the frozen soil samples were 170 mm in length and 100 mm in diameter. A summary of the ultrasonic test program including the soil type, temperature and initial porosity of each sample is given in Table 5.1.

TABLE 5.1: Summary of the test soil type, temperature and initial porosity of each sample

Ultrasonic test program						
Soil type	Clay			Silt		Till
Temperature	-20°C	-10°C	-2°C	-20°C	-2°C	-20°C
Initial porosity	0.57	0.57	0.60	0.33	0.33	0.28

The initial water content of the clay soil was measured as 0.503. Based on the specific gravity of most clay minerals (ranging from 2 to 3 g/cm^3, but normally around 2.65 g/cm^3 (Blake and Steinhardt, 2008)), the initial porosity of the sample was most likely around 0.57. We performed the ultrasonic test firstly on the clay sample at a freezing temperature of -20°C. The ultrasonic transmitter applied a sinusoidal impulse with a frequency of 54 kHz to the left end of the sample. Figure 5.4a shows the ultrasonic input signal (at the transmitter location) and the output signal (at the receiver location). The first arrival time of the P1 wave is 0.75 ms and subsequently the P1 wave velocity can be obtained as 2,433 m/s (travelling distance (sample's height), divided by the first arrival time). Figure 5.4b shows the transfer function H_4 based on the ultrasonic input and output signals. The transfer function H_4 shows that the ultrasonic measurement mostly concentrates at a frequency bandwidth between 65 kHz and 78 kHz. With the product of the transfer functions H_1 and H_3, determined in the previous calibration process, we obtained the experimental transfer function H_2 (Figure 5.4c) that represents the inherent properties of the testing frozen soil sample at -20°C. Figure 5.4d shows the real ultrasonic sensing setup for the frozen soil tests.

The transfer function H_4 depends on both ultrasonic transducer characteristics and the soil properties. On the other hand, the transfer function H_2 is dependent on the properties of the test sample and transducer diameter, but independent on the characteristics of the transducer. By means of calibration, we can eliminate the contribution of the transducer to the original transfer function H_4 using the relation $H_2 = H_4/(H_1H_3)$ (H_1H_3 is determined in the calibration process). The dominant frequency of the transfer function H_2 (around 68 kHz) is different from the dominant frequency of the transfer function H_4 (around 75 kHz). The strong response around 75 kHz observed in the measurement of H_4 is likely due to the characteristics of the ultrasonic transducers (resonant frequency). However, the transfer function H_2 is not affected by the 75 kHz frequency component in the measured signal because of the calibration process.

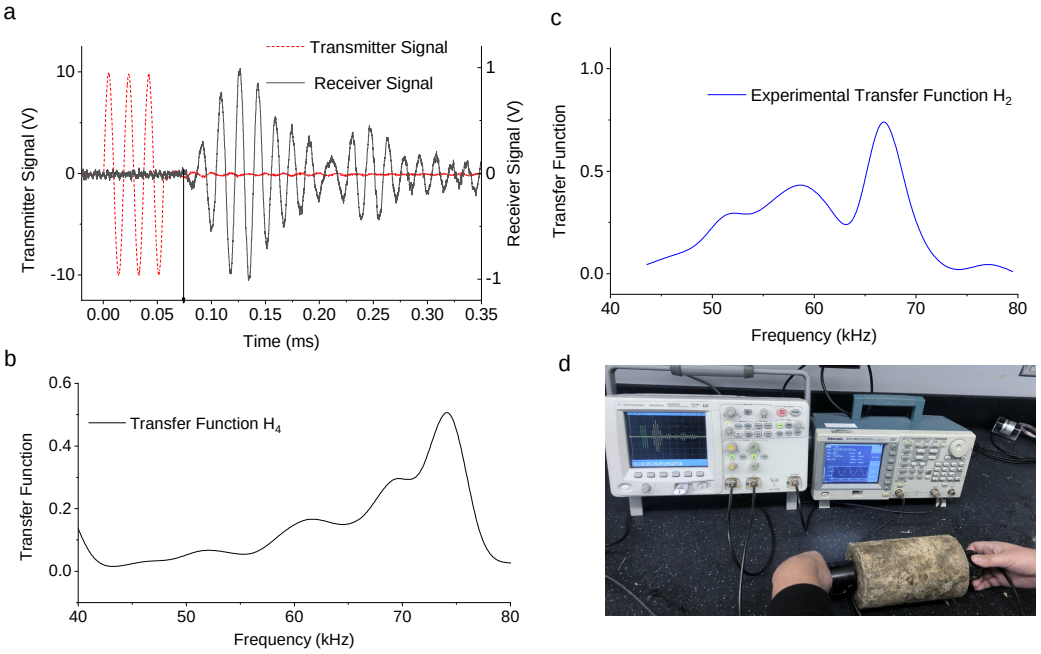

FIGURE 5.4: Ultrasonic signal and transfer functions at -20°C. **a** Ultrasonic input and output signals at the transmitter and receiver locations, respectively. **b** Transfer function H_4 (ultrasonic output divided by input signal in frequency domain). **c** Normalized experimental transfer function H_2 (transfer function H_4 divided by H_1H_3). **d** Ultrasonic sensing setup.

Figure 5.5a shows the comparison between the experimental measurement and numerical predictions of the transfer function H_2 for the selected two candidate clusters showing the most optimum properties of the clay sample at -20°C. The theoretical transfer function H_2 obtained by means of our proposed spectral element multiphase poromechanical solver shows a good agreement with the experimental measurement. Figure 5.5b and Figure 5.5c show the top two candidate clusters (the subspace between the porosity and degree of saturation of unfrozen water as well as the subspace between the bulk modulus and shear modulus, respectively) resulted from the inversion procedures based on the ranking of the loss function. The two components of the loss function, as defined in Equation 5.4 in Methods, are the difference between the experimental and theoretical P1 wave velocities (the theoretical value is given in Section 5.5.1) and the experimental and theoretical transfer functions H_2, respectively. Both the P1 wave velocity and transfer function H_2 are independent of the force applied to the soil sample by the transducer but dependent on the properties of the test soil sample. Our results, as presented in Figure 5.5b and 5.5c, show that the top two candidate clusters predict similar P1 wave velocity. Figure 5.5a also illustrates that those two clusters predict similar transfer functions H_2. The predicted P1 wave velocity in those two clusters (2,199 m/s and 2,200 m/s for the candidates 1 and 2,

respectively) is sufficiently close to the measured P wave velocity (2,267 m/s).

We recognize the non-uniqueness and uncertainty in the inversion results due to the highly nonlinear and non-convex nature of the inverse poromechanical problem. The optimization space (composed of bulk modulus [K], shear modulus [G], porosity [n], the degree of saturation of unfrozen water [S_r]) is highly non-convex. The direct search in the entire space is almost impossible to find the most optimum soil parameters for test samples. To address this issue, we divided the search space into smaller subspaces, which ensures the parameter space is well explored to mitigate the local minimum issue. The inversion algorithm determines multiple possible solutions for the sample properties based on the measured P1 wave velocity and the transfer function H_2.

The first candidate cluster as shown in Figure 5.5b and Figure 5.5c is concentrated to a porosity of 0.46, degree of saturation of unfrozen water of 93%, a bulk modulus of 10.3 GPa, and a shear modulus of 11.6 GPa. The second candidate cluster has an average porosity of 0.53, degree of saturation of unfrozen water of 12%, a bulk modulus of 6.3 GPa, and a shear modulus of 5.9 GPa. These two candidates are acceptable solutions, since they both show excellent agreement with the measured P1 wave velocity and transfer function H_2. However, additional information, such as test temperature, soil types, soil moisture characteristics, or other complementary conventional characterization tests, can be used to add more constraints to the solution and to more accurately select the most probable solution. In this case, the measurement was taken at a temperature of -20°C. The first candidate cluster is not a plausible solution given its extremely high degree of saturation of unfrozen water at -20°C, despite the fact that it has a relatively smaller loss function than the second candidate. We found the second candidate cluster is also consistent with our prior geotechnical testing (porosity ranges from 0.5-0.6). Within the candidate 2 cluster, the predicted porosity ranges from 0.52 to 0.53; the degree of saturation of unfrozen water ranges from 12% to 15%; the bulk modulus of solid skeleton is between 6.2 GPa and 6.8 GPa, and the shear modulus of solid skeleton ranges from 5.9 GPa to 6.2 GPa. Other physical properties such as the degree of saturation of ice, volumetric water content and volumetric ice content can also be obtained based on the porosity and degree of saturation of unfrozen water.

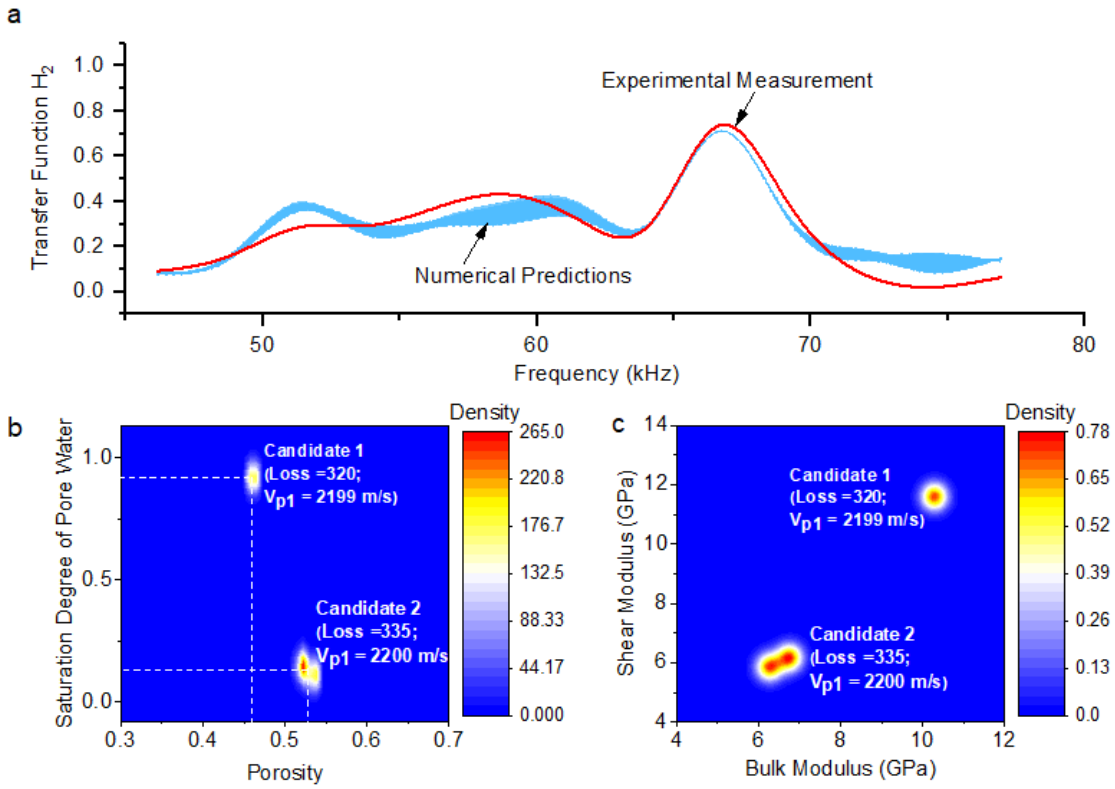

FIGURE 5.5: Experimental and theoretical transfer functions H_2 obtained through our proposed spectral element multiphase poromechanical solver as well as the top two optimum candidates in the inverse solution for the clay sample at -20°C. **a** Comparison between the experimental and theoretical transfer functions H_2. **b** Density contour of top two candidate clusters at a subspace between the degree of saturation of unfrozen water and porosity. **c** Density contour of top two candidate clusters at a subspace between the shear modulus and bulk modulus of the solid skeleton.

Figure 5.6 illustrates the inversion process by means of the Neighborhood algorithm for the second candidate cluster. Figure 5.6a shows that the Neighborhood algorithm generates random search points to cover the searching space in the first step. By means of the Voronoi decomposition, more sampling points were generated around the locations where the loss function is relatively smaller than that in other locations (Figure 5.6b). Within 20 iterations, the searching space is converged to the minimum location (Figure 5.6b). The sampling points between the degree of saturation of unfrozen water and porosity are summarized in Figure 5.6c. It shows that the solution is converged to a point where the degree of saturation of unfrozen water is 12% and the porosity is 0.53. The updates of each parameter (porosity, degree of saturation of unfrozen water, bulk modulus and shear modulus of the solid skeleton) are shown in Figure 5.6d. The iteration number in Figure 5.6d represents the number of times that the forward problem is solved independently. The loss function was reduced from 6000 to 335 in 100 iterations.

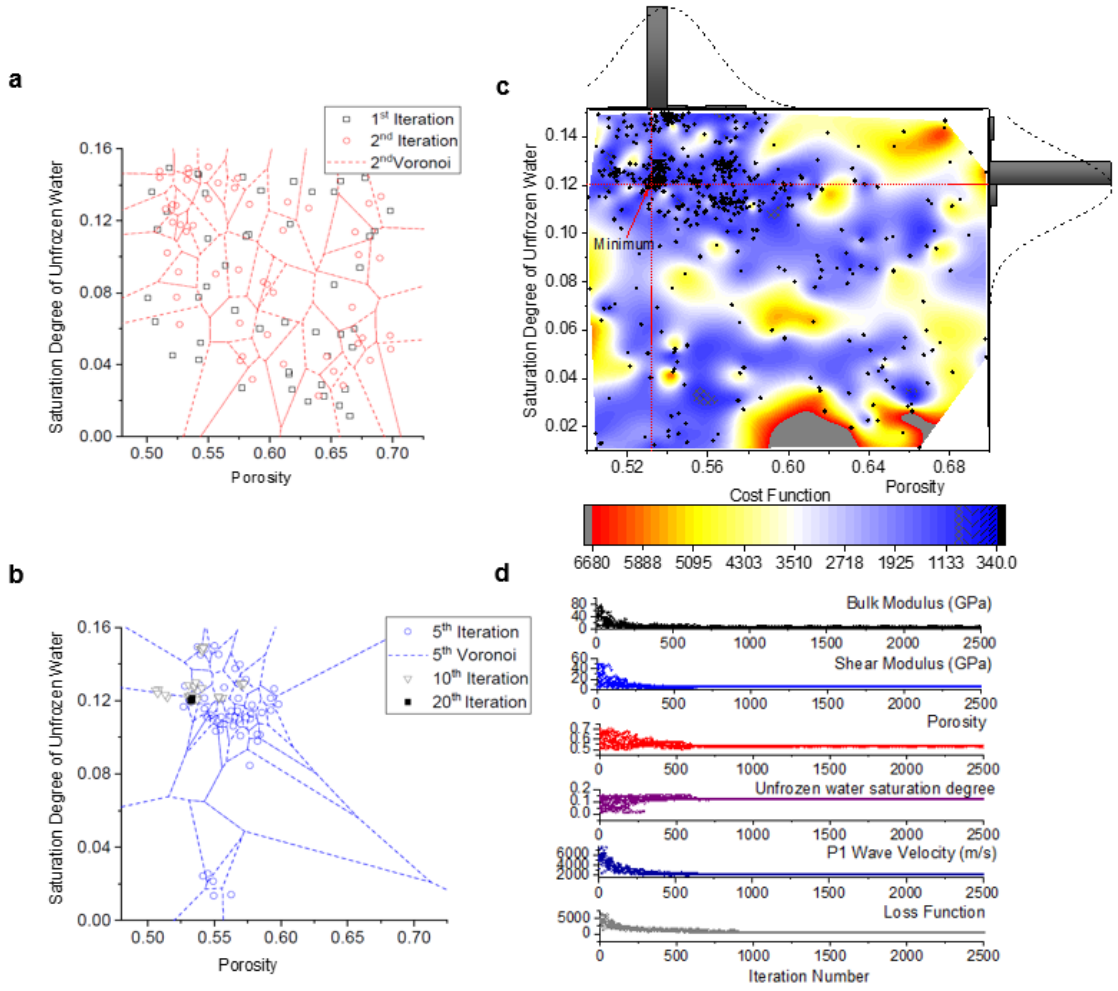

FIGURE 5.6: Inversion results for the second candidate cluster. **a** Visualization of the Neighborhood algorithm searching method in the 1^{st}, $2nd$, 5^{th} and 20^{th} iteration. **b** Sampling points in the subspace between the degree of saturation of unfrozen water and porosity. **c** Updates of each parameter through the Neighborhood algorithm as well as the loss function with the iteration number

We also performed the ultrasonic test for the same clay soil sample at a freezing temperature of -10°C using the same setup and input electrical signals. Figure 5.7a illustrates the ultrasonic input and output signals in the time domain. Figure 5.7b shows the experimental transfer function H_2. The measured P1 wave velocity is 1,976 m/s. Figure 5.7c and Figure 5.7d show the density contours of the top two candidate clusters that have the lowest loss function in comparison with other searching points in the subspace between the degree of saturation of unfrozen water and porosity as well as the subspace between shear modulus and bulk modulus, respectively. In the first candidate cluster, the degree of saturation of unfrozen water and porosity converged to 11% and 0.47, respectively. The shear modulus and bulk modulus were also converged to 4.4 and 7.4 GPa, respectively. In the second

candidate cluster, the degree of saturation of unfrozen water and porosity converged to 18% and 0.45, respectively. The shear modulus and bulk modulus were converged to 5.4 and 6.0 GPa, respectively. Our results show that the predicted P1 wave velocity (1,970 m/s) in the second candidate cluster matches better with the measured P1 wave velocity (1,976 m/s) in comparison with the first candidate cluster (even though the overall loss function is relatively smaller in candidate 1 due to the contribution of the transfer function H_2 component). Theoretically, both candidates are acceptable for the prediction of the properties of the frozen soil sample. However, with the previous measurement under -20°C, we expect that the degree of saturation of unfrozen water increases by increasing the temperature. The degree of saturation of unfrozen water at -20°C was 12%. Under the current freezing temperature of -10°C, candidates 1 and 2 predict a degree of saturation of unfrozen water of 11% and 18%, respectively. Therefore, it is most likely that the test sample has the following properties: a shear modulus of solid skeleton of 5.4 GPa, a bulk modulus of solid skeleton of 6.0 GPa, a porosity of 0.45, and a degree of saturation of unfrozen water of 18%.

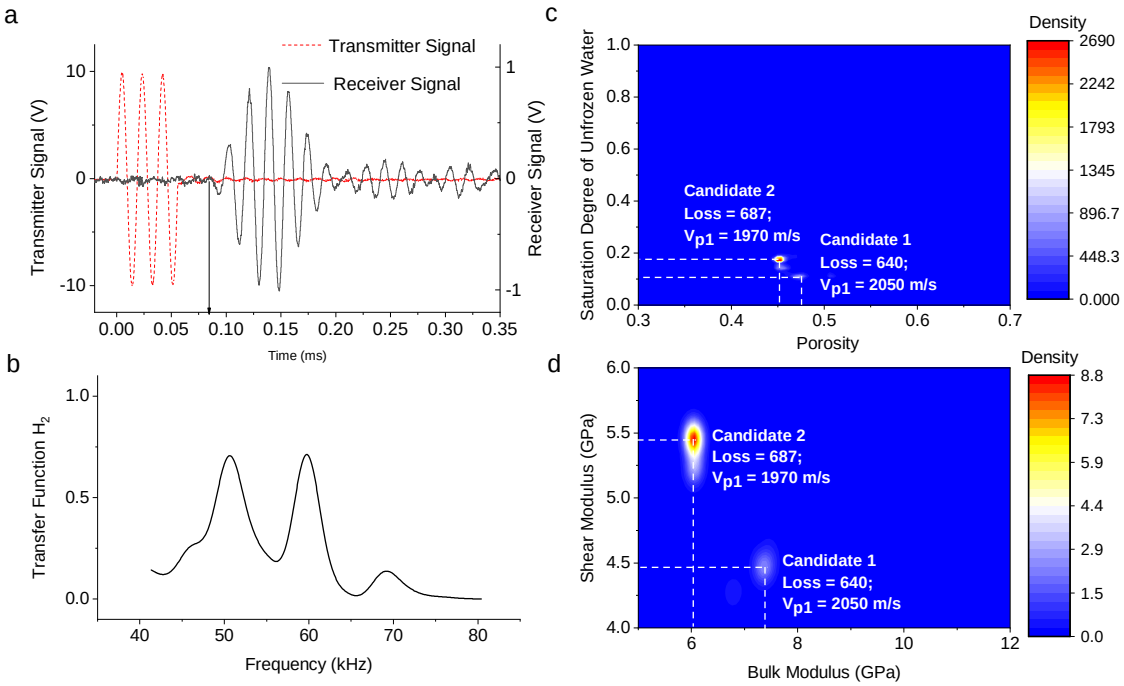

FIGURE 5.7: Ultrasonic measurement and inversion results summary for the clay sample at -10°C. **a** Ultrasonic input and output signals in the time domain. **b** Experimental transfer function H_2. **c** Density contour of top two candidate clusters at a subspace between the degree of saturation of unfrozen water and porosity. **d** Density contour of top two candidate clusters at a subspace between the shear modulus and bulk modulus of the solid skeleton.

As mentioned previously, we also performed the ultrasonic tests for the silt and till soil samples under -20°C. Figure 5.8 summarizes the ultrasonic measurements, the experimental transfer function H_2 and the top two candidate clusters that have the lowest loss functions for the silt soil sample. Based on the traditional geotechnical tests performed in the laboratory, the initial porosity of the silt sample is around 0.33. The candidate 1 cluster determined by our inverse multiphase poromechanical algorithm (Figure 5.8c and Figure 5.8d) represents the properties of the frozen silt soil sample as follows: a shear modulus of solid skeleton of 12.2 GPa, a bulk modulus of solid skeleton of 12.4 GPa, a porosity of 0.30, and a degree of saturation of unfrozen water of 11%. Similarly, Figure 5.9 shows the ultrasonic measurements, the experimental transfer function H_2 and the top two candidate clusters that have the lowest loss functions for the till soil sample. The initial porosity of the till sample is around 0.28 based on the traditional geotechnical tests performed in the laboratory. The candidate 1 cluster determined by our inverse multiphase poromechanical algorithm (Figure 5.9c and Figure 5.9d) represents the properties of the frozen till soil sample as follows: a shear modulus of solid skeleton of 10.9 GPa, a bulk modulus of solid skeleton of 20.5 GPa, a porosity of 0.28, and a degree of saturation of unfrozen water of 6.7%.

The ultrasonic test was also performed for the silt and clay samples under a freezing temperature of -2°C. Figure 5.10 shows the ultrasonic measurements, the experimental transfer function H_2 and the top two candidate clusters that have the lowest loss functions for the silt soil sample under -2°C. Based on the conventional geotechnical tests performed in the laboratory to determine the porosity and previous ultrasonic test results at -20°C, the candidate 1 cluster determined by our inverse multiphase poromechanical algorithm (Figure 5.10c and 5.10d) represents the properties of the silt sample at -2°C as follows: a shear modulus of solid skeleton of 10 GPa, a bulk modulus of solid skeleton of 12 GPa, a porosity of 0.25, and a degree of saturation of unfrozen water of 26%. Similarly, Figure 5.11 shows the ultrasonic measurements, the experimental transfer function H_2 and the top two candidate clusters that have the lowest loss functions for the new clay soil sample under -2°C. Based on the traditional geotechnical tests performed in the laboratory, the initial porosity of the new clay sample is around 0.60. The candidate 1 cluster determined by our inverse multiphase poromechanical algorithm (Figure 5.11c and 5.11d) represents the properties of the new clay sample under -2°C as follows: a shear modulus of solid skeleton of 4.4 GPa, a bulk modulus of solid skeleton of 4.2 GPa, a porosity of 0.58, and a degree of saturation of unfrozen water of 64%.

5.4 Discussion and conclusions

We developed a spectral element multiphase poromechanical transfer function method and a Quantitative Ultrasound (QUS) sensing system that can be used as a portable and instant characterization tool for frozen or permafrost soil samples. With a simple portable setup, the physical and mechanical properties are measured using only a single ultrasonic test. Compared with traditional methods (TDR, FDR, TDT and NMR) for the measurement of only unfrozen water content, our proposed technique offers clear advantages. In our QUS sensing system, the unfrozen water content can be determined without any specific empirical relations unlike the traditional methods that rely on intensive laboratory calibration to determine the empirical equations between the relative dielectric permittivity and unfrozen water content. Our proposed spectral element multiphase poromechanical transfer function considers the multiphase physics of wave propagation in the test samples and makes no assumptions about the soil types, ice content, porosity, and testing temperature. Furthermore, the above-mentioned traditional methods (TDR, FDR, TDT and NMR) can only estimate the unfrozen water content; but the information on ice content, porosity and mechanical properties can not be evaluated. In terms of the mechanical properties, the proposed ultrasonic technique also shows clear advantages compared with the traditional RC and BE tests. In the proposed ultrasonic sensing technique, the bulk modulus and shear modulus of solid skeleton particles can be determined at the same time without costly and time-consuming laboratory geophysical setups.

The inverse spectral element multiphase poromechanical algorithm is highly non-linear and non-convex. The components of the stiffness matrix as shown in Appendix B involve soil parameters such as bulk modulus, shear modulus, the saturation degree of unfrozen water, and porosity, which make the algebraic operations highly non-linear. Given the ultrasonic measurements in terms of the P1 wave velocity and experimental transfer function H_2, multiple possible theoretical predictions with similar loss functions can match well with the experimental measurements. The proposed inversion scheme successfully locates these possible solutions that fit well with the measured P1 wave velocity and transfer function H_2. However, additional information may be required to make the final decisions on the most probable soil properties. The non-uniqueness nature and the inherent uncertainty of this inverse problem are due to the lack of constraints of the soil parameters. Supplementary information (e.g., prior tests and typical values for soil properties) can reduce the search space and add constraints on the inversion analysis. For

example, the two most probable solutions (clusters) were selected based on the ranking of the loss function in this paper. Traditional geotechnical tests performed in the process of preparing soil samples provided estimated soil porosity. Combining with the measured freezing temperature, we can eliminate the first candidate from the inversion results at a temperature of -20°C for the frozen clay sample (Figure 5.5).

We further verified the inversion results by comparing the predicted soil properties at -20°C and -10 °C. Our results showed that the degree of saturation of unfrozen water increases (from 12% to 17%) with the temperature increase. The porosity slightly decreases (from 0.53 to 0.45) with the increase of temperature. This is explained by the reduction in volume when the in-situ ice is transformed into porewater. In addition, the variation of volumetric ice content (from 0.47 to 0.37, calculated by $n(1 - S_r)$) is consistent with the temperature increase. The volume of ice is about 9% higher than that of water under the same weight. This is consistent with the 8% variation of total volume (The volume reduction is mostly reflected by the reduction in the porosity). Meanwhile, the volumetric unfrozen water content increased from 0.06 to 0.08. Both bulk modulus and shear modulus are reduced (from 6.3 GPa to 6 GPa in the bulk modulus; from 5.9 GPa to 5.4 GPa in shear modulus) when the temperature increases from -20°C to -10°C. Such a conclusion is consistent with the temperature-dependent feature of elastic properties of frozen soil reported by Wang, Zhu, Ma, and Niu (2006). Comparing the inversion results of the silt sample at -20°C and -2°C, the degree of saturation of unfrozen water increased from 11% to 26%, which is consistent with the thermodynamic model of silt derived by Xiao, Lai, and Zhang (2020). The till soil sample has a relatively lower degree of saturation of unfrozen water in comparison to clay and silt sample due to the existence of sand in the test soil sample. However, the till soil sample has the largest bulk modulus in comparison to other test samples due to the existence of limestone.

Future work on the ultrasonic characterization of permafrost should explore ways to reduce the uncertainty in the proposed inverse spectral element multiphase poromechanical transfer function. The uncertainty originates from the non-uniqueness in the inverse analysis (local minima problem) and the limited number of constraints in the inversion analysis. Even though the local minima problem has been mitigated by performing inversion analysis in smaller optimization subspace, it is recommended to integrate other techniques (e.g., electrical resistance test and thermal imaging) with the proposed ultrasonic method to further reduce the uncertainty of the permafrost characterization.

5.5 Supplementary materials

5.5.1 Calculation of P1 wave velocity

The P1 wave velocity (v_{p1}) is determined by a third degree characteristic equation:

$$\begin{aligned}\Lambda^3\tilde{R} - \Lambda^2\left((\rho_{11}\tilde{R}_{iw} + \rho_{22}\tilde{R}_{si} + \rho_{33}\tilde{R}_{sw}) - 2(R_{11}R_{33}\rho_{23} + R_{33}R_{12}\rho_{12})\right)\\ +\Lambda\left((R_{11}\tilde{\rho}_{iw} + R_{22}\tilde{\rho}_{si} + R_{33}\tilde{\rho}_{sw}) - 2(\rho_{11}\rho_{23}R_{23} + \rho_{33}\rho_{12}R_{12})\right) - \tilde{\rho} = 0\end{aligned} \tag{5.6}$$

where

$$\begin{aligned}\tilde{R} &= R_{11}R_{22}R_{33} - R_{23}^2R_{11} - R_{12}^2R_{33}\\ \tilde{R}_{sw} &= R_{11}R_{22} - R_{12}^2\\ \tilde{R}_{iw} &= R_{22}R_{33} - R_{23}^2\\ \tilde{R}_{si} &= R_{11}R_{33}\\ \tilde{\rho} &= \rho_{11}\rho_{22}\rho_{33} - \rho_{23}^2\rho_{11} - \rho_{12}^2\rho_{33}\\ \tilde{\rho}_{sw} &= \rho_{11}\rho_{22} - \rho_{12}^2\\ \tilde{\rho}_{iw} &= \rho_{22}\rho_{33} - \rho_{23}^2\\ \tilde{\rho}_{si} &= \rho_{11}\rho_{33}\end{aligned}$$

The roots of the third degree characteristic equation, denoted as Λ_1, Λ_2 and Λ_3, can be found by computing the eigenvalues of the companion matrix. The velocities of the three types of P-wave ($V_{p1} > V_{p2} > V_{p3}$) are given in the Equation 5.7. The P1 wave velocity (V_{p1}) is the fastest one among those three velocities.

$$V_{p1} = \sqrt{\frac{1}{\Lambda_1}};\quad V_{p2} = \sqrt{\frac{1}{\Lambda_2}}; V_{p3} = \sqrt{\frac{1}{\Lambda_3}} \tag{5.7}$$

5.5.2 Supplementary testing program

The ultrasonic measurements, the experimental transfer function H_2 and the top two candidate clusters that have the lowest loss functions for silt, till and clay soil samples at various freezing temperatures are given in Figure 5.8 to Figure 5.11.

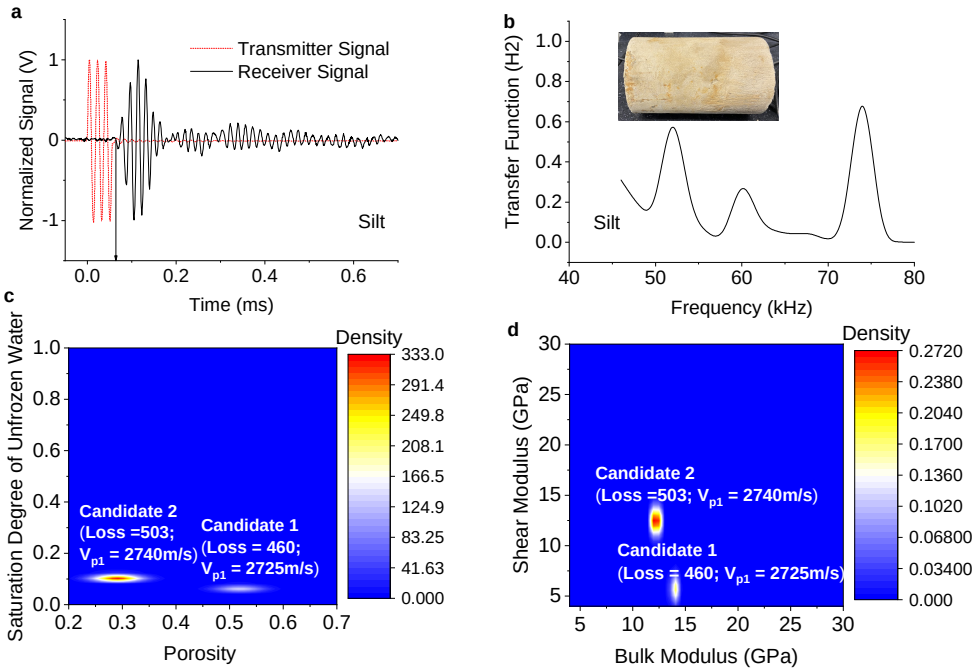

FIGURE 5.8: Ultrasonic measurement and inversion results summary for the silt sample at -20°C. **a** Ultrasonic input and output signals in the time domain. **b** Experimental transfer function H_2. **c** Density contour of top two candidate clusters at a subspace between the degree of saturation of unfrozen water and porosity. **d** Density contour of top two candidate clusters at a subspace between the shear modulus and bulk modulus of the solid skeleton.

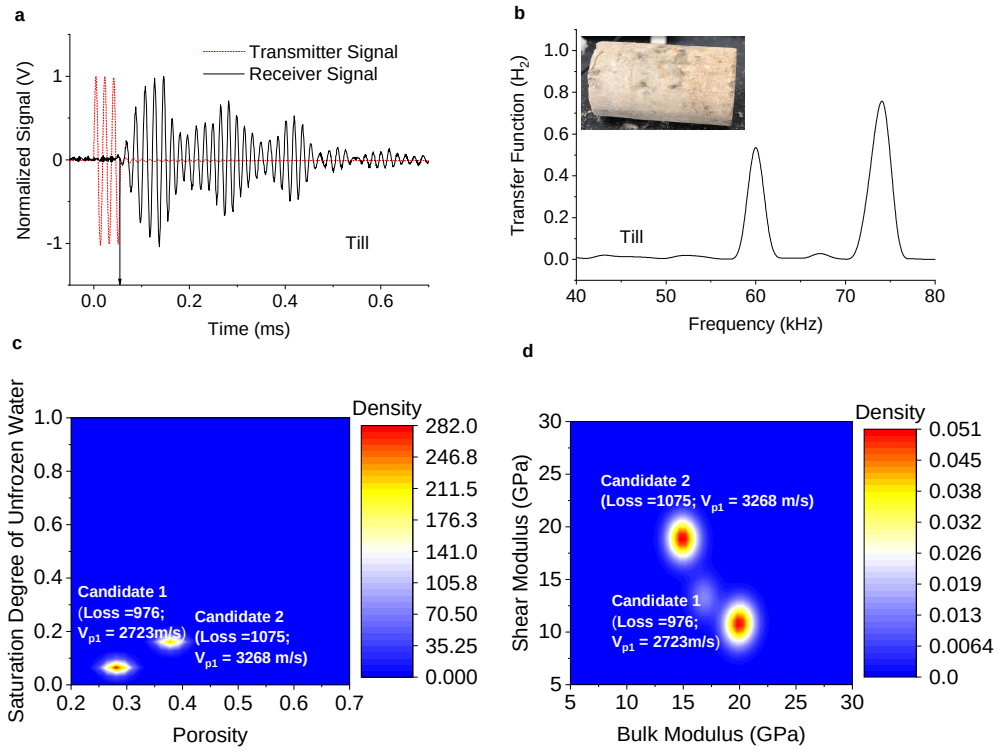

FIGURE 5.9: Ultrasonic measurement and inversion results summary for the till sample (a mix of silt, clay, sand, and limestone) sample at -20°C. **a** Ultrasonic input and output signals in the time domain. **b** Experimental transfer function H_2. **c** Density contour of top two candidate clusters at a subspace between the degree of saturation of unfrozen water and porosity. **d** Density contour of top two candidate clusters at a subspace between the shear modulus and bulk modulus of the solid skeleton.

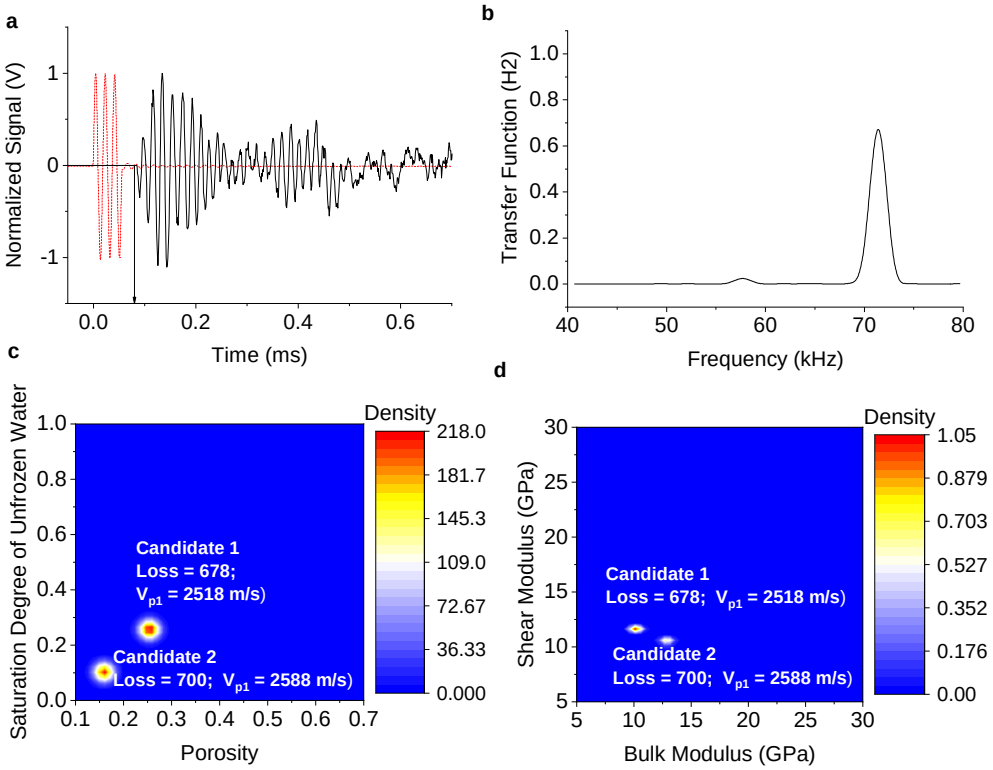

FIGURE 5.10: Ultrasonic measurement and inversion results summary for the silt sample at -2°C. **a** Ultrasonic input and output signals in the time domain. **b** Experimental transfer function H_2. **c** Density contour of top two candidate clusters at a subspace between the degree of saturation of unfrozen water and porosity. **d** Density contour of top two candidate clusters at a subspace between the shear modulus and bulk modulus of the solid skeleton.

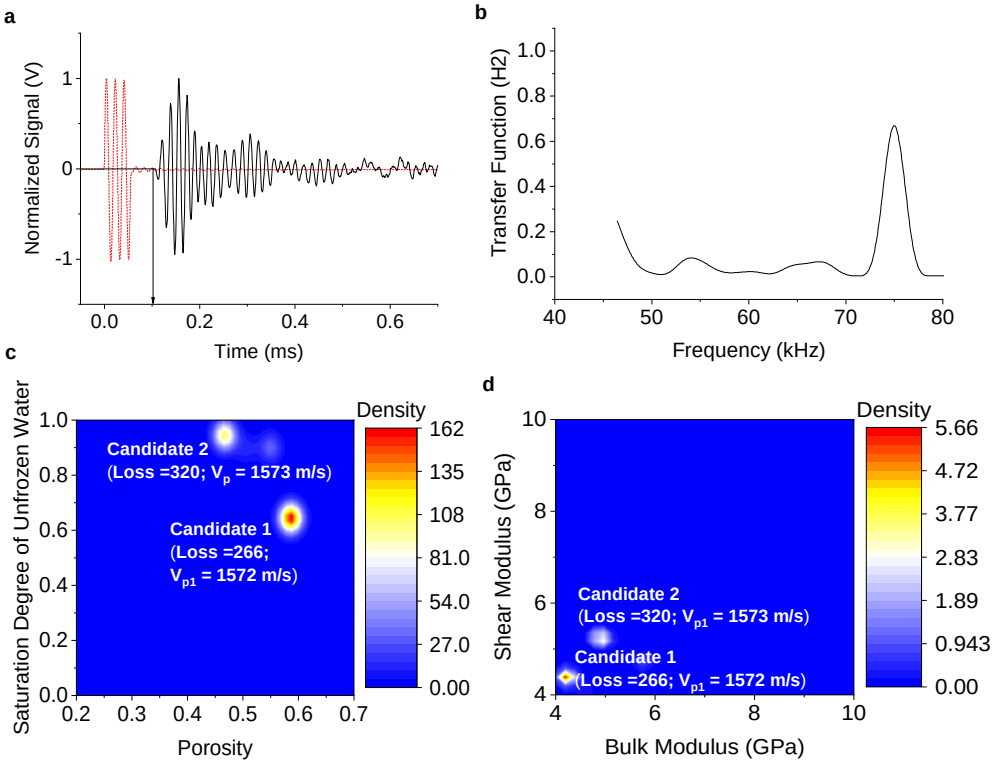

FIGURE 5.11: Ultrasonic measurement and inversion results summary for the new clay sample at -2°C. **a** Ultrasonic input and output signals in the time domain. **b** Experimental transfer function H_2. **c** Density contour of top two candidate clusters at a subspace between the degree of saturation of unfrozen water and porosity. **d** Density contour of top two candidate clusters at a subspace between the shear modulus and bulk modulus of the solid skeleton.

5.5.3 Spectral element multiphase poromechanical model

Kinematics assumptions

The Green-Lagrange strain tensor (ϵ_{ij}) for infinitesimal deformations expressed as displacement vector u_i^1, u_i^2 and u_i^3 for solid skeleton, pore water and pore ice are shown in Equation 5.8.

$$\begin{cases} \epsilon_{ij}^1 = \frac{1}{2}(u_{i,j}^1 + u_{j,i}^1) \\ \epsilon_{ij}^2 = \frac{1}{3}\epsilon_{kk}^2 \delta_{ij} \quad (\epsilon_{kk}^2 = u_{k,k}^2) \\ \epsilon_{ij}^3 = \frac{1}{2}(u_{i,j}^3 + u_{j,i}^3) \end{cases} \tag{5.8}$$

where δ_{ij} is the identity tensor.

The strain tensor of pore water ϵ_{ij}^2 is diagonal since the shear deformation does not exist in pore water component.

Constitutive model

The constitutive models defined as the relation between the stress and strain tensors for solid skeleton, pore water and pore ice are given in Equation 5.9:

$$\begin{cases} \sigma_{ij}^1 = (K_1\theta_1 + C_{12}\theta_2 + C_{13}\theta_3)\delta_{ij} + 2\mu_1 d_{ij}^1 + \mu_{13} d_{ij}^3 \\ \sigma^2 = C_{12}\theta_1 + K_2\theta_2 + C_{23}\theta_3 \\ \sigma_{ij}^3 = (K_3\theta_3 + C_{23}\theta_2 + C_{13}\theta_1)\delta_{ij} + 2\mu_3 d_{ij}^3 + \mu_{13} d_{ij}^1 \end{cases} \tag{5.9}$$

in which σ^1, σ^2 and σ^3 are the effective stress, pore water pressure and ice pressure, respectively. The definition of each term (e.g., K_1, C_{12}, C_{13}, μ_1, μ_{13}, K_2, C_{23}, K_3, μ_3) in Equation 5.9 is given in Appendix A. The term θ_m, d_{ij}^m and ϵ_{ij}^m (m, ranging from 1 to 3, represents the different phases) are defined as follows:

$$\begin{cases} \theta_m = \epsilon_{kk}^m \\ d_{ij}^m = \epsilon_{ij}^m - \frac{1}{3}\delta_{ij}\theta_m \\ \epsilon_{ij}^m = \frac{1}{2}(u_{i,j}^m + u_{j,i}^m). \end{cases}$$

Conservation laws

The momentum conservation considers the acceleration of each component and the existing relative motion of the pore ice and pore water phases with respect to the solid skeleton.

The momentum conservation for the three phases is given by Equation 5.10.

$$\begin{cases} \sigma^1_{ij,j} = \rho_{11}\ddot{u}^1_i + \rho_{12}\ddot{u}^2_i + \rho_{13}\ddot{u}^3_i - b_{12}(\dot{u}^2_i - \dot{u}^1_i) - b_{13}(\dot{u}^3_i - \dot{u}^1_i) \\ \sigma^2_{,i} = \rho_{12}\ddot{u}^1_i + \rho_{22}\ddot{u}^2_i + \rho_{23}\ddot{u}^3_i + b_{12}(\dot{u}^2_i - \dot{u}^1_i) + b_{23}(\dot{u}^2_i - \dot{u}^3_i) \\ \sigma^3_{ij,j} = \rho_{13}\ddot{u}^1_i + \rho_{23}\ddot{u}^2_i + \rho_{33}\ddot{u}^3_i - b_{23}(\dot{u}^2_i - \dot{u}^1_i) + b_{13}(\dot{u}^3_i - \dot{u}^1_i). \end{cases} \tag{5.10}$$

in which the expressions for the density terms (ρ_{ij} or $\bar{\rho}$ in matrix form) and viscous matrix (b_{ij} or $\bar{b}$ in matrix form) are given in Appendix A; $\ddot{u}$ and $\dot{u}$ represent second and first derivative of displacement vectors with respect to time; the subscript i represents the component in r, θ and z direction in cylindrical coordinates.

Through the infinitesimal kinematic assumptions, the stress-strain constitutive model and conversation of momentum, the field equation can be written in the matrix form, as shown in Equation 5.11.

$$\bar{\rho}\begin{bmatrix}\ddot{u}^1_i\\ \ddot{u}^2_i\\ \ddot{u}^3_i\end{bmatrix} + \bar{b}\begin{bmatrix}\dot{u}^1_i\\ \dot{u}^2_i\\ \dot{u}^3_i\end{bmatrix} = \bar{R}\,\nabla\nabla\cdot\begin{bmatrix}u^1_i\\ u^2_i\\ u^3_i\end{bmatrix} - \bar{\mu}\,\nabla\times\nabla\times\begin{bmatrix}u^1_i\\ u^2_i\\ u^3_i\end{bmatrix}. \tag{5.11}$$

in which the matrix $\bar{R}$ and $\bar{\mu}$ are given in Appendix A.

By performing divergence operation ($\nabla\cdot$) and curl operation ($\nabla\times$) on both sides of Equation 5.11, the field equation in the frequency domain can be written as Equation 5.12.

$$\begin{cases} -\bar{\rho}\,\omega^2\,\nabla\cdot\begin{bmatrix}u^1_i\\ u^2_i\\ u^3_i\end{bmatrix} - \bar{b}\,i\,\omega\,\nabla\cdot\begin{bmatrix}u^1_i\\ u^2_i\\ u^3_i\end{bmatrix} = \bar{R}\,\nabla^2\nabla\cdot\begin{bmatrix}u^1_i\\ u^2_i\\ u^3_i\end{bmatrix} \\ -\bar{\rho}\,\omega^2\,\nabla\times\begin{bmatrix}u^1_i\\ u^2_i\\ u^3_i\end{bmatrix} - \bar{b}\,i\,\omega\,\nabla\times\begin{bmatrix}u^1_i\\ u^2_i\\ u^3_i\end{bmatrix} = \bar{\mu}\,\nabla^2\nabla\times\begin{bmatrix}u^1_i\\ u^2_i\\ u^3_i\end{bmatrix} \end{cases} \tag{5.12}$$

Using the Helmholtz decomposition theorem allows us to decompose the displacement field, $\bar{u}$ (equivalent to u_i), into the longitudinal potential and transverse vector components

as follows,

$$\begin{cases} \bar{u}^1 = \nabla\phi_1 + \nabla \times \bar{\psi}_1 \quad and \quad \nabla \cdot \bar{\psi}_1 = 0 \\ \bar{u}^2 = \nabla\phi_2 + \nabla \times \bar{\psi}_2 \quad and \quad \nabla \cdot \bar{\psi}_2 = 0 \\ \bar{u}^3 = \nabla\phi_3 + \nabla \times \bar{\psi}_3 \quad and \quad \nabla \cdot \bar{\psi}_3 = 0 \end{cases} \tag{5.13}$$

By substituting Equation 5.13 into the field equation of motion, Equation 5.12, we obtain two sets of uncoupled partial differential equations relative to the compressional wave P related to the Helmholtz scalar potentials , and to the shear wave S related to the Helmholtz vector potential, respectively (Equation 5.14). In the axi-symmetric condition, only the second components exits in vector $\bar{\psi}$, which is denoted as ψ in the future. It should be mentioned that the field equations in Laplace domain can be easily obtained by replacing ω with $i.s$ ($i^2 = -1$ and s the Laplace variable).

$$\begin{cases} -\bar{\rho}\,\omega^2 \begin{bmatrix} \phi_1 \\ \phi_2 \\ \phi_3 \end{bmatrix} - \bar{b}\,i\,\omega \begin{bmatrix} \phi_1 \\ \phi_2 \\ \phi_3 \end{bmatrix} = \bar{R}\,\nabla^2 \begin{bmatrix} \phi_1 \\ \phi_2 \\ \phi_3 \end{bmatrix} \\ -\bar{\rho}\,\omega^2 \begin{bmatrix} \psi_1 \\ \psi_2 \\ \psi_3 \end{bmatrix} - \bar{b}\,i\,\omega \begin{bmatrix} \psi_1 \\ \psi_2 \\ \psi_3 \end{bmatrix} = \bar{\mu}\,\nabla^2 \begin{bmatrix} \psi_1 \\ \psi_2 \\ \psi_3 \end{bmatrix}. \end{cases} \tag{5.14}$$

Solution for the longitudinal waves (P waves) by eigen decomposition

Equation (5.14) shows that ϕ_1, ϕ_2 and ϕ_3 are coupled in the field equations. The diagonalization of such a matrix is required to decouple the system. Equation (5.14) is then rearranged into Equation (5.15):

$$\nabla^2 \begin{bmatrix} \phi_1 \\ \phi_2 \\ \phi_3 \end{bmatrix} = \underbrace{-\bar{R}^{-1}(\bar{\rho}\omega^2 + \bar{b}\,i\,\omega)}_{\bar{K}} \begin{bmatrix} \phi_1 \\ \phi_2 \\ \phi_3 \end{bmatrix} \tag{5.15}$$

where the $\bar{K}$ matrix can be rewritten using the Eigen decomposition:

$$\bar{K} = \bar{P}\,\bar{D}\,\bar{P}^{-1} \tag{5.16}$$

where $\bar{P}$ is the eigenvector and $\bar{D}$ is the eigenvalue matrix of $\bar{K}$.

By setting $\bar{\phi} = \bar{P}\bar{y}$, where $\bar{y} = [\phi_{p1}, \phi_{p2}, \phi_{p3}]$, we can obtain $\nabla^2 \bar{y} = \bar{D}\bar{y}$. The equation of longitudinal wave has been decoupled. In cylindrical coordinates, the solution for $\bar{y} = [\phi_{p1}, \phi_{p2}, \phi_{p3}]$ is summarized as follows:

$$\begin{cases} \phi_{p1}(r,z) = Ae^{-\sqrt{k^2+D_{11}}\, z} J_0(k\, r) \\ \phi_{p2}(r,z) = Be^{-\sqrt{k^2+D_{22}}\, z} J_0(k\, r) \\ \phi_{p3}(r,z) = Ce^{-\sqrt{k^2+D_{33}}\, z} J_0(k\, r) \end{cases} \tag{5.17}$$

where k is the wave number; coefficient A, B and C will be determined by boundary conditions; D_{11}, D_{22}, and D_{33} are the diagonal components of $\bar{D}$; J_0 is the Bessel function of the first kind. For simplicity, The term $\sqrt{k^2 + D_{11}}$, $\sqrt{k^2 + D_{22}}$ and $\sqrt{k^2 + D_{33}}$ is denoted as k_{p1}, k_{p2} and k_{p3}, respectively.

Now, the P wave potentials can be written as:

$$\begin{Bmatrix} \phi_1 \\ \phi_2 \\ \phi_3 \end{Bmatrix} = \begin{Bmatrix} p_{11} & p_{12} & p_{13} \\ p_{21} & p_{22} & p_{23} \\ p_{31} & p_{32} & p_{33} \end{Bmatrix} \begin{Bmatrix} \phi_{p1} \\ \phi_{p2} \\ \phi_{p3} \end{Bmatrix} \tag{5.18}$$

where p_{ij} are the components for the eigenvector of $\bar{P}$.

Solution for shear waves (S waves)

The solutions for the S wave potentials can be solved in a similar manner. The Equation 5.19 is firstly rearranged into Equation 5.20:

$$-\bar{\rho}\,\omega^2 \begin{bmatrix} \psi_1 \\ \psi_2 \\ \psi_3 \end{bmatrix} - \bar{b}\, i\, \omega \begin{bmatrix} \psi_1 \\ \psi_2 \\ \psi_3 \end{bmatrix} = \bar{\mu}\, \nabla^2 \begin{bmatrix} \psi_1 \\ \psi_2 \\ \psi_3 \end{bmatrix} \tag{5.19}$$

$$\underbrace{-\bar{\rho}\omega^2 - \bar{b}\, i\, \omega}_{\bar{A}} \begin{bmatrix} \psi_1 \\ \psi_2 \\ \psi_3 \end{bmatrix} = \bar{\mu}\, \nabla^2 \begin{bmatrix} \psi_1 \\ \psi_2 \\ \psi_3 \end{bmatrix} \tag{5.20}$$

Since ψ_w can be expressed as a function of ψ_s and ψ_i (shown in Equation 5.21), the Equation 5.20 is further simplified and rearranged into Equation 5.22.

$$\begin{cases} A_{21}\psi_1 + A_{22}\psi_2 + A_{23}\psi_3 = 0 \\ \psi_2 = -\frac{A_{21}\psi_1 + A_{23}\psi_3}{A_{22}} \end{cases} \tag{5.21}$$

$$\nabla^2 \begin{bmatrix} \psi_1 \\ \psi_3 \end{bmatrix} = \underbrace{\begin{bmatrix} \mu_{11} & \mu_{13} \\ \mu_{13} & \mu_{33} \end{bmatrix}^{-1} \bar{C}}_{\bar{N}} \begin{bmatrix} \psi_1 \\ \psi_3 \end{bmatrix}. \tag{5.22}$$

where

$$\bar{C} = \begin{pmatrix} A_{11} - \frac{A_{12}A_{21}}{A_{22}} & A_{13} - \frac{A_{12}A_{23}}{A_{22}} \\ A_{31} - \frac{A_{32}A_{21}}{A_{22}} & A_{33} - \frac{A_{32}A_{23}}{A_{22}} \end{pmatrix}$$

The $\bar{N}$ matrix can be rewritten using the eigen decomposition ($\bar{N} = \bar{Q}\,\bar{G}\,\bar{Q}^{-1}$), where $\bar{Q}$ is the eigenvector and $\bar{G}$ is the eigenvalue matrix of $\bar{N}$. By setting $\bar{\psi} = \bar{Q}\,\bar{y}'$ where $\bar{y}' = [\psi_{s1}, \psi_{i1}]$, we can obtain:

$$\psi_{s1} = Ee^{-\sqrt{k^2+G_{11}}\,z} J_1(k\,r) \tag{5.23}$$

$$\psi_{i1} = Fe^{-\sqrt{k^2+G_{22}}\,z} J_1(k\,r) \tag{5.24}$$

where J_1 is the Bessel function of the first kind with order 1. G_{11} and G_{22} are the diagonal components of matrix $\bar{G}$. For simplicity, the term $\sqrt{k^2+G_{11}}$ and $\sqrt{k^2+G_{22}}$ is denoted as k_{s1} and k_{s2}.

Finally, the solution of S wave potentials can be written as:

$$\begin{Bmatrix} \psi_1 \\ \psi_3 \end{Bmatrix} = \begin{Bmatrix} Q_{11} & Q_{12} \\ Q_{21} & Q_{22} \end{Bmatrix} \begin{Bmatrix} \psi_{s1} \\ \psi_{i1} \end{Bmatrix} \tag{5.25}$$

where Q_{ij} are the components for eigenvector of $\bar{Q}$.

Layer element with finite thickness

By including both incident wave and reflected wave, the potentials for a layer with finite thickness can be written in Equation 5.26:

$$\begin{bmatrix} u_{r1}^1 \\ u_{z1}^1 \\ u_{z1}^2 \\ u_{r1}^3 \\ u_{z1}^3 \\ u_{r2}^1 \\ u_{z2}^1 \\ u_{z2}^2 \\ u_{r2}^3 \\ u_{z2}^3 \end{bmatrix} = \begin{bmatrix} & & \\ & S_1 & \\ & & \end{bmatrix} \begin{bmatrix} A_1 \\ B_1 \\ C_1 \\ E_1 \\ F_1 \\ A_2 \\ B_2 \\ C_2 \\ E_2 \\ F_2 \end{bmatrix} \tag{5.26}$$

where the components of S_1 is given in Appendix B; the subscript 1 and 2 represent the nodes for the upper and lower layer, respectively. The coefficient A to F is determined by the boundary condition.

The matrix of effective stress, pore water pressure and pore ice pressure in the frequency domain is shown in Equation 5.27 in which the components for matrix S_2 can be found in the Appendix B.

$$\begin{bmatrix} \sigma_{r1}^1 \\ \sigma_{z1}^1 \\ p_1 \\ \sigma_{r1}^3 \\ \sigma_{z1}^3 \\ \sigma_{r2}^1 \\ \sigma_{z2}^1 \\ p_2 \\ \sigma_{r2}^3 \\ \sigma_{z2}^3 \end{bmatrix} = \begin{bmatrix} & & \\ & S_2 & \\ & & \end{bmatrix} \begin{bmatrix} A_1 \\ B_1 \\ C_1 \\ E_1 \\ F_1 \\ A_2 \\ B_2 \\ C_2 \\ E_2 \\ F_2 \end{bmatrix} \tag{5.27}$$

According to the Cauchy stress principle, the traction force (T) is taken as the dot product between the stress tensor and the unit vector along the outward normal direction. Due to the convection that the upward direction is negative, the upper boundary becomes

negative. Similarly, to make the sign consistent, the N matrix is applied to matrix $S_2 \cdot S_1^{-1}$. In the future, the matrix $N \cdot S_2 \cdot S_1^{-1}$ will be denoted as the G matrix.

$$\begin{bmatrix} T_{r1}^1 \\ T_{z1}^1 \\ T_1 \\ T_{r1}^3 \\ T_{z1}^3 \\ T_{r2}^1 \\ T_{z2}^1 \\ T_2 \\ T_{r2}^3 \\ T_{z2}^3 \end{bmatrix} = \begin{bmatrix} -\sigma_{r1}^1 \\ -\sigma_{z1}^1 \\ -p_1 \\ -\sigma_{r1}^3 \\ -\sigma_{z1}^3 \\ \sigma_{r2}^1 \\ \sigma_{z2}^1 \\ p_2 \\ \sigma_{r2}^3 \\ \sigma_{z2}^3 \end{bmatrix} = \underbrace{N \cdot S_2 \cdot S_1^{-1}}_{G} \cdot \begin{bmatrix} u_{r1}^1 \\ u_{z1}^1 \\ u_{z1}^2 \\ u_{r1}^3 \\ u_{z1}^3 \\ u_{r2}^1 \\ u_{z2}^1 \\ u_{z2}^2 \\ u_{r2}^3 \\ u_{z2}^3 \end{bmatrix} \tag{5.28}$$

where

$$N = \begin{bmatrix} -1 & 0 & 0 & 0 & 0 & 0 & 0 & 0 & 0 & 0 \\ 0 & -1 & 0 & 0 & 0 & 0 & 0 & 0 & 0 & 0 \\ 0 & 0 & -1 & 0 & 0 & 0 & 0 & 0 & 0 & 0 \\ 0 & 0 & 0 & -1 & 0 & 0 & 0 & 0 & 0 & 0 \\ 0 & 0 & 0 & 0 & -1 & 0 & 0 & 0 & 0 & 0 \\ 0 & 0 & 0 & 0 & 0 & 1 & 0 & 0 & 0 & 0 \\ 0 & 0 & 0 & 0 & 0 & 0 & 1 & 0 & 0 & 0 \\ 0 & 0 & 0 & 0 & 0 & 0 & 0 & 1 & 0 & 0 \\ 0 & 0 & 0 & 0 & 0 & 0 & 0 & 0 & 1 & 0 \\ 0 & 0 & 0 & 0 & 0 & 0 & 0 & 0 & 0 & 1 \end{bmatrix} \tag{5.29}$$

The radial component of the applied load decomposed from the external load is defined as:

$$f_r(r) = \sum_{m=1}^{\infty} F_m J_0(k_m r) \tag{5.30}$$

where

$$F_m(m) = \frac{2r_0 \sin(r_0 k_m)}{r_\infty^2 k_m J_1^2(r_\infty k_m)}$$

where r_0 is the radius of the contacting area of the ultrasonic transmitter; n is the total mode number; r_∞ is the diameter of the soil sample.

Chapter 6

Seismic physics-based characterization of permafrost sites using surface waves

Abstract

The adverse effects of climate warming on the built environment in (sub)arctic regions are unprecedented and accelerating. According to Canada's Changing Climate Report (2019), in the Arctic regions, temperatures have been warming at approximately twice the rate of the rest of the world. This drastic trend in climate warming will no doubt affect permafrost temperatures and conditions, continued rise in greenhouse gas emissions, and further adding to the high cost of development in northern regions. Planning and design of climate-resilient northern infrastructure as well as predicting deterioration of permafrost from climate model simulations require characterizing permafrost sites accurately and efficiently. Here, we propose a novel algorithm for analysis of surface waves to quantitatively estimate the physical and mechanical properties of a permafrost site. We show the existence of two types of Rayleigh waves (R1 and R2; R1 travels relatively faster than R2). The R2 wave velocity is highly sensitive to the physical properties (e.g., unfrozen water content, ice content, and porosity) of permafrost or soil layers while it is less sensitive to their mechanical properties (e.g., shear modulus and bulk modulus). The R1 wave velocity, on the other hand, depends strongly on the soil type and mechanical

Liu H., Maghoul P., Shalaby A., 2021. *Seismic physics-based characterization of permafrost sites using surface waves*, The Cryosphere Discuss. [preprint], in Review.
https://doi.org/10.5194/tc-2021-219.

properties of permafrost or soil layers. In-situ surface wave measurements revealed the experimental dispersion relations of both types of Rayleigh waves from which relevant properties of a permafrost site can be derived by means of our proposed hybrid inverse and multi-phase poromechanical approach. Our study demonstrates the potential of surface wave techniques coupled with our proposed data-processing algorithm to characterize a permafrost site more accurately. Our proposed technique can be used in early detection and warning systems to monitor infrastructure impacted by permafrost-related geohazards, and to detect the presence of layers vulnerable to permafrost carbon feedback and emission of greenhouse gases into the atmosphere.

6.1 Introduction

Permafrost is defined as the ground that remains at or below 0°C for at least two consecutive years. The upper layer of the ground in permafrost areas, termed as the active layer, may undergo seasonal thaw and freeze cycles. The thickness of the active layer depends on local geological and climate conditions such as vegetation, soil composition, air temperature, solar radiation and wind speed.

Within the permafrost, the distribution of ice formations is highly variable. Ground ice can be present under distinctive forms including (1) pore ice, (2) segregated ice, and (3) ice-wedge (Couture and Pollard, 2017; Mackay, 1972). Pore water, which fills or partially fills the pore space of the soil, freezes in-place when the temperature drops below the freezing point (Porter and Opel, 2020). On the other hand, segregated ice is formed when water migrates to the freezing front and it can cause excessive deformations in frost-susceptible soils. Frost-susceptible soils, e.g. silty or silty clay soils, have relatively high capillary potential and moderate intrinsic permeability. During the winter months, ground ice expands as the ground freezes, and forms cracks in the subsurface (Liljedahl, Boike, Daanen, Fedorov, Frost, Grosse, Hinzman, Iijma, Jorgenson, Matveyeva, et al., 2016). Ice wedges are large masses of ice formed over many centuries by repeated frost cracking and ice vein growth.

Design and construction of structures on permafrost normally follow one of two broad principles which are based on whether the frozen foundation soil in ice-rich permafrost is thaw-stable or thaw-unstable. This distinction is determined by the amount of ice content within the permafrost. Ice-rich permafrost contains ice in excess of its water content at saturation. The construction on thaw-unstable permafrost is challenging and

requires remedial measures since upon thawing, permafrost will experience significant thaw-settlement and suffer loss of strength to values significantly lower than that for similar material in an unfrozen state. Consequently, remedial measures for excessive soil settlements or design of new infrastructure in permafrost zones affected by climate warming would require a reasonable estimation of the ice content within the permafrost (frozen soil). The rate of settlement relies on the mechanical properties of the foundation permafrost at the construction site. Furthermore, a warming climate can accelerate the microbial breakdown of organic carbon stored in permafrost and can increase the release of greenhouse gas emissions, which in return would accelerate climate change (Schuur, McGuire, Schädel, Grosse, Harden, Hayes, Hugelius, Koven, Kuhry, Lawrence, et al., 2015).

Several in-situ techniques have been employed to characterize or monitor permafrost conditions. For example, techniques such as remote sensing (Witharana, Bhuiyan, Liljedahl, Kanevskiy, Epstein, Jones, Daanen, Griffin, Kent, and Jones, 2020; Bhuiyan, Witharana, and Liljedahl, 2020; Zhang, Witharana, Liljedahl, and Kanevskiy, 2018), and ground penetrating radar (GPR) (Munroe, Doolittle, Kanevskiy, Hinkel, Nelson, Jones, Shur, and Kimble, 2007; Christiansen, Matsuoka, and Watanabe, 2016; Williams, Haltigin, and Pollard, 2011) have been used to detect ice-wedge formations within the permafrost layers. Also, electrical resistivity tomography (ERT) has been extensively used to qualitatively detect pore-ice or segregated ice in permafrost based on the correlation between the electrical conductivity and the physical properties of permafrost (e.g., unfrozen water content and ice content) (Glazer, Dobiński, Marciniak, Majdański, and Błaszczyk, 2020; Hauck, 2013; Scapozza, Lambiel, Baron, Marescot, and Reynard, 2011; You, Yu, Pan, Wang, and Guo, 2013). The apparent resistivity measurement by ERT is higher in areas having high ice contents (You, Yu, Pan, Wang, and Guo, 2013); however, at high resistivity gradients, the inversion results become less reliable, especially for the investigation of permafrost base (Hilbich, Marescot, Hauck, Loke, and Mäusbacher, 2009; Marescot, Loke, Chapellier, Delaloye, Lambiel, and Reynard, 2003). Furthermore, in ERT investigations, the differentiation between ice and certain geomaterials can be highly uncertain due to their similar electrical resistivity properties (Kneisel, Hauck, Fortier, and Moorman, 2008). GPR has been also used for mapping the thickness of the active layer; however, its application is limited to a shallow penetration depth in conductive layers due to the signal attenuation and high electromagnetic noise in ice and water (Kneisel, Hauck, Fortier, and Moorman, 2008). It is worth mentioning that none of the above-mentioned methods characterizes the mechanical

properties of permafrost layers.

Non-destructive seismic testing, including multi-channel analysis of surface waves (MASW) (Dou and Ajo-Franklin, 2014; Glazer, Dobiński, Marciniak, Majdański, and Błaszczyk, 2020), passive seismic test with ambient seismic noise (James, Knox, Abbott, Panning, and Screaton, 2019; Overduin, Haberland, Ryberg, Kneier, Jacobi, Grigoriev, and Ohrnberger, 2015), seismic reflection (Brothers, Herman, Hart, and Ruppel, 2016), and seismic refraction method (Wagner, Mollaret, Günther, Kemna, and Hauck, 2019) have been previously employed to map the permafrost layer based on the measurement of shear wave velocity. In the current seismic testing practice, it is commonly considered that the permafrost layer (frozen soil) is associated with a higher shear wave velocity due to the presence of ice in comparison to unfrozen ground. However, the porosity and soil type can also significantly affect the shear wave velocity (Liu, Maghoul, and Shalaby, 2020b). In other words, a relatively higher shear wave velocity could be associated to an unfrozen soil layer with a relatively lower porosity or stiffer solid skeletal frame, and not necessarily related to the presence of a frozen soil layer. Therefore, the detection of permafrost layer and permafrost base from only the shear wave velocity may lead to inaccurate and even misleading interpretations.

Here, we present a hybrid inverse and multi-phase poromechanical approach for in-situ characterization of permafrost sites using surface wave techniques. In our method, we quantify the physical properties such as ice content, unfrozen water content, and porosity as well as the mechanical properties such as the shear modulus and bulk modulus of permafrost or soil layers. Through the mechanical properties of the solid skeleton frame, we can also predict the soil type and the sensitivity of the permafrost layer to permafrost carbon feedback and emission of greenhouse gases to the atmosphere. We also determine the depth of the permafrost table and permafrost base. The role of two different types of Rayleigh waves in characterizing the permafrost is presented based on an MASW seismic investigation in a field located at SW Spitsbergen, Norway. Multiphase poromechanical dispersion relations are developed for the interpretation of the experimental seismic measurements at the surface based on the spectral element method. Our results demonstrate the potential of seismic surface wave testing accompanied with our proposed hybrid inverse and poromechanical dispersion model for the assessment and quantitative characterization of permafrost sites.

6.2 Methods

6.2.1 Methodology overview

Figure 6.1 shows the overview of the proposed hybrid inverse and poromechanical approach for in-situ characterization of permafrost sites. We can obtain the experimental dispersion relations for R1 and R2 Rayleigh wave types from the surface wave measurements. Then, we use the experimental dispersion of R2 waves to characterize the physical properties of the layers. A random sample is initially generated to ensure that soil parameters are not affected by a local minimum. Then the forward three-phase poromechanical dispersion solver is used to compute the theoretical dispersion relation of the R2 wave. Therefore, we can rank samples based on the L_2 norm between the experimental and theoretical dispersion relations. Based on the ranking of each sample, the Voronoi polygons (Neighborhood sampling method) are used to generate better samples with a smaller objective function until the solution converges. We can select the best samples with the minimum loss function and obtain the most likely physical properties and thickness of the active layer, permafrost layer, and unfrozen ground. After obtaining the physical properties, the mechanical properties can be derived based on the dispersion relation of the R1 wave mode in a similar manner, as summarized in Figure 6.1h (optimization variables exclude the physical properties and the thickness of each layer in this process).

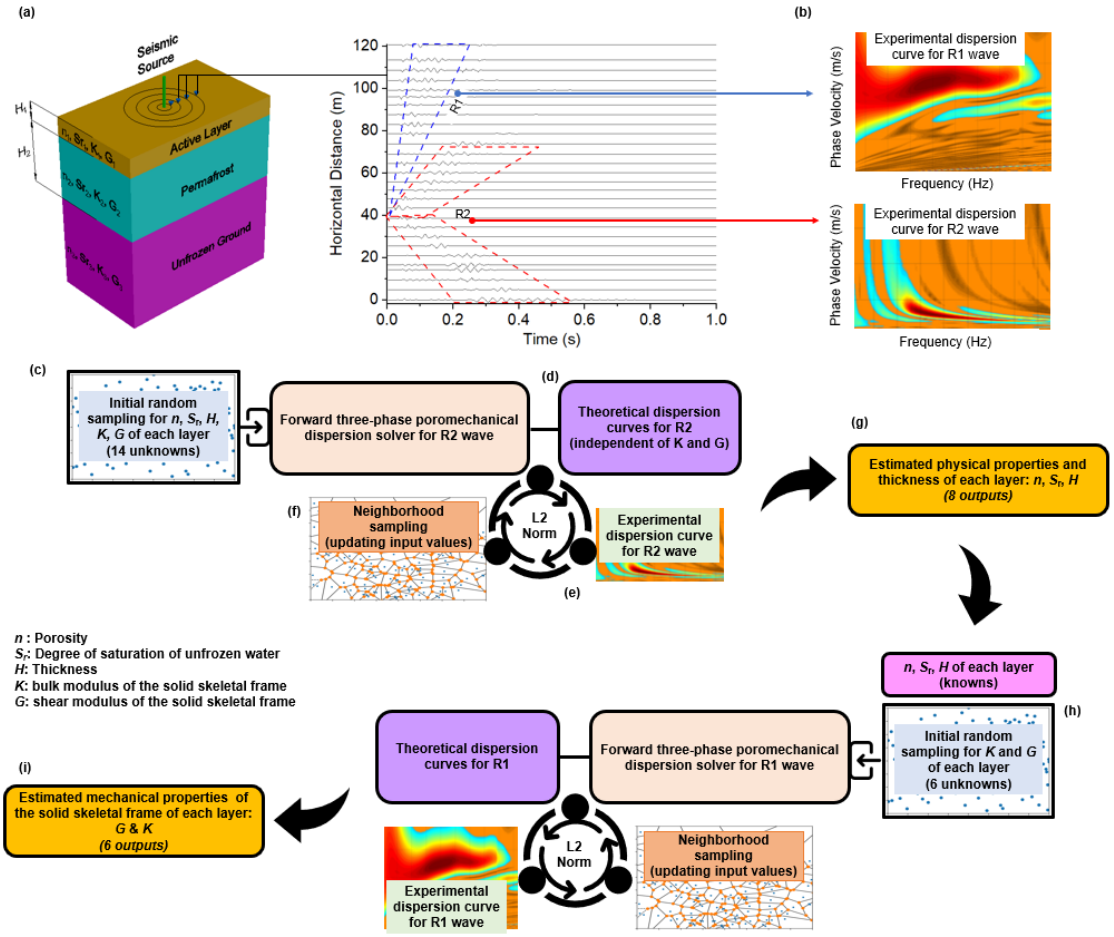

FIGURE 6.1: **a** A general schematic of the MASW test at a permafrost site **b** Dispersion relations of R1 and R2 waves obtained from the experimental measurements. **c** Initial guess of the physical properties of active layer, permafrost layer and unfrozen ground. **d** Calculation of the theoretical dispersion relation of R2 wave using the forward three-phase poromechanical dispersion solver. **e** Solution ranking based on L_2 norm for R2 dispersion relations (experimental vs theoretical) using the hybrid inverse and poromechanical approach. **f** Neighborhood sampling for the reduction of L_2 norm using the hybrid inverse and poromechanical approach. **g** Select the best samples based on the minimum L_2 norm and obtain the physical properties and thickness for each layer. **h** Repeat the steps for dispersion inversion (c-f) of R1 dispersion relation to derive the mechanical properties of active layer, permafrost layer and unfrozen ground. **i** Select the best samples based on the minimum L_2 norm and obtain the mechanical properties.

6.2.2 Rayleigh wave dispersion relations

We consider the frozen soil specimen to be composed of three phases: solid skeletal frame, pore-water, and pore-ice. Through the infinitesimal kinematic assumption (Equation 6.3), the stress-strain constitutive model (Carcione and Seriani, 2001) (Equation 6.4), and the conservation of momentum (Equation 6.5), the field equations can be written in the matrix form (Equation 6.6). The matrix $\bar{\rho}$, $\bar{b}$, $\bar{R}$ and $\bar{\mu}$ are given in Section 6.5.4. The field equations can also be written in the frequency domain by performing convolution with $e^{i\omega t}$. The field

equations in the Laplace domain are obtained by replacing ω with $i \cdot s$ ($i^2 = -1$ and s the Laplace variable).

To obtain the spectral element solution, the Helmholtz decomposition is used to decouple the P waves (P1, P2, and P3) and S waves (S1 and S2). The displacement vector ($\bar{u}$) is composed of the P wave scalar potentials ϕ and S wave vector potentials $\bar{\psi} = (\psi_r, \psi_\theta, \psi_z)$. Since P waves exist in the solid skeleton, pore-ice and pore-water phases, three P wave potentials are used, including ϕ_s, ϕ_i and ϕ_f (Equation 6.8). The detailed steps for obtaining the closed-form solutions for P waves and S waves using the Eigen decomposition are summarized in Section 6.5.4. After obtaining the stiffness matrix for each layer, the global stiffness matrix, H, can be assembled by applying the continuity conditions at layer interfaces. The stiffness assembling method is shown in Figure 6.2.

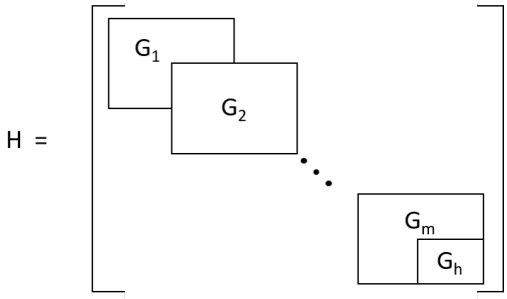

FIGURE 6.2: Construction of the global stiffness matrix

The dispersion relation is obtained by setting a zero stress condition at the surface ($z = 0$). To obtain the non-trivial solution, the determinant of the global stiffness matrix has to be zero, as expressed in Equation 6.1 (Zomorodian and Hunaidi, 2006).

$$\det H(\omega, k) = 0. \tag{6.1}$$

The global stiffness matrix, $H(\omega, k)$, is a function of angular frequency ω and wavenumber k. For a constant frequency, the value of the wavenumber can be determined when the determinant of the global stiffness matrix is zero. The dispersion curve is also commonly displayed as frequency versus phase velocity, $v = \frac{\omega}{k}$. The different wavenumbers determined at a given frequency correspond to dispersion curves of different modes. To extract the fundamental mode of the R1 wave, the velocities of P1 wave and S1 wave are calculated first for the given physical properties and mechanical properties of each layer. The global stiffness matrix for the R1 wave can be decomposed into the components related only to the P1 and S1 wave velocities. This is viable since we have proved that the R1 wave is generated by the interaction between the P1 and S1 waves. This approach avoids the

difficulties in differentiating the higher modes of R2 wave from the fundamental mode of the R1 wave. The detailed root search method has been documented in Liu, Maghoul, Shalaby, Bahari, and Moradi (2020).

6.2.3 Inversion

The aim function is defined as the Euclidean norm between the experimental and numerical results of the dispersion relations. The problem is formulated in Equation 6.2:

$$\begin{cases} minimize\ f(\boldsymbol{x}) = \frac{1}{2}\sum_{i=1}^{N}(y_i - \bar{y}_i(\boldsymbol{x}))^2 \\ subject\ to\ a_i \leq x_i \leq b_i,\ i\ = 1,\ \ldots, m \end{cases} \tag{6.2}$$

where f is the objective function; $\boldsymbol{x} = (x_1, x_2, ...x_m)$ is the optimization variable (e.g., porosity, and degree of saturation of unfrozen water, bulk modulus and shear modulus of solid skeleton frame as well as thickness of each layer); the constant a_i and b_i are limits or bounds for each variable; m is the total number of variables; y and $\bar{y}$ are the numerical and experimental dispersion relations for the R1 or R2 waves.

Here, we used the neighborhood algorithm that benefits from the Voronoi cells to search the high-dimensional parameter space and reduce overall cost function (Sambridge, 1999). The algorithm contains only two tuning parameters. The neighborhood sampling algorithm includes the following steps: a random sample is initially generated to ensure the soil parameters are not affected by the local minima. Based on the ranking of each sample, the Voronoi polygons are used to generate better samples with a smaller objective function. The optimization parameters are scaled between 0 and 1 to properly evaluate the Voronoi polygon limit. After generating a new sample, the distance calculation needs to be updated. Through enough iterations of these processes, the aim function can be reduced. The detailed description of the neighborhood algorithm is described by Sambridge (1999).

6.3 Results

6.3.1 Fast and slow Rayleigh wave dispersion relations.

From a poromechanical point of view, permafrost (frozen soil) is a multi-phase porous medium that is composed of a solid skeletal frame and pores filled with water and ice with different proportions. Here, we analyze the seismic wave propagation in permafrost

based on the three-phase poroelastodynamic theory. Three types of P wave (P1, P2 and P3) and two types of S wave (S1, S2) coexist in three-phase frozen porous media (Carcione, Gurevich, and Cavallini, 2000; Carcione and Seriani, 2001; Carcione, Santos, Ravazzoli, and Helle, 2003). The P1 and S1 waves are strongly related to the longitudinal and transverse waves propagating in the solid skeletal frame, respectively, but are also dependent on the interactions with pore ice and pore water (Carcione and Seriani, 2001). The P2 and S2 waves propagate mainly within pore ice (Leclaire, Cohen-Ténoudji, and Aguirre-Puente, 1994). Similarly, the P3 wave is due to the interaction between the pore water and the solid skeletal frame. The velocity of different types of P waves and S waves is provided in Section 6.5.1.

Here a uniform frozen soil layer is used to show the propagation of different types of P and S waves and subsequently the formation of Rayleigh waves (R1 and R2) at the surface. It is assumed that an impulse load with a dominant frequency of 100 Hz is applied at the ground surface. The wave propagation analysis was performed in clayey soils by assuming a porosity (n) of 0.5, a degree of saturation of unfrozen water (Sr) of 50%, a bulk modulus (K) of 20.9 GPa and a shear modulus (G) of 6.85 GPa for the solid skeletal frame (Helgerud, Dvorkin, Nur, Sakai, and Collett, 1999). The velocities of the P1 and P2 waves are calculated as 2,628 m/s and 910 m/s, respectively, based on the relations given in Section 6.5.1. The velocity of P3 wave (16 m/s) is relatively insignificant in comparison to P1 and P2 wave velocities. Similarly, the velocities of the S1 and S2 waves are calculated as 1,217 m/s and 481 m/s, respectively. Accordingly, the observed displacements measured at the ground surface with an offset from the impulse load ranging from 0 to 120 m are illustrated in Figure 6.3a. Figure 6.3b and 6.3c illustrate the appearance of two types of Rayleigh waves (R1 and R2) in a three-phase permafrost subsurface at 70 ms and 100 ms, respectively. The animation in Section 6.5.2 show the propagation of P, S, and R waves in the domain. Our results convincingly demonstrate that R1 waves appear due to the interaction of P1 and S1 waves. The phase velocity of R1 waves is slightly slower than the phase velocity of S1 waves. Similarly, the phase velocity of R2 waves is also slightly slower than the phase velocity of S2 waves. Briefly, the order of phase velocities of different waves propagating within the domain is as follows: P1>P2>S1>R1>S2>R2>P3. The seismic measurements shown in Figure 6.3a are indeed a combination of both R1 and R2 waves.

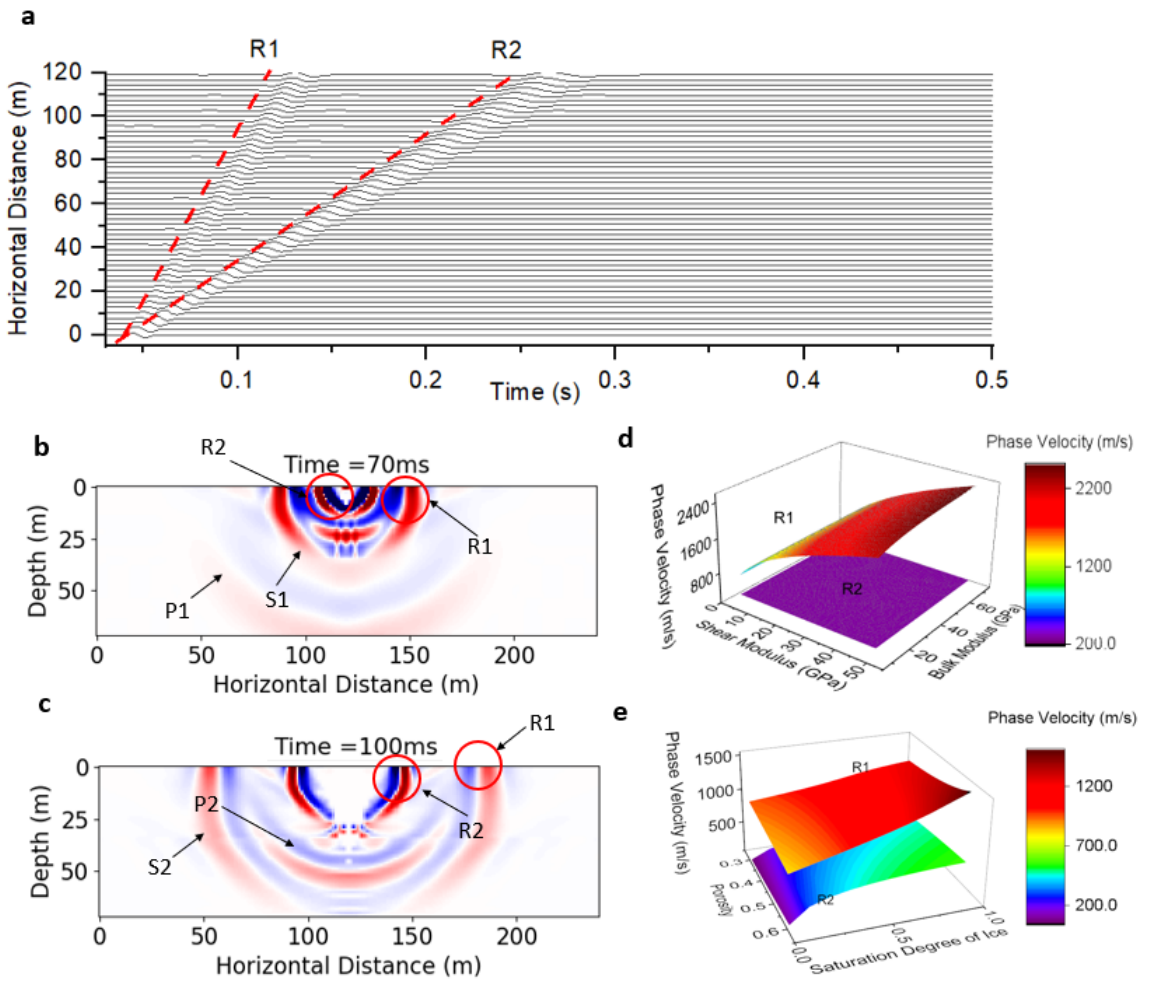

FIGURE 6.3: **a** Theoretical time-series measurements for R1 and R2 Rayleigh waves at the ground surface **b** Displacement contour at time 70 ms. **c** Displacement contour at time 100 ms with the labeled R1 and R2 Rayleigh waves. **d** Effect of shear modulus and bulk modulus of the solid skeletal frame on phase velocity of R1 and R2 waves. **e** Effect of degree of saturation of ice on the phase velocity of R1 and R2 waves.

The phase velocities of R1 and R2 waves are a function of physical properties (e.g., degree of saturation of unfrozen water, degree of saturation of ice, and porosity) and mechanical properties of the solid skeletal frame (e.g., bulk modulus and shear modulus). Figure 6.3d illustrates the effect of shear modulus and bulk modulus of the solid skeletal frame on the phase velocity of R1 and R2 waves. Similarly, Figure 6.3e illustrates the effect of porosity and degree of saturation of ice on the phase velocity of R1 and R2 waves. It can be seen that the phase velocity of the R1 wave is mostly sensitive to the shear modulus of the solid skeletal frame; it is also dependent on the bulk modulus, porosity, and degree of saturation of ice. On the other hand, the phase velocity of the R2 wave is almost independent of the mechanical properties of the solid skeletal frame (Figure 6.3d),

while it is strongly affected by the porosity and degree of saturation of ice (Figure 6.3e).

Our results also show that an increase in the degree of saturation of ice leads to an increase in the phase velocity of both types of Rayleigh waves. An increase in porosity leads to an increase in the phase velocity of R2. However, an increase in porosity may lead to either a decrease or an increase in the phase velocity of R1 wave, depending on the level of the degree of saturation of ice. Hence, we use the phase velocity of R2 waves identified by processing the seismic surface wave measurements to characterize the physical properties (e.g., porosity, degree of saturation of ice or degree of saturation of unfrozen water) of permafrost or soil layers.

6.3.2 In-situ case study in permafrost characterization.

The case study site is located at the Fuglebekken coastal area in SW Spitsbergen, Svalbard (77°00'30"N and 15°32'00"E). The study area has a a thick layer of unconsolidated sediments that are suitable for near-surface geophysical investigations (Glazer, Dobiński, Marciniak, Majdański, and Błaszczyk, 2020). The unconsolidated sedimentary rock contains a high proportion of pore spaces; consequently, they can accumulate a large volume of pore-water or pore-ice. From meteorological records, the mean annual air temperature (MAAT) at the testing site was historically below the freezing point, but more recently and due to a trend of climate warming, the MAAT recorded in 2016 is approaching 0°C (Glazer, Dobiński, Marciniak, Majdański, and Błaszczyk, 2020). Glazer, Dobiński, Marciniak, Majdański, and Błaszczyk (2020) performed both seismic surveys (MASW test) and electrical resistivity investigations at the site in October 2017 to study the evolution and formation of permafrost considering surface watercourses and marine terrace. The MASW test was performed by using the geophone receivers distributed at 2 m spacing. Figure 6.4a shows the test site. Figure 6.4b illustrates the collected original seismic measurements at distances between 0 m and 120 m (hereafter referred to Section 1). The R1 and R2 Rayleigh waves are identified by visual inspection to obtain the experimental dispersion relations (Figure 6.4c and 6.4d). The phase velocity of R1 wave increases with frequency from 24 Hz to 80 Hz. The phase velocity of R2 wave decreases with frequency in the span of 18 Hz to 32 Hz.

In our simulations, the permafrost site is modeled as a three-layered system, consisting of an active layer at the surface followed by two permafrost layers. The ERT results reported by Glazer, Dobiński, Marciniak, Majdański, and Błaszczyk (2020) proved that the active layer is almost completely unfrozen during the MASW testing performed in September. The degree of saturation of unfrozen water is considered 100% for the active

layer in our study. The temperature of the permafrost layer remains below or at 0°C year round, but the volumetric ice content of the test site is unknown. Therefore, in our simulation, the degree of saturation of unfrozen water in the permafrost layer is considered to be between 1% and 85% to be conservative. The porosity of all three layers is distributed between 0.1 and 0.7. We previously showed that the dispersion relation of the R2 wave is strongly dependent on the physical properties (e.g., porosity and degree of saturation of unfrozen water). Hence, the R2 dispersion relation (Figure 6.4d) is used first to determine the most probable distributions of porosity and degree of saturation of unfrozen water with depth. The other physical properties such as degree of saturation of ice, volumetric water content and volumetric ice content can also be obtained by knowing porosity and degree of saturation of unfrozen water.

The mechanical properties of the solid skeletal frame in each layer are then obtained using the R1 wave dispersion relation. The mechanical properties can be then used to determine whether the permafrost site is ice-rich. In fact, the direct detection of the thin ice lenses using low frequency seismic waves is highly impossible due to the mismatch between the thickness of the ice segregation layers and the wavelength generated in seismic tests. However, the mechanical properties of permafrost reveal the mineral composition of the soil and soil type, which is valuable in the classification of ice-rich permafrost or even detection of whether the permafrost layer is prone to greenhouse gases carbon dioxide and methane emission to the atmosphere.

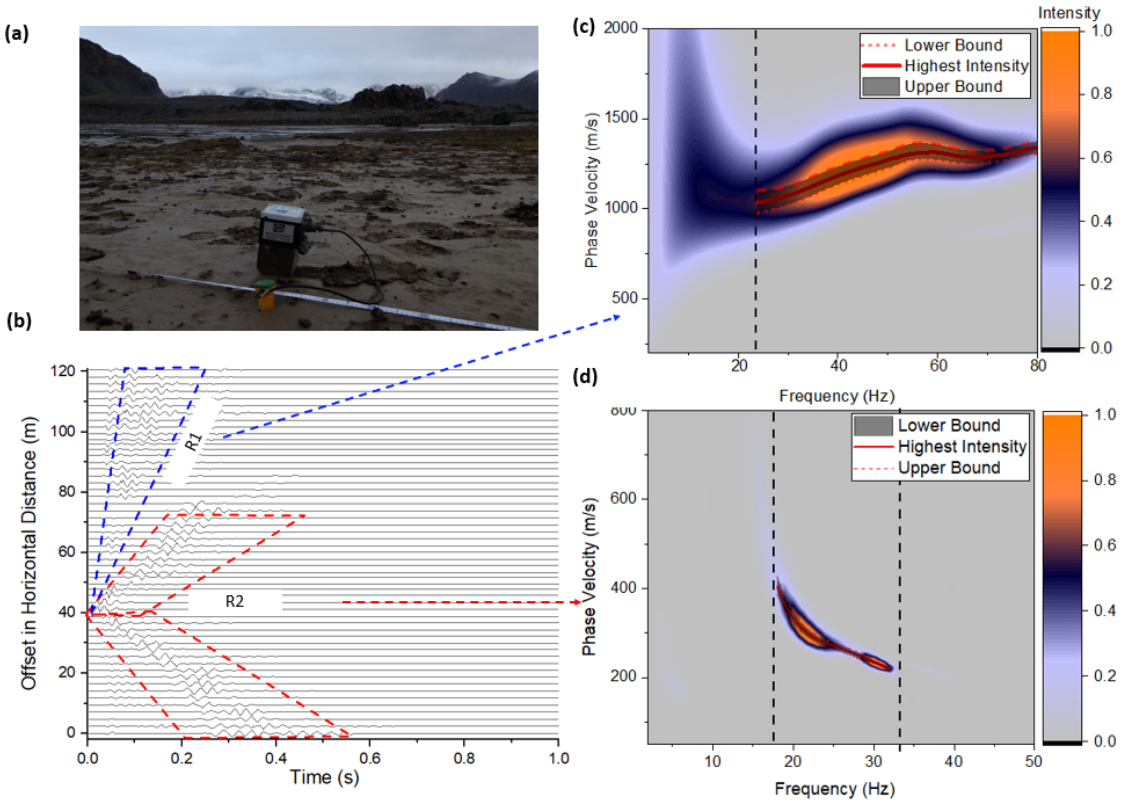

FIGURE 6.4: Surface wave measurement in Section 1 (from 0 m to 120 m). **a** Study area in Holocene, Fuglebekken, SW Spitsbergen. **b** Waveform data from the measurements at different offsets in horizontal distance. **c** Experimental dispersion image for R1 wave. **d** Experimental dispersion image for R2 wave

Figure 6.5a shows the probabilistic distribution of the degree of saturation of unfrozen water with depth in Section 1. Our results show that the active layer has a thickness of about 1.5 m. The predicted permafrost layer (second layer) has a nearly 32% of degree of saturation of unfrozen pore water. Given the high ice-to-water ratio, we therefore interpret the permafrost is currently in a stable frozen state. Figure 6.5b shows the degree of saturation of ice with depth. The degree of saturation of ice in the permafrost layer (second layer) is about 68%. Figure 6.5c illustrates the porosity distribution with depth. The porosity is around 0.61 in the first layer (active layer), 0.44 in the second layer (permafrost) and 0.56 in the third layer (permafrost). Figure 6.5d and 6.5e show the predicted mechanical properties of the solid skeletal frame (shear modulus and bulk modulus) in each layer. The predicted shear modulus and bulk modulus for the solid skeletal frame in the permafrost layer (second layer) are about 13.0 GPa and 12.7 GPa, which are in the range for silty-clayey soils (Vanorio, Prasad, and Nur, 2003). Figure 6.5f and 6.5g show the comparison between the numerical and experimental dispersion relations for R2 and R1 waves, respectively. The numerical predictions are sufficiently close to the experimental dispersion curves for

both R1 and R2 waves.

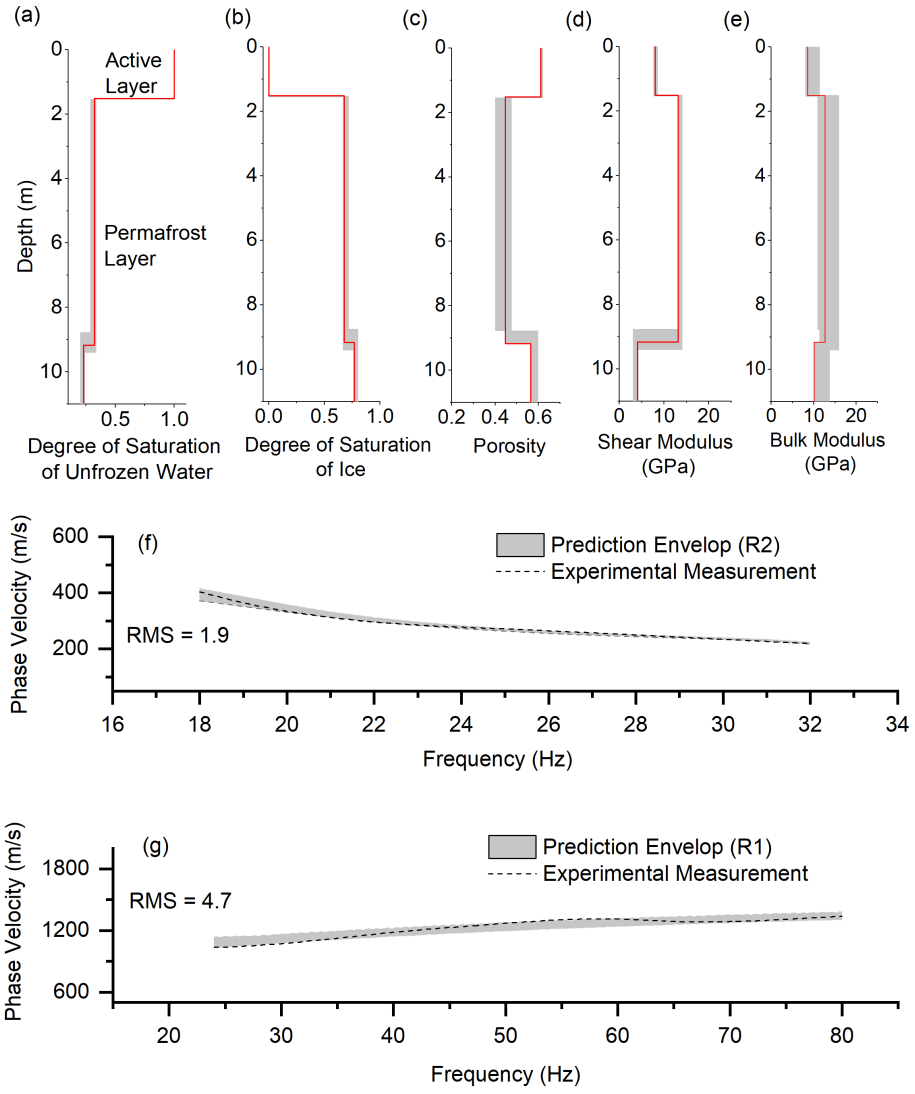

FIGURE 6.5: Surface wave inversion results for Section 1: 0m to 120m. **a** Degree of saturation of unfrozen water, **b** Degree of saturation of ice, **c** Porosity distribution, **d** Shear modulus of solid skeletal frame, **e** Bulk modulus of solid skeletal frame, **f** Experimental and numerical dispersion curves for R2 wave, **g** Experimental and numerical dispersion curves for R1 wave.

Figure 6.6 illustrates the inversion process of the surface wave measurements for the R2 wave by means of the Neighborhood algorithm. Initially, 20 random samples were employed in the entire space (to avoid the local minimum problem). Voronoi decomposition is used to generate representative sampling points about the best samples in the previous steps. Figure 6.6a shows the entire set of sampling points in the subspace between the porosity and the thickness of the active layer. Most sampling points are concentrated

at the location where the porosity is 0.61 and the thickness of the active layer is 1.5 m. Similarly, in the subspace of the degree of saturation of unfrozen water and the porosity of the permafrost layer (second layer), our results showed that the permafrost layer (second layer) is most likely having a degree of saturation of unfrozen water of 32% and a porosity of 0.44. Figure 6.6c shows the updates of each parameter (thickness, degree of saturation of unfrozen water and porosity) with the number of run in our forward solver. Our results show that the Neighborhood algorithm fully explores the searching space of each parameter. Figure 6.6c also illustrates that the solution converged after roughly 4,000 iterations and the loss function was reduced from 1000 to only only 27 at the end.

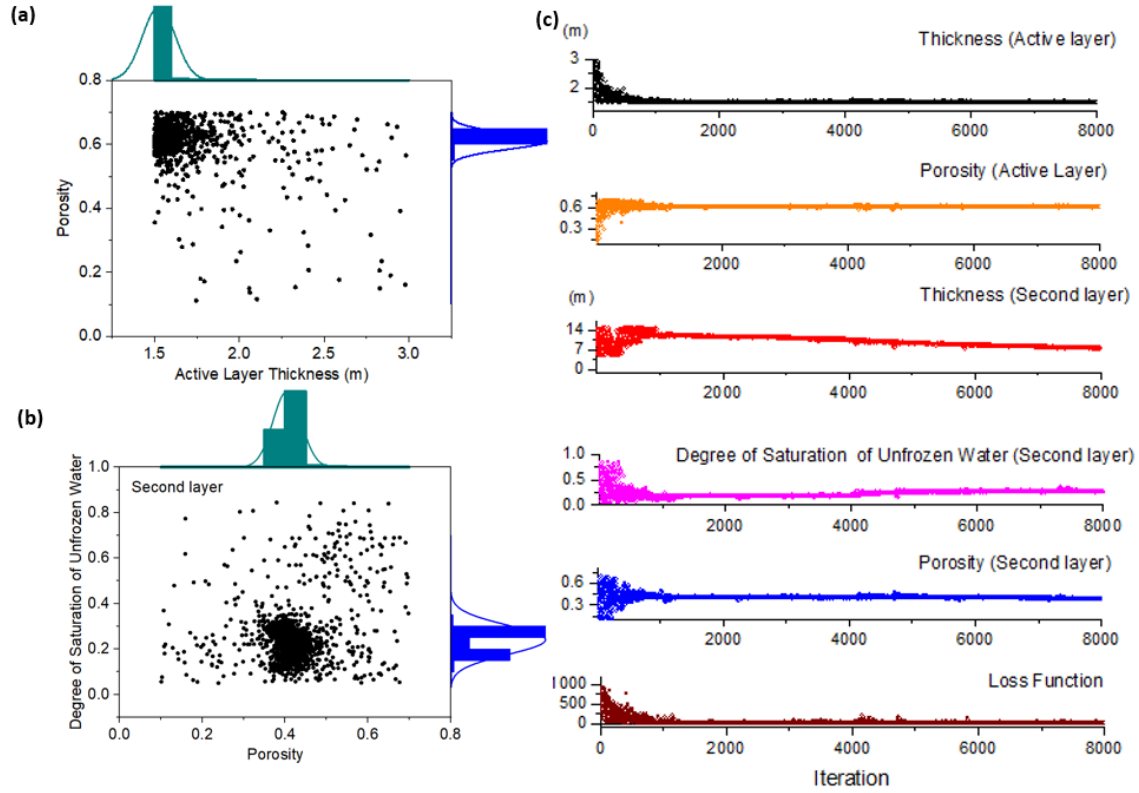

FIGURE 6.6: Inversion process for the R2 wave dispersion relation. **a** Sampling subspace between the degree of saturation of unfrozen water and the thickness of the active layer. **b** Sampling subspace between the degree of saturation of unfrozen water and the thickness of the permafrost layer. **c** Updates of thicknesses of the active layer and permafrost layer as well as the physical properties in each layer by means of the Neighborhood algorithm

We have previously shown the inversion process and results for Section 1 from 0 m to 120 m. Five additional sections spanning from 120 m to 600 m were also studied using a similar approach. The seismic measurements and dispersion relations for each section are given in Section 6.5.3. Figure 6.7a shows the distribution of the degree of saturation of unfrozen water in the ground based on the five independent MASW tests.

The result demonstrates that the permafrost table is generally located at about 1.5-1.9 m below the ground surface. It was reported by Dolnicki, Grabiec, Puczko, Gawor, Budzik, and Klementowski (2013) and Dobiński and Leszkiewicz (2010) that the active layer in Hornsund is approximately 1.5–2.0 m deep for areas not covered by tundra vegetation. The ERT results reported by Glazer, Dobiński, Marciniak, Majdański, and Błaszczyk, 2020 for the same testing site also indicated that active layer is roughly located at a depth of 2 m. We predicted that at the offset distance from 360 m to 480 m, the volumetric ice content in the second layer is the highest (about 0.44). Figure 6.7b illustrates the distribution of the predicted porosity in the test site. We also predicted a higher porosity ranging from 0.57 to 0.69 in the active layer than other layers spanning from 0 m to 600 m. Similarly, figure 6.7c illustrates the distribution of the predicted degree of saturation of unfrozen water in the test site. Sufficient agreement exists between the numerical and experimental dispersion relations for the R2 wave (Figure 6.7d) which confirms the acceptance of the predicted values for the volumetric ice content (calculated as the product of porosity and the degree of saturation of ice) and porosity. Similarly, we obtain the mechanical properties of the solid skeletal frame for each layer (Figure 6.7e) based on the phase velocity of R1 waves.

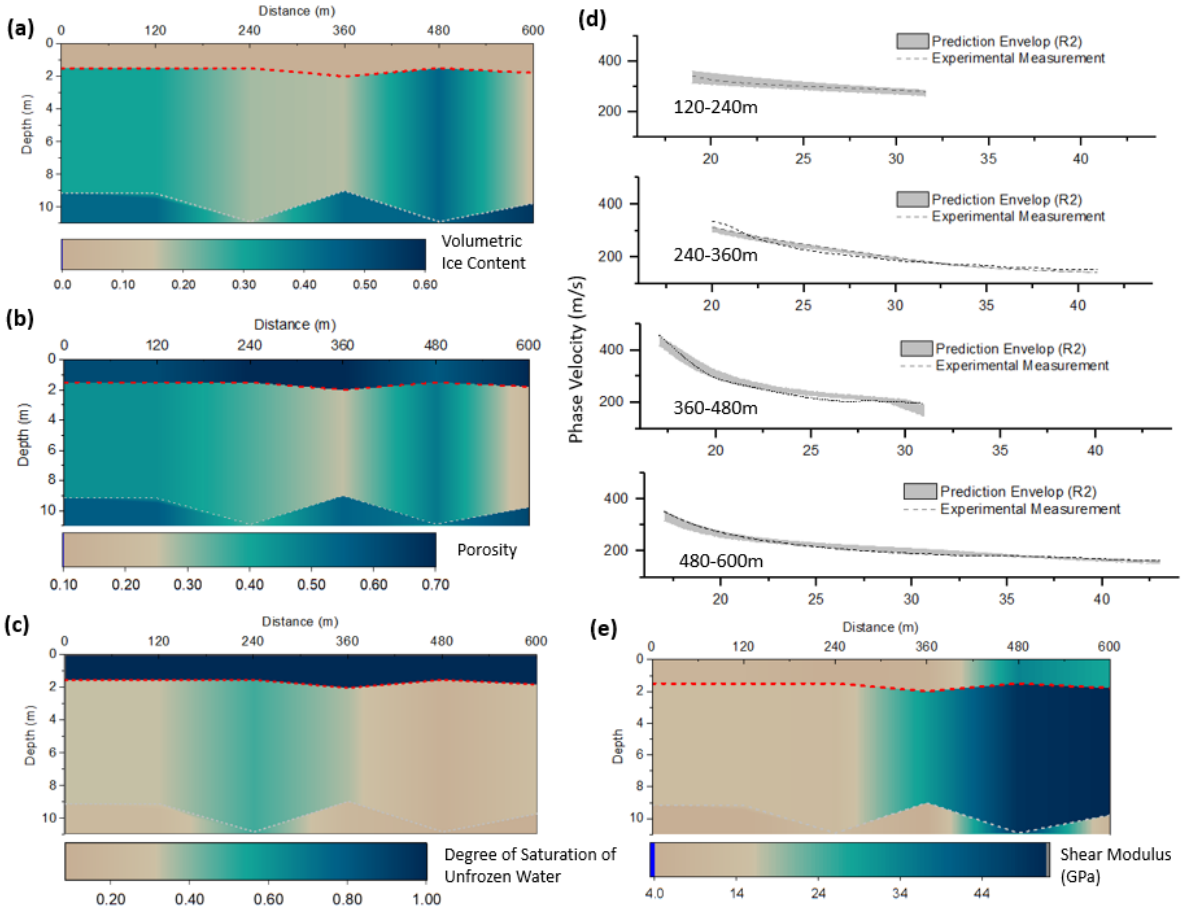

FIGURE 6.7: Summary of the inversion results at the offset distance from 0 m to 600 m. **a** Volumetric ice content distribution. **b** Soil porosity distribution. **c** Distribution of degree of saturation of unfrozen water. **d** Comparison between the numerical and experimental dispersion curves for R2 wave. **e** Distribution of the shear modulus of the solid skeletal frame..

6.4 Discussion and conclusion

We developed a hybrid inverse and multi-phase poromechanical approach to quantitatively estimate the physical and mechanical properties of a permafrost site. The identification of two distinctive types of Rayleigh waves in the surface wave field measurements in permafrost sites is critical for quantitative characterization of the layers. The identification of the R2 wave allows the quantitative characterization of physical properties of soil layers independently without making assumptions of the mechanical properties of the layers. This approach simplifies the inversion of the multi-layered three-phase poromechanical model since the dependent optimization variables are largely reduced. The inversion results from the R2 wave dispersion relation can be further used in the characterization of the mechanical properties of soil layers based on the R1 wave dispersion relation. This also

increases the stability and convergence rate of the inversion solver and makes the analysis more efficient.

In ice-rich permafrost that contains ice in excess of the water content required to fill pore space in the unfrozen state (normally shown as ice lenses), the direct detection of the thin ice lenses using the surface waves is almost impossible due to the mismatch between the thickness of the ice segregation layers and the wavelength generated in the seismic tests. However, the mechanical properties of the solid skeletal frame can reveal the type of soil, which can be used to identify an ice-rich permafrost layer. Furthermore, the sensitivity of the permafrost layer to permafrost carbon feedback and emission of greenhouse gases (e.g., methane, carbon dioxide etc.) to the atmosphere can be determined. For example, if the mechanical properties of the solid skeletal frame correspond to the ones for peat we can perform more detailed investigation to assess the sensitivity of the permafrost to greenhouse gases emission.

Additional work on the characterization of permafrost should explore ways to reduce the uncertainty in the proposed hybrid inverse and multi-phase poromechanical approach. The uncertainty originates from the non-uniqueness in the inverse analysis (local minima problem) and the limited number of constraints in the inversion analysis. It is recommended to use other geophysical methods to improve the resolution and reduce uncertainty of the permafrost mapping. With the proposed seismic wave-based method as the main investigation tool, ERT, GPR and electromagnetic (EM) Tomography can augment the investigation data and supply additional constraints to the inversion analysis.

The proposed hybrid inverse and multi-phase poromechanical approach can potentially be used for the design of an early warning system for permafrost by means of an active or passive seismic test. The seismic noise from traffic can generate stress waves as they travel on the permafrost foundation. Pre-installed geophones can be used to capture the propagation of R1 and R2 waves. By applying the proposed signal processing approach, we can estimate the physical and mechanical properties of permafrost for monitored sites. The early warning system can provide long-term tracking of permafrost conditions particularly when the ice content or mechanical properties of permafrost approach critical values.

6.5 Supplementary materials

6.5.1 Definition of phase velocities

The velocities of the three types of P waves are determined by a third degree characteristic equation:

$$\Lambda^3\tilde{R} - \Lambda^2\left((\rho_{11}\tilde{R}_{iw} + \rho_{22}\tilde{R}_{si} + \rho_{33}\tilde{R}_{sw}) - 2(R_{11}R_{33}\rho_{23} + R_{33}R_{12}\rho_{12})\right)$$
$$+\Lambda\left((R_{11}\tilde{\rho}_{iw} + R_{22}\tilde{\rho}_{si} + R_{33}\tilde{\rho}_{sw}) - 2(\rho_{11}\rho_{23}R_{23} + \rho_{33}\rho_{12}R_{12})\right) - \tilde{\rho} = 0$$

where

$$\tilde{R} = R_{11}R_{22}R_{33} - R_{23}^2R_{11} - R_{12}^2R_{33}$$
$$\tilde{R}_{sw} = R_{11}R_{22} - R_{12}^2$$
$$\tilde{R}_{iw} = R_{22}R_{33} - R_{23}^2$$
$$\tilde{R}_{si} = R_{11}R_{33}$$
$$\tilde{\rho} = \rho_{11}\rho_{22}\rho_{33} - \rho_{23}^2\rho_{11} - \rho_{12}^2\rho_{33}$$
$$\tilde{\rho}_{sw} = \rho_{11}\rho_{22} - \rho_{12}^2$$
$$\tilde{\rho}_{iw} = \rho_{22}\rho_{33} - \rho_{23}^2$$
$$\tilde{\rho}_{si} = \rho_{11}\rho_{33}$$

The roots of the third degree characteristic equation, denoted as Λ_1, Λ_2 and Λ_3, can be found by computing the eigenvalues of the companion matrix (Horn and Johnson, 2012). The velocities of the three types of P-wave ($v_{p1} > v_{p2} > v_{p3}$) are given as follows:

$$v_{p1} = \sqrt{\frac{1}{\Lambda_1}};\quad v_{p2} = \sqrt{\frac{1}{\Lambda_2}}; v_{p3} = \sqrt{\frac{1}{\Lambda_3}}$$

The velocities of the two types of S-wave are determined by a second degree characteristic equation:

$$\delta^2\rho_{22}\tilde{\mu}_{si} - \delta(\mu_{11}\tilde{\rho}_{iw} + \mu_{33}\tilde{\rho}_{sw}) + \tilde{\rho} = 0$$

The roots of this second degree characteristic equation is denoted by δ_1 and δ_2. The velocities of the two types of S-wave ($v_{s1} > v_{s2}$) are given as follows:

$$v_{s1} = \sqrt{\frac{1}{\delta_1}};\quad v_{s2} = \sqrt{\frac{1}{\delta_2}};$$

6.5.2 Animation

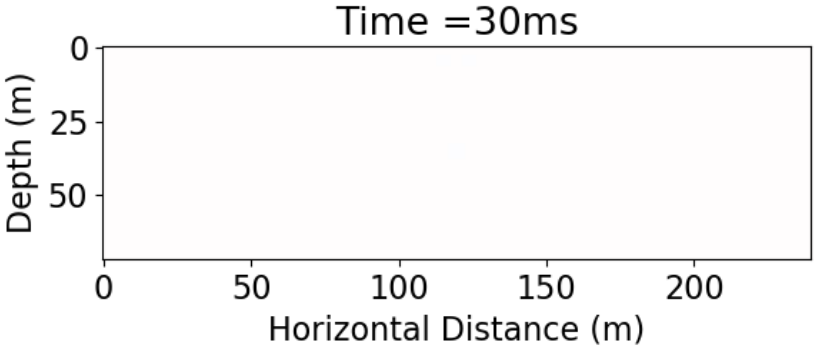

6.5.3 Inversion results for other sections

The inversion results for the sections ranging from 120 m to 600 m are summarized in Figure 6.5.1 to Figure 6.5.4.

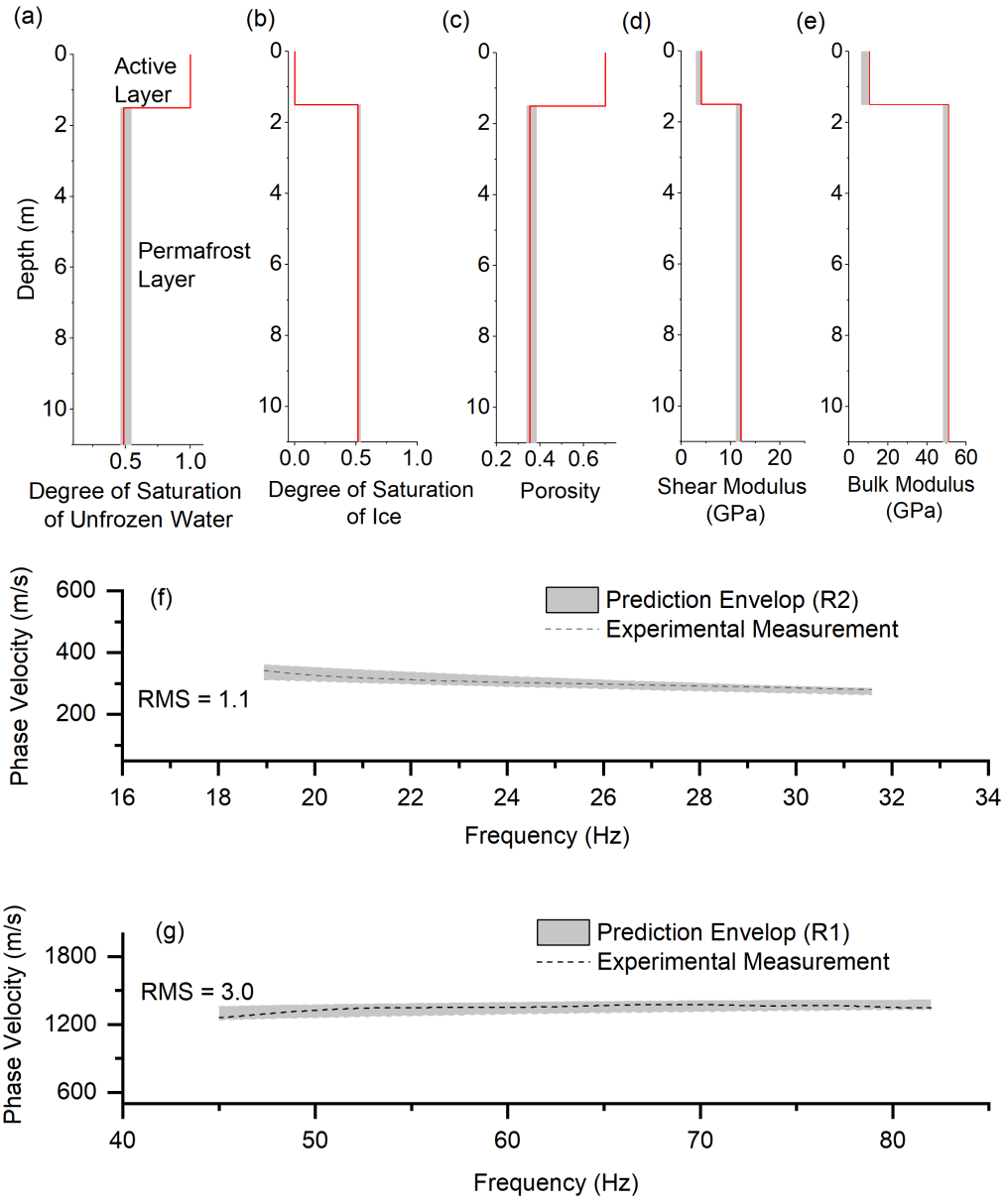

FIGURE 6.5.1: Surface wave inversion results for Section 2: 120m to 240m. **a** Degree of saturation of unfrozen water, **b** Degree of saturation of ice, **c** Porosity distribution, **d** Shear modulus of solid skeletal frame, **e** Bulk modulus of solid skeletal frame, **f** Experimental and numerical dispersion curves for R2 wave, **g** Experimental and numerical dispersion curves for R1 wave.

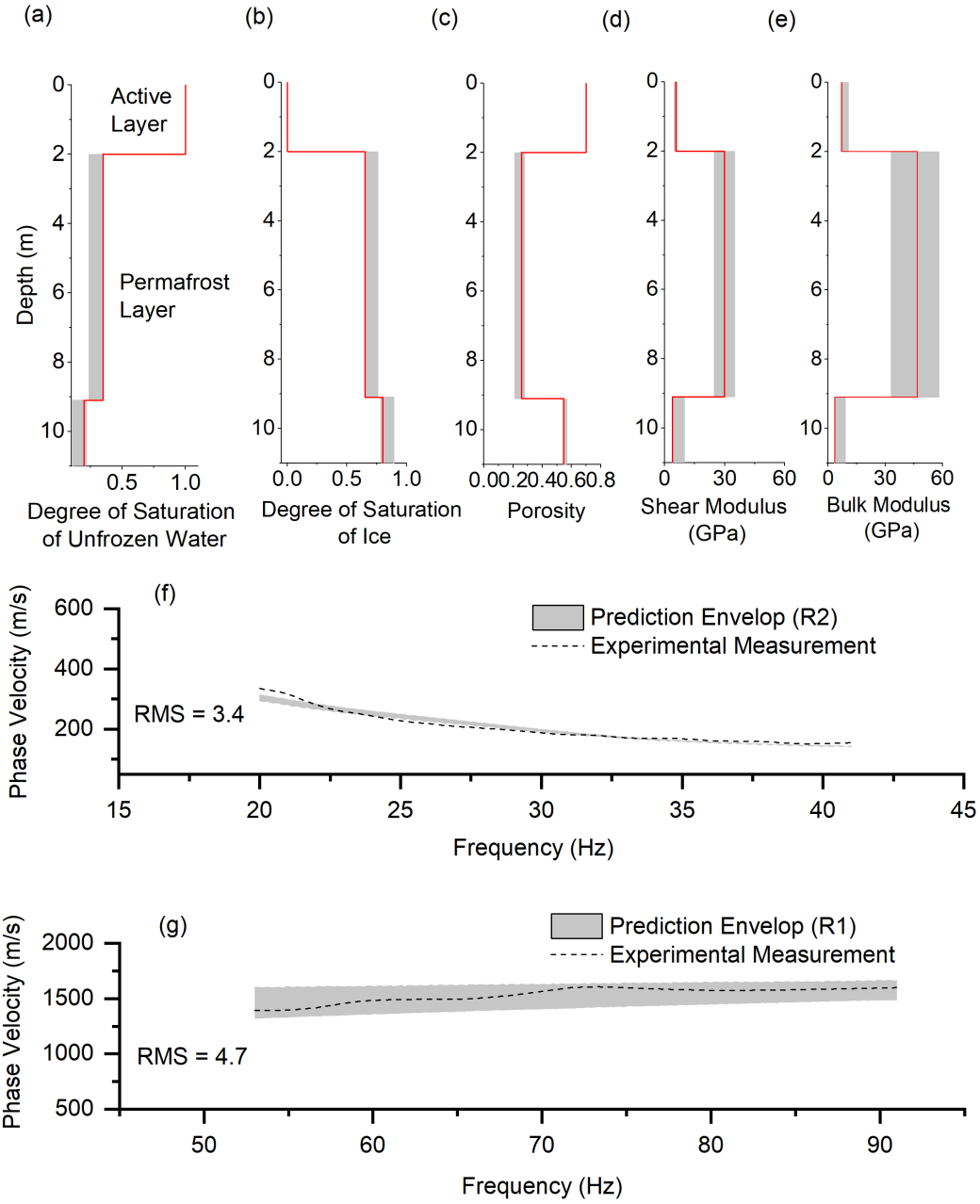

FIGURE 6.5.2: Surface wave inversion results for Section 3: 240m to 360m. **a** Degree of saturation of unfrozen water, **b** Degree of saturation of ice, **c** Porosity distribution, **d** Shear modulus of solid skeletal frame, **e** Bulk modulus of solid skeletal frame, **f** Experimental and numerical dispersion curves for R2 wave, **g** Experimental and numerical dispersion curves for R1 wave.

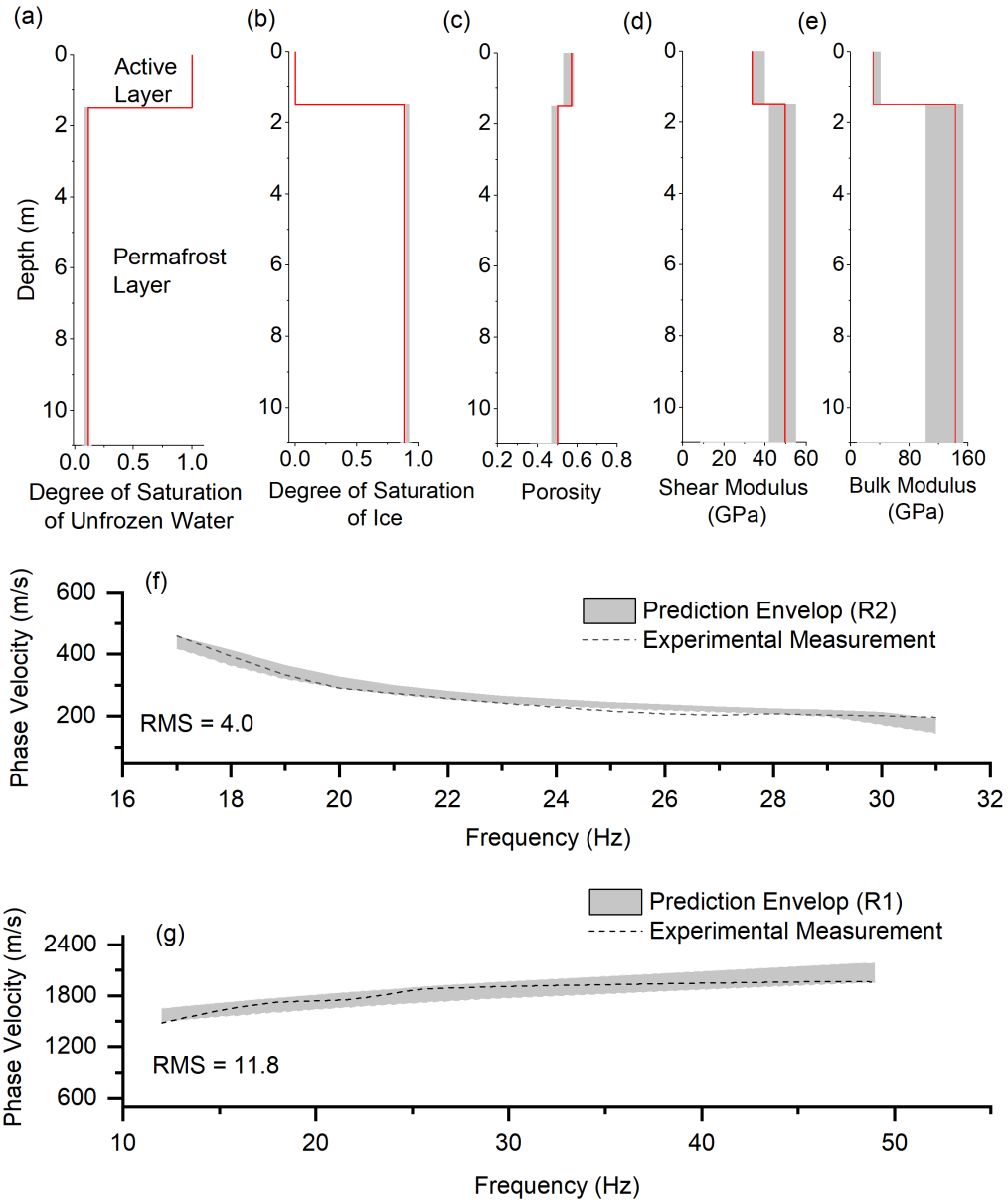

FIGURE 6.5.3: Surface wave inversion results for Section 4 (from 360m to 480m). **a** Degree of saturation of unfrozen water, **b** Degree of saturation of ice, **c** Porosity distribution, **d** Shear modulus of solid skeletal frame, **e** Bulk modulus of solid skeletal frame, **f** Experimental and numerical dispersion curves for R2 wave, **g** Experimental and numerical dispersion curves for R1 wave.

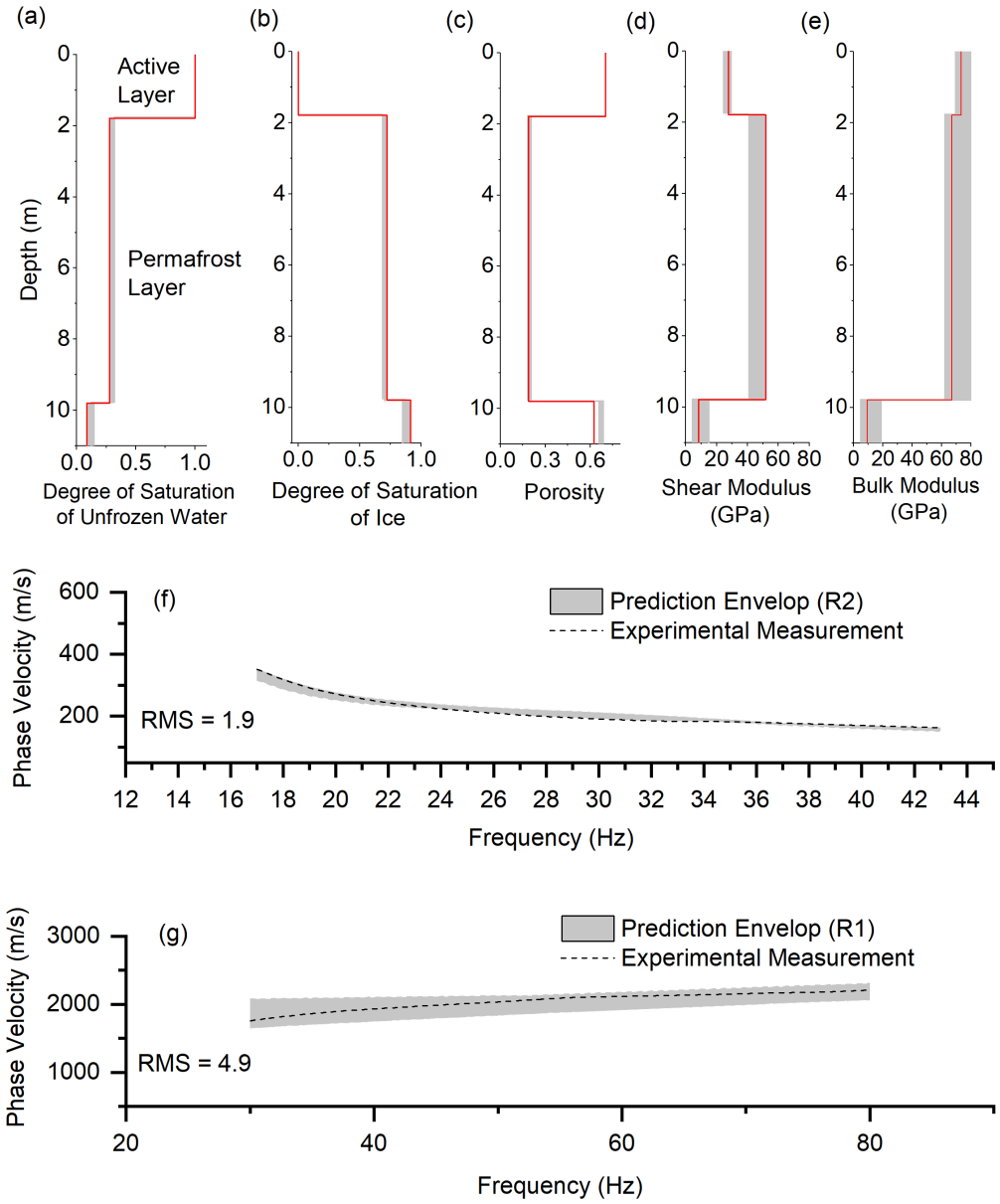

FIGURE 6.5.4: Surface wave inversion results for Section 5 (from 480m to 600m). **a** Degree of saturation of unfrozen water, **b** Degree of saturation of ice, **c** Porosity distribution, **d** Shear modulus of solid skeletal frame, **e** Bulk modulus of solid skeletal frame, **f** Experimental and numerical dispersion curves for R2 wave, **g** Experimental and numerical dispersion curves for R1 wave.

6.5.4 Forward three-phase poromechanical model

The three-phase poromechanical model in Chapter 6 is used to construct the global stiffness matrix which includes elements from both soil layers with finite thickness and infinite layer. However, the poromechanical model in Chapter 5 is used to define the transfer function H_2 for frozen soil samples with finite thickness.

Kinematics assumptions

The Green-Lagrange strain tensor (ϵ_{ij}) for infinitesimal deformations expressed as displacement vector u^1, u^2 and u^3 for the solid skeleton, pore water and pore ice are shown in Equation 6.3.

$$\begin{cases} \epsilon_{ij}^1 = \frac{1}{2}(u_{i,j}^1 + u_{j,i}^1) \\ \epsilon_{ij}^2 = \frac{1}{3}\epsilon_{kk}^2\delta_{ij} \quad (\epsilon_{kk}^2 = u_{k,k}^2) \\ \epsilon_{ij}^3 = \frac{1}{2}(u_{i,j}^3 + u_{j,i}^3) \end{cases} \tag{6.3}$$

where δ_{ij} is the identity tensor.

The strain tensor of pore water ϵ_{ij}^2 is diagonal since the shear deformation does not exist in pore water component.

Constitutive model

The constitutive models defined as the relation between the stress and strain tensors for solid skeleton, pore water and pore ice are given in Equation 6.4:

$$\begin{cases} \sigma_{ij}^1 = (K_1\theta_1 + C_{12}\theta_2 + C_{13}\theta_3)\delta_{ij} + 2\mu_1 d_{ij}^1 + \mu_{13} d_{ij}^3 \\ \sigma^2 = C_{12}\theta_1 + K_2\theta_2 + C_{23}\theta_3 \\ \sigma_{ij}^3 = (K_3\theta_3 + C_{23}\theta_2 + C_{13}\theta_1)\delta_{ij} + 2\mu_3 d_{ij}^3 + \mu_{13} d_{ij}^1 \end{cases} \tag{6.4}$$

in which σ^1, σ^2 and σ^3 are the effective stress, pore water pressure and ice pressure, respectively. The definition of each term (e.g., K_1, C_{12}, C_{13}, μ_1, μ_{13}, K_2, C_{23}, K_3, μ_3) in Equation 6.4 is given in Appendix A. The term θ_m, d_{ij}^m and ϵ_{ij}^m (m, ranging from 1 to 3,

represents the different phases) are defined as follows:

$$\begin{cases} \theta_m = \epsilon^m_{kk} \\ d^m_{ij} = \epsilon^m_{ij} - \frac{1}{3}\delta_{ij}\theta_m \\ \epsilon^m_{ij} = \frac{1}{2}(u^m_{i,j} + u^m_{j,i}). \end{cases}$$

Conservation laws

The momentum conservation considers the acceleration of each component and the existing relative motion of the pore ice and pore water phases with respect to the solid skeleton. The momentum conservation for the three phases is given by Equation 6.5.

$$\begin{cases} \sigma^1_{ij,j} = \rho_{11}\ddot{u}^1_i + \rho_{12}\ddot{u}^2_i + \rho_{13}\ddot{u}^3_i - b_{12}(\dot{u}^2_i - \dot{u}^1_i) - b_{13}(\dot{u}^3_i - \dot{u}^1_i) \\ \sigma^2_{,i} = \rho_{12}\ddot{u}^1_i + \rho_{22}\ddot{u}^2_i + \rho_{23}\ddot{u}^3_i + b_{12}(\dot{u}^2_i - \dot{u}^1_i) + b_{23}(\dot{u}^2_i - \dot{u}^3_i) \\ \sigma^3_{ij,j} = \rho_{13}\ddot{u}^1_i + \rho_{23}\ddot{u}^2_i + \rho_{33}\ddot{u}^3_i - b_{23}(\dot{u}^2_i - \dot{u}^1_i) + b_{13}(\dot{u}^3_i - \dot{u}^1_i) \end{cases} \tag{6.5}$$

in which the expressions for the density terms (ρ_{ij} or $\bar{\rho}$ in matrix form) and viscous matrix (b_{ij} or $\bar{b}$ in matrix form) are given in Appendix A; $\ddot{u}$ and $\dot{u}$ represent second and first derivative of displacement vectors with respect to time; the subscript i represents the component in r, θ and z direction in cylindrical coordinates.

Through the infinitesimal kinematic assumptions, the stress-strain constitutive model and conversation of momentum, the field equation can be written in the matrix form, as shown in Equation 6.6.

$$\bar{\rho}\begin{bmatrix} \ddot{u}^1_i \\ \ddot{u}^2_i \\ \ddot{u}^3_i \end{bmatrix} + \bar{b}\begin{bmatrix} \dot{u}^1_i \\ \dot{u}^2_i \\ \dot{u}^3_i \end{bmatrix} = \bar{R}\,\nabla\nabla\cdot\begin{bmatrix} u^1_i \\ u^2_i \\ u^3_i \end{bmatrix} - \bar{\mu}\,\nabla\times\nabla\times\begin{bmatrix} u^1_i \\ u^2_i \\ u^3_i \end{bmatrix} \tag{6.6}$$

in which the matrix $\bar{R}$ and $\bar{\mu}$ are given in Appendix A.

By performing divergence operation ($\nabla\cdot$) and curl operation ($\nabla\times$) on both sides of Equation 6.6, the field equation in the frequency domain can be written as Equation 6.7.

$$\begin{cases} -\bar{\rho}\,\omega^2\,\nabla\cdot\begin{bmatrix} u_i^1 \\ u_i^2 \\ u_i^3 \end{bmatrix} - \bar{b}\,i\,\omega\,\nabla\cdot\begin{bmatrix} u_i^1 \\ u_i^2 \\ u_i^3 \end{bmatrix} = \bar{R}\,\nabla^2\nabla\cdot\begin{bmatrix} u_i^1 \\ u_i^2 \\ u_i^3 \end{bmatrix} \\ -\bar{\rho}\,\omega^2\,\nabla\times\begin{bmatrix} u_i^1 \\ u_i^2 \\ u_i^3 \end{bmatrix} - \bar{b}\,i\,\omega\,\nabla\times\begin{bmatrix} u_i^1 \\ u_i^2 \\ u_i^3 \end{bmatrix} = \bar{\mu}\,\nabla^2\nabla\times\begin{bmatrix} u_i^1 \\ u_i^2 \\ u_i^3 \end{bmatrix}. \end{cases} \tag{6.7}$$

Using the Helmholtz decomposition theorem allows us to decompose the displacement field, $\bar{u}$ (equivalent to u_i), into the longitudinal potential and transverse vector components as follows:

$$\begin{cases} \bar{u}^1 = \nabla\phi_1 + \nabla\times\bar{\psi}_1 \quad and \quad \nabla\cdot\bar{\psi}_1 = 0 \\ \bar{u}^2 = \nabla\phi_2 + \nabla\times\bar{\psi}_2 \quad and \quad \nabla\cdot\bar{\psi}_2 = 0 \\ \bar{u}^3 = \nabla\phi_3 + \nabla\times\bar{\psi}_3 \quad and \quad \nabla\cdot\bar{\psi}_3 = 0. \end{cases} \tag{6.8}$$

By substituting Equation 6.8 into the field equation of motion, Equation 6.7, we obtain two sets of uncoupled partial differential equations relative to the compressional wave P related to the Helmholtz scalar potentials , and to the shear wave S related to the Helmholtz vector potential, respectively (Equation 6.9). In the axi-symmetric condition, only the second components exits in vector $\bar{\psi}$, which is denoted as ψ in the future. It should be mentioned that the field equations in Laplace domain can be easily obtained by replacing ω with $i.s$ ($i^2 = -1$ and s the Laplace variable).

$$\begin{cases} -\bar{\rho}\,\omega^2\begin{bmatrix} \phi_1 \\ \phi_2 \\ \phi_3 \end{bmatrix} - \bar{b}\,i\,\omega\begin{bmatrix} \phi_1 \\ \phi_2 \\ \phi_3 \end{bmatrix} = \bar{R}\,\nabla^2\begin{bmatrix} \phi_1 \\ \phi_2 \\ \phi_3 \end{bmatrix} \\ -\bar{\rho}\,\omega^2\begin{bmatrix} \psi_1 \\ \psi_2 \\ \psi_3 \end{bmatrix} - \bar{b}\,i\,\omega\begin{bmatrix} \psi_1 \\ \psi_2 \\ \psi_3 \end{bmatrix} = \bar{\mu}\,\nabla^2\begin{bmatrix} \psi_1 \\ \psi_2 \\ \psi_3 \end{bmatrix}. \end{cases} \tag{6.9}$$

Solution for the longitudinal waves (P waves) by eigen decomposition

Equation (6.9) shows that ϕ_1, ϕ_2 and ϕ_3 are coupled in the field equations. The diagonalization of such a matrix is required to decouple the system. Equation (6.9) is then rearranged into Equation (6.10):

$$\nabla^2 \begin{bmatrix} \phi_1 \\ \phi_2 \\ \phi_3 \end{bmatrix} = \underbrace{-\bar{R}^{-1}(\bar{\rho}\omega^2 + \bar{b}\, i\, \omega)}_{\bar{K}} \begin{bmatrix} \phi_1 \\ \phi_2 \\ \phi_3 \end{bmatrix} \tag{6.10}$$

where the $\bar{K}$ matrix can be rewritten using the Eigen decomposition:

$$\bar{K} = \bar{P}\, \bar{D}\, \bar{P}^{-1} \tag{6.11}$$

where $\bar{P}$ is the eigenvector and $\bar{D}$ is the eigenvalue matrix of $\bar{K}$.

By setting $\bar{\phi} = \bar{P}\bar{y}$, where $\bar{y} = [\phi_{p1}, \phi_{p2}, \phi_{p3}]$, we can obtain $\nabla^2 \bar{y} = \bar{D}\bar{y}$. The equation of longitudinal wave has been decoupled. In cylindrical coordinates, the solution for $\bar{y} = [\phi_{p1}, \phi_{p2}, \phi_{p3}]$ is summarized as follows:

$$\begin{cases} \phi_{p1}(r,z) = Ae^{-\sqrt{k^2+D_{11}}\, z} J_0(k\, r) \\ \phi_{p2}(r,z) = Be^{-\sqrt{k^2+D_{22}}\, z} J_0(k\, r) \\ \phi_{p3}(r,z) = Ce^{-\sqrt{k^2+D_{33}}\, z} J_0(k\, r) \end{cases} \tag{6.12}$$

where k is the wave number; coefficient A, B and C will be determined by boundary conditions; D_{11}, D_{22}, and D_{33} are the diagonal components of $\bar{D}$; J_0 is the Bessel function of the first kind. For simplicity, The terms $\sqrt{k^2 + D_{11}}$, $\sqrt{k^2 + D_{22}}$ and $\sqrt{k^2 + D_{33}}$ are denoted as k_{p1}, k_{p2} and k_{p3}, respectively.

Now, the P wave potentials can be written as:

$$\begin{Bmatrix} \phi_s \\ \phi_w \\ \phi_i \end{Bmatrix} = \begin{Bmatrix} p_{11} & p_{12} & p_{13} \\ p_{21} & p_{22} & p_{23} \\ p_{31} & p_{32} & p_{33} \end{Bmatrix} \begin{Bmatrix} \phi_{p1} \\ \phi_{p2} \\ \phi_{p3} \end{Bmatrix} \tag{6.13}$$

where p_{ij} are the components for the eigenvector of $\bar{P}$.

Solution for shear waves (S waves)

The solutions for the S wave potentials can be solved in a similar manner. The Equation 6.14 is firstly rearranged into Equation 6.15:

$$-\bar{\rho}\,\omega^2 \begin{bmatrix} \psi_s \\ \psi_w \\ \psi_i \end{bmatrix} - \bar{b}\,i\,\omega \begin{bmatrix} \psi_s \\ \psi_w \\ \psi_i \end{bmatrix} = \bar{\mu}\,\nabla^2 \begin{bmatrix} \psi_s \\ \psi_w \\ \psi_i \end{bmatrix} \tag{6.14}$$

$$\underbrace{-\bar{\rho}\omega^2 - \bar{b}\,i\,\omega}_{\bar{A}} \begin{bmatrix} \psi_s \\ \psi_w \\ \psi_i \end{bmatrix} = \bar{\mu}\,\nabla^2 \begin{bmatrix} \psi_s \\ \psi_w \\ \psi_i \end{bmatrix} \tag{6.15}$$

where the matrix $\bar{A}$ is given in Appendix A.

Since ψ_w can be expressed as a function of ψ_s and ψ_i (shown in Equation 6.16), the Equation 6.15 is further simplified and rearranged into Equation 6.17.

$$\begin{cases} A_{21}\psi_s + A_{22}\psi_w + A_{23}\psi_i = 0 \\ \psi_w = -\frac{A_{21}\psi_s + A_{23}\psi_i}{A_{22}} \end{cases} \tag{6.16}$$

$$\nabla^2 \begin{bmatrix} \psi_s \\ \psi_i \end{bmatrix} = \underbrace{\begin{bmatrix} \mu_{11} & \mu_{13} \\ \mu_{13} & \mu_{33} \end{bmatrix}^{-1} \bar{C}}_{\bar{N}} \begin{bmatrix} \psi_s \\ \psi_i \end{bmatrix}. \tag{6.17}$$

where

$$\bar{C} = \begin{pmatrix} A_{11} - \frac{A_{12}A_{21}}{A_{22}} & A_{13} - \frac{A_{12}A_{23}}{A_{22}} \\ A_{31} - \frac{A_{32}A_{21}}{A_{22}} & A_{33} - \frac{A_{32}A_{23}}{A_{22}} \end{pmatrix}$$

The $\bar{N}$ matrix can be rewritten using the eigen decomposition ($\bar{N} = \bar{Q}\,\bar{G}\,\bar{Q}^{-1}$), where $\bar{Q}$ is the eigenvector and $\bar{G}$ is the eigenvalue matrix of $\bar{N}$. By setting $\bar{\psi} = \bar{Q}\,\bar{y}'$ where $\bar{y}' = [\psi_{s1}, \psi_{i1}]$, we can obtain:

$$\psi_{s1} = Ee^{-\sqrt{k^2+G_{11}}\,z} J_1(k\,r) \tag{6.18}$$

$$\psi_{i1} = Fe^{-\sqrt{k^2+G_{22}}\,z} J_1(k\,r) \tag{6.19}$$

where J_1 is the Bessel function of the first kind with order 1. G_{11} and G_{22} are the diagonal components of matrix $\bar{G}$. For simplicity, the term $\sqrt{k^2+G_{11}}$ and $\sqrt{k^2+G_{22}}$ is denoted as k_{s1} and k_{s2}.

Finally, the solution of the S wave potentials can be written as:

$$\begin{Bmatrix} \psi_s \\ \psi_i \end{Bmatrix} = \begin{Bmatrix} Q_{11} & Q_{12} \\ Q_{21} & Q_{22} \end{Bmatrix} \begin{Bmatrix} \psi_{s1} \\ \psi_{i1} \end{Bmatrix} \tag{6.20}$$

where Q_{ij} are the components for eigenvector of $\bar{Q}$.

Layer element with finite thickness

By including both incident wave and reflected wave, the potentials for a layer with finite thickness can be written in Equation 6.21:

$$\begin{bmatrix} u_{r1}^1 \\ u_{z1}^1 \\ u_{z1}^2 \\ u_{r1}^3 \\ u_{z1}^3 \\ u_{r2}^1 \\ u_{z2}^1 \\ u_{z2}^2 \\ u_{r2}^3 \\ u_{z2}^3 \end{bmatrix} = \begin{bmatrix} & & & & & & & & & \\ & & & & & & & & & \\ & & & & & & & & & \\ & & & & & & & & & \\ & & & & S_1 & & & & & \\ & & & & & & & & & \\ & & & & & & & & & \\ & & & & & & & & & \\ & & & & & & & & & \\ & & & & & & & & & \end{bmatrix} \begin{bmatrix} A_1 \\ B_1 \\ C_1 \\ E_1 \\ F_1 \\ A_2 \\ B_2 \\ C_2 \\ E_2 \\ F_2 \end{bmatrix} \tag{6.21}$$

where the components of S_1 is given in Appendix B; the subscript 1 and 2 represent node for the upper and lower layer, respectively. The coefficient A to F is determined by the boundary condition.

The matrix of effective stress, pore water pressure and pore ice pressure in the frequency domain is shown in Equation 6.22 in which the components for matrix S_2 can be found in

the Appendix B.

$$\begin{bmatrix} \sigma^1_{r1} \\ \sigma^1_{z1} \\ p_1 \\ \sigma^3_{r1} \\ \sigma^3_{z1} \\ \sigma^1_{r2} \\ \sigma^1_{z2} \\ p_2 \\ \sigma^3_{r2} \\ \sigma^3_{z2} \end{bmatrix} = \begin{bmatrix} & & & & & & & & & \\ & & & & & & & & & \\ & & & & & & & & & \\ & & & & & & & & & \\ & & & & S_2 & & & & & \\ & & & & & & & & & \\ & & & & & & & & & \\ & & & & & & & & & \\ & & & & & & & & & \\ & & & & & & & & & \end{bmatrix} \begin{bmatrix} A_1 \\ B_1 \\ C_1 \\ E_1 \\ F_1 \\ A_2 \\ B_2 \\ C_2 \\ E_2 \\ F_2 \end{bmatrix}. \tag{6.22}$$

According to the Cauchy stress principle, the traction force (T) is taken as the dot product between the stress tensor and the unit vector along the outward normal direction. Due to the convection that the upward direction is negative, the upper boundary becomes negative. Similarly, to make the sign consistent, the N matrix is applied to matrix $S_2 \cdot S_1^{-1}$. In the future, the matrix $N \cdot S_2 \cdot S_1^{-1}$ will be denoted as the G_i matrix, in which i denotes the layer number.

$$\begin{bmatrix} T^1_{r1} \\ T^1_{z1} \\ T_1 \\ T^3_{r1} \\ T^3_{z1} \\ T^1_{r2} \\ T^1_{z2} \\ T_2 \\ T^3_{r2} \\ T^3_{z2} \end{bmatrix}_i = \begin{bmatrix} -\sigma^1_{r1} \\ -\sigma^1_{z1} \\ -p_1 \\ -\sigma^3_{r1} \\ -\sigma^3_{z1} \\ \sigma^1_{r2} \\ \sigma^1_{z2} \\ p_2 \\ \sigma^3_{r2} \\ \sigma^3_{z2} \end{bmatrix}_i = \underbrace{N \cdot S_2 \cdot S_1^{-1}}_{G_i} \cdot \begin{bmatrix} u^1_{r1} \\ u^1_{z1} \\ u^2_{z1} \\ u^3_{r1} \\ u^3_{z1} \\ u^1_{r2} \\ u^1_{z2} \\ u^2_{z2} \\ u^3_{r2} \\ u^3_{z2} \end{bmatrix}_i \tag{6.23}$$

where

$$N = \begin{bmatrix} -1 & 0 & 0 & 0 & 0 & 0 & 0 & 0 & 0 & 0 \\ 0 & -1 & 0 & 0 & 0 & 0 & 0 & 0 & 0 & 0 \\ 0 & 0 & -1 & 0 & 0 & 0 & 0 & 0 & 0 & 0 \\ 0 & 0 & 0 & -1 & 0 & 0 & 0 & 0 & 0 & 0 \\ 0 & 0 & 0 & 0 & -1 & 0 & 0 & 0 & 0 & 0 \\ 0 & 0 & 0 & 0 & 0 & 1 & 0 & 0 & 0 & 0 \\ 0 & 0 & 0 & 0 & 0 & 0 & 1 & 0 & 0 & 0 \\ 0 & 0 & 0 & 0 & 0 & 0 & 0 & 1 & 0 & 0 \\ 0 & 0 & 0 & 0 & 0 & 0 & 0 & 0 & 1 & 0 \\ 0 & 0 & 0 & 0 & 0 & 0 & 0 & 0 & 0 & 1 \end{bmatrix}. \tag{6.24}$$

Layer element with infinite thickness

By assuming that no wave reflects back to a semi-infinite element, one-node element with infinite thickness is applied. The matrix for the displacement components in one-node layer are written as Equation 6.25. The matrix S_1 is reduced into a 5 by 5 matrix (S_{1ij} where i and j range from 1 to 5). The value of each components are shown in Appendix B.

$$\begin{bmatrix} u^1_{r1} \\ u^1_{z1} \\ u^2_{z1} \\ u^3_{r1} \\ u^3_{z1} \end{bmatrix} = \begin{bmatrix} \\ \\ S_1 \\ \\ \\ \end{bmatrix} \begin{bmatrix} A_1 \\ B_1 \\ C_1 \\ E_1 \\ F_1 \end{bmatrix}. \tag{6.25}$$

Similarly, the matrix of effective stress components and porewater pressure in the frequency domain is shown in Equation 6.26. The matrix S_2 is reduced into a 5 by 5 matrix (S_{2ij} where i and j range from 1 to 5). The matrix G_h in Figure 6.2 is calculated as $G_h = S_2\, S_1^{-1}$. The value of each components are shown in Appendix B.

$$\begin{bmatrix} \sigma^1_{r1} \\ \sigma^1_{z1} \\ p_1 \\ \sigma^3_{r1} \\ \sigma^3_{z1} \end{bmatrix} = \begin{bmatrix} \\ \\ S_2 \\ \\ \\ \end{bmatrix} \begin{bmatrix} A_1 \\ B_1 \\ C_1 \\ E_1 \\ F_1 \end{bmatrix}. \tag{6.26}$$

Connecting section

Part III (Chapter 5 and 6), presented multiphase poroelastodynamic solvers for both laboratory and in-situ characterization of permafrost soils. Chapter 5 presented an ultrasonic sensing technique and a physics-based signal interpretation method based on a spectral element multiphase poromechanical approach to overcome critical gaps in permafrost characterization. The study demonstrates the potential of the ultrasonic sensing technique for the rapid characterization of permafrost samples in terms of both physical and mechanical properties. The Quantitative Ultrasound (QUS) package developed in this study can be used in a laboratory setup or brought to the site for in-situ investigation of permafrost samples. Chapter 6 presented a novel algorithm for analysis of surface waves to quantitatively estimate the physical and mechanical properties of a permafrost site. It was concluded that the R2 wave velocity is highly sensitive to the physical properties (e.g., unfrozen water content, ice content, and porosity) of permafrost or soil layers while it is less sensitive to their mechanical properties (e.g., shear modulus and bulk modulus). The R1 wave velocity, on the other hand, depends strongly on the soil type and mechanical properties of permafrost or soil layers. This study demonstrates the potential of surface wave techniques coupled with the proposed data-processing algorithm to characterize a permafrost site more accurately.

The next part, Part IV, presents the programming and further applications of the advanced solvers developed in Part I to Part III based on the spectral element technique.

Part IV: Programming and Further Applications

Chapter 7

GeoNDT: an open source physics-based multiphase geomechanical solver for geotechnical and geophysical applications

Abstract

In this paper, we present the GeoNDT software, which is developed to provide fast and robust solutions for the interpretation of non-destructive testing (NDT) measurements used in geotechnical and geophysical applications. The software includes a Python so-called glue to facilitate transfer of geomechanical parameters under JavaScript Object Notation to an advanced computational geomechanical forward solver called PoroSEM. PoroSEM, written in Fortran language, is able to model the propagation of stress waves and dispersion relations in dry (elastodynamic), saturated (two-phase poroelastodynamic), and three-phase frozen (multiphase poroelastodynamic) geomaterials using the meshless spectral element method. PoroSEM is called in the Python modules by means of Numpy F2PY that automatically generates the Fortran to Python bindings. GeoNDT is flexible, general-purpose, and can be used seamlessly for advanced signal interpretation in geophysical laboratory testing including the bender element (BE) and ultrasonic pulse velocity

Liu H., Maghoul P., Mantelet G., Shalaby A., 2021. *GeoNDT: an open source physics-based multiphase geomechanical solver for geotechnical and geophysical applications*, Acta Geotechnica, Manuscript ID: AGEO-D-21-00565, in Review (2021).

(UPV) tests, characterization of complex multiphase geomaterials, in-situ shallow seismic geophysics including the falling weight deflectometer (FWD) and multichannel analysis of surface waves (MASW) tests. The advanced physics-based signal interpretation feature of GeoNDT allows the quantitative characterization of geophysical and geomechanical properties of geomaterials and multilayered geosystems independently without making any simplified assumptions as common in the current practice.

7.1 Introduction

Non-destructive testing (NDT) plays an important role in the engineering, construction, and geophysical fields. The application of NDT in civil engineering is broad from quality control, structural health monitoring of infrastructure, geophysical and geotechnical field investigation, and material characterization to detection of underground anomaly, among others. More specifically in geotechnical engineering, the shear wave velocity of foundation soil is of great importance in the design of earthquake-resistant structures and determining the soil layers sensitive to liquefaction and resistance loss.

The most common techniques used for non-destructive evaluation and geophysical surveys include seismic methods, sonic echo/impulse response tests, ultrasonic tests, electrical resistivity tests, ground penetrating radar, magnetic methods, and gravity methods. The non-destructive material characterization tools, depending on the application and size, can be used in a laboratory setup or in the field. The GeoNDT software proposed in this paper provides advanced signal interpretation methods for ultrasonic-based as well as seismic-based geophysical surveys. Hereafter, we will briefly review the popular NDT techniques used in geotechnical engineering and the state-of-the-art literature regarding the physics-based signal interpretation methods.

The Bender Element (BE) test is one of the most popular laboratory techniques used for the evaluation of the shear wave velocity of soil samples. The BE utilizes piezo-ceramic materials for the conversion of an electrical signal into mechanical energy. Two bender elements are placed at the two ends of the soil specimen in which one BE is used to introduce a mechanical impulse and the other one is used to receive the propagating pulse. In a recent study by Liu, Cascante, Maghoul, and Shalaby (2021), the inefficiency of existing empirical methods in the selection of S-waves was discussed. They showed that the participation of P-waves, especially in loose sands and soft clays, cannot be predicted by existing empirical methods, which leads to an incorrect interpretation of S-waves arrival

time. They proposed a physics-based finite element model to study the soil-BE interaction so that sound recommendations can be given to improve the interpretation of BE tests in different soils (Liu, Cascante, Maghoul, and Shalaby, 2021). The Ultrasonic Pulse Velocity (UPV) test is commonly used for anomaly detection and strength evaluation of construction materials (e.g., concrete and steel). In the UPV test, an electrical charge is transmitted to the ultrasonic transmitter to generate the mechanical energy at one side of a test sample. The ultrasonic wave travels through the testing specimen and the induced motion is captured by an ultrasonic receiver. In the current practice, the first arrival time is used for the evaluation of P-wave velocity. However, the P-wave velocity alone is insufficient for full characterization of geomaterial samples, especially for determining the physical properties (Liu, Maghoul, and Shalaby, 2020b; Liu, Maghoul, and Thomson, 2021). The complex wave propagation in multiphase materials (e.g., saturated and frozen soils) and interactions with boundaries can be studied using the physics-based geomechanical models to better interpret the ultrasonic measurements.

The Multichannel Analysis of Surface Waves (MASW) is one of the most popular techniques for the in-situ evaluation of the shear wave velocity in different soil layers. In the MASW test, a vertical impact load is used to generate Rayleigh waves that propagate into different soil layers. The induced dynamic response is captured by a series of Geophones located at the ground surface. The interpretation of MASW measurements requires physics-based models to numerically reproduce the experimental dispersion relation for the prediction of the soil stratigraphy and soil properties. Falling weight deflectometer (FWD) is another in-situ testing method used to evaluate the mechanical properties of pavement structures. The FWD test measures the surface deflections induced by a dropping mass from a specific height onto a load plate placed on the pavement surface. Geophones are used to record the time histories of the vertical deflections of the pavement surface at various distances from the center of the load plate. Similarly, the interpretation of FWD measurements requires physics-based models to inversely analyze the measured displacement at various locations for the evaluation of the mechanical properties of pavement structures.

In the NDT techniques mentioned above, the dynamic response or dispersion analysis can be used to better interpret the measured signals by modeling the wave propagation in the ground, soil samples, and other construction materials. The dynamic response or dispersion analysis can be performed using various physics-based models. The existing methods used for solving these physics-based models are briefly reviewed as follows.

The elastodynamic model can be solved using numerical methods such as finite element (Fantuzzi, 2014; Huthwaite, 2014; Idesman, Schmidt, and Foley, 2011; Velichko and Wilcox, 2010) and finite difference methods (Bernth and Chapman, 2011; Dovgilovich and Sofronov, 2015; Saenger, Gold, and Shapiro, 2000; Zahradník and Priolo, 1995). The finite element method mainly has the following steps: a) discretization of the domain; b) selection of the interpolation functions (to provide an approximation of the unknown solution within an element) c) formulation of the system of equations and d) solution of the system of equations. In the finite difference method, the discretization of the domain is also required and the finite difference is used to replace the derivatives; in the end, a recursive algorithm is used to solve the system of equations. The boundary element method is also used for solving the elastodynamic model (Manolis, 1983; Banerjee, Ahmad, and Manolis, 1986; Cheng and Peng, 2005; Schanz and Antes, 1997; Kamalian, Jafari, Sohrabi-Bidar, Razmkhah, and Gatmiri, 2006). The boundary element method fits boundary values into the integral equation based on the given boundary conditions rather than values throughout the space defined by a partial differential equation. Then, the obtained integral equation is used again to calculate the solution at any desired point inside the study domain in the post-processing stage. The spectral element method was also developed for the solution of the elastodynamic model, which is mostly used for the soil response analysis in the FWD test (Al-Khoury, Scarpas, Kasbergen, and Blaauwendraad, 2001; Lee, 2014). The spectral element method combines the exact solution of wave propagation with the finite element framework of multilayered systems (Al-Khoury, Scarpas, Kasbergen, and Blaauwendraad, 2001). The advantage of the spectral element method is that one element is sufficient to describe a whole layer without the need for subdivisions or discretization, which results in a relatively smaller size of the system of equations and hence more computationally efficient. Recently, Liu, Maghoul, Shalaby, Bahari, and Moradi (2020) developed the dispersion relation of Rayleigh wave based on the spectral element method for the interpretation of MASW measurements.

The poroelastodynamic model is important in studying the interaction between the pore water and solid skeleton within saturated soils. The solution of the poroelastodynamic model has been developed through finite element method (Phillips and Wheeler, 2008; Panneton and Atalla, 1997; Berger, Bordas, Kay, and Tavener, 2017), analytical solution (limited to single-layer) (Zheng, Zhao, and Ding, 2013; Zhou, He, and Di, 2016; Chen, Beskou, and Qian, 2018; Zhou, He, Di, Guo, and Zhang, 2017), boundary element method (Ozyazicioglu and Ozkan, 2011; Soares and Godinho, 2020; Maghoul, Gatmiri, and

Duhamel, 2011a; Maghoul, Gatmiri, and Duhamel, 2011b) and spectral element method (Liu, Maghoul, Shalaby, Bahari, and Moradi, 2020; Liu, Maghoul, and Shalaby, 2021a). The extension of the poroelastodynamic model in frozen soil is another important area in studying the wave propagation in frozen or permafrost soils. The Biot theory of poroelasticity for three-phase media (solid skeleton, pore-water, and pore-ice) was developed by Leclaire, Cohen-Ténoudji, and Aguirre-Puente (1994), Carcione, Gurevich, and Cavallini (2000), Carcione and Seriani (2001), and Carcione, Santos, Ravazzoli, and Helle (2003). The solution was obtained through various numerical methods, such as a grid method based on the Fourier differential operator and a Runge–Kutta time-integration algorithm (Carcione and Seriani, 2001), finite element method (Santos and Sheen, 2007) and Zener element method (Liu, Greenhalgh, and Zhou, 2009). However, to the best of our knowledge, there is no commercially available software to solve the poroelastodynamic model and its extension for three-phase soils for multi-layered systems.

In the above-mentioned NDT applications, the measurements are mostly only available at locations where sensors are deployed. For example, the displacement measurement that is used for the site characterization is only monitored at the ground surface (rather than the entire domain) in the seismic tests. In the ultrasonic test or BE test, the measurement used for material characterization is only available at the receiver locations. In the volume-discretization numerical methods (e.g., finite element and finite difference methods), the solution is obtained by discretizing the entire domain. However, only the solutions obtained at the sensor locations are useful in the interpretation of NDT measurements and the computations in the remaining domain are not necessary. Therefore, the discretization of the entire domain significantly increases the computational time and cost.

In the GeoNDT software, by means of the meshless spectral element method, the solution can be accurately obtained at desired locations without solving the entire domain. GeoNDT supports the wave propagation analysis and dispersion analysis in multiphase media (dry, saturated and frozen geomaterials). In this paper, the structure of GeoNDT software and theoretical background of various computational geomechanical models are presented. Then, several case studies (e.g.,BE tests for dry and saturated soil samples, FWD tests for pavement system, MASW based liquefaction analysis and ultrasonic test for the scour detection around pile foundations) are presented to demonstrate the powerful capability of the GeoNDT software in NDT applications.

7.2 GeoNDT structure and theoretical background

7.2.1 GeoNDT structure

Considering the computational efficiency and user-friendly environment, the GeoNDT software is developed using a dual layer/hybrid Python and Fortran environment to benefit from the strengths of the two languages, as follows: a) Fortran is a compiled language; it is closer to the material architecture it is executed on; it benefits from established mathematical libraries and thus compensates for the lower computational performance of interpreted languages such as Python under CPU intensive tasks; b) Python is a user-friendly language; it has a wide support online; it has a rich set of high-quality scientific computational libraries and frameworks; and it offers improved code reusability, faster and cost-effective development. One of Python's scientific libraries, Numpy, proposes the F2PY tool (Peterson, 2009) to efficiently bind Fortran and Python functions together, and helped us develop a framework that can simply a) load data from configuration files, in formats widely supported in the IT field (such as JavaScript Object Notation (JSON)), and b) calls Fortran subroutines. Python's slower overhead and function calls is alleviated by its ability to effectively load interchangeable models by using Object Oriented Programming (OOP) practices such as inheritance and composition.

GeoNDT uses state-of-the-art practices, and the Fortran and Python languages are combined to obtain a tradeoff between a resourceful user-friendly environment and high computational efficiency. In the hybrid Python and Fortran environment, the dependencies required to be installed include a Fortran compiler (e.g., GFortran, Intel Fortran, Absoft Fortran), Fortran Linear Algebra Package (LAPACK), as well as several Python libraries (e.g., Numpy, Scipy, Joblib and Matplotlib). The definition of a setup script that can be easily interpreted by Python setuptools enables and simplifies automatic installation of these required libraries on both Windows and Linux operating systems.

The main components of GeoNDT include a) the Python setup script, called `Setup.py`, that automatically writes the Python-Fortran interface using the F2PY tool and installs required python dependencies for GeoNDT (Numpy, Scipy, Joblib, Matplotlib); b) a Fortran-written computational geomechanics source code, called `PoroSEM.f90`, that includes several subroutines for dynamic analyses of finite (for laboratory geotechnical testing) and half-space (for in-situ seismic geophysical testing) domains for dry (`one_phase_finite.f90` and `one_phase_infinite.f90`), saturated (`two_phase_finite.f90` and `two_phase_infinite`), and frozen soils

(three_phase_finite.f90 and three_phase_infinite.f90) as well as dispersion analyses (one_phase_dispersion.f90, two_phase_dispersion.f90, and three_phase_dispersion.f90); c) independent Python geomechanical modules and classes (e.g., one_phase_dispersion.py, one_phase_dynamic.py, two_phase_dispersion.py, two_phase_dynamic.py, three_phase_dispersion.py and three_phase_dyna inheriting from generic classes, and offering the ability to extend existing models, and connect to future Fortran subroutines as they are added to enrich our model; and d) Python main script (main.py) to set up the geomechanical model (e.g., the specification of python modules and classes, material properties, geometry, time interval and time step, and the position of sensors during geophysical measurements as inputs).

Figure 7.1 shows a simplified representation of execution in the dual hybrid Fortran/Python approach. Functionalities provided by Python, such as the dataclasses in Python 3.7, that allows neat description of the Python geomechanical modules and classes, or the native JSON package, can be assembled to enable the parsing of a configuration file, and its translation to a dictionary of parameters. These geomechanical parameters can then be easily transferred, for example, as dummy arguments to Python geomechanical modules and classes as well as target Fortran subroutines with a handful lines of source code. Python layer (Python geomechanical modules and classes as well as Python main program, main.py) presents to Fortran subroutines (implemented in PoroSEM.f90) a set of inputs from JSON files. F2PY provides bindings from Fortran to Python and vice versa, so that Python functions or methods can call Fortran subroutines, and likewise, Fortran subroutines can call back Python functions. The Python layer also benefits from Python libraries such as Joblib to enable parallel computing, thus executing simultaneously multiple Fortran calls.

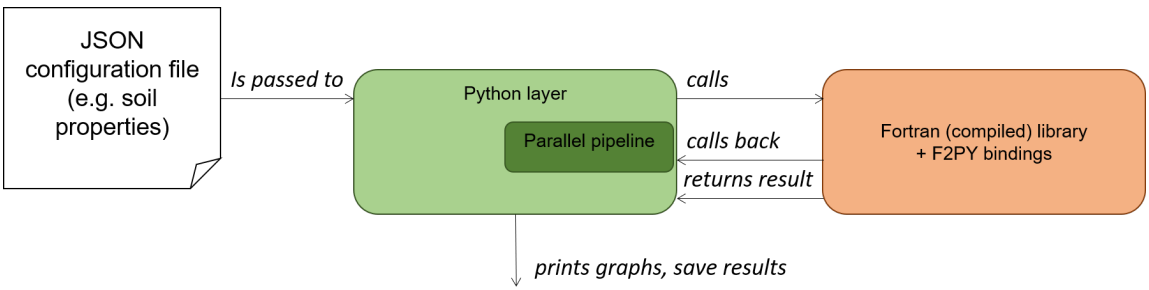

FIGURE 7.1: Simplified representation of execution in the dual hybrid Fortran/Python approach

The logical structure of the computational source code in GeoNDT is presented as a matrix in Figure 7.2. Each Python module and class (from bottom layer) corresponds to

a set of Fortran subroutines (top layer) to be bound. Fortran and Python modules are organized depending on the application and logical function they intend to achieve (e.g. one-phase, two-phase, or three-phase solver), as presented in dashed columns in Figure 7.2. By means of the F2PY tool, these Fortran subroutines (`*.f90`) are converted into Python wrapper (PoroSEM library) in which various solver functions (e.g., `one_phase_finite`, `one_phase_infinite`, `one_phase_dispersion`, `two_phase_finite`, `two_phase_infinite`, `two_phase_dispersion`, `three_phase_finite`, `three_phase_infinite`, `three_phase_dispersion`) are defined. The selection of these functions depends on the type of analysis (dynamic response analysis or dispersion analysis) and the soil domain in each geophysical application (finite domain for laboratory geophysical testing or half-space domain in in-situ seismic geophysical testing). The PoroSEM library is then imported to the Python geomechanical modules and classes, which is then called in the Python main program (`main.py`) for geophysical applications.

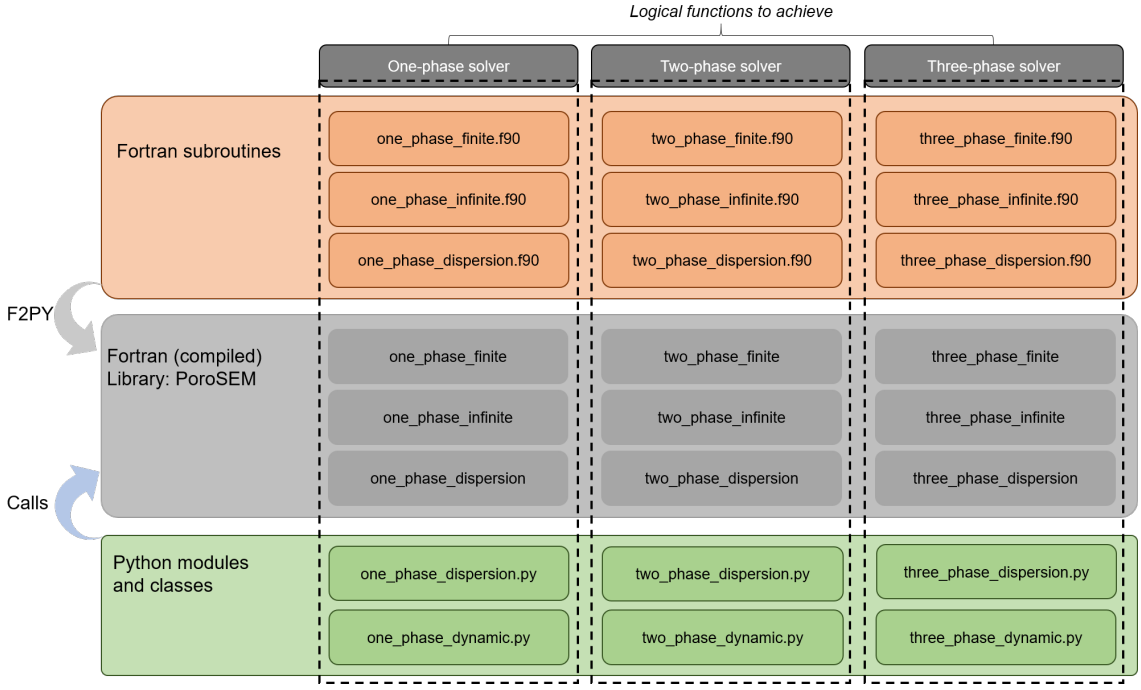

FIGURE 7.2: Logical structure of the source code in GeoNDT package

As mentioned above, the Python geomechanical modules and classes are developed for the dynamic response and dispersion analyses of bounded or half-space geomaterials. In the Python geomechanical modules and classes, designed for the dynamic response analysis, several components are included to a) call the desired function through the PoroSEM library; b) define external loads in the Laplace domain; c) perform inverse Laplace transform. The Python joblib library, imported in various python modules, offers

a simple and efficient option to parallel computing (see Figure 7.1); an approach that can make GeoNDT span up to multiple CPU cores and threads in parallel to solve a) the dispersion analysis, b) the geomechanical models, and c) root searching algorithm for inverse calculations.

The Python main program (`main.py`) of GeoNDT can provide the Python geomechanical modules and classes with inputs from different sources, either under JSON, CSV or XML format, or even under static TXT format requiring specific parsing. The main benefit of the JSON format is that Python comes with a native package to load the file and obtain the data on a flexible dictionary. In the case of the one-phase solver (e.g., `one_phase_dispersion.py` and `one_phase_dynamic.py`), for instance, the P-wave velocity, S-wave velocity, (equivalent to the Young's modulus and Poisson's ratio) and density are required for dynamic response or dispersion analyses in GeoNDT. The two-phase solver (e.g., `two_phase_dispersion.py` and `two_phase_dynamic.py`), on the other hand, needs the porosity, P-wave velocity, S-wave velocity, (equivalent to the Young's modulus and Poisson's ratio) and density as inputs of geomaterial properties. In the three-phase solver (e.g., `three_phase_dispersion.py` and `three_phase_dynamic.py`), the porosity, ice content, P-wave velocity, S-wave velocity (equivalent to the Young's modulus and Poisson's ratio), and density of the solid skeleton are required as the inputs of geomaterial properties. Other inputs including geometrical parameters (e.g., the diameter and thickness of each soil layer), the specification of the nodes corresponding to the external load and sensor locations, and the time/frequency ranges are also required in GeoNDT. The distribution of the external load in the Laplace domain is pre-defined in Python geomechanical modules and classes for the dynamic analysis. Subclassing the implementation allows users to override this method for extending the model to their needs. Other properties (e.g., properties of pore water and pore ice, number of cores in parallel computing, number of iteration in the inverse Laplace transform) are also optional inputs in GeoNDT and can either be set to defaults or added by subclassing in our Python geomechanical modules and classes.

The main steps used in the Python main program (`main.py`), modules and classes as well as Fortran PoroSEM library are summarized in Figure 7.3 and are briefly described as follows:

- Input geomaterial properties, geometry of the modeling domain and other parameters (e.g., the specification of the nodes corresponding to the external load and sensor locations, and the time/frequency ranges). These inputs are firstly defined in JSON configuration file, and then parsed to a Python dictionary, as shown in Figure 7.3.

- Determine solver types (e.g., one-phase solver, two-phase solver and three-phase solver) based on the degree of complexity of geomaterials or geostructures to be analyzed, as listed in Figure 7.3.

- Determine the analysis types, which can be dynamic response analysis or dispersion analysis (Figure 7.3). As illustrated in Figure 7.4, each of the solvers (e.g., one-phase solver, two-phase solver and three-phase solver) has options for performing either dynamic response analysis or dispersion analysis.

- Call the corresponding Python modules and classes based on the selected solver and analysis types. For example, by selecting the one-phase solver for dynamic analysis, the corresponding Python modules that should be called is `one_phase_dynamic.py`, as indicated in Figure 7.4.

- Determine the attribute (finite or half-space) of the last layer in the domain for the dynamic analysis, as shown in Figure 7.4. In GeoNDT, it is assumed that the dispersion analysis is performed for only the half-space domain.

- Call the corresponding Python functions (e.g., `run_f()`, `run_f()`, `run()`, `run_R1()`, `run_R2()`) embedded in Python modules and classes based on the selected attribute of the last layer in the domain. As shown in Figure 7.4, the Python functions, `run_f()` and `run_i()`, should be called for dynamic analysis in finite domain and half-space domain, respectively. For the dispersion analysis in the one-phase solver and two-phase solver, the Python function, `run()`, should be called. In the three-phase solver, the Python function, `run_R1()` and `run_R2()` are called for the dispersion analysis of R1 and R2 Rayleigh waves.

- Compute the displacement, stress and stiffness matrices of each layer based on the selected Fortran subroutine (`PoroSEM.f90`). Then assemble the global stiffness matrix based on the stiffness matrix calculated for each layer, as shown in Figure 7.3.

- For the dynamic analysis, the `PoroSEM.f90` code obtains the dynamic response (e.g., displacement or stress) for the given input load in the Laplace domain. Then the Python-based inverse Laplace transform (Horváth, Horváth, Almousa, and Telek, 2020) is used to calculate the response in the time domain, as shown in Figure 7.3. The inverse Laplace transform is a time intensive task that can be quickened by using a thread pool. Python Joblib enables parallel computing to take advantage of multicore and multithreaded architectures offered by modern workstations.

- For the dispersion analysis, the global stiffness matrix is exported from PoroSEM.f90 and the Python-based root searching algorithm (Liu, Maghoul, Shalaby, Bahari, and Moradi, 2020) is applied to determine the dispersion relation for the given domain, as shown in Figure 7.3. The global stiffness matrix is a function of angular frequency and wavenumber. For a constant frequency, the value of the wavenumber can be determined when the determinant of the global stiffness matrix is zero. The different wavenumbers determined at a given frequency correspond to dispersion curves of different modes.

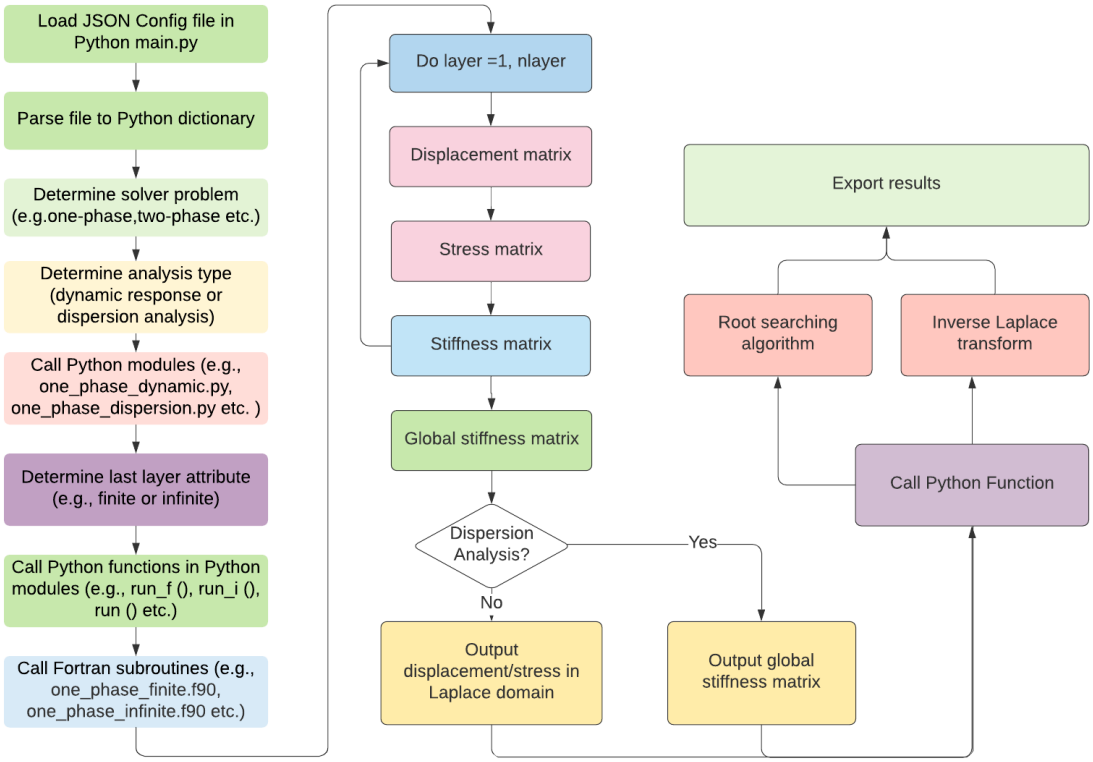

FIGURE 7.3: Overall flow and main steps in the Python main program, modules and classes as well as Fortran PoroSEM library

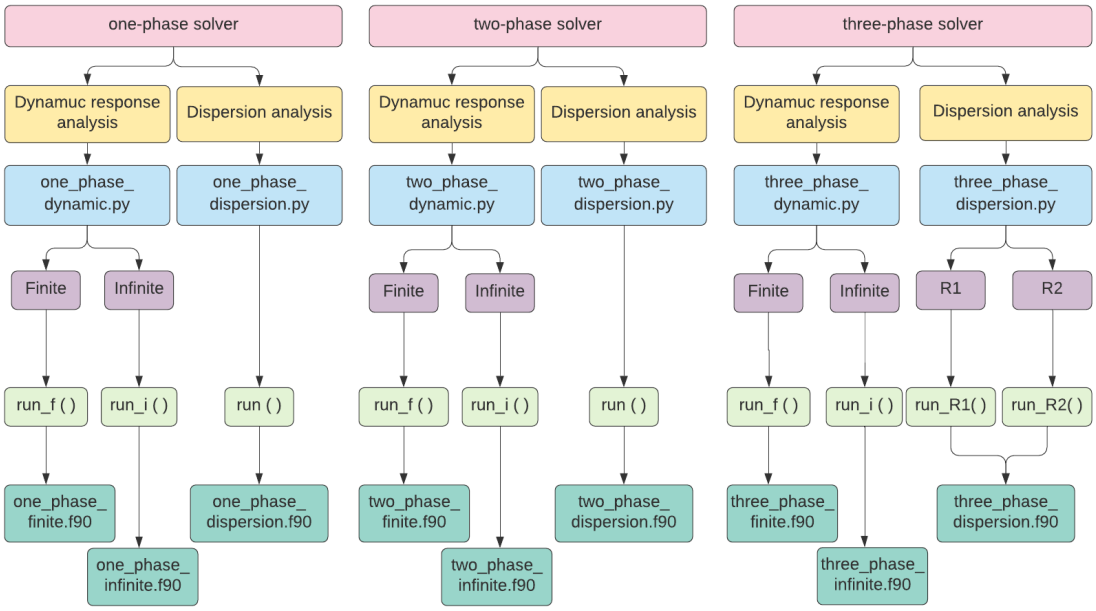

FIGURE 7.4: Selection of solver types and corresponding Python modules and Fortran subroutines

7.2.2 Theoretical background

Based on the assumption of infinitesimal deformation, the governing equation of elastodynamic model (one-phase solver) that describes elastic wave propagation in dry geomaterials, is written as (Liu, Maghoul, Shalaby, Bahari, and Moradi, 2020):

$$(\lambda + 2\mu)\,\nabla\nabla\cdot \mathrm{u_i} - \mu\nabla\times\nabla\times \mathrm{u_i} = \rho\ddot{\mathrm{u}}_\mathrm{i} \tag{7.1}$$

where λ and μ are the Lamé coefficients; u_i is the displacement vector; ρ is the bulk density of soil; $\ddot{u}_i$ is the second derivative of displacement in terms of time.

In saturated geomaterials, by assuming the infinitesimal deformation of the solid skeleton, the governing equations of two-phase poromechanical model (two-phase solver) is written in matrix form, as shown in Equation 7.2. The detailed description of the two-phase poromechanical model can be found in Liu, Maghoul, and Shalaby (2020b).

$$\boldsymbol{\rho}\begin{bmatrix}\ddot{u}_i\\ \ddot{w}_i\end{bmatrix} + \boldsymbol{b}\begin{bmatrix}\dot{u}_i\\ \dot{w}_i\end{bmatrix} = \boldsymbol{R}\nabla\nabla\cdot\begin{bmatrix}u_i\\ w_i\end{bmatrix} - \boldsymbol{\mu}\nabla\times\nabla\times\begin{bmatrix}u_i\\ w_i\end{bmatrix} \tag{7.2}$$

where

$$\boldsymbol{\rho} = \begin{bmatrix} \rho & \rho_f \\ \rho_f & m \end{bmatrix} \quad \boldsymbol{b} = \begin{bmatrix} 0 & 0 \\ 0 & b \end{bmatrix}$$

$$\boldsymbol{R} = \begin{bmatrix} \lambda_c + 2\mu & \alpha m \\ \alpha m & M \end{bmatrix} \quad \boldsymbol{\mu} = \begin{bmatrix} \mu & 0 \\ 0 & 0 \end{bmatrix}$$

where u_i is the displacement vector of the solid skeleton; w_i is the fluid displacement relative to the solid skeleton; λ and μ are the Lamé constants; α is the Biot coefficient; M is $1/(\frac{\phi}{K_f} + \frac{\alpha-\phi}{K_s})$ in which K_f is the bulk modulus of the fluid; K_s is the bulk modulus of the solid skeleton and ϕ is the porosity. $\lambda_c = \lambda + \alpha^2 M$; $m = \rho_f \beta/\phi$ in which β is the tortuosity which is used to describe the diffusion properties in porous media, and ρ_f is the density of pore-water, taken as 1000 kg/m^3. The drag-force damping coefficient b is calculated as (Zhang, Xu, and Xia, 2011): $b = \eta/\kappa\ F$, where η is the fluid dynamic viscosity and κ is the permeability coefficient; F is the viscous correction factor (Johnson, Koplik, and Dashen, 1987).

In three-phase frozen geomaterials, through the infinitesimal kinematic assumption, the stress-strain constitutive model (Carcione and Seriani, 2001; Liu, Maghoul, Shalaby, and Douglas, 2021; Liu, Maghoul, and Shalaby, 2021b) and conversation of momentum, the field equation of three phase poromechanical model (three-phase solver) can be written in the matrix form, as shown in Equation 7.3. The terms in matrix $\boldsymbol{\rho}$, $\boldsymbol{b}$, $\boldsymbol{R}$ and $\boldsymbol{\mu}$ can be found in Carcione and Seriani (2001), Liu, Maghoul, Shalaby, and Douglas (2021), and Liu, Maghoul, and Shalaby (2021b).

$$\boldsymbol{\rho} \begin{bmatrix} \ddot{u}_i^s \\ \ddot{u}_i^w \\ \ddot{u}_i^i \end{bmatrix} + \boldsymbol{b} \begin{bmatrix} \dot{u}_i^s \\ \dot{u}_i^w \\ \dot{u}_i^i \end{bmatrix} = \boldsymbol{R}\nabla\nabla\cdot \begin{bmatrix} u_i^s \\ u_i^w \\ u_i^i \end{bmatrix} - \boldsymbol{\mu}\nabla\times\nabla\times \begin{bmatrix} u_i^s \\ u_i^w \\ u_i^i \end{bmatrix} \tag{7.3}$$

where

$$\boldsymbol{\rho} = \begin{bmatrix} \rho_{11} & \rho_{12} & \rho_{13} \\ \rho_{12} & \rho_{22} & \rho_{23} \\ \rho_{13} & \rho_{23} & \rho_{33} \end{bmatrix} \quad \boldsymbol{b} = \begin{bmatrix} b_{12}+b_{13} & -b_{12} & -b_{13} \\ -b_{12} & b_{12}+b_{23} & -b_{23} \\ -b_{13} & -b_{23} & b_{13}+b_{23} \end{bmatrix}$$

$$\boldsymbol{R} = \begin{bmatrix} R_{11} & R_{12} & R_{13} \\ R_{12} & R_{22} & R_{23} \\ R_{13} & R_{23} & R_{33} \end{bmatrix} \qquad \boldsymbol{\mu} = \begin{bmatrix} \mu_{11} & 0 & \mu_{13} \\ 0 & 0 & 0 \\ \mu_{13} & 0 & \mu_{33} \end{bmatrix}$$

GeoNDT solves the above-mentioned geomechanical models through the spectral element method. The important steps used in the spectral element method include: a) decomposing the displacement fields into longitudinal and transverse vector components by means of Helmholtz's decomposition, then we can obtain several uncoupled partial differential equations (the number of equations depends on the number of phases in soils); b) performing the Laplace transform for the time variable treatment; c) decomposing each of the uncoupled partial differential equations into two independent functions in radial and vertical directions in cylindrical coordinates; d) deriving two-node element solutions for a layer with finite thickness; e) deriving one-node element solutions for the half-space layer. GeoNDT calculates the stiffness matrix of each layer and then assembles the global stiffness matrix using a method similar to the finite element framework. With the input boundary conditions (external forces), GeoNDT obtains the solution in the Laplace or Frequency domain. For dynamic analysis, the inverse Laplace transform is used to obtain the solution in the time domain. For dispersion analysis, the root searching algorithm is used to determine the dispersion relation for the given system. More details about this procedure can be find in Liu, Maghoul, Shalaby, Bahari, and Moradi (2020), Liu, Maghoul, and Shalaby (2020b), and Liu, Cascante, Maghoul, and Shalaby (2021).

7.3 GeoNDT application examples

In this section, GeoNDT is used to study four different NDT applications, including BE tests for dry and saturated soil samples, FWD tests for pavement systems, liquefaction analysis for foundation soils using MASW and ultrasonic test for the scour detection around pile foundations.

7.3.1 Bender Element testing

GeoNDT can efficiently study the three-dimensional wave propagation within soil samples in the BE test. In this case study, the soil sample is assumed to be 7.0 cm in diameter and 14 cm in height. The density of the dry sand is 1,800 kg/m^3. The P-wave and S-wave velocities of the soil sample are assumed as 380 m/s and 240 m/s (equivalent to a Young's

modulus of 242 MPa and Poisson's ratio of 0.168), respectively (Liu, Cascante, Maghoul, and Shalaby, 2021). A 10 kHz impulse is applied at the base of a soil sample to simulate the BE transmitter motion. GeoNDT can model the wave propagation within the soil specimen with only two nodes (one at the transmitter and the other one at the receiver location) and one element. Based on the provided time range, Young's modulus, Poisson's ratio, density as well as the geometrical parameters of the soil sample, GeoNDT predicts the dynamic response at the receiver location by calling the Python module `one_phase_dynamic.py` and Python function `run_f()`. The JSON configuration file and code example for BE modeling in the Python main program is shown in Listing 1 and 2, respectively. The BE transmitter signal and predicted signal at the receiver location are shown in Figure 7.5.

```
{
"input":{
    "tmin": 3e-4,     # minimum time (s)
    "tmax": 150e-5,   # maximum time (s)
    "tlin": 200,      # number of points within tmin and tmax
    "E": [2.42e8],    # Young's modulus (Pa)
    "mu": [0.168],    # Poisson's ratio
    "rho": [1800],    # density (kg/m^3)
    "H": [0.14],      # thickness (m)
    "r": 0.0001,      # radial location of ultrasonic receiver
    "rmax": 0.035,    # radius of soil sample
    "node": 1,        # output node
    "loc": 3,         # input node
    "st": 0,          # displacement output
    "lap_num": 50,    # number of iteration in inverse Laplace transform
    "ncore": -1       # the number of cores (-1 denotes for all cores)}
}
```

LISTING 7.1: JSON configuration file (BE_dry.json) for BE test within the dry soil sample

```
from geondt import one_phase_dynamic
import json

with open('BE_dry.json', "r") as f:
    data = json.load(f)

BE = one_phase_dynamic(**data["input"])
```

```
yt = BE.run_f() # run model for finite domain
```

LISTING 7.2: Python main program for wave propagation modeling within the dry soil sample in BE test by the GeoNDT

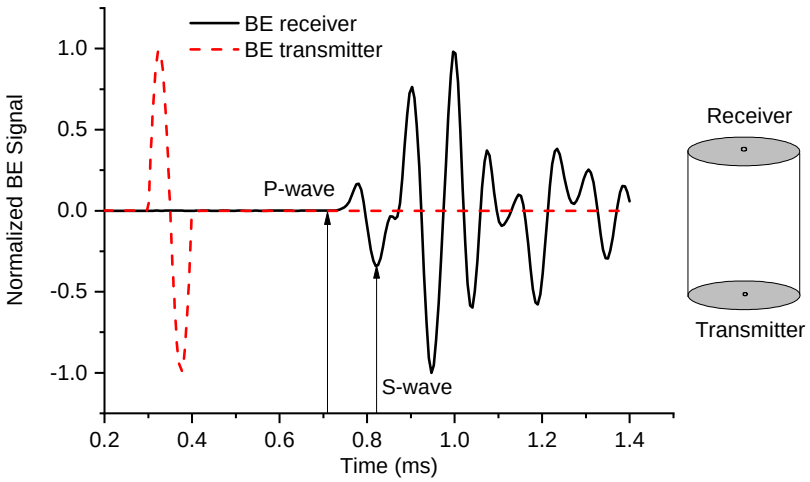

FIGURE 7.5: Predicted dynamic response at the BE receiver location for the dry soil sample by GeoNDT

Users can easily modify the input signal at the BE transmitter location by defining a Python function that describes the input signal in the Laplace domain. For example, a 10 kHz impulse can be defined and passed to Python module (`one_phase_dynamic.py`) as shown in Listing 3 (assuming the same inputs as the Listing 1).

```
import numpy as np
from geondt import one_phase_dynamic
import json

def load(s):
    ''' Define external load in the Laplace domain (for BE example)'''
    fn1=-2e4*(np.exp(-np.complex(s)/(2000)))*np.pi/(4e8*np.pi**2+np.complex
    (s)**2)
    fn2=2e4*(np.exp(-np.complex(s)/(2500)))*np.pi/(4e8*np.pi**2+np.complex(
    s)**2)
    fn=fn1+fn2
    return fn

with open('BE_dry.json', "r") as f:
    data = json.load(f)

BE = one_phase_dynamic(**data["input"])
```

```
BE.load_f = load
yt = BE.run_f() # run model for finite domain
```

LISTING 7.3: Customize the input signal in BE test by GeoNDT

Similarly, GeoNDT can study the wave propagation in saturated soil samples in the BE test. In this case study, the dynamic response at the BE receiver location is studied for soil sample with a volumetric water content of 20% and 50%. The P-wave and S-wave velocities of the saturated soil sample can be calculated based on the properties of solid skeleton and volumetric water content (Foti, Lai, and Lancellotta, 2002), as shown in Equation 7.4.

$$V_p = \sqrt{\frac{K_{sk} + \frac{4}{3}G + \frac{K_F}{\phi}}{(1-\phi)\rho_s + \phi\rho_f}} \tag{7.4a}$$

$$V_s = \sqrt{\frac{V_p^2 - \frac{K_f}{\phi(\phi(\rho_f - \rho_s)+\rho_s)}}{2\frac{1-\mu^{sk}}{1-2\mu^{sk}}}} \tag{7.4b}$$

where K_{sk} is the bulk modulus of the soil skeleton, taken as 30 kPa; G is the shear modulus of the soil skeleton, taken as 18 kPa; K_f is the bulk modulus of pore water, taken as 2.25 GPa; ϕ is the porosity or volumetric water content; ρ_s and ρ_f are the density of soil particles and pore water, taken as 2700 kg/m^3 and 1000 kg/m^3, respectively; μ_{sk} is the Poisson's ratio of the soil skeleton, taken as 0.25 (Foti, Lai, and Lancellotta, 2002).

Based on Equation 7.4, the shear wave velocities for the soil sample with a volumetric water content of 20% and 50% are 87 m/s and 99 m/s, respectively. Figure 7.6 illustrates the effect of volumetric water content on the BE measurement at the receiver location. The BE measurement is predicted to be sensitive to the amount of volumetric water content in soil samples (as shown in Figure 7.6). This case study also demonstrates the potential for the measurement of porosity by means of the BE test. The JSON configuration file and sample code for Python main program for the BE testing in the saturated soil sample is given in Listing 4 and 5, respectively. The input parameters are firstly defined and then passed to the Python module `two_phase_dynamic.py` for the prediction of the dynamic response at the BE receiver location.

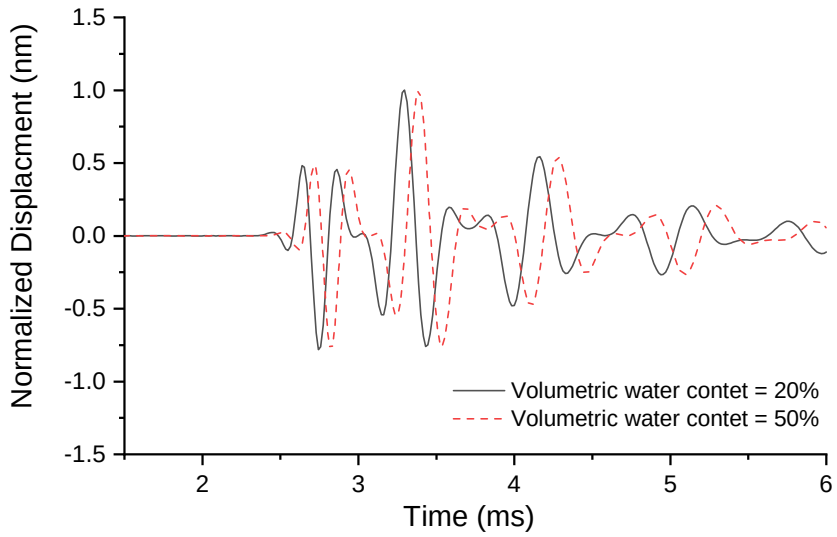

FIGURE 7.6: GeoNDT modeling of the BE test in two saturated soil samples with volumetric water contents of 20% and 50%

```
{
"input": {
    "tmin": 4e-5,     # minimum time (s)
    "tmax": 600e-5,   # maximum time (s)
    "tlin": 400,      # number of points within tmin and tmax
    "E": [465066],    # Young's modulus (Pa)
    "mu": [0.47],     # Poisson's ratio
    "rho": [1800],    # density (kg/m^3)
    "H": [0.14],      # thickness (m)
    "kh": [10e-6],    # permeability coefficient (m^2) of bulk soil
    "porosity": [0.2], # porosity
    "r": 0.0001,      # radial location of ultrasonic receiver
    "rmax": 0.035,    # radius of soil sample
    "node": 1,        # output node
    "loc": 3,         # input node
    "st": 0,          # displacement output
    "lap_num": 50,    # number of iteration in inverse Laplace transform
    "ncore": -1       # the number of cores (-1 denotes for all cores)}
}
```

LISTING 7.4: JSON configuration file (BE_saturated.json) for BE test within the saturated soil sample

```
from geondt import two_phase_dynamic
import json

```

```
with open('BE_saturate.json', "r") as f:
    data = json.load(f)

BE = two_phase_dynamic(**data["input"])
yt = BE.run_f() # run model for finite domain
```

LISTING 7.5: Wave propagation modeling in the saturated soil sample in the BE test by GeoNDT

7.3.2 Falling Weight Deflectometer

The dynamic response model in GeoNDT is validated with the FWD case study performed by Al-Khoury, Scarpas, Kasbergen, and Blaauwendraad (2001). A pavement with a three-layer system (asphalt, concrete and subgrade) is subjected to a 50 kN impact load with a 25 ms duration. A detailed description of such a system can be found in Al-Khoury, Scarpas, Kasbergen, and Blaauwendraad (2001). The deflection results at various radial locations (0 mm, 300 mm and 600 mm) calculated by GeoNDT are compared with the results reported by Al-Khoury, Scarpas, Kasbergen, and Blaauwendraad (2001). As shown in Figure 7.7, an excellent agreement is achieved despite different methods employed for time-variable treatment.

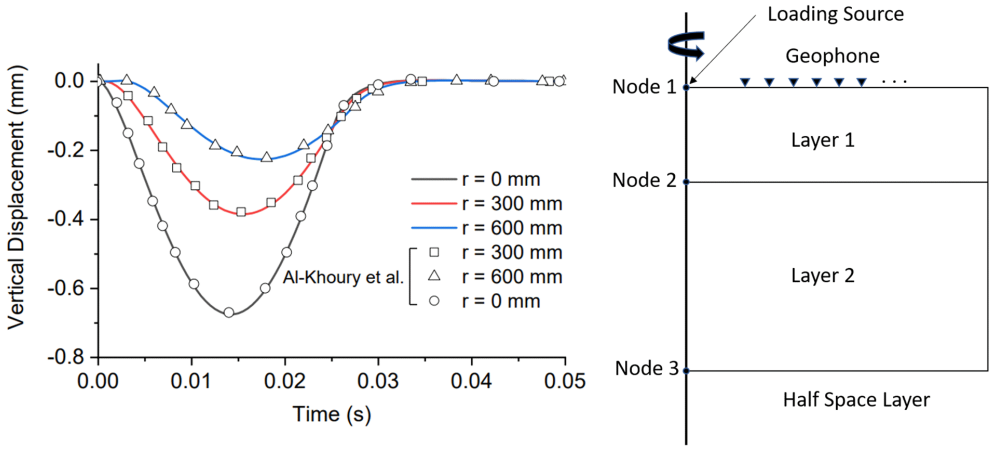

FIGURE 7.7: Validation of the dynamic response of a three-layer pavement system during a FWD test in comparison with Al-Khoury, Scarpas, Kasbergen, and Blaauwendraad (2001)

The mandatory and optional parameters (e.g., mechanical properties, the thickness of each layer, sensor locations and so on) need to be defined first in the JSON configuration file, as illustrated in Listing 6. It should be noted that the thickness in the last layer is not

used for the calculation. However, it is required to provide an arbitrary input to ensure consistency in the dimension of variables. The Python code considering a three-layer system with non-reflecting boundary conditions in the last layer is demonstrated in Listing 7. By calling Python module `one_phase_dynamic.py` and Python function `run_i()` in GeoNDT, the user can obtain the dynamic response at the pavement surface at any given location.

```
{
"input":{
    "tmin": 0.001,  # minimum time (s)
    "tmax": 0.05,   # maximum time (s)
    "tlin": 200,    # number of points within tmin and tmax
    "E": [1000.0e6, 200.0e6, 100.0e6], # Young's modulus (Pa)
    "mu": [0.35, 0.35, 0.35],          # Poisson's ratio
    "rho": [2300.0, 2000.0,1500.0],    # density (kg/m^3)
    "H": [0.15, 0.25, 5],              # thickness (m)
    "r": 0,         # radial  distance  of sensor location
    "rmax": 20,     # maximum radius
    "node": 2,      # node for sensor location
    "loc": 2,       # node for impact load}
}
```

LISTING 7.6: JSON configuration file (FWD.json) for the FWD test

```
from geondt import one_phase_dynamic
import json

with open('FWD.json', "r") as f:
    data = json.load(f)

FWD = one_phase_dynamic(**data["input"])
yt = FWD.run_i() # run model for infinite domain
```

LISTING 7.7: Python main program for the dynamic response analysis of the FWD Test by GeoNDT

GeoNDT also supports the inversion analysis to back-calculate the mechanical properties of pavement layers. For the demonstration purpose, the synthetic displacement measurements at 0 mm shown in Figure 7.7 are used to determine the mechanical properties in each pavement layer. Various methods such as the trust region reflective (TRR) method, Powell method, BFGS algorithm, TNC algorithm (available in Python Scipy library) are used to reduce the Euclidean distances between the synthetic and calculated

displacement. In this inversion analysis, it is assumed that Young's modulus and Poisson's ratio are unknown. Figure 7.8 shows the loss function using the above-mentioned algorithms. It is found that the prediction by TRR method has the minimum loss function in comparison to other methods. The updates of Young's modulus are also given in Figure 7.8b. After 700 iteration, Young's modulus converged to 755 MPa, 194 MPa and 100 MPa for first, second and third layer, respectively. Overall, these predicted values are consistent with the original values used by Al-Khoury, Scarpas, Kasbergen, and Blaauwendraad (2001), which shows the potential of GeoNDT in the evaluation of the pavement system properties by the FDW test.

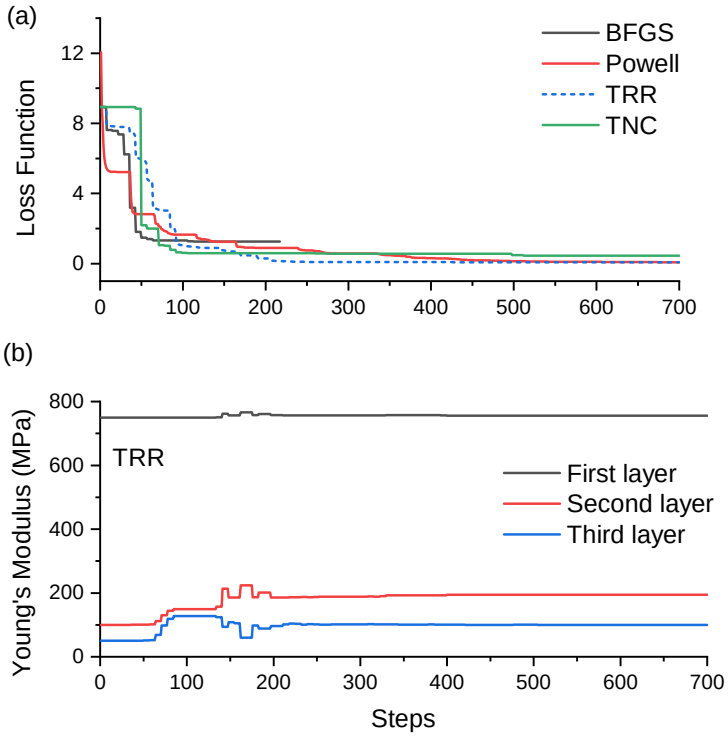

FIGURE 7.8: Inversion results of the FWD test (a) loss function of four different methods (2) update of Young's modulus by the TRR method

The implementation of GeoNDT-based inversion analysis is given in Listing 8. Firstly, users need to define the objective function in Python that takes optimization variables as inputs (i.e. Young's modulus and Poisson's ratio in this case study). Then based on the provided bounds and initial guess of each variable, various Python optimization functions (e.g., BFGS, Powell, TRR and TNC) can be used to find the best solution with the minimum objective function. In this case study, it is found the initial guesses can play an important role in the final prediction of the pavement structure properties due to the limitations of the

local optimization methods. The global optimization methods are expected to reduce the effect of initial guesses on the final solutions (this can also be easily integrated in GeoNDT).

```
import numpy as np
from geondt import one_phase_dynamic
from scipy.optimize import minimize

def obj(x):
    global yt_m, tmin, tmax. tlin, rho, r, rmax, H, loc, node
    E = np.array([x[0],x[1],x[2]])*(10.0**6)    # Young's  modulus (Pa)
    mu = [x[3],x[4],x[5]] # Poisson's ratio
    FWD=one_phase_dynamic(tmin,tmax,tlin,E,mu,rho,H,r,rmax,loc,node)
    yt = FWD.run_i()
    loss = np.abs(yt-yt_m)) # loss function (yt_m is experimental
    measurement)
    return loss

bnds = ((500,1500),(100,500),(50,200),(0.15,0.4),(0.15,0.4),(0.15,0.4)) #
    Bounds for each variable
init = (750,100,50,0.1,0.1,0.15) # Inital guess for each variable
results = minimize(obj,init,method='Powell',bounds=bnds) # Optimization
```

LISTING 7.8: GeoNDT inversion analysis for the FWD test

7.3.3 MASW application for liquefaction analysis

The shear wave velocities obtained by the MASW test can be used for the liquefaction analysis of a site. In this case study, the three-layer system studied by Wood, Cox, Green, Wotherspoon, Bradley, and Cubrinovski (2017) is used to demonstrate the liquefaction analysis using GeoNDT. The MASW dispersion measurement is used firstly to predict the shear wave velocity of each layer through an inversion analysis. The sample code for MASW inversion analysis is given in Listing 9. By means of the TRR method, the calculated dispersion curve fits well with the experimental dispersion curve, as shown in Figure 7.9a. Figure 7.9b shows the corresponding loss function that is reduced to almost zero after 1800 iterations. It is found that the shear wave velocity is 100 m/s, 125 m/s and 300 m/s for the first, second and third layer, respectively. The update of shear wave velocity and thickness of each layer in MASW inversion analysis is given in Figure 7.10. Based on the relation between volumetric water content and shear wave velocity derived by Foti, Lai, and Lancellotta (2002), the volumetric water content is computed as 0.243, 0.245 and 0.262 for the first, second and third layer, respectively.

```python
import numpy as np
from geondt import one_phase_dispersion
from scipy.optimize import minimize

def obj(x):
    global f1, f2, flin, yt_m
    mu = [0.3, 0.3, 0.3]  # Poisson's ratio
    vs = np.array([x[0]**2, x[1]**2, x[2]**2])   # S-wave velocity (m/s)
    H = np.array([x[3],x[4], 5]) # Thickness (m)
    E = rho1*vs*2*(1+mu) # Young's modulus (Pa)
    MASW = one_phase_dispersion(f1, f2, flin, E, mu, rho, H)
    yt = MASW.run() # Numerical prediction
    loss = np.sum(np.abs(yt-yt_m))  # yt_m is the experimental measurement
    return loss

bnds = ((50,500),(50,500),(50,500),(1,10),(1,10)) # bounds for each
    variable
init = (50,50,50,5,5) #initial guess of each variable
res = minimize(fun,init,method='trust-constr',bounds=bnds) # Optimization
```

LISTING 7.9: Dispersion and inversion analysis for MASW test using GeoNDT

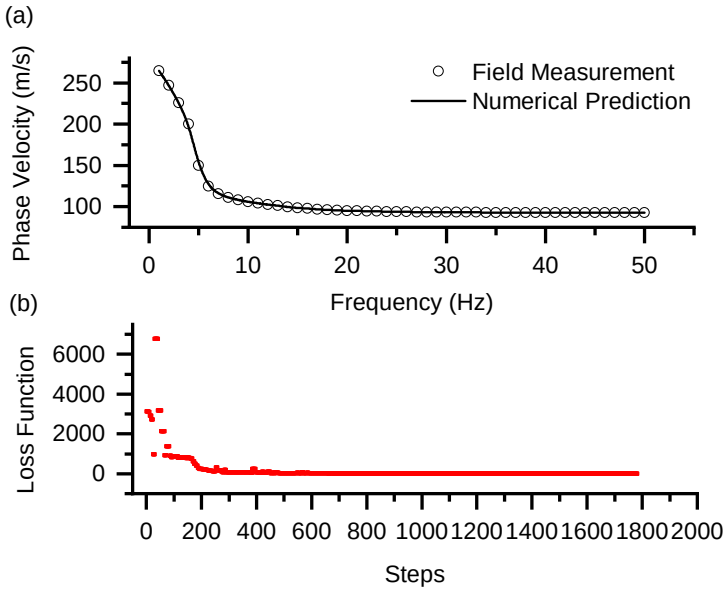

FIGURE 7.9: Application of GeoNDT for the MASW test (a) comparison between the experimental and numerical dispersion curves. (b) loss function with iteration steps

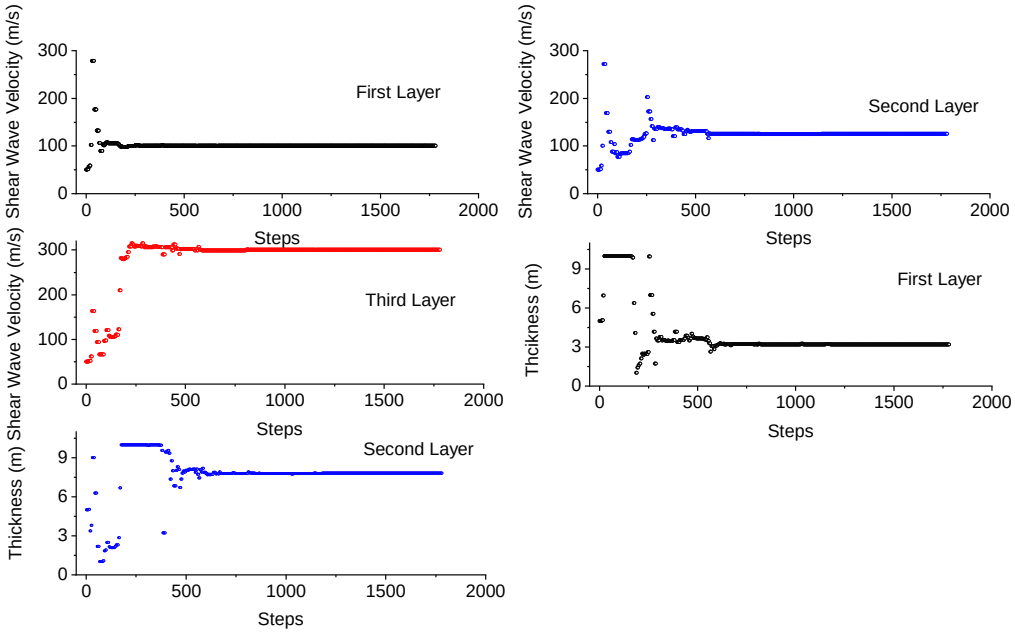

FIGURE 7.10: Update of shear wave velocity and thickness of each layer in the MASW inversion analysis

In this case study, the liquefaction analysis is performed under a blasting load. The soil layers are assumed to be saturated and the two-phase poroelastodynamic solver in the GeoNDT is used to predict the ground surface response. The cyclic stress ratio (CSR) and cyclic resistance ratio (CRR) are evaluated using Equation 7.5 (Andrus and Stokoe II, 2000; Liew, Xiao, Liu, and Rudenko, 2020):

$$CSR = 1.0 \left(\frac{a_{max}}{g} \right) \left(\frac{\sigma_v}{\sigma'_v} \right) r_d \tag{7.5a}$$

$$CRR = \left(a \left(\frac{V_{s1}}{100} \right)^2 + b \left(\frac{1}{V^*_{s1} - V_{s1}} - \frac{1}{V^*_{s1}} \right) \right) MSF \tag{7.5b}$$

where a_{max} is the peak horizontal ground surface acceleration; σ_v and σ'_v is vertical total stress and vertical effective stress; r_d is the shear stress reduction coefficient; V_{s1} is the corrected shear wave velocity; V^*_{s1} is an upper limit of V_{s1}, taken as 215 m/s (Andrus and Stokoe II, 2000); MSF is the magnitude scaling factor, taken as 1.82 (Liew, Xiao, Liu, and Rudenko, 2020); a and b are the empirical coefficients taken as 0.022 and 2.8, respectively (Andrus and Stokoe II, 2000).

The blasting load is assumed to be a Gaussian function with a duration of 0.2 ms (Wang, Lu, and Bai, 2008). The blasting load is applied at the top of the third layer (half space).

The maximum horizontal acceleration is determined using the poroelastodynamic solver in GeoNDT from 0 m to 100 m from the source load at the ground surface. The saturated unit weight is assumed to be 21 kN/m^3 (Kumar, Choudhury, and Bhargava, 2014). The water table is assumed to be at the ground surface. The stress-corrected velocity (V_{s1}) is evaluated based on the proposed relation presented by Andrus and Stokoe II (2000). As shown in Figure 7.11, the horizontal peak acceleration is 0.8 m/s^2 based on the two-phase poroelastodynamic solver of GeoNDT. The factor of safety is then evaluated by the ratio of CRR to CRS, as shown in Figure 7.12. The factor of safety is below the allowable value of 1.5 above the depth of 21 m. The JSON configuration file and python code for this case study is given in Listings 10 and 11, respectively.

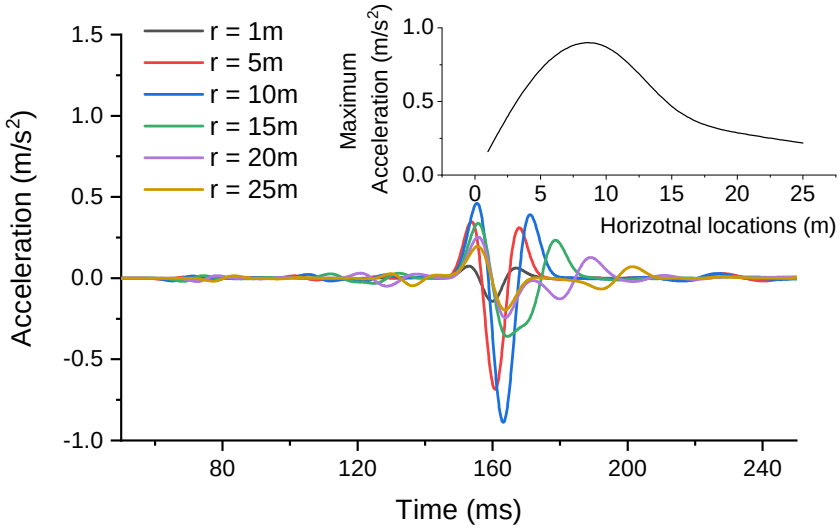

FIGURE 7.11: Horizontal acceleration distribution under a blasting load at the ground surface

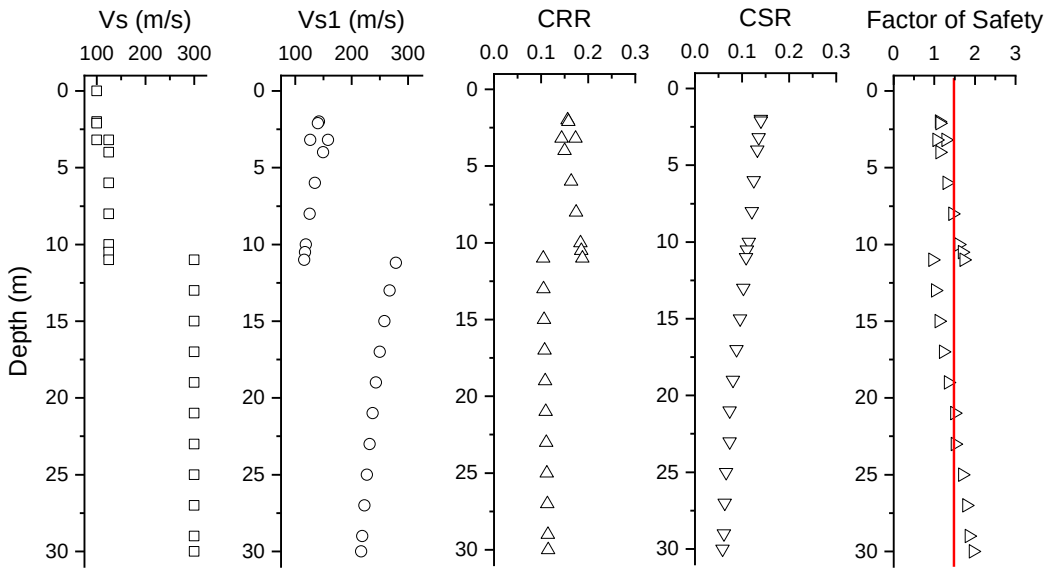

FIGURE 7.12: Liquefaction analysis under a blasting load

```
{
"input": {
  "tmin": 0.001,  # minimum time (s)
  "tmax": 0.5,    # maximum time (s)
  "tlin": 200,    # number of points within tmin and tmax
  "E": [5.98e7, 8.12e7, 5.85e8, 5.85e8],  # Young's modulus (Pa)
  "mu": [0.3, 0.3, 0.3, 0.3],             # Poisson's ratio
  "rho": [2300.0, 2000.0,2500.0, 2500.0], # density (kg/m^3)
  "H": [3.2,7.8,19, 10],                  # thickness (m)
  "kh": [10e-6,10e-6,10e-6,10e-6],        # permeability coefficient (m^2)
  "porosity": [0.243, 0.245, 0.262, 0.262], # porosity
  "r": 10,        # radial location of ultrasonic receiver
  "rmax": 50,     # radius of soil sample
  "node": 1,      # output node
    "loc": 10,      # input node
  "st": 0,        # displacement output
  "lap_num": 35,  # number of iteration in inverse Laplace transform
  "ncore": -1,    # the number of cores (-1 denotes for all cores)}
}
```

LISTING 7.10: JSON configuration file (seismic_saturate.json) used for the seismic response analysis under a blasting load

```
from geondt import two_phase_dynamic
import json

```

```
with open('seismic_saturate.json', "r") as f:
    data = json.load(f)

seismic = two_phase_dynamic(**data["input"])
yt = seismic.run_i() # run model for half_space domain
```

LISTING 7.11: Python main program in GeoNDT for the seismic response analysis under a blasting load

7.3.4 Ultrasonic test for pile scour detection

The ultrasonic test has been used for pile integrity tests, especially for the anomaly detection in the piles (Beckhaus and Heinzelmann, 2015). In this case study, we demonstrate that GeoNDT can also be used to detect the scour around pile foundations using the ultrasonic test. Scour around pile foundations can decrease the stability of the pile structure and thus requires early detection. At the scour location, the interface of the pile and soil can be considered as zero-stress boundary conditions (air interface). The acoustic impedance, defined as the product of density and acoustic velocity, describes the resistance that the stress wave encounters as it passes through another media. With an air interface at the scour location, almost all the wave energy will be reflected. For the soil with a high acoustic impedance, the wave reflection is reduced in comparison to the air boundary condition. Therefore, we can determine the scour location based on the amplitude of the reflective wave. The reflection coefficient at the pile-soil interface can be used to indicate the extent of the scour, as shown in Equation 7.6.

$$F = \frac{Z_l - Z_0}{Z_l + Z_0} \tag{7.6}$$

where F is the reflection coefficient; Z_l is the acoustic impedance of pile; Z_0 is the acoustic impedance of soil.

A value of 1 for the reflection coefficient represents the air interface (scour condition). A value of 0 for the reflection coefficient shows the same impedance of the pile and surrounding soil (extreme condition). In this test, two pipes are required for the installation of ultrasonic transmitter and receiver, as shown in Figure 7.13. It is assumed that the input voltage has a frequency of 50 kHz. The ultrasonic transmitter is located at the center location, while the ultrasonic receiver is located 0.4 m away from the ultrasonic transmitter. The radius of the pile is assumed as 0.5 m. The P-wave and S-wave velocities for the concrete pile is assumed to be 3500 m/s and 2000 m/s, respectively. The ultrasonic receiver

measurement is normalized based on the incident wave amplitude, as labeled in Figure 7.14. Based on the elastodynamic solver in GeoNDT, the amplitude of the reflective wave is 0.6 (reflection coefficient of 1) for the scour location, as shown in Figure 7.14.

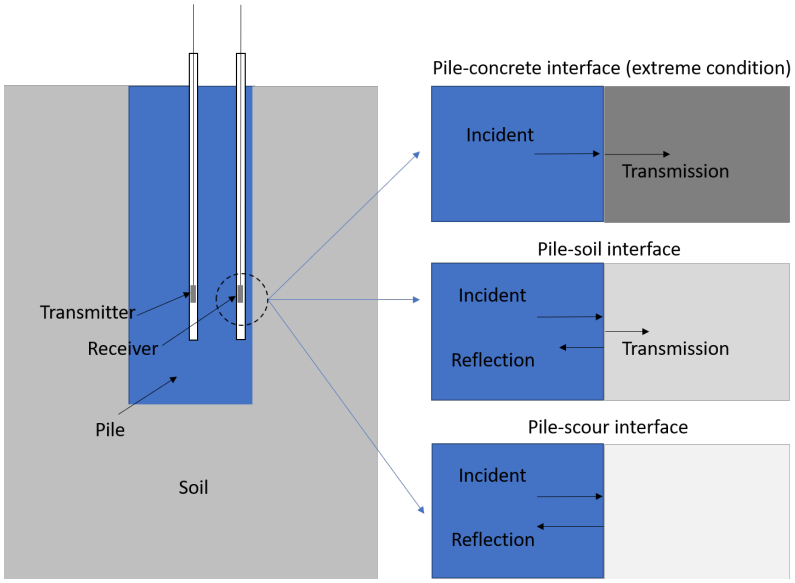

FIGURE 7.13: Pile-soil interaction conditions and configuration of the ultrasonic-based pile integrity test

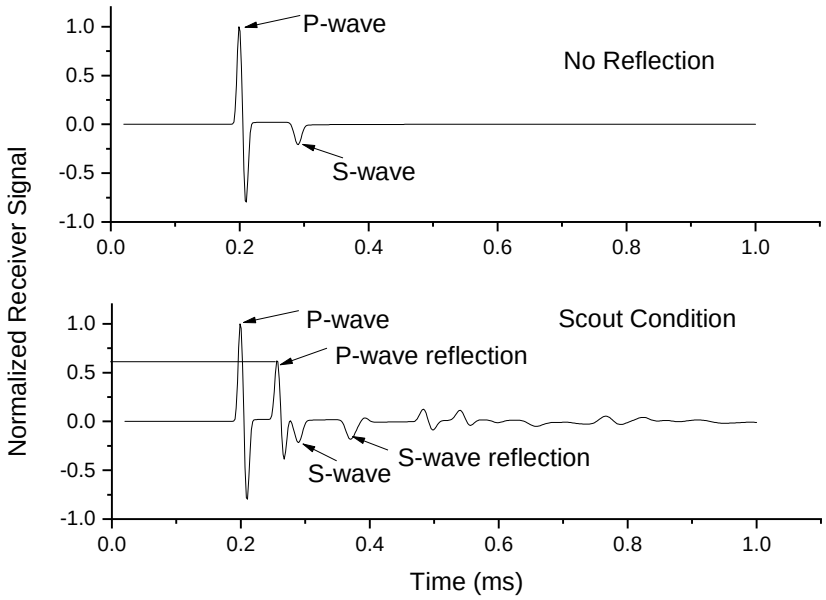

FIGURE 7.14: Ultrasonic receiver signal with no reflection (perfect contact between the pile and surrounding soil with same impedance) and scour condition (air contact)

With P-wave velocities of surrounding soil varying from 1000 m/s to 200 m/s, the relation between reflection coefficient at the pile-soil interface and the amplitude of the

reflective wave is shown in Figure 7.15. In the scour condition (air interface), the reflection coefficient is one, and the reflection amplitude in the ultrasonic receiver is 0.6. The reflection coefficient and reflection amplitude from the ultrasonic receiver tends to decrease when the wave velocity of the surrounding soil increases. Therefore, based on the reflection amplitude from the ultrasonic receiver, we can evaluate the pile-soil interaction, especially in the condition of scour around the pile. The JSON configuration file and sample code for this case study in the Python main program in GeoNDT is given in Listings 12 and 13, respectively.

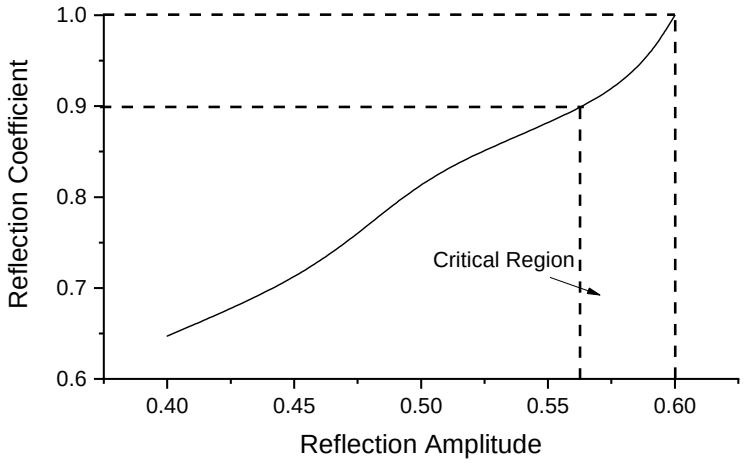

FIGURE 7.15: Relation between the reflection coefficient at the pile-soil interface and reflection amplitude at the ultrasonic receiver location

```
{
"input":{
    "tmin": 2e-5,     # minimum time (s)
    "tmax": 100e-5,   # maximum time (s)
    "tlin": 500,      # number of points within tmin and tmax
    "E": [2.41e10, 2.41e10, 1.76e7],    # Young's modulus (Pa)
    "mu": [0.258, 0.258, 0.1],          # Poisson's ratio
    "rho": 2400, 2400, 1800],           # density (kg/m^3)
    "H": [0.4,0.1,10],                  # thickness (m)
    "r": 0,           # radial location of ultrasonic receiver
    "rmax": 5,        # radius of soil sample
    "node": 4,        # output node
    "loc": 2,         # input node
}
```

LISTING 7.12: JSON configuration file (pile.json) for the scour detection around a pile foundation

```
from geondt import one_phase_dynamic
import json

def load(s):
    ''' Define external load in the Laplace domain (for pile-soil
    interaction example)'''
    fn1 = -100*10**3*(np.exp(-np.complex(s)/(10*10**3)))*np.pi/(10*10.0**9
    *np.pi**2 + np.complex(s)**2)
    fn2 = 100*10**3*(np.exp(-np.complex(s)/(12.5*10**3)))*np.pi/(10*10.0**9
     *np.pi**2 + np.complex(s)**2)
    fn = fn1 + fn2
    return fn

with open('pile.json', "r") as f:
    data = json.load(f)

pile = one_phase_dynamic(**data["input"])
pile.load_i = load
yt = pile.run_i()
```

LISTING 7.13: Python main program in GeoNDT for the scour detection around a pile foundation using ultrasonic testing

7.4 Conclusion

In this paper, a meshless computational software, GeoNDT, is proposed for the geotechnical non-destructive testing applications including BE test, ultrasonic testing, FWD and MASW in multiphase, multilayered geo-systems. GeoNDT can efficiently and accurately describe the wave propagation in geomaterials without discretizing the entire domain. GeoNDT can provide the solution in both frequency domain for dispersion analysis and time domain for dynamic response analysis. Based on the case studies performed in this paper, it is concluded:

- GeoNDT can model the wave propagation within dry and saturated soil samples in the BE test. In saturated soil sample, The BE measurement is predicted to be sensitive to the extent of volumetric water content of a saturated soil sample.
- GeoNDT is capable of modeling the dynamic response of pavement structure and inverse analysis in the FWD test. It is found that the TRR method is more efficient in the inversion analysis in comparison to BFGS, Powell and TNC methods.

- GeoNDT also supports dispersion analysis that can be used for the MASW inversion analysis and liquefaction analysis. Based on the shear wave velocity obtained from GeoNDT solvers, the factor of safety at any depth can be calculated to evaluate the risk of liquefaction under a blasting load.
- GeoNDT can be used for the ultrasonic-based pile integrity test for the scour detection around a pile and asses the pile-soil interaction based on the amplitude of the reflective wave measured by the ultrasonic receiver. The ultrasonic test can potentially be used to detect the location of the scour based on the amplitude of the reflective wave.

Chapter 8

Conclusions and future research plans

8.1 Conclusion

The main objective of this thesis was to develop efficient non-invasive techniques and advanced signal interpretation methods for the characterization of multiphase geomaterials in both laboratory scale and field investigation. A summary of each project with its major contributions are presented as follows.

8.1.1 Integrated approach for MASW dispersion analysis

A semi-analytical forward solver was developed for the dispersion analysis using the spectral element method. An effective Brent's root-finding method was applied to obtain the exact dispersion curve. Based on the numerical case studies, it is concluded that when the stiffness of soil layers increases monotonically with depth, the phase velocity decreases monotonically with frequency. The non-continuity of the soil stratigraphy, such as having soft or stiff intermediate layers, also induces non-continuity in the dispersion curves. The number of transition points reflects the number of layers in the field. Such an understanding of the dispersion curve can be used for the determination in initial guesses of the soil stratigraphy for the inversion analysis. The trust region reflective method was used in the inversion analysis to reduce the Euclidean distance between the experimental and numerically calculated dispersion curves. Based on a case study in Arnarbaeli in south Iceland, it is found that the integrated approach proposed in this study effectively determines the soil stratigraphy as well as the soil properties to match the measured dispersion curve within

only 300 runs of the forward solver.

8.1.2 Experimental investigation and numerical modeling of piezoelectric bender element motion

The response of different media to a BE motion is thoroughly studied via a piezoelectric-solid mechanics FE model as well as experimental tests. The numerical results are compared with the motion of the BE in the air, transparent soil, as well as the Ottawa sand captured by a laser vibrometer. It is concluded that the proposed piezoelectric-mechanical model captures the motion of the BE with sufficient accuracy in the air, transparent soil, as well as the Ottawa sand. The best agreement was achieved for the BE motion in the air. The numerical response obtained by the proposed model is consistent with the laser vibrometer measurement at the sides of the Ottawa sand specimen. Furthermore, the numerical predictions show a reasonable agreement with the laser measurements in terms of the distribution of dispersion curves for both symmetric and antisymmetric modes. A reasonable agreement between the numerical BE response and experimental BE measurement is achieved at the receiver location. The shear wave velocity and damping ratio obtained through the proposed model are consistent with the ones obtained by the resonant column test. The proposed numerical method shows that there is a significant P-wave/S-wave interaction that demonstrates why the empirical methods for the selection of S-waves in BE testing could be incorrect depending on the different parameters that affect the participation of P-waves. The proposed piezoelectric-mechanical model can be used to study the complex wave interactions, which significantly improves the interpretation of the effects of P-waves on BE test results. The proposed model clearly show that the interpretation of BE measurements in clays could be more challenging because of the strong participation of P-waves on the response of BE.

8.1.3 Laboratory-scale characterization of saturated soil samples

An ultrasonic-based characterization of soil samples is developed for the instant measurement of soil properties including Young's modulus and Poisson's ratio (compression/shear wave velocity), and porosity. The developed meshless semi-analytical algorithm reduces the computational effort significantly in comparison to standard numerical techniques such as the finite element method. In fact, the advantage of such a solution is that the

dynamic response is evaluated at the receiver location only rather than the entire domain.The soil response in other locations is not measured in the real application and does not factor in soil characterization. It is concluded that high-frequency impulse loads (with predominant frequency of up to 5 kHz) is required to trigger the effect of porosity for soils with relatively low Young's modulus (e.g clay, silt and sand). For stiffer materials, such as very dense gravels, an impulse load with predominant frequency of 0.5 MHz is required to characterize their porous nature. The characterization of soil properties has been proved as a highly non-convex optimization problem in this paper. The differential evolution algorithm, as a global optimization method, is found efficient and effective in finding the optimum soil properties, such that the difference between the predicted and measured stress waves is minimized. In conclusion, the developed method in interpreting dynamic response of saturated soil can be used for the immediate characterization of Young's modulus, Poisson's ratio, and porosity for a given soil specimen.

8.1.4 Ultrasonic characterization of permafrost samples

A spectral element multiphase poromechanical transfer function method is developed for the signal interpretation of ultrasonic measurements for the first time. We show that our proposed transfer function, i.e. a ratio of induced displacement and applied force in the frequency domain, is independent of the distribution of the stress force applied by the transducer to the permafrost sample. Our signal interpretation approach is objective unlike the existing subjective empirical signal interpretation methods. Our proposed ultrasonic sensing technique can directly measure several physical and mechanical properties of frozen soils in a single ultrasonic test by interpreting the full signal unlike existing techniques that normally relate only one or two parameters for a soil sample to the measured signal in each test. Similar to other problems involving inverse analyses, we can ensure the accuracy of the results or reduce the uncertainty in the inverse analysis by providing complementary information through conventional tests to determine temperature, soil type, density, and so on. Our results demonstrate the proposed ultrasonic sensing technique and the signal interpretation method based on the spectral element multiphase poromechanical approach can be used in a laboratory setup or in the field for rapid and reliable characterization of permafrost samples.

8.1.5 In-situ characterization of permafrost

A hybrid inverse and multi-phase poromechanical approach is developed for in-situ characterization of permafrost sites using surface wave techniques. In our method, we quantify the physical properties such as ice content, unfrozen water content, and porosity as well as the mechanical properties such as the shear modulus and bulk modulus of permafrost or soil layers. Through the mechanical properties of the solid skeleton frame, we can also predict the soil type and the sensitivity of the permafrost layer to permafrost carbon feedback and emission of greenhouse gases to the atmosphere. We also determine the depth of the permafrost table and permafrost base. The role of two different types of Rayleigh waves in characterizing the permafrost is presented based on an MASW seismic investigation in a field located at SW Spitsbergen, Norway. Multiphase poromechanical dispersion relations are developed for the interpretation of the experimental seismic measurements at the surface based on the spectral element method. Our results demonstrate the potential of seismic surface wave testing accompanied with our proposed hybrid inverse and poromechanical dispersion model for the assessment and quantitative characterization of permafrost sites.

8.1.6 GeoNDT software development

A meshless computational software, GeoNDT, can be used seamlessly for advanced signal interpretation in geophysical investigation and laboratory testing including BE test, ultrasonic test, FWD test and MASW test in multiphase, multilayered geo-systems. GeoNDT can efficiently and accurately describe the wave propagation in geomaterials without discretizing the entire domain. GeoNDT can also provide the solution in both frequency domain for dispersion analysis and time domain for dynamic response analysis.

8.2 Recommendations for future work

- *Extension of current geomechanical models*

  The current solvers are still limited to horizontally distributed soil layers. In the future work, these solvers can be extended for soil domain that is non-homogeneous in horizontal direction. The developed multiphase geomechanical models can also be further extended to four phases (i.e., solid skeleton, pore air, pore water, and pore ice) for unsaturated soils based on the similar framework (spectral element method) developed in this research.

- *Development of joint geophysical permafrost mapping*

  Geophysical techniques can be used to examine the spatial distribution of permafrost deposits. However, a single geophysical investigation method normally yields an uncertain permafrost mapping result. A combination of different geophysical methods will largely improve resolution and uncertainty. Seismic methods (i.e. MASW) constitute the best way to quantify the amount of ice and water in permafrost since freezing has remarkable effect on seismic wave velocities. With the MASW seismic wave-based method as the main investigation method, the ERT, GPR and EM Tomography work as the complementary investigation methods to provide more information and constraints to the predicted solution. The preliminary results in terms of the permafrost distribution obtained in ERT, GPR or EM Tomography method can provide a reasonable initial guess and more constraints in MASW solver.

Bibliography

Abate, Joseph and Valkó, Peter P (2004). "Multi-precision Laplace transform inversion". In: *International Journal for Numerical Methods in Engineering* 60.5, pp. 979–993.

Abo-Zena, Anas (1979). "Dispersion function computations for unlimited frequency values". In: *Geophysical Journal International* 58.1, pp. 91–105.

Abramowitz, Milton (1985). "l. A. Stegun, 1972: Handbook of Mathematical Functions". In: *National Bureau of Standards Applied Mathematics Series* 55, pp. 589–626.

Ahsan, Mansoor and Choudhry, Mohammad Ahmad (2017). "System identification of an airship using trust region reflective least squares algorithm". In: *International Journal of Control, Automation and Systems* 15.3, pp. 1384–1393.

Al-Khoury, Rafid, Scarpas, A, Kasbergen, C, and Blaauwendraad, J (2001). "Spectral element technique for efficient parameter identification of layered media. I. Forward calculation". In: *International Journal of Solids and Structures* 38.9, pp. 1605–1623.

Andrus, Ronald D and Stokoe II, Kenneth H (2000). "Liquefaction resistance of soils from shear-wave velocity". In: *Journal of Geotechnical and Geoenvironmental Engineering* 126.11, pp. 1015–1025.

Arroyo, Arroyo, Muir, D, Greening, P.D, Medina, L, and Rio, J (2006). "Effects of sample size on bender-based axial G_0 measurements". In: *Géotechnique* 56.1, pp. 39–52.

Arroyo, Marcos, Medina, L, and Muir Wood, D (2002). "Numerical modelling of scale effects in bender-based pulse tests". In: *NUMOG VIII, Pande, GN & Pietruszczak, S.(eds)*, pp. 589–594.

Arulnathan, Rajendram, Boulanger, Ross W, and Riemer, Michael F (1998). "Analysis of bender element tests". In: *Geotechnical Testing Journal* 21.2, pp. 120–131.

Banerjee, Prasanta K, Ahmad, Shahid, and Manolis, George D (1986). "Transient elastodynamic analysis of three-dimensional problems by boundary element method". In: *Earthquake Engineering & Structural Dynamics* 14.6, pp. 933–949.

Beaty, Kristen S, Schmitt, Douglas R, and Sacchi, Mauricio D (2002). "Simulated annealing inversion of multimode Rayleigh wave dispersion curves for geological structure". In: *Geophysical Journal International* 151.2, pp. 622–631.

Beckhaus, Karsten and Heinzelmann, Harald (2015). "Ultrasonic Integrity Testing for Bored Piles-A Challenge". In: *International Symposium Non-Destructive Testing in Civil Engineering*.

Berger, Lorenz, Bordas, Rafel, Kay, David, and Tavener, Simon (2017). "A stabilized finite element method for finite-strain three-field poroelasticity". In: *Computational Mechanics* 60.1, pp. 51–68.

Bernth, Henrik and Chapman, Chris (2011). "A comparison of the dispersion relations for anisotropic elastodynamic finite-difference grids". In: *Geophysics* 76.3, WA43–WA50.

Bhuiyan, Md Abul Ehsan, Witharana, Chandi, and Liljedahl, Anna K (2020). "Use of Very High Spatial Resolution Commercial Satellite Imagery and Deep Learning to Automatically Map Ice-Wedge Polygons across Tundra Vegetation Types". In: *Journal of Imaging* 6.12, p. 137.

Biot, Maurice A (1956a). "Theory of elastic waves in a fluid-saturated porous solid. 1. Low frequency range". In: *J. Acoust. Soc. Am.* 28, pp. 168–178.

Biot, Maurice A (1956b). "Theory of propagation of elastic waves in a fluid-saturated porous solid. II. Higher frequency range". In: *The Journal of the Acoustical Society of America* 28.2, pp. 179–191.

Blake, George R. and Steinhardt, Gary C. (2008). *Particle-size distribution In: Encyclopedia of soil science*.

Brocanelli, Diego and Rinaldi, Victor (1998). "Measurement of low-strain material damping and wave velocity with bender elements in the frequency domain". In: *Canadian Geotechnical Journal* 35.6, pp. 1032–1040.

Brothers, Laura L, Herman, Bruce M, Hart, Patrick E, and Ruppel, Carolyn D (2016). "Subsea ice-bearing permafrost on the US Beaufort Margin: 1. Minimum seaward extent defined from multichannel seismic reflection data". In: *Geochemistry, Geophysics, Geosystems* 17.11, pp. 4354–4365.

Budhu, Muniram (2015). *Soil mechanics fundamentals*. John Wiley & Sons.

Butcher, AP, Campanella, RG, Kaynia, AM, and Massarsch, KR (2005). "Seismic cone downhole procedure to measure shear wave velocity–A guideline prepared by ISSMGE TC10: Geophysical Testing in Geotechnical Engineering". In: *Proc. XVIth Inter. Conf. on Soil Mechanics and Geotechnical Engineering, May 2006, Osaka, Japan*.

Camacho-Tauta, Javier, Cascante, G, Viana DA Fonseca, A, and A Santos, J (2015). "Time and frequency domain evaluation of bender element systems". In: *Géotechnique* 65.7, pp. 548–562.

Camacho-Tauta, Javier, Jimenez-Alvarez, J.D, and Reyes-Ortiz, O.J (2012). "A procedure to calibrate and perform the bender element test". In: *Dyna* 79.176, pp. 10–18.

Campanella, Richard (1994). "Field methods for dynamic geotechnical testing: An overview of capabilities and needs". In: *Dynamic Geotechnical Testing II*.

Carcione, José M, Gurevich, Boris, and Cavallini, Fabio (2000). "A generalized Biot–Gassmann model for the acoustic properties of shaley sandstones". In: *Geophysical Prospecting* 48.3, pp. 539–557.

Carcione, José M, Santos, Juan E, Ravazzoli, Claudia L, and Helle, Hans B (2003). "Wave simulation in partially frozen porous media with fractal freezing conditions". In: *Journal of Applied Physics* 94.12, pp. 7839–7847.

Carcione, José M and Seriani, Géza (2001). "Wave simulation in frozen porous media". In: *Journal of Computational Physics* 170.2, pp. 676–695.

Castagna, John P, Batzle, Michael L, and Eastwood, Raymond L (1985). "Relationships between compressional-wave and shear-wave velocities in clastic silicate rocks". In: *Geophysics* 50.4, pp. 571–581.

Castellini, Mirko, Di Prima, Simone, and Iovino, Massimo (2018). "An assessment of the BEST procedure to estimate the soil water retention curve: A comparison with the evaporation method". In: *Geoderma* 320, pp. 82–94.

Cercato, Michele (2009). "Addressing non-uniqueness in linearized multichannel surface wave inversion". In: *Geophysical Prospecting* 57.1, pp. 27–47.

Chai, HY, Zhang, DJ, Lu, HL, et al. (2015). "Behavior of Rayleigh waves in layered saturated porous media using thin-layer method". In: *Chinese Journal of Geotechnical Engineering* 37.6, pp. 1132–1141.

Chen, Juan (1994a). "Time domain fundamental solution to Biot's complete equations of dynamic poroelasticity. Part I: two-dimensional solution". In: *International Journal of Solids and Structures* 31.10, pp. 1447–1490.

Chen, Juan (1994b). "Time domain fundamental solution to biot's complete equations of dynamic poroelasticity Part II: three-dimensional solution". In: *International Journal of Solids and Structures* 31.2, pp. 169–202.

Chen, Yuyan, Beskou, Niki D, and Qian, Jiang (2018). "Dynamic response of an elastic plate on a cross-anisotropic poroelastic half-plane to a load moving on its surface". In: *Soil Dynamics and Earthquake Engineering* 107, pp. 292–302.

Cheng, Yumin and Peng, Miaojuan (2005). "Boundary element-free method for elastodynamics". In: *Science in China Series G: Physics and Astronomy* 48.6, pp. 641–657.

Christiansen, Hanne H, Matsuoka, Norikazu, and Watanabe, Tatsuya (2016). "Progress in understanding the dynamics, internal structure and palaeoenvironmental potential of ice wedges and sand wedges". In: *Permafrost and Periglacial Processes* 27.4, pp. 365–376.

Clayton, Christopher RI (1995). *The standard penetration test (SPT): methods and use*. Construction Industry Research and Information Association.

Couture, Nicole J and Pollard, Wayne H (2017). "A Model for Quantifying Ground-Ice Volume, Yukon Coast, Western Arctic Canada". In: *Permafrost and Periglacial Processes* 28.3, pp. 534–542.

Crestaux, Thierry, Le Maıtre, Olivier, and Martinez, Jean-Marc (2009). "Polynomial chaos expansion for sensitivity analysis". In: *Reliability Engineering & System Safety* 94.7, pp. 1161–1172.

D4015-15e1, ASTM (2015). *Standard test methods for modulus and damping of soils by resonant-column method*.

Da Fonseca, Antonio Viana, Ferreira, Cristiana, and Fahey, Martin (2008). "A framework interpreting bender element tests, combining time-domain and frequency-domain methods". In: *Geotechnical Testing Journal* 32.2, pp. 91–107.

Daubechies, Ingrid, Lu, J.F, and Wu, H.T (2011). "Synchrosqueezed wavelet transforms: An empirical mode decomposition-like tool". In: *Applied and Computational Harmonic Analysis* 30.2, pp. 243–261.

Dobiński, W and Leszkiewicz, J (2010). "Active layer and permafrost occurrence in the vicinity of the Polish Polar Station, Hornsund, Spitsbergen in the light of geophysical research". In: *Problemy Klimatologii Polarnej* 20, pp. 129–142.

Dolnicki, Piotr, Grabiec, Mariusz, Puczko, Dariusz, Gawor, Łukasz, Budzik, Tomasz, and Klementowski, Jan (2013). "Variability of temperature and thickness of permafrost active layer at coastal sites of Svalbard". In:

Dou, Shan and Ajo-Franklin, Jonathan B (2014). "Full-wavefield inversion of surface waves for mapping embedded low-velocity zones in permafrost". In: *Geophysics* 79.6, EN107–EN124.

Dou, Shan, Nakagawa, Seiji, Dreger, Douglas, and Ajo-Franklin, Jonathan (2016). "A rock-physics investigation of unconsolidated saline permafrost: P-wave properties from laboratory ultrasonic measurements". In: *Geophysics* 81.1, WA233–WA245.

Dou, Shan, Nakagawa, Seiji, Dreger, Douglas, and Ajo-Franklin, Jonathan (2017). "An effective-medium model for P-wave velocities of saturated, unconsolidated saline permafrost". In: *Geophysics* 82.3, EN33–EN50.

Dovgilovich, Leonid and Sofronov, Ivan (2015). "High-accuracy finite-difference schemes for solving elastodynamic problems in curvilinear coordinates within multiblock approach". In: *Applied Numerical Mathematics* 93, pp. 176–194.

Duliu, Octavian G (1999). "Computer axial tomography in geosciences: an overview". In: *Earth-Science Reviews* 48.4, pp. 265–281.

Dunsch, Robert and Breguet, Jean-Marc (2007). "Unified mechanical approach to piezoelectric bender modeling". In: *Sensors and Actuators A: physical* 134.2, pp. 436–446.

Eid, Hisham T and Stark, Timothy D (1998). "Undrained shear strength from cone penetration test". In: *Proc., 1st Int. Conf. on Site Characterization—ISC*. Vol. 98, pp. 1021–1025.

Fam, M.A, Cascante, Giovanni, and Dusseault, Maurice (2002). "Large and small strain properties of sands subjected to local void increase". In: *Journal of Geotechnical and Geoenvironmental Engineering* 128.12, pp. 1018–1025.

Fantuzzi, Nicholas (2014). "New insights into the strong formulation finite element method for solving elastostatic and elastodynamic problems". In: *Curved and Layered Structures* 1.open-issue.

Finas, Mathieu, Ali, H, Cascante, G, and Vanheeghe, P (2016). "Automatic Shear Wave Velocity Estimation in Bender Element Testing". In: *Geotechnical Testing Journal* 39.4, pp. 557–567.

Foti, Sebastiano, Lai, Carlo G, and Lancellotta, Renato (2002). "Porosity of fluid-saturated porous media from measured seismic wave velocities". In: *Géotechnique* 52.5, pp. 359–373.

Geertsma, J and Smit, Dirk (1961). "Some aspects of elastic wave propagation in fluid-saturated porous solids". In: *Geophysics* 26.2, pp. 169–181.

Glazer, Michał, Dobiński, Wojciech, Marciniak, Artur, Majdański, Mariusz, and Błaszczyk, Małgorzata (2020). "Spatial distribution and controls of permafrost development in non-glacial Arctic catchment over the Holocene, Fuglebekken, SW Spitsbergen". In: *Geomorphology*, p. 107128.

Graff, Karl F (1991). *Wave motion in elastic solids*. Courier Corporation.

Greening, Paul, Nash, DFT, Benahmed, N, Ferreira, C, and Fonseca, A Viana da (2003). "Comparison of shear wave velocity measurements in different materials using time and frequency domain techniques". In: *Proceedings of Deformation Characteristics of Geomaterials, Lyon, France*, pp. 381–386.

Gu, Qingqing, Zhu, Lianhua, Zhang, Yonghao, and Liu, Haihu (2019). "Pore-scale study of counter-current imbibition in strongly water-wet fractured porous media using lattice Boltzmann method". In: *Physics of Fluids* 31.8, p. 086602.

Gu, Xiaoqiang, Yang, J, Huang, M, and Gao, G (2015). "Bender element tests in dry and saturated sand: Signal interpretation and result comparison". In: *Soils and Foundations* 55.5, pp. 951–962.

Hallikainen, Martti T, Ulaby, Fawwaz T, Dobson, Myron C, El-Rayes, Mohamed A, and Wu, Lil-Kun (1985). "Microwave dielectric behavior of wet soil-part 1: Empirical models and experimental observations". In: *IEEE Transactions on Geoscience and Remote Sensing* 1, pp. 25–34.

Han, De-hua, Nur, Amos, and Morgan, Dale (1986). "Effects of porosity and clay content on wave velocities in sandstones". In: *Geophysics* 51.11, pp. 2093–2107.

Hardy, Stuart, Zdravkovic, Lidija, and Potts, David M (2002). "Numerical interpretation of continuously cycled bender element tests". In: *Numerical models in geomechanics. NUMOG VIII*, pp. 595–600.

Haskell, Norman A (1953). "The dispersion of surface waves on multilayered media". In: *Bulletin of the seismological Society of America* 43.1, pp. 17–34.

Hauck, Christian (2013). "New concepts in geophysical surveying and data interpretation for permafrost terrain". In: *Permafrost and Periglacial Processes* 24.2, pp. 131–137.

Helgerud, MB, Dvorkin, Jack, Nur, A, Sakai, A, and Collett, T (1999). "Elastic-wave velocity in marine sediments with gas hydrates: Effective medium modeling". In: *Geophysical Research Letters* 26.13, pp. 2021–2024.

Hilbich, Christin, Marescot, L, Hauck, Christian, Loke, MH, and Mäusbacher, R (2009). "Applicability of electrical resistivity tomography monitoring to coarse blocky and ice-rich permafrost landforms". In: *Permafrost and Periglacial Processes* 20.3, pp. 269–284.

Horn, Roger A and Johnson, Charles R (2012). *Matrix analysis*. Cambridge university press.

Horváth, Gábor, Horváth, Illés, Almousa, Salah Al-Deen, and Telek, Miklós (2020). "Numerical inverse Laplace transformation using concentrated matrix exponential distributions". In: *Performance Evaluation* 137, p. 102067.

Hoyos, Laureano R, Suescún-Florez, E.A, and Puppala, A.J (2015). "Stiffness of intermediate unsaturated soil from simultaneous suction-controlled resonant column and bender element testing". In: *Engineering Geology* 188, pp. 10–28.

Huthwaite, Peter (2014). "Accelerated finite element elastodynamic simulations using the GPU". In: *Journal of Computational Physics* 257, pp. 687–707.

Idesman, Alexander, Schmidt, M, and Foley, Jason (2011). "Accurate finite element modeling of linear elastodynamics problems with the reduced dispersion error". In: *Computational Mechanics* 47.5, pp. 555–572.

Ingale, Ritesh, Patel, Anjan, and Mandal, A (2020). "Numerical modelling of bender element test in soils". In: *Measurement* 152, p. 107310.

Irfan, Muhammad, Cascante, Giovanni, Basu, Dipanjan, and Khan, Zahid (2019). "Novel evaluation of bender element transmitter response in transparent soil". In: *Géotechnique*, pp. 1–12.

James, Stephanie R, Knox, HA, Abbott, RE, Panning, MP, and Screaton, EJ (2019). "Insights into permafrost and seasonal active-layer dynamics from ambient seismic noise monitoring". In: *Journal of Geophysical Research: Earth Surface* 124.7, pp. 1798–1816.

Jianwen, Liang and Hongbing, You (2004). "Dynamic stiffness matrix of a poroelastic multi-layered site and its Green's functions". In: *Earthquake Engineering and Engineering Vibration* 3.2, p. 273.

Johnson, David Linton, Koplik, Joel, and Dashen, Roger (1987). "Theory of dynamic permeability and tortuosity in fluid-saturated porous media". In: *Journal of fluid mechanics* 176, pp. 379–402.

Jovičić, V and Coop, M (1998). "The measurement of stiffness anisotropy in clays with bender element tests in the triaxial apparatus". In: *Geotechnical Testing Journal* 21.1, pp. 3–10.

Jovicic, Vojkan, Coop, Matthew, and Simic, M (1996). "Objective criteria for determining G max from bender element tests". In: *Geotechnique* 46.2, pp. 357–362.

Kamal, Ayman and Giurgiutiu, Victor (2014). "Stiffness transfer matrix method (STMM) for stable dispersion curves solution in anisotropic composites". In: *Health Monitoring of Structural and Biological Systems 2014*. Vol. 9064. International Society for Optics and Photonics, p. 906410.

Kamalian, Mohsen, Jafari, Mohammad Kazem, Sohrabi-Bidar, Abdollah, Razmkhah, Arash, and Gatmiri, Behrouz (2006). "Time-domain two-dimensional site response analysis of non-homogeneous topographic structures by a hybrid BE/FE method". In: *Soil Dynamics and Earthquake Engineering* 26.8, pp. 753–765.

Karl, Lutz, Haegeman, W, Pyl, L, and Degrande, G (2003). "Measurement of material damping with bender elements in triaxial cell". In: *Deformation Characteristics of Geomaterials*, pp. 3–11.

Karray, Mourad, Ben Romdhan, Mohamed, Hussien, Mahmoud N, and Éthier, Yannic (2015). "Measuring shear wave velocity of granular material using the piezoelectric ring-actuator technique (P-RAT)". In: *Canadian Geotechnical Journal* 52.9, pp. 1302–1317.

Ke, Ganpan, Dong, Hefeng, Kristensen, Åge, and Thompson, Mark (2011). "Modified Thomson–Haskell matrix methods for surface-wave dispersion-curve calculation and their accelerated root-searching schemes". In: *Bulletin of the Seismological Society of America* 101.4, pp. 1692–1703.

Kennett, BLN (1974). "Reflections, rays, and reverberations". In: *Bulletin of the Seismological Society of America* 64.6, pp. 1685–1696.

Kézdi, Árpád and Rétháti, László (1974). *Handbook of soil mechanics*. Vol. 1. Elsevier Amsterdam.

Khan, Qasim, Moon, Sung-Woo, and Ku, Taeseo (2020). "Idealized sine wave approach to determine arrival times of shear wave signals using bender elements". In: *Geotechnical Testing Journal* 43.1, pp. 171–193.

King, Michael S, Zimmerman, Robert W, and Corwin, RF (1988). "Seismic and electrical properties of unconsolidated permafrost". In: *Geophysical Prospecting* 36.4, pp. 349–364.

Kirar, Bablu and Maheshwari, BK (2018). "Dynamic properties of soils at large strains in Roorkee region using field and laboratory tests". In: *Indian Geotechnical Journal* 48.1, pp. 125–141.

Kneisel, Christof, Hauck, Christian, Fortier, Richard, and Moorman, Brian (2008). "Advances in geophysical methods for permafrost investigations". In: *Permafrost and Periglacial Processes* 19.2, pp. 157–178.

Knopoff, L (1964). "A matrix method for elastic wave problems". In: *Bulletin of the Seismological Society of America* 54.1, pp. 431–438.

Kulhawy, Fred H and Mayne, Paul W (1990). *Manual on estimating soil properties for foundation design*. Tech. rep. Electric Power Research Inst.

Kumar, Ranjan, Choudhury, Deepankar, and Bhargava, Kapilesh (2014). "Prediction of blast-induced vibration parameters for soil sites". In: *International Journal of Geomechanics* 14.3, p. 04014007.

Kuster, Guy T and Toksöz, M Nafi (1974). "Velocity and attenuation of seismic waves in two-phase media: Part I. Theoretical formulations". In: *Geophysics* 39.5, pp. 587–606.

Leclaire, Ph, Cohen-Ténoudji, Frédéric, and Aguirre-Puente, Jaime (1994). "Extension of Biot's theory of wave propagation to frozen porous media". In: *The Journal of the Acoustical Society of America* 96.6, pp. 3753–3768.

Lee, Changho, Truong, Q Hung, and Lee, Jong-Sub (2010). "Cementation and bond degradation of rubber–sand mixtures". In: *Canadian Geotechnical Journal* 47.7, pp. 763–774.

Lee, Hyung Suk (2014). "Viscowave–a new solution for viscoelastic wave propagation of layered structures subjected to an impact load". In: *International Journal of Pavement Engineering* 15.6, pp. 542–557.

Lee, Jong-Sub and Santamarina, J Carlos (2005). "Bender elements: performance and signal interpretation". In: *Journal of Geotechnical and Geoenvironmental Engineering* 131.9, pp. 1063–1070.

Lee, Myung W and Waite, William F (2008). "Estimating pore-space gas hydrate saturations from well log acoustic data". In: *Geochemistry, Geophysics, Geosystems* 9.7.

Leong, Eng Choon, Yeo, Sir Hoon, and Rahardjo, Harianto (2005). "Measuring shear wave velocity using bender elements". In: *Geotechnical Testing Journal* 28.5, pp. 488–498.

Liew, Min, Xiao, Ming, Liu, Shimin, and Rudenko, Douglas (2020). "In situ seismic investigations for evaluating geotechnical properties and liquefaction potential of fine coal tailings". In: *Journal of Geotechnical and Geoenvironmental Engineering* 146.5, p. 04020014.

Liljedahl, Anna K, Boike, Julia, Daanen, Ronald P, Fedorov, Alexander N, Frost, Gerald V, Grosse, Guido, Hinzman, Larry D, Iijma, Yoshihiro, Jorgenson, Janet C, Matveyeva, Nadya, et al. (2016). "Pan-Arctic ice-wedge degradation in warming permafrost and its influence on tundra hydrology". In: *Nature Geoscience* 9.4, pp. 312–318.

Lin, Chih-Ping, Lin, Chun-Hung, and Chien, Chih-Jung (2017). "Dispersion analysis of surface wave testing–SASW vs. MASW". In: *Journal of Applied Geophysics* 143, pp. 223–230.

Lin, L, Li, S, Liu, XL, and Chen, WW (2019). "Prediction of relative density of carbonate soil by way of a dynamic cone penetration test". In: *Géotechnique Letters* 9.2, pp. 154–160.

Liu, Hongwei, Cascante, Giovanni, Maghoul, Pooneh, and Shalaby, Ahmed (2021). "Experimental Investigation and Numerical Modeling of Piezoelectric Bender Element Motion and Wave Propagation Analysis in Soils". In: *Canadian Geotechnical Journal* ja.

Liu, Hongwei, Maghoul Pooneh Shalaby, Ahmed, and Thomson, Douglas (2021). "Ultrasonic characterization of permafrost samples using spectral element multiphase poromechanical transfer functions". In:

Liu, Hongwei, Maghoul, P, Bahari, A, and Kavgic, M (2019). "Feasibility study of snow melting system for bridge decks using geothermal energy piles integrated with heat pump in Canada". In: *Renewable Energy* 136, pp. 1266–1280.

Liu, Hongwei, Maghoul, Pooneh, and Shalaby, Ahmed (2019). "Optimum insulation design for buried utilities subject to frost action in cold regions using the Nelder-Mead algorithm". In: *International Journal of Heat and Mass Transfer* 130, pp. 613–639.

Liu, Hongwei, Maghoul, Pooneh, and Shalaby, Ahmed (Apr. 2020a). *Intelligent MASW*. Version 1.0.0. DOI: 10.5281/zenodo.3776875. URL: https://doi.org/10.5281/zenodo.3776875.

Liu, Hongwei, Maghoul, Pooneh, and Shalaby, Ahmed (2020b). "Laboratory-scale characterization of saturated soil samples through ultrasonic techniques". In: *Scientific Reports* 10.1, pp. 1–17.

Liu, Hongwei, Maghoul, Pooneh, and Shalaby, Ahmed (2021a). "A Poro-elastodynamic Forward Solver for Dispersion Analysis of Saturated Multilayer Systems". In: *International Conference of the International Association for Computer Methods and Advances in Geomechanics*. Springer, pp. 637–644.

Liu, Hongwei, Maghoul, Pooneh, and Shalaby, Ahmed (2021b). "Seismic physics-based characterization of permafrost sites using surface waves". In: *The Cryosphere, Under Review*.

Liu, Hongwei, Maghoul, Pooneh, Shalaby, Ahmed, Bahari, Ako, and Moradi, Farid (2020). "Integrated approach for the MASW dispersion analysis using the spectral element technique and trust region reflective method". In: *Computers and Geotechnics* 125, p. 103689.

Liu, Hongwei, Maghoul, Pooneh, Shalaby, Ahmed, and Douglas, Thomson (2021). "Pore-scale quantitative characterization of permafrost samples using ultrasonic waves". In: *Communications Engineering, Submitted*.

Liu, Xu, Greenhalgh, Stewart, and Zhou, Bing (2009). "Transient solution for poro-viscoacoustic wave propagation in double porosity media and its limitations". In: *Geophysical Journal International* 178.1, pp. 375–393.

Lorenzo, Juan M, Hicks, Jason, and Vera, Emilio E (2014). "Integrated seismic and cone penetration test observations at a distressed earthen levee: Marrero, Louisiana, USA". In: *Engineering Geology* 168, pp. 59–68.

Lowe, Michael JS (1995). "Matrix techniques for modeling ultrasonic waves in multilayered media". In: *IEEE Transactions on Ultrasonics, Ferroelectrics, and Frequency Control* 42.4, pp. 525–542.

Mackay, J Ross (1972). "The world of underground ice". In: *Annals of the Association of American Geographers* 62.1, pp. 1–22.

Maghoul, Pooneh and Gatmiri, Behrouz (2017). "Theory of a Time Domain Boundary Element Development for the Dynamic Analysis of Coupled Multiphase Porous Media". In: *Journal of Multiscale Modelling* 8.03n04, p. 1750007.

Maghoul, Pooneh, Gatmiri, Behrouz, and Duhamel, Denis (2011a). "Boundary integral formulation and two-dimensional fundamental solutions for dynamic behavior analysis of unsaturated soils". In: *Soil Dynamics and Earthquake Engineering* 31.11, pp. 1480–1495.

Maghoul, Pooneh, Gatmiri, Behrouz, and Duhamel, Denis (2011b). "Wave propagation in unsaturated poroelastic media: Boundary integral formulation and three-dimensional fundamental solution". In: *Computer Modelling in Engineering and Sciences* 78.1, pp. 51–76.

Malmgren, Lars, Saiang, David, Töyrä, Jimmy, and Bodare, Anders (2007). "The excavation disturbed zone (EDZ) at Kiirunavaara mine, Sweden—by seismic measurements". In: *Journal of Applied Geophysics* 61.1, pp. 1–15.

Manolis, George D (1983). "A comparative study on three boundary element method approaches to problems in elastodynamics". In: *International Journal for Numerical Methods in Engineering* 19.1, pp. 73–91.

Marescot, L, Loke, MH, Chapellier, D, Delaloye, R, Lambiel, C, and Reynard, E (2003). "Assessing reliability of 2D resistivity imaging in mountain permafrost studies using the depth of investigation index method". In: *Near Surface Geophysics* 1.2, pp. 57–67.

Mase, Thomas G. and Mase, George E. (2009). *Continuum mechanics for engineers*. CRC press.

Matin, MA, Akai, Daisuke, Kawazu, N, Hanebuchi, M, Sawada, K, and Ishida, M (2010). "FE modeling of stress and deflection of PZT actuated micro-mirror: Effect of crystal anisotropy". In: *Computational Materials Science* 48.2, pp. 349–359.

Matsushima, Jun, Suzuki, Makoto, Kato, Yoshibumi, Nibe, Takao, and Rokugawa, Shuichi (2008). "Laboratory experiments on compressional ultrasonic wave attenuation in partially frozen brines". In: *Geophysics* 73.2, N9–N18.

Mavko, Gary, Mukerji, Tapan, and Dvorkin, Jack (2020). *The rock physics handbook*. Cambridge university press.

Medina, Jimmy E, Buiochi, Flávio, and Adamowski, Júlio C (2006). "Numerical modeling of a circular piezoelectric ultrasonic transducer radiating in water". In: *ABCM symposium Series in Mechatronics*. Vol. 2, pp. 458–464.

Mok, Young-Jin, Kim, Jung-Han, and Kang, Byung-Soo (2003). "A pilot study of in-hole seismic method". In: *Journal of the Korean Geotechnical Society* 19.3, pp. 23–31.

Montgomery, James and Chen, Stephen (2010). "An analysis of the operation of differential evolution at high and low crossover rates". In: *IEEE congress on evolutionary computation*. IEEE, pp. 1–8.

Mulmi, Sarju, Sato, T, and Kuwano, R (2008). "Performance of plate type piezo-ceramic transducers for elastic wave measurements in laboratory soil specimens". In: *Seisan Kenkyu* 60.6, pp. 565–569.

Multiphysics, COMSOL (1998). "Introduction to COMSOL multiphysics®". In: *COMSOL Multiphysics, Burlington, MA* 9, p. 2018.

Munroe, Jeffrey S, Doolittle, Jim A, Kanevskiy, Mikhail Z, Hinkel, Kenneth M, Nelson, Frederick E, Jones, Benjamin M, Shur, Yuri, and Kimble, John M (2007). "Application of ground-penetrating radar imagery for three-dimensional visualisation of near-surface structures in ice-rich permafrost, Barrow, Alaska". In: *Permafrost and Periglacial Processes* 18.4, pp. 309–321.

Myers, Oliver J., Anjanappa, M, and Freidhoff, C.B (2010). "Numerical modeling of a circularly interdigitated piezoelectric microactuator". In: *Journal of Microelectromechanical Systems* 19.5, pp. 1098–1104.

Nazarian, Soheil and Stokoe, Kenneth H (1984). "Nondestructive testing of pavements using surface waves". In: *Transportation Research Record* 993, pp. 67–79.

Noborio, Kosuke (2001). "Measurement of soil water content and electrical conductivity by time domain reflectometry: a review". In: *Computers and Electronics in Agriculture* 31.3, pp. 213–237.

Nocedal, Jorge and Wright, Stephen (2006). *Numerical optimization*. Springer Science & Business Media.

Obrzud, Rafal (2012). "The hardening soil model: A practical guidebook". In: *PC100701 Report*.

Olafsdottir, Elin Asta, Erlingsson, Sigurdur, and Bessason, Bjarni (2017). "Tool for analysis of multichannel analysis of surface waves (MASW) field data and evaluation of shear wave velocity profiles of soils". In: *Canadian Geotechnical Journal* 55.2, pp. 217–233.

Overduin, Pier P, Haberland, Christian, Ryberg, Trond, Kneier, Fabian, Jacobi, Tim, Grigoriev, Mikhail N, and Ohrnberger, Matthias (2015). "Submarine permafrost depth from ambient seismic noise". In: *Geophysical Research Letters* 42.18, pp. 7581–7588.

Ozyazicioglu, Mehmet H and Ozkan, Yener M (2011). "A boundary element formulation for axi-symmetric problems in poro-elasticity". In: *Proceedings of the 33rd International Conference on Boundary Elements and Other Mesh Reduction Methods, CA Brebbia and V. Popov, Eds*, pp. 165–176.

O'Donovan, J, O'Sullivan, Catherine, and Marketos, G (2012). "Two-dimensional discrete element modelling of bender element tests on an idealised granular material". In: *Granular Matter* 14.6, pp. 733–747.

O'Donovan, J, O'sullivan, Catherine, Marketos, G, and Wood, D Muir (2015). "Analysis of bender element test interpretation using the discrete element method". In: *Granular Matter* 17.2, pp. 197–216.

Pan, Yudi, Xia, Jianghai, and Zeng, Chong (2013). "Verification of correctness of using real part of complex root as Rayleigh-wave phase velocity with synthetic data". In: *Journal of Applied Geophysics* 88, pp. 94–100.

Panneton, Raymond and Atalla, Noureddine (1997). "An efficient finite element scheme for solving the three-dimensional poroelasticity problem in acoustics". In: *The Journal of the Acoustical Society of America* 101.6, pp. 3287–3298.

Park, Choon Byong, Miller, Richard D, and Xia, Jianghai (1998). "Imaging dispersion curves of surface waves on multi-channel record". In: *SEG Technical Program Expanded Abstracts 1998*. Society of Exploration Geophysicists, pp. 1377–1380.

Pelton, John R (2005). "Near-surface seismology: Surface-based methods". In: *Near-surface geophysics*. Society of Exploration Geophysicists, pp. 219–264.

Périard, Yann, Gumiere, S José, Long, Bernard, Rousseau, Alain N, and Caron, Jean (2016). "Use of X-ray CT scan to characterize the evolution of the hydraulic properties of a soil under drainage conditions". In: *Geoderma* 279, pp. 22–30.

Peterson, Pearu (2009). "F2PY: a tool for connecting Fortran and Python programs". In: *International Journal of Computational Science and Engineering* 4.4, pp. 296–305.

Phillips, Phillip Joseph and Wheeler, Mary F (2008). "A coupling of mixed and discontinuous Galerkin finite-element methods for poroelasticity". In: *Computational Geosciences* 12.4, pp. 417–435.

Porter, Trevor J and Opel, Thomas (2020). "Recent advances in paleoclimatological studies of Arctic wedge-and pore-ice stable-water isotope records". In: *Permafrost and Periglacial Processes*.

Prat, Michel, Bisch, PH, Millard, A, Mestat, Ph, Pijaudier-Calot, G, et al. (1995). *La modélisation des ouvrages*.

Proceq (2006). *Operating Instructions–Concrete Test Hammer N*. Tech. rep. Schwerzenbach, Switzerland.

Rabbani, Vahid, Bahari, A, Hodaei, M, Maghoul, P, and Wu, N (2019). "Three-dimensional free vibration analysis of triclinic piezoelectric hollow cylinder". In: *Composites Part B: Engineering* 158, pp. 352–363.

Rajapakse, RKND and Senjuntichai, Teerapong (1995). "Dynamic response of a multilayered poroelastic medium". In: *Earthquake Engineering & Structural dynamics* 24.5, pp. 703–722.

Raymer, LL, Hunt, ER, and Gardner, John S (1980). "An improved sonic transit time-to-porosity transform". In: *SPWLA 21st annual logging symposium*. OnePetro.

Rehman, Faisal, El-Hady, Sherif M, Atef, Ali H, and Harbi, Hussein M (2016). "Multichannel analysis of surface waves (MASW) for seismic site characterization using 2D genetic algorithm at Bahrah area, Wadi Fatima, Saudi Arabia". In: *Arabian Journal of Geosciences* 9.8, p. 519.

Rizzi, SA and Doyle, JF (1992). "A spectral element approach to wave motion in layered solids". In: *ASME Transactions Journal of Vibration Acoustics* 114.4, pp. 569–577.

Robertson, Peter K (1986). "In situ testing and its application to foundation engineering". In: *Canadian Geotechnical Journal* 23.4, pp. 573–594.

Roblee, Clifford J, Stokoe, KH, Fuhriman, Mark D, and Nelson, Priscilla P (1994). "Crosshole SH-wave measurements in rock and soil". In: *Dynamic geotechnical testing II*. ASTM International.

Saenger, Erik H, Gold, Norbert, and Shapiro, Serge A (2000). "Modeling the propagation of elastic waves using a modified finite-difference grid". In: *Wave Motion* 31.1, pp. 77–92.

Sambridge, Malcolm (1999). "Geophysical inversion with a neighbourhood algorithm—I. Searching a parameter space". In: *Geophysical Journal International* 138.2, pp. 479–494.

Santos, Juan E and Sheen, Dongwoo (2007). "Finite element methods for the simulation of waves in composite saturated poroviscoelastic media". In: *SIAM Journal on Numerical Analysis* 45.1, pp. 389–420.

Scapozza, Cristian, Lambiel, Christophe, Baron, Ludovic, Marescot, Laurent, and Reynard, Emmanuel (2011). "Internal structure and permafrost distribution in two alpine periglacial talus slopes, Valais, Swiss Alps". In: *Geomorphology* 132.3-4, pp. 208–221.

Schanz, Martin and Antes, Heinz (1997). "A new visco-and elastodynamic time domain boundary element formulation". In: *Computational Mechanics* 20.5, pp. 452–459.

Schindler, Uwe, Durner, Wolfgang, Von Unold, G, Mueller, L, and Wieland, R (2010). "The evaporation method: Extending the measurement range of soil hydraulic properties using the air-entry pressure of the ceramic cup". In: *Journal of Plant Nutrition and Soil Science* 173.4, pp. 563–572.

Schnaid, Fernando, Odebrecht, Edgar, Rocha, Marcelo Maia, and Paula Bernardes, George de (2009). "Prediction of soil properties from the concepts of energy transfer in dynamic penetration tests". In: *Journal of geotechnical and geoenvironmental engineering* 135.8, pp. 1092–1100.

Schuur, Edward AG, McGuire, A David, Schädel, C, Grosse, Guido, Harden, JW, Hayes, Daniel J, Hugelius, Gustaf, Koven, Charles D, Kuhry, Peter, Lawrence, David M, et al. (2015). "Climate change and the permafrost carbon feedback". In: *Nature* 520.7546, pp. 171–179.

Schwab, FA and Knopoff, L (1972). "Fast surface wave and free mode computations". In: *Methods in Computational Physics: Advances in Research and Applications*. Vol. 11. Elsevier, pp. 87–180.

Soares, Delfim and Godinho, Luis (2020). "Nonlinear analysis of interacting saturated porous and elastic media by time-domain FEM/BEM iterative coupling procedures". In: *Engineering Analysis with Boundary Elements* 117, pp. 299–308.

Steeples, Don W and Miller, Richard D (1998). "Avoiding pitfalls in shallow seismic reflection surveys". In: *Geophysics* 63.4, pp. 1213–1224.

Stein, Jean and Kane, Douglas L (1983). "Monitoring the unfrozen water content of soil and snow using time domain reflectometry". In: *Water Resources Research* 19.6, pp. 1573–1584.

Storn, Rainer and Price, Kenneth (1997). "Differential evolution–a simple and efficient heuristic for global optimization over continuous spaces". In: *Journal of Global Optimization* 11.4, pp. 341–359.

Subcommittee, Permafrost (1988). "Glossary of permafrost and related ground-ice terms". In: *Associate Committee on Geotechnical Research, National Research Council of Canada, Ottawa* 156.

Takahashi, T, Takeuchi, T, and Sassa, K (2006). "ISRM suggested methods for borehole geophysics in rock engineering". In: *International Journal of Rock Mechanics and Mining Sciences* 43.3, pp. 337–368.

Testing, American Society for and Materials (2005). *Standard Test Methods for Laboratory Determination of Water (Moisture) Content of Soil and Rock by Mass: ASTM D 2216-05*. ASTM International.

Tillmann, A, Englert, A, Nyari, Zs, Fejes, I, Vanderborght, Jan, and Vereecken, H (2008). "Characterization of subsoil heterogeneity, estimation of grain size distribution and hydraulic conductivity at the Krauthausen test site using cone penetration test". In: *Journal of Contaminant Hydrology* 95.1-2, pp. 57–75.

Topp, Clarke G, Davis, James L, and Annan, Aa P (1980). "Electromagnetic determination of soil water content: Measurements in coaxial transmission lines". In: *Water resources research* 16.3, pp. 574–582.

Tosaya, Carol and Nur, Amos (1982). "Effects of diagenesis and clays on compressional velocities in rocks". In: *Geophysical Research Letters* 9.1, pp. 5–8.

Vanorio, Tiziana, Prasad, Manika, and Nur, Amos (2003). "Elastic properties of dry clay mineral aggregates, suspensions and sandstones". In: *Geophysical Journal International* 155.1, pp. 319–326.

Velichko, Alexander and Wilcox, Paul D (2010). "A generalized approach for efficient finite element modeling of elastodynamic scattering in two and three dimensions". In: *The Journal of the Acoustical Society of America* 128.3, pp. 1004–1014.

Viggiani, Giulia and Atkinson, JH (1995). "Interpretation of bender element tests". In: *Géotechnique* 45.1, pp. 149–154.

Wagner, Anna M, Lindsey, Nathaniel J, Dou, Shan, Gelvin, Arthur, Saari, Stephanie, Williams, Christopher, Ekblaw, Ian, Ulrich, Craig, Borglin, Sharon, Morales, Alejandro, et al. (2018). "Permafrost Degradation and Subsidence Observations during a Controlled Warming Experiment". In: *Scientific Reports* 8.1, pp. 1–9.

Wagner, FM, Mollaret, Coline, Günther, Thomas, Kemna, Andreas, and Hauck, C (2019). "Quantitative imaging of water, ice and air in permafrost systems through petrophysical joint inversion of seismic refraction and electrical resistivity data". In: *Geophysical Journal International* 219.3, pp. 1866–1875.

Wang, Da-yan, Zhu, Yuan-lin, Ma, Wei, and Niu, Yong-hong (2006). "Application of ultrasonic technology for physical–mechanical properties of frozen soils". In: *Cold Regions Science and Technology* 44.1, pp. 12–19.

Wang, Lugen and Rokhlin, SI (2001). "Stable reformulation of transfer matrix method for wave propagation in layered anisotropic media". In: *Ultrasonics* 39.6, pp. 413–424.

Wang, Songhe, Qi, Jilin, Yu, Fan, and Liu, Fengyin (2016). "A novel modeling of settlement of foundations in permafrost regions". In: *Geomechanics and Engineering* 10.2, pp. 225–245.

Wang, Xiangrong, Wang, Hui, Liang, Robert Y, Zhu, Hehua, and Di, Honggui (2018). "A hidden Markov random field model based approach for probabilistic site characterization using multiple cone penetration test data". In: *Structural Safety* 70, pp. 128–138.

Wang, Zhongqi, Lu, Yong, and Bai, Chunhua (2008). "Numerical analysis of blast-induced liquefaction of soil". In: *Computers and Geotechnics* 35.2, pp. 196–209.

Wathelet, Marc, Jongmans, D, and Ohrnberger, M (2004). "Surface-wave inversion using a direct search algorithm and its application to ambient vibration measurements". In: *Near surface geophysics* 2.4, pp. 211–221.

Wenzlau, Fabian and Müller, Tobias M (2009). "Finite-difference modeling of wave propagation and diffusion in poroelastic media". In: *Geophysics* 74.4, T55–T66.

Wiebe, Th and Antes, H (1991). "A time domain integral formulation of dynamic poroelasticity". In: *Acta Mechanica* 90.1-4, pp. 125–137.

Williams, KK, Haltigin, T, and Pollard, WH (2011). "Ground Penetrating Radar Detection of Ice Wedge Geometry: Implications for Climate Change Monitoring". In: *AGUFM* 2011, pp. C41C–0420.

Witharana, Chandi, Bhuiyan, Md Abul Ehsan, Liljedahl, Anna K, Kanevskiy, Mikhail, Epstein, Howard E, Jones, Benjamin M, Daanen, Ronald, Griffin, Claire G, Kent, Kelcy, and Jones, Melissa K Ward (2020). "Understanding the synergies of deep learning and data fusion of multispectral and panchromatic high resolution commercial satellite imagery for automated ice-wedge polygon detection". In: *ISPRS Journal of Photogrammetry and Remote Sensing* 170, pp. 174–191.

Wood, Clinton M, Cox, Brady R, Green, Russell A, Wotherspoon, Liam M, Bradley, Brendon A, and Cubrinovski, Misko (2017). "Vs-based evaluation of select liquefaction case histories from the 2010–2011 Canterbury earthquake sequence". In: *Journal of Geotechnical and Geoenvironmental Engineering* 143.9, p. 04017066.

Wu, Yuxin, Nakagawa, Seiji, Kneafsey, Timothy J, Dafflon, Baptiste, and Hubbard, Susan (2017). "Electrical and seismic response of saline permafrost soil during freeze-thaw transition". In: *Journal of Applied Geophysics* 146, pp. 16–26.

Wyllie, MRJ, Gardner, GHF, and Gregory, AR (1962). "Studies of elastic wave attenuation in porous media". In: *Geophysics* 27.5, pp. 569–589.

Xiao, Zean, Lai, Yuanming, and Zhang, Jun (2020). "A thermodynamic model for calculating the unfrozen water content of frozen soil". In: *Cold Regions Science and Technology* 172, p. 103011.

Xiu, Dongbin and Hesthaven, Jan S (2005). "High-order collocation methods for differential equations with random inputs". In: *SIAM Journal on Scientific Computing* 27.3, pp. 1118–1139.

Yao, Yanbin and Liu, Dameng (2012). "Comparison of low-field NMR and mercury intrusion porosimetry in characterizing pore size distributions of coals". In: *Fuel* 95, pp. 152–158.

Yoshikawa, Kenji and Overduin, Pier Paul (2005). "Comparing unfrozen water content measurements of frozen soil using recently developed commercial sensors". In: *Cold Regions Science and Technology* 42.3, pp. 250–256.

You, Yanhui, Yu, Qihao, Pan, Xicai, Wang, Xinbin, and Guo, Lei (2013). "Application of electrical resistivity tomography in investigating depth of permafrost base and permafrost structure in Tibetan Plateau". In: *Cold Regions Science and Technology* 87, pp. 19–26.

Youn, Jun-Ung, Choo, Y.W, and Kim, D.S (2008). "Measurement of small-strain shear modulus G max of dry and saturated sands by bender element, resonant column, and torsional shear tests". In: *Canadian Geotechnical Journal* 45.10, pp. 1426–1438.

Zahradník, Jiří and Priolo, Enrico (1995). "Heterogeneous formulations of elastodynamic equations and finite-difference schemes". In: *Geophysical Journal International* 120.3, pp. 663–676.

Zhang, Weixing, Witharana, Chandi, Liljedahl, Anna K, and Kanevskiy, Mikhail (2018). "Deep convolutional neural networks for automated characterization of arctic ice-wedge polygons in very high spatial resolution aerial imagery". In: *Remote Sensing* 10.9, p. 1487.

Zhang, Yu, Xu, Yixian, and Xia, Jianghai (2011). "Analysis of dispersion and attenuation of surface waves in poroelastic media in the exploration-seismic frequency band". In: *Geophysical Journal International* 187.2, pp. 871–888.

Zheng, Pei, Zhao, She-Xu, and Ding, Ding (2013). "Dynamic Green's functions for a poroelastic half-space". In: *Acta Mechanica* 224.1, pp. 17–39.

Zhou, Shunhua, He, Chao, and Di, Honggui (2016). "Dynamic 2.5-D green s function for a poroelastic half-space". In: *Engineering Analysis with Boundary Elements* 67, pp. 96–107.

Zhou, Shunhua, He, Chao, Di, Honggui, Guo, Peijun, and Zhang, Xiaohui (2017). "An efficient method for predicting train-induced vibrations from a tunnel in a poroelastic half-space". In: *Engineering Analysis with Boundary Elements* 85, pp. 43–56.

Zhou, Yan-guo, Chen, Y.M, and Ding, H.J (2007). "Analytical modeling of sandwich beam for piezoelectric bender elements". In: *Applied Mathematics and Mechanics* 28.12, p. 1581.

Zhou, Yan-guo, Chen, Y.M, Ding, H.J, and Chen, W.Q (2008). "Modeling of sensor function for piezoelectric bender elements". In: *Journal of Zhejiang University-SCIENCE A* 9.1, pp. 1–7.

Zomorodian, SM Ali and Hunaidi, Osama (2006). "Inversion of SASW dispersion curves based on maximum flexibility coefficients in the wave number domain". In: *Soil Dynamics and Earthquake Engineering* 26.8, pp. 735–752.

Appendix A and B are used in Chapters 5 and 6.

Appendix A

Parameters definition

The matrix $\boldsymbol{\rho}$, $\boldsymbol{b}$, $\boldsymbol{R}$ and $\boldsymbol{\mu}$ are shown as following:

$$\boldsymbol{\rho} = \begin{bmatrix} \rho_{11} & \rho_{12} & \rho_{13} \\ \rho_{12} & \rho_{22} & \rho_{23} \\ \rho_{13} & \rho_{23} & \rho_{33} \end{bmatrix} \quad \boldsymbol{b} = \begin{bmatrix} b_{12}+b_{13} & -b_{12} & -b_{13} \\ -b_{12} & b_{12}+b_{23} & -b_{23} \\ -b_{13} & -b_{23} & b_{13}+b_{23} \end{bmatrix}$$

$$\boldsymbol{R} = \begin{bmatrix} R_{11} & R_{12} & R_{13} \\ R_{12} & R_{22} & R_{23} \\ R_{13} & R_{23} & R_{33} \end{bmatrix} \quad \boldsymbol{\mu} = \begin{bmatrix} \mu_{11} & 0 & \mu_{13} \\ 0 & 0 & 0 \\ \mu_{13} & 0 & \mu_{33} \end{bmatrix}$$

where

$\rho_{13} = -(a_{13}-1)\phi_s\rho_s - (a_{31}-1)\phi_i\rho_i$:

$\rho_{33} = (a_{13}-1)\phi_s\rho_s + (a_{23}-1)\phi_w\rho_w + a_{31}\phi_i\rho_i$:

$\kappa_i = \kappa_{i0}\phi^3/[(1-s_r^2)(1-\phi)^3]$:

$\kappa_s = \kappa_{s0}s_r^3$:

$\mu_{13} = (1-g_1)(1-g_3)\mu_{av}$:

$\mu_{im} = \phi_i\mu_i/[1+\alpha\gamma(1-\phi_i)]$: shear modulus of the matrix formed by the ice

$\mu_{sm} = (1-\phi_w-\bar{\xi}\phi_i)\mu_s/[1+\alpha\gamma(\phi_w+\bar{\xi}\phi_i)]$: soil skeleton-frame shear modulus

$\rho_{12} = -(a_{12}-1)\phi_w\rho_w$:

$b_{13} = b_{13}^0(\phi_i\phi_s)^2$: friction coefficient between soil skeleton and ice matrix

$b_{23} = \eta_w\phi_w^2/\kappa_i$: friction coefficient between porewater and ice matrix

$c_1 = K_{sm}/(\phi_s K_s)$: consolidation coefficient for the soil skeleton

$c_3 = K_{im}/(\phi_i K_i)$: consolidation coefficient for the ice

$g_3 = \mu_{im}/(\phi_i\mu_i)$:

$K_1 = [(1-c_1)\phi_s]^2K_{av} + K_{sm}$:

$K_3 = [(1-c_3)\phi_i]^2K_{av} + K_{im}$:

$K_{im} = \phi_i K_i/[1+\alpha(1-\phi_i)]$: bulk modulus of the matrix formed by the ice

$K_{sm} = (1-\phi_w-\bar{\xi}\phi_i)K_s/[1+\alpha(\phi_w+\bar{\xi}\phi_i)]$: bulk modulus of the matrix formed by the solid phase

$R_{11} = [(1-c_1)\phi_s]^2K_{av} + K_{sm} + 4\mu_{11}/3$:

$Sc_2 = C_{13} - \frac{1}{3}\mu_{13}$:

$Sc_3 = K_3 - \frac{2}{3}\mu_3$:

$Sc_4 = C_{13} - \frac{1}{3}\mu_{13}$:

$\mu_{11} = [(1-g_1)\phi_s]^2\mu_{av} + \mu_{sm}$:

$\mu_{33} = [(1-g_3)\phi_i]^2\mu_{av} + \mu_{im}$:

$\rho_{11} = a_{13}\phi_s\rho_s + (a_{12}-1)\phi_w\rho_w + (a_{31}-1)\phi_i\rho_i$

$\rho_{22} = (a_{12}+a_{23}-1)\phi_w\rho_w$:

$\rho_{23} = -(a_{23}-1)\phi_w\rho_w$:

$a_{12} = r_{12}\frac{\phi_s(\phi_w\rho_w+\phi_i\rho_i)}{\phi_w\rho_w(\phi_w+\phi_i)} + 1$: tortuosity for water flowing through the soil skeleton

$a_{13} = r_{13}\frac{\phi_i(\phi_s\rho_s+\phi_i\rho_i)}{\phi_s\rho_s(\phi_s+\phi_i)} + 1$: tortuosity for solid grains flowing through the ice matrix

$a_{23} = r_{23}\frac{\phi_s(\phi_w\rho_w+\phi_s\rho_s)}{\phi_w\rho_w(\phi_w+\phi_s)} + 1$: tortuosity for water flowing through the ice matrix

$a_{31} = r_{31}\frac{\phi_s(\phi_s\rho_s+\phi_i\rho_i)}{\phi_i\rho_i(\phi_s+\phi_i)} + 1$: tortuosity for ice flowing through the rock frame

$b_{12} = \eta_w\phi_w^2/\kappa_s$: friction coefficient between soil skeleton and porewater

$g_1 = \mu_{sm}/(\phi_s\mu_s)$:

$R_{12} = (1-c_1)\phi_s\phi_w K_{av}$:

$R_{13} = (1-c_1)(1-c_3)\phi_s\phi_i K_{av} + 2\mu_{13}/3$:

$R_{22} = \phi_w^2 K_{av}$:

$R_{23} = (1-c_3)\phi_w\phi_i K_{av}$:

$R_{33} = [(1-c_3)\phi_i]^2 K_{av} + K_{im} + 4\mu_{33}/3$:

Appendix B

Spectral element matrix components

The components of $\mathbf{S_1}$ matrix are shown as following:

$S_1(1,1) = -kp_{11}$	$S_1(1,2) = -kp_{12}$
$S_1(1,3) = -kp_{13}$	$S_1(1,4) = k_{s1}q_{11}$
$S_1(1,5) = k_{s2}q_{12}$	$S_1(1,6) = kp_{11}\left(-e^{-hk_{p1}}\right)$
$S_1(1,7) = kp_{12}\left(-e^{-hk_{p2}}\right)$	$S_1(1,8) = kp_{13}\left(-e^{-hk_{p3}}\right)$
$S_1(1,9) = k_{s1}q_{11}\left(-e^{-hk_{s1}}\right)$	$S_1(1,10) = k_{s2}q_{12}\left(-e^{-hk_{s2}}\right)$

$S_1(2,1) = -k_{p1}p_{11}$	$S_1(2,2) = -k_{p2}p_{12}$
$S_1(2,3) = -k_{p3}p_{13}$	$S_1(2,4) = kq_{11}$
$S_1(2,5) = kq_{12}$	$S(2,6) = e^{-hk_{p1}}k_{p1}p_{11}$
$S_1(2,7) = e^{-hk_{p2}}k_{p2}p_{12}$	$S_1(2,8) = e^{-hk_{p3}}k_{p3}p_{13}$
$S_1(2,9) = e^{-hk_{s1}}kq_{11}$	$S_1(2,10) = e^{-hk_{s2}}kq_{12}$

$S_1(3,1) = -k_{p1}p_{21}$	$S(3,2) = -k_{p2}p_{22}$
$S_1(3,3) = -k_{p3}p_{23}$	$S_1(3,4) = k(G_1q_{11} + G_2q_{21})$
$S_1(3,5) = k(G_1q_{12} + G_2q_{22})$	$S_1(3,6) = e^{-hk_{p1}}k_{p1}p_{21}$
$S_1(3,7) = e^{-hk_{p2}}k_{p2}p_{22}$	$S_1(3,8) = e^{-hk_{p3}}k_{p3}p_{23}$
$S_1(3,9) = e^{-hk_{s1}}k(G_1q_{11} + G_2q_{21})$	$S_1(3,10) = e^{-hk_{s2}}k(G_1q_{12} + G_2q_{22})$

$S_1(4,1) = -k_{p1}p_{21}$	$S(4,2) = -k_{p2}p_{22}$
$S_1(4,3) = -k_{p3}p_{23}$	$S_1(4,4) = k(G_1q_{11} + G_2q_{21})$
$S_1(4,5) = k(G_1q_{12} + G_2q_{22})$	$S_1(4,6) = e^{-hk_{p1}}k_{p1}p_{21}$
$S_1(4,7) = e^{-hk_{p2}}k_{p2}p_{22}$	$S_1(4,8) = e^{-hk_{p3}}k_{p3}p_{23}$
$S_1(4,9) = e^{-hk_{s1}}k(G_1q_{11} + G_2q_{21})$	$S_1(4,10) = e^{-hk_{s2}}k(G_1q_{12} + G_2q_{22})$

$S_1(5,1) = -k_{p1}p_{21}$	$S(5,2) = -k_{p2}p_{22}$
$S_1(5,3) = -k_{p3}p_{23}$	$S_1(5,4) = k(G_1q_{11} + G_2q_{21})$
$S_1(5,5) = k(G_1q_{12} + G_2q_{22})$	$S_1(5,6) = e^{-hk_{p1}}k_{p1}p_{21}$
$S_1(5,7) = e^{-hk_{p2}}k_{p2}p_{22}$	$S_1(5,8) = e^{-hk_{p3}}k_{p3}p_{23}$
$S_1(5,9) = e^{-hk_{s1}}k(G_1q_{11} + G_2q_{21})$	$S_1(5,10) = e^{-hk_{s2}}k(G_1q_{12} + G_2q_{22})$

$S_1(6,1) = -k_{p1}p_{21}$	$S(6,2) = -k_{p2}p_{22}$
$S_1(6,3) = -k_{p3}p_{23}$	$S_1(6,4) = k(G_1q_{11} + G_2q_{21})$
$S_1(6,5) = k(G_1q_{12} + G_2q_{22})$	$S_1(6,6) = e^{-hk_{p1}}k_{p1}p_{21}$
$S_1(6,7) = e^{-hk_{p2}}k_{p2}p_{22}$	$S_1(6,8) = e^{-hk_{p3}}k_{p3}p_{23}$
$S_1(6,9) = e^{-hk_{s1}}k(G_1q_{11} + G_2q_{21})$	$S_1(6,10) = e^{-hk_{s2}}k(G_1q_{12} + G_2q_{22})$

$S_1(7,1) = -k_{p1}p_{21}$	$S(7,2) = -k_{p2}p_{22}$
$S_1(7,3) = -k_{p3}p_{23}$	$S_1(7,4) = k(G_1q_{11} + G_2q_{21})$
$S_1(7,5) = k(G_1q_{12} + G_2q_{22})$	$S_1(7,6) = e^{-hk_{p1}}k_{p1}p_{21}$
$S_1(7,7) = e^{-hk_{p2}}k_{p2}p_{22}$	$S_1(7,8) = e^{-hk_{p3}}k_{p3}p_{23}$
$S_1(7,9) = e^{-hk_{s1}}k(G_1q_{11} + G_2q_{21})$	$S_1(7,10) = e^{-hk_{s2}}k(G_1q_{12} + G_2q_{22})$

$S_1(8,1) = -k_{p1}p_{21}$	$S(8,2) = -k_{p2}p_{22}$
$S_1(8,3) = -k_{p3}p_{23}$	$S_1(8,4) = k(G_1q_{11} + G_2q_{21})$
$S_1(8,5) = k(G_1q_{12} + G_2q_{22})$	$S_1(8,6) = e^{-hk_{p1}}k_{p1}p_{21}$
$S_1(8,7) = e^{-hk_{p2}}k_{p2}p_{22}$	$S_1(8,8) = e^{-hk_{p3}}k_{p3}p_{23}$
$S_1(8,9) = e^{-hk_{s1}}k(G_1q_{11} + G_2q_{21})$	$S_1(8,10) = e^{-hk_{s2}}k(G_1q_{12} + G_2q_{22})$

$S_1(9,1) = -k_{p1}p_{21}$	$S(9,2) = -k_{p2}p_{22}$
$S_1(9,3) = -k_{p3}p_{23}$	$S_1(9,4) = k(G_1q_{11} + G_2q_{21})$
$S_1(9,5) = k(G_1q_{12} + G_2q_{22})$	$S_1(9,6) = e^{-hk_{p1}}k_{p1}p_{21}$
$S_1(9,7) = e^{-hk_{p2}}k_{p2}p_{22}$	$S_1(9,8) = e^{-hk_{p3}}k_{p3}p_{23}$
$S_1(9,9) = e^{-hk_{s1}}k(G_1q_{11} + G_2q_{21})$	$S_1(9,10) = e^{-hk_{s2}}k(G_1q_{12} + G_2q_{22})$

$S_1(10,1) = -k_{p1}p_{21}$	$S(10,2) = -k_{p2}p_{22}$
$S_1(10,3) = -k_{p3}p_{23}$	$S_1(10,4) = k(G_1q_{11} + G_2q_{21})$
$S_1(10,5) = k(G_1q_{12} + G_2q_{22})$	$S_1(10,6) = e^{-hk_{p1}}k_{p1}p_{21}$
$S_1(10,7) = e^{-hk_{p2}}k_{p2}p_{22}$	$S_1(10,8) = e^{-hk_{p3}}k_{p3}p_{23}$
$S_1(10,9) = e^{-hk_{s1}}k(G_1q_{11} + G_2q_{21})$	$S_1(10,10) = e^{-hk_{s2}}k(G_1q_{12} + G_2q_{22})$

The components of $\boldsymbol{S_2}$ stress matrix are shown as following:

$$
\begin{aligned}
S_2(1,1) &= kk_{p1}(2p_{11}\mu_1 + p_{31}\mu_{13}) \\
S_2(1,2) &= kk_{p2}(2p_{12}\mu_1 + p_{32}\mu_{13}) \\
S_2(1,3) &= kk_{p3}(2p_{13}\mu_1 + p_{33}\mu_{13}) \\
S_2(1,4) &= -\tfrac{1}{2}\left(k^2 + k_{s1}^2\right)(2q_{11}\mu_1 + q_{21}\mu_{13}) \\
S_2(1,5) &= -\tfrac{1}{2}\left(k^2 + k_{s2}^2\right)(2q_{12}\mu_1 + q_{22}\mu_{13}) \\
S_2(1,6) &= -e^{-hk_{p1}}kk_{p1}(2p_{11}\mu_1 + p_{31}\mu_{13}) \\
S_2(1,7) &= e^{-hk_{p2}}kk_{p2}(2p_{12}\mu_1 + p_{32}\mu_{13}) \\
S_2(1,8) &= -e^{-hk_{p3}}kk_{p3}(2p_{13}\mu_1 + p_{33}\mu_{13}) \\
S_2(1,9) &= -\tfrac{1}{2}e^{-hk_{s1}}\left(k^2 + k_{s1}^2\right)(2q_{11}\mu_1 + q_{21}\mu_{13}) \\
S_2(1,10) &= -\tfrac{1}{2}e^{-hk_{s2}}\left(k^2 + k_{s2}^2\right)(2q_{12}\mu_1 + q_{22}\mu_{13})
\end{aligned}
$$

$$
\begin{aligned}
S_2(2,1) &= -(p_{11}S_{c1} + p_{31}S_{c2})k^2 + C_{12}\left(k_{p1}^2 - k^2\right)p_{21} + k_{p1}^2(p_{11}(S_{c1} + 2\mu_1) + p_{31}(S_{c2} + \mu_{13})) \\
S_2(2,2) &= -(p_{12}S_{c1} + p_{32}S_{c2})k^2 + C_{12}\left(k_{p2}^2 - k^2\right)p_{22} + k_{p2}^2(p_{12}(S_{c1} + 2\mu_1) + p_{32}(S_{c2} + \mu_{13})) \\
S_2(2,3) &= -(p_{13}S_{c1} + p_{33}S_{c2})k^2 + C_{12}\left(k_{p3}^2 - k^2\right)p_{23} + k_{p3}^2(p_{13}(S_{c1} + 2\mu_1) + p_{33}(S_{c2} + \mu_{13})) \\
S_2(2,4) &= kk_{s1}(2q_{11}\mu_1 + q_{21}\mu_{13}) \\
S_2(2,5) &= kk_{s2}(2q_{12}\mu_1 + q_{22}\mu_{13}) \\
S_2(2,6) &= e^{-hk_{p1}}\left(-(p_{11}S_{c1} + p_{31}S_{c2})k^2 + C_{12}\left(k_{p1}^2 - k^2\right)p_{21} + k_{p1}^2(p_{11}(S_{c1} + 2\mu_1) + p_{31}(S_{c2} + \mu_{13}))\right) \\
S_2(2,7) &= e^{-hk_{p2}}\left(-(p_{12}S_{c1} + p_{32}S_{c2})k^2 + C_{12}\left(k_{p2}^2 - k^2\right)p_{22} + k_{p2}^2(p_{12}(S_{c1} + 2\mu_1) + p_{32}(S_{c2} + \mu_{13}))\right) \\
S_2(2,8) &= e^{-hk_{p3}}\left(-(p_{13}S_{c1} + p_{33}S_{c2})k^2 + C_{12}\left(k_{p3}^2 - k^2\right)p_{23} + k_{p3}^2(p_{13}(S_{c1} + 2\mu_1) + p_{33}(S_{c2} + \mu_{13}))\right) \\
S_2(2,9) &= e^{-hk_{s1}}kk_{s1}(2q_{11}\mu_1 + q_{21}\mu_{13}) \\
S_2(2,10) &= e^{-hk_{s2}}kk_{s2}(2q_{12}\mu_1 + q_{22}\mu_{13})
\end{aligned}
$$

$$
\begin{aligned}
S_2(3,1) &= (k_{p1} - k)(k + k_{p1})(C_{12}p_{11} + k_2p_{21} + C_{23}p_{31}) \\
S_2(3,2) &= -(k - k_{p2})(k + k_{p2})(C_{12}p_{12} + k_2p_{22} + C_{23}p_{32}) \\
S_2(3,3) &= -(k - k_{p3})(k + k_{p3})(C_{12}p_{13} + k_2p_{23} + C_{23}P_{33}) \\
S_2(3,4) &= 0 \\
S_2(3,5) &= 0 \\
S_2(3,6) &= e^{-hk_{p1}}(k_{p1} - k)(k + k_{p1})(C_{12}p_{11} + k_2p_{21} + C_{23}p_{31}) \\
S_2(3,7) &= e^{-hk_{p2}}(k_{p2} - k)(k + k_{p2})(C_{12}p_{12} + k_2p_{22} + C_{23}p_{32}) \\
S_2(3,8) &= e^{-hk_{p3}}(k_{p3} - k)(k + k_{p3})(C_{12}p_{13} + k_2p_{23} + C_{23}P_{33}) \\
S_2(3,9) &= 0 \\
S_2(3,10) &= 0
\end{aligned}
$$

$$
\begin{aligned}
S_2(4,1) &= kk_{p1}(p_{11}\mu_{13} + 2p_{31}\mu_3) \\
S_2(4,2) &= kk_{p2}(p_{12}\mu_{13} + 2p_{32}\mu_3) \\
S_2(4,3) &= kk_{p3}(p_{13}\mu_{13} + 2P_{33}\mu_3) \\
S_2(4,4) &= -\tfrac{1}{2}\left(k^2 + k_{s1}^2\right)(q_{11}\mu_{13} + 2q_{21}\mu_3) \\
S_2(4,5) &= -\tfrac{1}{2}\left(k^2 + k_{s2}^2\right)(q_{12}\mu_{13} + 2q_{22}\mu_3) \\
S_2(4,6) &= -e^{-hk_{p1}}kk_{p1}(p_{11}\mu_{13} + 2p_{31}\mu_3) \\
S_2(4,7) &= -e^{-hk_{p2}}kk_{p2}(p_{12}\mu_{13} + 2p_{32}\mu_3) \\
S_2(4,8) &= -e^{-hk_{p3}}kk_{p3}(p_{13}\mu_{13} + 2P_{33}\mu_3) \\
S_2(4,9) &= -\tfrac{1}{2}e^{-hk_{s1}}\left(k^2 + k_{s1}^2\right)(q_{11}\mu_{13} + 2q_{21}\mu_3) \\
S_2(4,10) &= -\tfrac{1}{2}e^{-hk_{s2}}\left(k^2 + k_{s2}^2\right)(q_{12}\mu_{13} + 2q_{22}\mu_3)
\end{aligned}
$$

$$
\begin{aligned}
S_2(5,1) &= -(p_{31}S_{c3} + p_{11}S_{c4})k^2 + C_{23}\left(k_{p1}^2 - k^2\right)p_{21} + k_{p1}^2(p_{11}(S_{c4} + \mu_{13}) + p_{31}(S_{c3} + 2\mu_3)) \\
S_2(5,2) &= -(p_{32}S_{c3} + p_{12}S_{c4})k^2 + C_{23}\left(k_{p2}^2 - k^2\right)p_{22} + k_{p2}^2(p_{12}(S_{c4} + \mu_{13}) + p_{32}(S_{c3} + 2\mu_3)) \\
S_2(5,3) &= -(P_{33}S_{c3} + p_{13}S_{c4})k^2 + C_{23}\left(k_{p3}^2 - k^2\right)p_{23} + k_{p3}^2(p_{13}(S_{c4} + \mu_{13}) + p_{33}(S_{c3} + 2\mu_3)) \\
S_2(5,4) &= -kk_{s1}(q_{11}\mu_{13} + 2q_{21}\mu_3) \\
S_2(5,5) &= -kk_{s2}(q_{12}\mu_{13} + 2q_{22}\mu_3) \\
S_2(5,6) &= e^{-hk_{p1}}\left(-(p_{31}S_{c3} + p_{11}S_{c4})k^2 + C_{23}\left(k_{p1}^2 - k^2\right)p_{21} + k_{p1}^2(p_{11}(S_{c4} + \mu_{13}) + p_{31}(S_{c3} + 2\mu_3))\right) \\
S_2(5,7) &= e^{-hk_{p2}}\left(-(p_{32}S_{c3} + p_{12}S_{c4})k^2 + C_{23}\left(k_{p2}^2 - k^2\right)p_{22} + k_{p2}^2(p_{12}(S_{c4} + \mu_{13}) + p_{32}(S_{c3} + 2\mu_3))\right) \\
S_2(5,8) &= e^{-hk_{p3}}\left(-(P_{33}S_{c3} + p_{13}S_{c4})k^2 + C_{23}\left(k_{p3}^2 - k^2\right)p_{23} + k_{p3}^2(p_{13}(S_{c4} + \mu_{13}) + p_{33}(S_{c3} + 2\mu_3))\right) \\
S_2(5,9) &= e^{-hk_{s1}}kk_{s1}(q_{11}\mu_{13} + 2q_{21}\mu_3) \\
S_2(5,10) &= e^{-hk_{s2}}kk_{s2}(q_{12}\mu_{13} + 2q_{22}\mu_3)
\end{aligned}
$$

$$
\begin{aligned}
S_2(6,1) &= kk_{p1}e^{-hk_{p1}}(2\mu_1 p_{11} + \mu_{13}p_{31}) \\
S_2(6,2) &= kk_{p2}e^{-hk_{p2}}(2\mu_1 p_{12} + \mu_{13}p_{32}) \\
S_2(6,3) &= kk_{p3}e^{-hk_{p3}}(2\mu_1 p_{13} + \mu_{13}p_{33}) \\
S_2(6,4) &= -\tfrac{1}{2}e^{-hk_{s1}}\left(k^2 + k_{s1}^2\right)(2\mu_1 q_{11} + \mu_{13}q_{21}) \\
S_2(6,5) &= -\tfrac{1}{2}e^{-hk_{s2}}\left(k^2 + k_{s2}^2\right)(2\mu_1 q_{12} + \mu_{13}q_{22}) \\
S_2(6,6) &= -kk_{p1}(2\mu_1 p_{11} + \mu_{13}p_{31}) \\
S_2(6,7) &= -kk_{p2}(2\mu_1 p_{12} + \mu_{13}p_{32}) \\
S_2(6,8) &= -kk_{p3}(2\mu_1 p_{13} + \mu_{13}p_{33}) \\
S_2(6,9) &= -\tfrac{1}{2}\left(k^2 + k_{s1}^2\right)(2\mu_1 q_{11} + \mu_{13}q_{21}) \\
S_2(6,10) &= -\tfrac{1}{2}\left(k^2 + k_{s2}^2\right)(2\mu_1 q_{12} + \mu_{13}q_{22})
\end{aligned}
$$

$$
\begin{aligned}
S_2(7,1) &= e^{-hk_{p1}}\left(-(p_{11}S_{c1}+p_{31}S_{c2})k^2+C_{12}\left(k_{p1}^2-k^2\right)p_{21}+k_{p1}^2(p_{11}(S_{c1}+2\mu_1)+p_{31}(S_{c2}+\mu_{13}))\right)\\
S_2(7,2) &= e^{-hk_{p2}}\left(-(p_{12}S_{c1}+p_{32}S_{c2})k^2+C_{12}\left(k_{p2}^2-k^2\right)p_{22}+k_{p2}^2(p_{12}(S_{c1}+2\mu_1)+p_{32}(S_{c2}+\mu_{13}))\right)\\
S_2(7,3) &= e^{-hk_{p3}}\left(-(p_{13}S_{c1}+p_{33}S_{c2})k^2+C_{12}\left(k_{p3}^2-k^2\right)p_{23}+k_{p3}^2(p_{13}(S_{c1}+2\mu_1)+p_{33}(S_{c2}+\mu_{13}))\right)\\
S_2(7,4) &= -e^{-hk_{s1}}kk_{s1}(2q_{11}\mu_1+q_{21}\mu_{13})\\
S_2(7,5) &= -e^{-hk_{s2}}kk_{s2}(2q_{12}\mu_1+q_{22}\mu_{13})\\
S_2(7,6) &= -(p_{11}S_{c1}+p_{31}S_{c2})k^2+C_{12}\left(k_{p1}^2-k^2\right)p_{21}+k_{p1}^2(p_{11}(S_{c1}+2\mu_1)+p_{31}(S_{c2}+\mu_{13}))\\
S_2(7,7) &= -(p_{12}S_{c1}+p_{32}S_{c2})k^2+C_{12}\left(k_{p2}^2-k^2\right)p_{22}+k_{p2}^2(p_{12}(S_{c1}+2\mu_1)+p_{32}(S_{c2}+\mu_{13}))\\
S_2(7,8) &= -(p_{13}S_{c1}+p_{33}S_{c2})k^2+C_{12}\left(k_{p3}^2-k^2\right)p_{23}+k_{p3}^2(p_{13}(S_{c1}+2\mu_1)+p_{33}(S_{c2}+\mu_{13}))\\
S_2(7,9) &= kk_{s1}(2q_{11}\mu_1+q_{21}\mu_{13})\\
S_2(7,10) &= kk_{s2}(2q_{12}\mu_1+q_{22}\mu_{13})
\end{aligned}
$$

$$
\begin{aligned}
S_2(8,1) &= e^{-hk_{p1}}(k_{p1}-k)(k+k_{p1})(C_{12}p_{11}+k_2p_{21}+C_{23}p_{31})\\
S_2(8,2) &= e^{-hk_{p2}}(k_{p2}-k)(k+k_{p2})(C_{12}p_{12}+k_2p_{22}+C_{23}p_{32})\\
S_2(8,3) &= e^{-hk_{p3}}(k_{p3}-k)(k+k_{p3})(C_{12}p_{13}+k_2p_{23}+C_{23}P_{33})\\
S_2(8,4) &= 0\\
S_2(8,5) &= 0\\
S_2(8,6) &= (k_{p1}-k)(k+k_{p1})(C_{12}p_{11}+k_2p_{21}+C_{23}p_{31})\\
S_2(8,7) &= (k_{p2}-k)(k+k_{p2})(C_{12}p_{12}+k_2p_{22}+C_{23}p_{32})\\
S_2(8,8) &= (k_{p3}-k)(k+k_{p3})(C_{12}p_{13}+k_2p_{23}+C_{23}P_{33})\\
S_2(8,9) &= 0\\
S_2(8,10) &= 0
\end{aligned}
$$

$$
\begin{aligned}
S_2(9,1) &= kk_{p1}e^{-hk_{p1}}(\mu_{13}p_{11}+2\mu_3p_{31})\\
S_2(9,2) &= kk_{p2}e^{-hk_{p2}}(\mu_{13}p_{12}+2\mu_3p_{32})\\
S_2(9,3) &= kk_{p3}e^{-hk_{p3}}(\mu_{13}p_{13}+2\mu_3p_{33})\\
S_2(9,4) &= -\tfrac{1}{2}e^{-hk_{s1}}\left(k^2+k_{s1}^2\right)(\mu_{13}q_{11}+2\mu_3q_{21})\\
S_2(9,5) &= -\tfrac{1}{2}e^{-hk_{s2}}\left(k^2+k_{s2}^2\right)(\mu_{13}q_{12}+2\mu_3q_{22})\\
S_2(9,6) &= -kk_{p1}(\mu_{13}p_{11}+2\mu_3p_{31})\\
S_2(9,7) &= -kk_{p2}(\mu_{13}p_{12}+2\mu_3p_{32})\\
S_2(9,8) &= -kk_{p3}(\mu_{13}p_{13}+2\mu_3p_{33})\\
S_2(9,9) &= -\tfrac{1}{2}\left(k^2+k_{s1}^2\right)(\mu_{13}q_{11}+2\mu_3q_{21})\\
S_2(9,10) &= -\tfrac{1}{2}\left(k^2+k_{s2}^2\right)(\mu_{13}q_{12}+2\mu_3q_{22})
\end{aligned}
$$

$$S_2(10,1) = e^{-hk_{p1}}\left(-(p_{31}S_{c3}+p_{11}S_{c4})k^2 + C_{23}\left(k_{p1}^2-k^2\right)p_{21} + k_{p1}^2(p_{11}(S_{c4}+\mu_{13})+p_{31}(S_{c3}+2\mu_3))\right)$$
$$S_2(10,2) = e^{-hk_{p2}}\left(-(p_{32}S_{c3}+p_{12}S_{c4})k^2 + C_{23}\left(k_{p2}^2-k^2\right)p_{22} + k_{p2}^2(p_{12}(S_{c4}+\mu_{13})+p_{32}(S_{c3}+2\mu_3))\right)$$
$$S_2(10,3) = e^{-hk_{p3}}\left(-(P_{33}S_{c3}+p_{13}S_{c4})k^2 + C_{23}\left(k_{p3}^2-k^2\right)p_{23} + k_{p3}^2(p_{13}(S_{c4}+\mu_{13})+p_{33}(S_{c3}+2\mu_3))\right)$$
$$S_2(10,4) = -e^{-hk_{s1}}kk_{s1}(q_{11}\mu_{13}+2q_{21}\mu_3)$$
$$S_2(10,5) = -e^{-hk_{s2}}kk_{s2}(q_{12}\mu_{13}+2q_{22}\mu_3)$$
$$S_2(10,6) = -(p_{31}S_{c3}+p_{11}S_{c4})k^2 + C_{23}\left(k_{p1}^2-k^2\right)p_{21} + k_{p1}^2(p_{11}(S_{c4}+\mu_{13})+p_{31}(S_{c3}+2\mu_3))$$
$$S_2(10,7) = -(p_{32}S_{c3}+p_{12}S_{c4})k^2 + C_{23}\left(k_{p2}^2-k^2\right)p_{22} + k_{p2}^2(p_{12}(S_{c4}+\mu_{13})+p_{32}(S_{c3}+2\mu_3))$$
$$S_2(10,8) = -(P_{33}S_{c3}+p_{13}S_{c4})k^2 + C_{23}\left(k_{p3}^2-k^2\right)p_{23} + k_{p3}^2(p_{13}(S_{c4}+\mu_{13})+p_{33}(S_{c3}+2\mu_3))$$
$$S_2(10,9) = kk_{s1}(q_{11}\mu_{13}+2q_{21}\mu_3)$$
$$S_2(10,10) = kk_{s2}(q_{12}\mu_{13}+2q_{22}\mu_3)$$